



**HAL**  
open science

# Development and analysis of methods for quantifying nucleation kinetics in agitated crystallizers and microfluidic systems

Ruel Cedeno

► **To cite this version:**

Ruel Cedeno. Development and analysis of methods for quantifying nucleation kinetics in agitated crystallizers and microfluidic systems. Materials Science [cond-mat.mtrl-sci]. Aix-Marseille Université, France; VISTEC, Thailand, 2021. English. NNT : 2021AIXM0373 . tel-03634067

**HAL Id: tel-03634067**

**<https://theses.hal.science/tel-03634067v1>**

Submitted on 7 Apr 2022

**HAL** is a multi-disciplinary open access archive for the deposit and dissemination of scientific research documents, whether they are published or not. The documents may come from teaching and research institutions in France or abroad, or from public or private research centers.

L'archive ouverte pluridisciplinaire **HAL**, est destinée au dépôt et à la diffusion de documents scientifiques de niveau recherche, publiés ou non, émanant des établissements d'enseignement et de recherche français ou étrangers, des laboratoires publics ou privés.



Distributed under a Creative Commons Attribution - NonCommercial - NoDerivatives 4.0 International License

# THÈSE DE DOCTORAT

Soutenue à Aix-Marseille Université  
en cotutelle avec VISTEC  
le 27 septembre 2021 par

## Ruel Cedeno

### Development and Analysis of Methods for Quantifying Nucleation Kinetics in Agitated Crystallizers and Microfluidic Systems

<b>Discipline</b> Physique et science de la matière	•	<b>Composition du jury</b> Tom LEYSSENS	Rapporteur
<b>Spécialité</b> Matière Condensée et Nanosciences	•	Université Catholique de Louvain	
<b>École doctorale</b> ED 352	•	Haiyan QU	Rapporteuse
<b>Laboratoire/Partenaires de recherche</b> Vidyasirimedhi Institute of Science and Technology (VISTEC)	•	University of Southern Denmark	
	•	Fabienne ESPITALIER	Examinatrice
	•	IMT-Mines Albi	
	•	Sareeya BUREEKAEW	Examinatrice
	•	VISTEC	
	•	Stéphane VEESLER	Directeur de thèse
	•	Université d'Aix-Marseille – CNRS	
	•	Adrian FLOOD	Directeur de thèse
	•	VISTEC	
	•	Nadine CANDONI	Codirectrice de thèse
	•	Université d'Aix-Marseille – CNRS	
	•	Romain GROSSIER	Invité
	•	CINaM – CNRS	

# Affidavit

I, undersigned, Ruel Cedeno, hereby declare that the work presented in this manuscript is my own work, carried out under the scientific direction of Stéphane Veessler, Adrian Flood, and Nadine Candoni, in accordance with the principles of honesty, integrity and responsibility inherent to the research mission. The research work and the writing of this manuscript have been carried out in compliance with both the French national charter for Research Integrity and the Aix-Marseille University charter on the fight against plagiarism.

This work has not been submitted previously either in this country or in another country in the same or in a similar version to any other examination body.

Place : Marseille 13009

Date : 27 septembre 2021



Cette œuvre est mise à disposition selon les termes de la [Licence Creative Commons Attribution - Pas d'Utilisation Commerciale - Pas de Modification 4.0 International](https://creativecommons.org/licenses/by-nc-nd/4.0/).

# List of Publications and Conferences

## Journal Articles

1. **Cedeno, R.**; Maosoongnern, S.; Flood, A.,  
Direct Measurements of Primary Nucleation Rates of p-Aminobenzoic Acid and Glutamic Acid and Comparison with Predictions from Induction Time Distributions.  
*Industrial & Engineering Chemistry Research* 2018, 57 (51), 17504-17515.
2. **Cedeno, R.**; Grossier, R.; Nerini, D.; Lagaize, M.; Candoni, N.; Flood, A.; Veessler, S.,  
Nucleation in Sessile Microdroplets: New Approach for Measuring Induction Time.  
*In preparation for submission*
3. **Cedeno, R.**; Grossier, R.; Lagaize, M.; Candoni, N.; Flood, A.; Veessler, S.,  
Evaporation Dynamics of Sessile Saline Droplets in Oil.  
*In preparation for submission*
4. **Cedeno, R.**; Grossier, R.; Lagaize, M.; Candoni, N.; Flood, A.; Veessler, S.,  
Nucleation Kinetics of Aqueous NaCl via Stochastic Approach  
*In preparation for submission*

## Conferences

1. **Oral Presentation** in French Crystallographic Association 2021. Grenoble, France, 29 June to 2 July 2021. Microdroplet Approach for Quantifying Nucleation Kinetics.
2. **Oral Presentation** in Asian Crystallization Technology Symposium ACTS 2021. Thailand, 26-28 May 2021. Quantifying Nucleation Kinetics via Sessile Microdroplet Approach.
3. **Oral Presentation** in Journées CRISTECH 2020. Ecully, France, 14-16 October 2020, Quantifying Nucleation Kinetics: A Multiscale Approach.
4. **Oral Presentation** in International Symposium on Industrial Crystallization. Germany, 30 August to 2 September 2021. Measuring Nucleation Rates via Sessile Microdroplet Approach : Influence of Diffusive Interactions.
5. **Oral Presentation** in American Conference on Crystal Growth and Epitaxy. USA, 2-4 August 2021. Quantifying Nucleation Kinetics via Sessile Microdroplet Approach.

# Abstract

Nucleation is a key step in crystallization processes which is a crucial unit operation in the manufacture and purification of products, occurring in almost all sorts of industries including foods, pharmaceuticals, cosmetics, fine chemicals, ceramics, metallurgy and electronics. Thus, fundamental understanding of its nucleation kinetics is of immense importance yet it remains poorly understood from both experimental and theoretical perspective. With these motivations, this thesis seeks to develop innovative methods in quantifying nucleation kinetics both in industrially-relevant agitated crystallizers and in fundamentally-oriented microfluidic systems. Starting with agitated crystallizers, a protocol for estimating primary nucleation was developed based on laser backscattering which involves extrapolating the nucleation rates to zero agitation. To validate the approach, a multiscale investigation of nucleation kinetic parameters was performed using various techniques in L, mL, and  $\mu\text{L}$  scales. This sheds light into the transferability of kinetic data for engineering purposes. To focus on the fundamental aspects of nucleation, an approach to extract nucleation kinetic parameters from evaporative microcrystallizers was developed, using microdroplets at pL scale. This involves the measurement of induction time via deliquescence-efflorescence cycle, the derivation of evaporation model to accurately determine the supersaturation at nucleation, and the use of a modified Poisson distribution to model the stochastic nature of nucleation and extract nucleation kinetic parameters. The combination of these three developments have led to a successful quantification of nucleation kinetic parameters in evaporating microdroplets (i.e; at variable supersaturation), demonstrating a remarkable agreement between theory and experiment.

*Keywords: nucleation, induction time, microfluidics, sessile microdroplets, stochastic*

# Résumé

La nucléation est une étape essentielle dans le processus de cristallisation, qui est notamment utilisé pour la fabrication et la purification de produits industriels (pharmaceutiques, cosmétiques, de chimie fine, alimentaires, céramiques, de métallurgie et d'électronique). Cependant, il reste encore des questions fondamentales, notamment sur la cinétique de nucléation qui est cruciale dans ces applications. Cette thèse cherche à mieux comprendre la nucléation des cristaux par le développement de méthodes innovantes pour quantifier cette cinétique de nucléation : dans des cristallisoirs agités à grande échelle (L, mL,  $\mu$ L) qui sont industriellement pertinents, ainsi qu'à petite échelle (nL, pL) dans des systèmes microfluidiques à base de microgouttelettes qui présentent un intérêt fondamental. A l'échelle du L, la mesure de la réflectance optique couplée à la spectroscopie Raman in situ nous a permis de suivre l'évolution du nombre de particules et de la concentration de la solution. Et par l'extrapolation du décompte des particules jusqu'à une vitesse d'agitation nulle, nous avons extrait la cinétique de nucléation primaire. A l'échelle du mL et du  $\mu$ L en systèmes agités, les paramètres de la cinétique de nucléation obtenus par l'approche de distribution du temps d'induction révèlent des écarts de six à sept ordres de grandeur, par rapport à ceux obtenus dans des volumes de l'ordre du L, ce qui les rend inexploitable à l'échelle industrielle. Toutefois, les valeurs d'énergie interfaciale effective  $\gamma_{\text{eff}}$  sont relativement cohérentes à toutes ces échelles. Tandis qu'à l'échelle du nL, en microfluidique à base de microgouttelettes dans des capillaires, l'énergie interfaciale effective  $\gamma_{\text{eff}}$  est élevée. Ceci est lié à la barrière thermodynamique élevée pour atteindre la nucléation. Par conséquent, la sursaturation doit y être très élevée pour nucléer, faisant ainsi de la nucléation homogène le mécanisme prédominant. A l'échelle du pL, la méthode microfluidique est basée sur la génération de microgouttelettes sessiles sur une surface. Le temps de nucléation est détecté par microscopie in situ et analyse d'images lors de cycles de déliquescence-efflorescence, la sursaturation au moment de la nucléation est déterminée avec précision à partir d'un modèle d'évaporation que j'ai développé, et la nature stochastique de la nucléation est analysée à l'aide d'une distribution de Poisson modifiée. Ainsi la combinaison de ces trois développements nous a permis de quantifier les paramètres de la cinétique de nucléation dans les microgouttelettes en évaporation, avec une cohérence entre la théorie et l'expérience.

Mot clé: *nucléation, temps d'induction, microfluidique, microgouttelette sessile, stochastique*

# Résumé étendu

La nucléation est une étape essentielle dans le processus de cristallisation qui est notamment utilisé pour la fabrication et la purification de produits industriels, comme les produits pharmaceutiques, les cosmétiques, la chimie fine, l'alimentaire, la céramique, la métallurgie et l'électronique. Pour ces industries qui produisent à grande échelle (plusieurs milliards d'euros), la nucléation joue un rôle central. Cependant, il reste encore des questions fondamentales, notamment sur la cinétique de nucléation, pour lesquelles nous n'avons pas encore de réponse claire. Poussée par ces questionnements, cette thèse cherche à mieux comprendre la nucléation des cristaux par le développement de méthodes innovantes pour quantifier la cinétique de nucléation.

L'objectif de la mesure de la cinétique de nucléation est d'aider à concevoir, optimiser et contrôler les processus industriels de cristallisation. Dans ce but, plusieurs approches sur les cristallisoirs agités ont été développées dont celles de Nyvlt, Kubota et Sangwal. Plus tard, Nagy a combiné l'approche de Nyvlt avec l'équation du bilan de population pour permettre la détermination simultanée des cinétiques de nucléation et de croissance. Bien que les méthodes proposées par Nyvlt, Kubota, Sangwal et Nagy offrent un moyen simple et rapide de caractériser la nucléation, leurs équations sont empiriques et les paramètres utilisés ne correspondent pas à des grandeurs physiques réelles pouvant être interprétées théoriquement. Pour améliorer cela, Mersmann et al. ont développé un modèle assez complexe intégrant plusieurs mécanismes de nucléation. De même, Kashchiev, Borrisova, Hammond et Roberts ont développé leur modèle KBHR, qui présente des paramètres de nucléation avec une signification physique réelle. Cependant, ces deux modèles sont multivariés et donc complexes. De plus, ils ont tendance à donner des valeurs physiquement impossibles, en particulier lorsque certaines inégalités restrictives ne sont pas satisfaites. En effet, l'étude de la cinétique de nucléation dans un cristallisoir industriel agité est difficile en raison de l'hydrodynamique et de la présence de surfaces étrangères (parois du cristallisateur, agitateurs, chicanes, capteurs, sondes) dont l'influence sur la nucléation n'est pas directement quantifiable. Ces résultats font intervenir de façon complexe les nucléations homogène, hétérogène et secondaire. Par conséquent, du point de vue de l'ingénierie, l'un de mes objectifs est de développer une méthode simple et fiable pour obtenir des paramètres de nucléation clés en tenant compte de l'influence de la nucléation primaire et de la nucléation secondaire.

Récemment, la quantification de la cinétique de nucléation s'est orientée vers la compréhension de ses mécanismes fondamentaux. Traditionnellement, les études fondamentales sur la nucléation étaient principalement menées sur des expériences vapeur-liquide. Depuis le développement des technologies microfluidiques, la nucléation peut être étudiée en solution dans des petits volumes et en multipliant les expériences. Ainsi son caractère intrinsèquement stochastique a été confirmé : des échantillons identiques dans des conditions identiques nucléent à des moments différents. Ce comportement est expliqué en mécanique statistique par la formation du noyau qui est traitée comme un « succès » à partir d'une série de fluctuations aléatoires, ce qui en fait un événement rare. Par conséquent, une analyse statistique d'un grand nombre d'expériences est nécessaire pour élucider pleinement la cinétique de nucléation, ce qui peut être traité à l'aide de technologies microfluidiques.

Avec les avancées récentes, la nucléation a également été étudiée au niveau moléculaire via des simulations théoriques notamment par des approches de dynamique moléculaire, métadynamique, mécanique moléculaire et Monte Carlo. Cependant, les prédictions théoriques sont encore d'un ordre de grandeur différent des données expérimentales. Outre les multiples idéalizations et approximations utilisées dans les simulations, l'écart pourrait être en partie dû au fait que les simulations sont normalement effectuées à très haute sursaturation. Ceci est nécessaire pour observer un événement « rare » dans une échelle de temps de calcul réaliste. En solution, cela est difficile à réaliser expérimentalement en grands volumes dû à la précipitation engendrée à très haute saturation. Heureusement, la nucléation étant "ralentie" dans les très petits volumes (nanolitre à femtolitre), de très fortes sursaturations peuvent y être étudiées. A noter que ce «ralentissement» ne signifie pas que la fréquence de nucléation  $J$  (nombre de germes par volume par temps) soit réduite, mais le nombre de germes diminue avec la réduction de volume tout en conservant  $J$ . Ainsi, en développant une approche expérimentale fiable en microfluidique, on pourra extraire des paramètres physiquement significatifs. Il s'agit d'une étape importante vers la réalisation d'un accord raisonnable entre la théorie et l'expérience.

Cette thèse vise donc à développer des approches innovantes pour quantifier la cinétique de nucléation à la fois dans des cristallisoirs agités à grande échelle (L, mL,  $\mu$ L) ainsi que dans des systèmes microfluidiques avec des volumes de la gamme du pL. Les résultats obtenus à travers ces différentes méthodes sont alors comparés afin d'atteindre une méthode de mesure du temps d'induction de la nucléation.



Le manuscrit de thèse comprend onze chapitres :

Le premier chapitre décrit les objectifs et le contenu de chaque chapitre. Le deuxième chapitre présente une étude bibliographique des concepts fondamentaux et du contexte qui sont essentiels à la compréhension du travail réalisé dans cette thèse. Cela comprend la présentation de la thermodynamique de la nucléation et la description des techniques de mesure existantes et des modèles mathématiques utilisés dans les études de nucléation. Le principe des systèmes microfluidiques et de l'évaporation des microgouttes sont également expliqués.

Le troisième chapitre présente les matériaux et les techniques utilisées dans ce travail de thèse. Comme matériaux modèle, j'ai principalement utilisé l'acide p-amibenzoïque (PABA) et le NaCl en milieu aqueux. À l'échelle du litre, le mélange est agité avec un agitateur magnétique et j'ai utilisé la mesure de la réflectance optique couplée à la spectroscopie Raman in situ pour suivre l'évolution du nombre de particules et de la concentration de la solution. Étant donné que le PABA s'ionise partiellement en solution, j'ai également utilisé la mesure de la conductimétrie en solution pour déterminer le début de la nucléation. Le temps d'induction est pris de manière déterministe comme l'inverse du produit du taux de nucléation par le volume. Pour les expériences à l'échelle du mL, j'ai utilisé une plate-forme de cristallisation basée sur la turbidimétrie. Lorsque la formation de cristaux/particules se produit, la transmission de la lumière diminue ce qui marque le début de la nucléation. Dans ces expériences, il existe un délai entre le démarrage réel de la nucléation et le moment où elle est détectée. Ceci est pris en compte en ajustant un paramètre dans le tracé de la distribution cumulée du temps d'induction. Pour les expériences en microfluidique, j'ai utilisé deux configurations : une première configuration qui consiste à générer des microgouttelettes dans des capillaires transparents (échelle  $\mu\text{L}$  à  $\text{nL}$ ) et une seconde configuration basée sur la génération de microgouttelettes sessiles plus petites sur une surface de verre revêtue de PMMA, immergée dans de l'huile PDMS (échelle  $\text{nL}$  à  $\text{pL}$ ). Pour la détection de la nucléation, j'ai utilisé respectivement la microscopie in situ et l'analyse d'images.

Les chapitres qui suivent décrivent tous les résultats obtenus au cours de la thèse. Un lien entre chaque chapitre et le reste de la thèse est décrit brièvement au début de chaque chapitre car ces derniers sont écrits de façon à pouvoir être compréhensible indépendamment. Ainsi, chaque chapitre a sa propre introduction avec étude bibliographique, sa méthodologie, sa discussion et sa conclusion.

Dans le quatrième chapitre, je propose une méthode pour quantifier la cinétique de nucléation primaire dans un cristallisateur agité de l'ordre du L, en utilisant une approche de comptage de particules. Celle-ci est basée sur la technique de

rétrodiffusion laser couplée à la spectroscopie Raman in situ. En supposant que la vitesse de nucléation secondaire varie de manière exponentielle avec la vitesse d'agitation et que la nucléation primaire est peu dépendante de l'agitation, mon approche utilise l'extrapolation du décompte des particules jusqu'à une vitesse d'agitation nulle afin d'extraire la cinétique de nucléation primaire. L'amplitude résultante des taux de nucléation est cohérente avec le modèle KBHR développée par Kashchiev, Borrisova, Hammond et Roberts.

Dans le chapitre 5, je compare les paramètres cinétiques de nucléation obtenus avec l'approche par comptage de particules à ceux donnés par l'approche de distribution du temps d'induction dans des flacons agités de l'ordre du mL. Les résultats révèlent alors des écarts de six à sept ordres de grandeur. Bien que la dynamique des fluides soient différentes dans les cristallisoirs de différentes géométries et tailles, elle n'explique pas des écarts aussi importants. En effet, ces écarts montrent plutôt que les taux de nucléation primaire obtenus avec ces techniques ne peuvent pas être utilisés pour l'interprétation des taux de nucléation à l'échelle industrielle.

Dans le chapitre 6, je quantifie la cinétique de nucléation à travers d'autres techniques : j'utilise la conductimétrie à l'échelle du L et la microscopie optique à l'échelle du  $\mu\text{L}$ , pour mesurer le temps d'induction. Les résultats montrent que les méthodes basées sur le temps d'induction donnent systématiquement des valeurs faibles de facteur cinétique pré-exponentiel (inférieures à  $10^6 \text{ m}^{-3}\text{s}^{-1}$ ). Tandis que les méthodes par comptage de particules et analyse KBHR donnent des valeurs proches de  $10^{11} \text{ m}^{-3}\text{s}^{-1}$ , et ce quelle que soit l'échelle. Cela renforce les conclusions du chapitre 5, sur l'inadéquation des temps d'induction mesurés dans les systèmes agités, comme références à l'échelle industrielle. D'autre part, toutes les méthodes utilisées semblent donner des valeurs relativement cohérentes de l'énergie interfaciale effective  $\gamma_{\text{eff}}$ , à l'exception de l'échelle  $\mu\text{L}$  qui donne des valeurs élevées de  $\gamma_{\text{eff}}$ . Ainsi en dessous du  $\mu\text{L}$ , la barrière thermodynamique est élevée pour atteindre la nucléation. Par conséquent, en microfluidique à base de microgouttelettes (qui remplacent les cristallisoirs), la sursaturation doit être très élevée pour nucléer, faisant ainsi de la nucléation homogène le mécanisme prédominant. De plus, l'utilisation de ces microgouttelettes de l'ordre du nL qui sont dispersées dans une phase continue, minimise la présence d'impuretés et de surfaces étrangères qui pourraient agir comme des sites de nucléation hétérogènes (pouvant abaisser la barrière énergétique). Malheureusement, les impuretés et les surfaces étrangères sont inévitables dans les cristallisoirs industriels à grande échelle. Ce chapitre souligne donc qu'une attention particulière est nécessaire dans l'interprétation des paramètres cinétiques de nucléation acquis à partir de différentes échelles et de différentes techniques de mesure.

Au chapitre 7, je me concentre sur la compréhension fondamentale de la nucléation primaire homogène en remplaçant les cristallisoirs agités (à orientation industrielle) par des microgouttelettes de volumes de l'ordre du pL, en microfluidique « ouverte », J'étudie alors la cinétique de nucléation du NaCl en solution, à l'aide d'un dispositif microfluidique développé au laboratoire. Sur ce dispositif, la dynamique d'évaporation des microgouttelettes dans l'huile PDMS environnant est due à la diffusion de l'eau. Cette dynamique d'évaporation a été étudiée auparavant grâce à une procédure d'analyse d'image basée sur l'écart type des pixels de niveau de gris. Ainsi des oscillations de cet écart-type ont été montrés dans le cas d'interactions entre les microgouttelettes. Pour ma part, je classifie les microgouttelettes en fonction du nombre d'oscillations, ce qui me permet de quantifier les interactions. Ensuite, je montre que le fait de ne pas tenir compte de ces interactions dans l'analyse des données cinétiques peut conduire à de graves inexactitudes dans l'estimation du paramètre de nucléation. Je souligne le fait que ces interactions ne seraient pas observables par des techniques de microscopie traditionnelles. De plus, grâce au contrôle de l'humidité ambiante, je montre que ces interactions disparaissent à faible taux d'humidité relative.

Au chapitre 8, je développe une méthode pour mesurer le temps d'induction, que je définie de manière appropriée dans le cas de l'évaporation des microgouttelettes. En effet, je devrais fixer le temps zéro au moment où la sursaturation finale est atteinte. Cependant, la sursaturation finale évolue continuellement avec le temps, dû à l'évaporation. Par conséquent, je fixe le temps zéro doit au point où la solution est saturée (et a donc la possibilité de nucléer). Ainsi quelle que soit la concentration initiale de la solution des microgouttelettes, le temps mis pour atteindre la nucléation à partir du temps zéro (i.e. le temps d'induction) doit être identique. Ainsi, dans un système d'évaporation, le temps d'induction est donc la différence entre le temps mis par la microgouttelette pour nucléer et le temps mis pour atteindre la saturation. Cependant, dans l'approche d'analyse d'image présentée dans le chapitre précédent, le moment auquel la microgouttelette atteint la saturation est expérimentalement inaccessible sans supposer un modèle de taux d'évaporation. Pour cela, je décris un nouveau protocole que j'ai développé, via le cycle de déliquescence-efflorescence, pour atteindre le temps d'induction.

Au chapitre 9, je complexifie le modèle d'évaporation précédent afin d'évaluer la sursaturation au moment de la nucléation dans la microgouttelette. Dans la littérature, une évaporation constante est souvent supposée. Bien que cette approximation soit raisonnable pour les gouttelettes diluées, la loi de Raoult suggère que les gouttes concentrées devraient avoir une activité de l'eau réduite. De plus, les réseaux de microgouttelettes s'évaporent plus lentement que les

microgouttelettes isolées en raison de la contribution des microgouttelettes voisines au taux d'humidité local. Enfin, la présence d'huile de PDMS autour de la microgouttelette et les changements de densité dus à la diffusion de l'eau dans l'huile PDMS, devraient avoir un impact sur le taux d'évaporation. Je valide mon nouveau modèle d'évaporation avec des données expérimentales. Puis, je montre que les différents comportements de la ligne de contact, c'est-à-dire avec un rayon de contact constant (CCR), ou avec un angle de contact constant (CCA) ou les deux (stick-slide (SS)), entraînent une évolution presque identique en termes de volume, en particulier dans l'échelle de temps pertinente pour les études de nucléation. De plus, je démontre pour la première fois que l'hypothèse d'un taux d'évaporation constant ainsi que la négligence des interactions diffusives entre les microgouttelettes peuvent entraîner de graves écarts dans la mesure de la concentration, en particulier pendant la nucléation. Avec mon modèle, on peut déterminer avec précision l'évolution temporelle de la concentration des microgouttelettes, ce qui est important pour quantifier la cinétique de cristallisation.

Le chapitre 10 est consacré à la détermination de la fonction de probabilité qui doit être utilisée pour modéliser la distribution expérimentale des temps d'induction. Dans la littérature, cette distribution est généralement ajustée à la distribution de Poisson, dans le cas d'expériences avec une sursaturation constante, car le taux de nucléation effectif est invariable avec le temps. Cependant, pour la nucléation par évaporation (qui est omniprésente dans la nature), la sursaturation évolue avec le temps, rendant la fonction de Poisson inapplicable. Bien que d'autres distributions empiriques telles que Weibull, Gompertz et Gumbell puissent décrire la dépendance temporelle du taux de nucléation effectif, les paramètres d'ajustement ne contiennent pas d'informations physiques pouvant être interprétées en théorie classique de la nucléation (CNT). Pour résoudre ce problème, j'explore l'utilisation d'une distribution de Poisson modifiée compatible avec la CNT, qui considère la dépendance temporelle de la force motrice de nucléation. Ainsi, je démontre dans ce chapitre, qu'en combinant la mesure du temps d'induction et le modèle d'évaporation développé dans les chapitres précédents, avec la distribution de Poisson modifiée, on peut obtenir des paramètres de cinétiques de nucléation précis qui sont en excellent accord avec les prédictions théoriques. En utilisant le système NaCl-eau, j'ai obtenu un facteur pré-exponentiel  $A$  de  $9,30 \times 10^{20} \text{ m}^{-3}\text{s}^{-1}$  et une énergie interfaciale de  $46,7 \text{ mJ/m}^2$  qui sont en accord de façon remarquable avec les valeurs expérimentales et théoriques existant dans la littérature. À notre connaissance, il s'agit du premier travail expérimental qui a utilisé une approche probabiliste pour mesurer l'énergie interfaciale du NaCl dans l'eau sans fixer la valeur du facteur pré-exponentiel. Compte tenu des nombreuses études de simulation sur la nucléation du NaCl, nos paramètres cinétiques expérimentaux

basés sur l'approche stochastique peuvent servir de référence supplémentaire pour valider les prédictions théoriques. De plus, notre approche expérimentale et notre protocole de traitement des données peuvent également être étendus pour étudier la nucléation d'autres sels, de cristaux biologiques et de principes actifs pharmaceutiques d'intérêt.

En résumé, dans la première partie de cette thèse j'ai développé des méthodes pour quantifier la cinétique de nucléation dans des cristallisoirs agités qui sont pertinents pour être transposés industriellement. Ces résultats seront utiles aux ingénieurs pour interpréter les données de cinétique de nucléation, pour les processus de mise à l'échelle, de conception, de contrôle et de cristallisation. La deuxième partie porte sur l'étude de la nucléation primaire homogène : j'ai tiré parti des avantages de la microfluidique à base de microgouttelettes. Ces résultats intéressent les théoriciens et les simulateurs car ils permettent de valider leurs approches numériques. C'est une étape importante vers la compréhension fondamentale de la nucléation et l'accord entre théorie et expérience.

# Contents

	Page
<b>Affidavit</b> .....	<b>ii</b>
<b>List of Publications and Conferences</b> .....	<b>iii</b>
<b>Abstract</b> .....	<b>iv</b>
<b>Résumé</b> .....	<b>v</b>
<b>Résumé étendu</b> .....	<b>vi</b>
<b>Chapter 1 Introduction</b> .....	<b>1</b>
1.1 Motivation.....	1
1.2 Background and Objective.....	1
1.3 Structure of the Thesis.....	3
<b>Chapter 2 Literature Review</b> .....	<b>6</b>
2.1 Fundamentals of Crystallization.....	6
2.1.1 Mechanisms of Nucleation.....	7
2.1.2 Classical Nucleation Theory.....	9
2.1.3 Two-step Nucleation Theory (2-SNT).....	12
2.2 Nucleation Kinetics: Approaches on Data Acquisition and Treatment ..	13
2.2.1 Deterministic Approach.....	13
2.2.2 Stochastic Approach.....	17
2.3 Droplet-based Microfluidics in Crystallization Studies.....	21
2.3.1 Principle of Droplet Generation in Microfluidics.....	22
2.3.2 Recent Advances in Microfluidics Crystallization.....	26
2.4 Principle of Microdroplet Evaporation.....	32
2.4.1 Contact Line Behavior (CCA, CCR, SS mode).....	33
2.4.2 Evaporation Rate Models.....	34
<b>Chapter 3 Materials and Methods</b> .....	<b>35</b>
3.1 Model Compounds.....	35
3.1.1 Para-Aminobenzoic acid (PABA).....	35
3.1.2 Glutamic acid (GA).....	35
3.1.3 Sodium chloride (NaCl).....	36
3.2 Polymers used in the microfluidic set-up.....	36
3.2.1 Polyetheretherketone (PEEK).....	36

3.2.2	Fluorinated ethylene propylene (FEP) .....	37
3.2.3	Polydimethylsiloxane (PDMS).....	37
3.2.4	Polymethylmethacrylate (PMMA) .....	37
3.3	Process Analytical Tools (PATs).....	38
3.3.1	Optical Reflectance Measurement (ORM) .....	38
3.3.2	In situ Raman spectroscopy .....	39
3.4	Experimental Setups .....	40
3.4.1	Setup for Liter Scale Experiments.....	40
3.4.2	Setup for mL Scale Experiments.....	42
3.4.3	Setup for $\mu$ L Scale Experiments .....	42
3.4.4	Setup for Sessile Microdroplet Experiment.....	44
<b>Chapter 4 Measuring Primary Nucleation Rates in Agitated Systems using Particle Count Approach .....</b>		<b>45</b>
4.1	Introduction.....	46
4.2	Materials and Methods.....	47
4.2.1	Chemicals and Equipment.....	47
4.2.2	Solubility Measurement .....	47
4.2.3	Calibration of in-situ Raman Spectroscopy.....	48
4.2.4	Calibration of In-situ 3D ORM .....	48
4.2.5	Crystallization Process Monitoring.....	50
4.3	Results and Discussion .....	50
4.3.1	Identification of Polymorphs .....	50
4.3.2	Solubility Data.....	51
4.3.3	Calibration Curves of ORM.....	52
4.3.4	Validation of ORM Measurement by Raman Spectroscopy .....	54
4.3.5	Total Nucleation Rates from in-situ ORM .....	55
4.3.6	Estimation of Primary Nucleation Rate.....	57
4.4	Conclusion .....	62
<b>Chapter 5 Nucleation Kinetics in Agitated Systems: Particle Counts vs Induction Time Approach .....</b>		<b>63</b>
5.1	Introduction.....	64
5.2	Materials and Methods.....	68
5.2.1	Chemicals and Equipment.....	68

5.2.2	Induction Time Measurement.....	68
5.2.3	Extraction of Nucleation Rate from Induction Time .....	68
5.3	Results and Discussion.....	70
5.3.1	Nucleation Rates from Induction Time Probability Distribution ..	70
5.3.2	Confidence Intervals of Estimated Parameters.....	74
5.3.3	Comparing Nucleation Kinetic Parameters.....	76
5.4	Conclusion .....	80
<b>Chapter 6 Quantifying Nucleation Kinetics: A Multi-scale Comparison .....</b>		<b>81</b>
6.1	Introduction.....	82
6.2	Material and Methods.....	83
6.2.1	Liter Scale.....	84
6.2.2	Milliliter Scale.....	86
6.2.3	Submicroliter Scale .....	88
6.3	Results and Discussion.....	89
6.4	Conclusion .....	93
<b>Chapter 7 Probing Nucleation in Microdroplets via Image Analysis: Effect of Diffusive Interactions.....</b>		<b>94</b>
7.1	Introduction.....	95
7.2	Materials and Methods.....	95
7.2.1	Details of Instrumentation.....	95
7.2.2	Microdroplet Generation.....	97
7.2.3	Humidity Regulation .....	98
7.2.4	Numerical Detection of Oscillations.....	99
7.3	Results and Discussion.....	99
7.3.1	Effect of Diffusive Interactions.....	100
7.3.2	Eliminating Diffusive Interactions.....	102
7.4	Conclusion .....	103
<b>Chapter 8 Nucleation in Sessile Microdroplets: Measuring Induction Time via Deliquescence-Efflorescence Cycle .....</b>		<b>104</b>
8.1	Introduction.....	105
8.2	Materials and Methods.....	106
8.3	Results and Discussion.....	107
8.3.1	Analysis of $\sigma$ -curves.....	107



8.3.2	Assessment of Reproducibility.....	109
8.3.3	Statistical Analysis.....	111
8.3.4	Checking for Possible Influence of Impurities .....	113
8.3.5	Nucleation Kinetic Parameter Estimation.....	114
8.4	Conclusion .....	117
<b>Chapter 9 Modeling the Evaporation Dynamics of Sessile Saline Microdroplets .....</b>		<b>118</b>
9.1	Introduction.....	119
9.2	Modeling.....	121
9.2.1	Influence of oil thickness on the evaporation rate.....	122
9.2.2	Considering the presence of neighboring droplet .....	124
9.2.3	Considering the evolution of droplet density as water evaporates.....	125
9.2.4	Dependence of water activity on solute concentration .....	127
9.2.5	Models for Contact Line Behavior.....	128
9.3	Materials and Methods.....	130
9.4	Results and Discussion.....	130
9.4.1	Model Predictions for Pure Microdroplets.....	130
9.4.2	Model Predictions for Saline Microdroplets.....	133
9.4.3	Implications on Crystallization Studies .....	137
9.5	Conclusion .....	139
<b>Chapter 10 Modeling the Nucleation Kinetics of Aqueous NaCl with Modified Poisson Distribution .....</b>		<b>140</b>
10.1	Introduction.....	141
10.2	Theory and Modeling .....	142
10.2.1	Classical Nucleation Theory for Ionic Systems .....	142
10.2.2	Modified Poisson Distribution Function.....	142
10.3	Results and Discussion.....	144
10.3.1	Kinetic Parameter Estimation.....	144
10.3.2	Comparison with Literature .....	146
10.3.3	Observing Confinement Effects .....	147
10.4	Conclusion .....	149
<b>Chapter 11 Concluding Remarks and Perspective .....</b>		<b>150</b>
11.1	Notable Findings .....	150

11.2 Perspective .....	152
11.2.1 Influence of interfering variables in Agitated Crystallizers .....	152
11.2.1 Evaporative microdroplet experiments.....	152
<b>References.....</b>	<b>154</b>
<b>Curriculum Vitae.....</b>	<b>Error! Bookmark not defined.</b>

## List of Figures

- Figure 2.1** Typical phase diagram of crystallization process showing the solubility curve (blue line) and metastable zone limit (green dotted line). ..... 7
- Figure 2.2** Schematic illustration of the mechanisms of nucleation. The blue spheres and prisms correspond to the monomer and crystal respectively. The orange plate corresponds to any foreign surface that is not the nucleating crystal. .... 8
- Figure 2.3** Free energy diagram of nucleation as a function of cluster radius  $r$ . ..... 9
- Figure 2.4** Schematic illustration of the static equilibrium of three interfacial energies  $\gamma_{sl}$  (substrate-liquid),  $\gamma_{sc}$ (substrate-cluster), and  $\gamma_{cl}$  (cluster-liquid) which are balanced at a contact angle  $\theta$  between the nucleating phase and the substrate.<sup>31</sup> ..... 11
- Figure 2.5** Principle of double pulse technique (Adapted from Revalor et. al.<sup>36</sup>)... 16
- Figure 2.6** Different designs for droplet generation in microfluidics <sup>51</sup> ..... 24
- Figure 2.7** Stages of droplet formation in a T-junction in squeezing regime. (A) At  $t = 0$  s, the droplet begins filling the channel. (B) At  $t = 0.2$  s, the droplet blocks the cross section. (C) At  $t = 0.3$  s, the droplet "neck" gets squeezed. (D) At  $t = 0.5$  s, the interfacial tension could not support the thinning of the "neck" resulting in the detachment of the droplet.<sup>52</sup>..... 25
- Figure 2.8** Three regimes of droplet formation in T-junctions (a) squeezing (b) dripping (c) jetting. Adapted from Zhu et. al. .... 26
- Figure 2.9** Schematic of the in-house developed microfluidic platform. (a) The droplet factory consists of syringe pumps and (b) multiport junction made of polyether ether ketone (PEEK) which is resistant to various types of solvent (c) the droplet characterization zone features a UV-VIS-NIR spectrophotometer (190 to 2300 nm). (d,e) The incubation and observation zones are composed of a thermostated bath and xyz-motorized camera with variable zoom capability. Adapted from Candoni et al.<sup>53</sup> ..... 27

<b>Figure 2.10</b> Schematic illustration of the setup for (a) solubility measurement and (b) polymorph screening directly from powder. Adapted from Peybernes et al. <sup>54-55</sup> .....	28
<b>Figure 2.11.</b> The image (a) and the schematic diagram (b) of the setup for generating microdroplets on PMMA surface under oil. ....	29
<b>Figure 2.12</b> Schematic illustration for obtaining the histogram and extracting the standard deviation of the gray-level pixels. ....	30
<b>Figure 2.13</b> Evolution of the gray-level standard deviation for an evaporating saline microdroplet. The scale bar corresponds to 50 $\mu\text{m}$ . ....	31
<b>Figure 2.14</b> Schematic illustration of a sessile droplet with spherical cap radius $R_s$ , contact radius $R$ , and contact angle $\theta$ . ....	32
<b>Figure 2.15</b> Schematic illustration of different contact line behavior. ....	33
<b>Figure 3.1</b> Chemical structure of model compounds (a) PABA and (b) GA. ....	35
<b>Figure 3.2</b> (a) Crystal structure of sodium chloride consisting of $\text{Na}^+$ (blue) and $\text{Cl}^-$ (green), (b) Solubility of NaCl in comparison with other salts (adapted from Daniela Feingold et al). ....	36
<b>Figure 3.3</b> Chemical structure of polymers used in generating microdroplets in capillaries (a) PEEK (b) FEP. ....	37
<b>Figure 3.4</b> Chemical structure of polymers used in sessile microdroplet generation (a) PDMS, (b) PMMA. ....	38
<b>Figure 3.5</b> Schematic Illustration of ORM Probe. (adapted from Adlington et al. <sup>77</sup> ) .....	38
<b>Figure 3.6</b> Schematic illustration of Raman spectroscopy (adapted from <a href="http://www.princetoninstruments.com/">www.princetoninstruments.com/</a> ) .....	39
<b>Figure 3.7</b> (a,b) Schematic diagram and photo of the particle-count approach using optical reflectance measurement and Raman spectroscopy, (c,d) schematic diagram and photo of the conductometry approach for measuring induction time. ....	40

<b>Figure 3.8</b> Dimensions of the crystallizer and its agitation system used in (a) particle-count approach (b) solution conductometry. The height of the liquid displayed are prior to the introduction of probes. ....	41
<b>Figure 3.9</b> (a) Schematic diagram and (b) photo of a turbidimetric crystallizer platform (Crystal16, Technobis). ....	42
<b>Figure 3.10</b> (a) Schematic illustration of the microfluidic experiment in tubes (b) photo of the experimental setup (c) closer look at the spirally-oriented microfluidic tubes embedded on a 3D-printed polymeric resin template (developed in this thesis). ....	43
<b>Figure 3.11</b> Schematic illustration of the setup for sessile microdroplet experiment. ....	44
<b>Figure 4.1</b> Optical micrographs of crystal samples of (a) PABA and (b) LGA used in polymorph identification and determination of particle-size distribution. ....	51
<b>Figure 4.2</b> Raman Spectra of dried powder obtained after nucleation of (a) PABA and (b) LGA. In (a), the absence of strong peak at $1700\text{ cm}^{-1}$ (characteristic peak of $\beta$ -form) <sup>96</sup> confirms that it is $\alpha$ -form. In (b), the absence of peak at $1130\text{ cm}^{-1}$ (characteristic peak of $\beta$ -form) <sup>97</sup> confirms that it is $\alpha$ -form. ..	51
<b>Figure 4.3</b> Temperature-dependent solubilities of $\alpha$ -PABA in 30 wt% aqueous ethanol (■) and $\alpha$ -LGA in water (●). The solid lines are the fit of the van't Hoff equation. Each point in PABA solubility line is an average of three measurements while that of LGA is based on Scholl et al <sup>95</sup> . ....	52
<b>Figure 4.4</b> Particle Size Distribution (PSD) (○) and Chord Length distribution (CLD) (●) of (a) PABA and (b) LGA. The length is in logarithmic scale .....	53
<b>Figure 4.5</b> Raw counts per second during the calibration of PABA (red) and LGA (blue) at 900 rpm. The steady counts across each incremental addition of seeds suggests a negligible breakage/agglomeration during calibration. ....	53

**Figure 4.6** Calibration curve relating ORM counts per second to actual number density of PABA at 500 rpm (●), 600 rpm (○), 700 rpm (▼), 800 rpm (△), 900 rpm (■). ..... 54

**Figure 4.7** (a) Raman spectra of solvent (red) and PABA solution at  $S = 0.25$  (orange), 0.5 (green), 0.75 (blue), 1.20 (black); (b) Effect of suspended solids on the reference peak area. A negligible correlation ( $R^2 < 0.05$ ) can be observed, however the presence of solids shifts the reference peak area of clear solution up by around 22 a.u. (c) Correlation between supersaturation ratio and relative peak area in clear solution (●) and with suspended solids (○). (d) Comparison of supersaturation profile of PABA at  $S_0 = 1.20$  obtained from in situ Raman spectroscopy (dotted line) against that obtained from in situ ORM (solid line). ..... 56

**Figure 4.8** Evolution of number density of (a) PABA and (b) LGA. Evolution of nucleation rate for (c) PABA and (d) LGA. .... 57

**Figure 4.9** Reproducibility of nucleation rates measured by ORM of (a) PABA at  $S_0 = 1.20$  and (b) LGA at  $S_0 = 2.50$  across different agitation rates. The solid line is a fit to an exponential function  $y = y_0 e^{kx}$ . For PABA, a relative standard error of 9.75% was obtained for  $y_0$  and 4.39% for  $k$  while for LGA, the relative standard error is 10.55% for  $y_0$  and 7.87% for  $k$ . Note that the nucleation rate here is in linear scale while that in Figure 4.10 is in logarithmic scale which displays a straight line for an exponential curve. .... 58

**Figure 4.10** Effect of agitation rate on the measured nucleation rate of PABA at  $S_0 = 1.20$  (●), 1.25(○), 1.32 (▼), 1.40 (△) and LGA at  $S = 2.50$  (×), 2.67 (■), 2.85 (▽), 3.05 (□). Note that the nucleation rate is in logarithmic scale where an exponential curve appears linear..... 59

**Figure 5.1** Experimentally obtained cumulative probability distribution  $P(t)$  of induction time for PABA (a) at supersaturation ratios  $S = 1.20$  (blue ▲), 1.25 (green ●), 1.32 (orange ◆), 1.40 (red ■) and LGA (b) at

supersaturation ratios $S = 2.50$ (blue ▲), $2.67$ (green ●), $2.85$ (orange ◆), $3.05$ (red ■).....	70
<b>Figure 5.2</b> Typical temperature profile used in induction time measurements via Crystal16. The excellent agreement between set-point temperature (gray) and the measured temperature inside the vial (orange) suggests an accurate temperature control. A sample data for the evolution of transmissivity (green) for LGA is shown.....	71
<b>Figure 5.3</b> Scatter plot of induction time against cycle number for LGA ( $S_0 = 2.50$ ). .....	72
<b>Figure 5.4</b> Estimation of CNT parameters of PABA from induction time distributions (▼) and from <i>in situ</i> ORM (●) and of LGA from induction time distributions (▽) and from <i>in situ</i> ORM (○) by fitting to equation (5.7) by non-linear least square regression. ....	77
<b>Figure 6.1</b> Overview of the experimental setup across different scales (a) liter-scale particle count approach (b) liter-scale deterministic induction time approach (c) mL scale probabilistic induction time approach (d) $\mu\text{L}$ scale probabilistic induction time approach.....	83
<b>Figure 6.2</b> (a) Schematic diagram of the experimental setups for liter-scale particle count approach (b) Photograph of the induction time measurement setup (c) Typical evolution of calibrated quantities: crystal size ( $L_{3,0}$ ), number density, and supersaturation ratio. ....	84
<b>Figure 6.3</b> (a) Schematic illustration of the L-scale induction time measurement setup via solution conductometry (b) Photograph of the setup (c) Typical evolution of relative conductivity and temperature. The time elapsed between the attainment of the final temperature and the onset of sustained decrease in conductivity is taken as the induction time.....	85
<b>Figure 6.4</b> (a) Schematic illustration of the setup, (b) typical temperature profile and evolution of transmissivity in induction time approach and (c) KBHR approach. ....	87

<b>Figure 6.5</b> (a) Schematic illustration of the microfluidic setup (b) Image of the microfluidic setup (c) Image of the portable spiral template containing droplets that facilitates the transfer from the generation bath to the observation bath. ....	88
<b>Figure 6.6</b> Results of nucleation rate measurement corresponding to each experimental method in Figure 6.1. (a) evolution of number density and supersaturation in the liter scale particle count approach (b) nucleation rate as a function of supersaturation based on induction time approach in the liter scale (c) cumulative probability of nucleation as a function of induction time for mL scale (d) cumulative probability of nucleation as a function of induction time in $\mu\text{L}$ scale. ....	89
<b>Figure 6.7</b> Nucleation rates obtained across various scales and techniques. Data points are fitted with classical nucleation theory.....	90
<b>Figure 7.1</b> Schematic diagram of the microdroplet generation system with humidity control module. ....	96
<b>Figure 7.2</b> Refractive index as a function of supersaturation ratio. The refractive index of the droplet matches that of the PDMS oil at $S = 1.395$ .....	98
<b>Figure 7.3</b> Assessment of the humidity regulation module showing a minimum and maximum RH of 10% and 95% respectively.....	98
<b>Figure 7.4</b> (a) Evolution of $\sigma$ of 4 neighbouring microdroplets denoted as droplet $h,i,j,k$ (b) Cumulative probability of nucleation as a function of induction time, classified according to number of sigma-oscillations, for the all arrays (370 microdroplets).....	100
<b>Figure 7.5</b> Evolution of $\sigma$ for 25 randomly selected microdroplets that corresponds to different relative humidity RH (a) RH = 55% and (b) RH = 10%. The $\sigma$ oscillations prior to nucleation disappear at low relative humidity. ....	103
<b>Figure 8.1</b> Typical time evolution of the $\sigma$ -curve (in blue) during an experiment where the RH (in orange) is stepped to create a cycle of deliquescence and efflorescence. The corresponding images in each specific time points are shown (scale bar = 20 $\mu\text{m}$ ).....	107



<b>Figure 8.2</b> Histograms of saturation time $t_{sat}$ , matching time $t_m$ , and nucleation time $t_n$ fitted with Gaussian curves.....	109
<b>Figure 8.3</b> Evolution of $\sigma$ -curve in a two-cycle experiment. Observe that the $\sigma$ -value for complete dissolution and matching time for both cycles are the same which confirms the validity of using $\sigma$ as a “calibration reference” for measuring the saturation time.....	110
<b>Figure 8.4</b> Cumulative probability distribution as a function of the dimensionless induction time. Each array contains around 56 microdroplets. ....	110
<b>Figure 8.5</b> Cumulative probability distribution as a function of the dimensionless induction time. Each array contains around 56 microdroplets. ....	111
<b>Figure 8.6</b> QQ-plot of the supersaturation at nucleation. If most of the data points lie close to the 45° line, the distribution tends to follow a normal distribution. ....	112
<b>Figure 8.7</b> Correlation between rank of microdroplets in terms of supersaturation at nucleation. The microdroplet that nucleated at the lowest supersaturation is ranked 1 and the one that nucleated at the highest supersaturation is ranked 175.....	114
<b>Figure 8.8</b> Distribution of dimensionless induction time for unperturbed droplets fitted with Weibull, Gompertz, Gaussian, and Poisson distribution functions (Weibull and Gompertz coincide).....	115
<b>Figure 9.1.</b> Illustration of microdroplet showing the equivalent spherical cap at different values of contact angle $\theta$ .....	122
<b>Figure 9.2.</b> Variation of aqueous NaCl density as a function of supersaturation ratio. <sup>181</sup> The regression line is $y = 998(1+0.205x)$ with $R^2 = 0.9984$ . ....	126
<b>Figure 9.3.</b> Variation of water activity (numerically equal to the equilibrium relative humidity, $RH_s$ ) as a function of supersaturation ratio. The data were taken from Table 6 of An et al. <sup>182</sup> .....	127
<b>Figure 9.4.</b> Model predictions of three contact line behavior models (CCR, CCA, SS) in comparison with experimental data obtained for pure water droplets by Rodriguez-Ruiz et. al. <sup>145</sup> Time evolution of (a) normalized contact	

radius, (b) Contact angle of the microdroplets with the substrate (c) normalized microdroplet height, and (d) Volume contraction. Error bars represent standard errors based on 3 replicates.....	132
<b>Figure 9.5.</b> Predicted evolution of microdroplet shape (pure water) for CCR, CCA, and SS models at discrete time points (every 1 hour). X,Y axis (lengths) are in terms of $R/R_0$ .....	133
<b>Figure 9.6.</b> Variation of the refractive index <sup>181</sup> with supersaturation ratio. ....	134
<b>Figure 9.7.</b> Model predictions (CCA) for saline microdroplets ( $V_0 = 67$ pL and $S_0 = 0.88$ ) in terms of (a) droplet volume and (b) supersaturation ratio in comparison with experimental data. The error bars at saturation time ( $S=1$ ) and matching time ( $S=1.395$ ) represent the standard deviation of the distribution of data points (190 droplets). The grey area corresponds to the time range where nucleation occurs.....	135
<b>Figure 9.8.</b> Evolution of the effective relative humidity $RH_{eff}$ for CCA and CCR against the humidity above the oil $RH_{\infty}$ . ....	136
<b>Figure 9.9.</b> Evolution of Peclet number for CCA and CCR models. (If Peclet number $\ll 1$ , the microdroplet is considered to have homogeneous composition) .....	137
<b>Figure 9.10.</b> Cumulative probability distribution of supersaturation ratio at nucleation $S_n$ based on two evaporation models. ....	138
<b>Figure 10.1.</b> Ratio of ionic activity coefficients $\gamma_{\pm}/\gamma_{\pm 0}$ based on the experimental data of Na et al. <sup>156</sup> .....	144
<b>Figure 10.2</b> Fitting of the modified Poisson distribution (eq. 10.5) with the experimental distribution of supersaturation ratio at nucleation for microdroplets with volumes $\sim 60$ pL and $\sim 4$ pL (measured at saturation). ....	145
<b>Figure 10.3</b> Comparison of our experimental results (dashed green line is via extrapolation of CNT from the 60-pL experiment) to relevant experimental literature data (exp) and theoretical simulations (sim). Experiments were based on efflorescence chamber (Gao et. al.) <sup>189</sup> , spherical void	

electrodynamic levitator trap (Na. et. al.)<sup>156</sup>, and microcapillaries (Desarnaud et. al.)<sup>67</sup> while the simulations were based on forward flux sampling (Jiang et. al.)<sup>191</sup> and seeded atomistic simulations (Zimmerman et. al.)<sup>3, 157</sup> .....146

**Figure 10.4** Comparison of 60-pL and 4-pL microdroplet in terms of (a) nucleation rate ( $J$  in  $m^{-3}s^{-1}$ ) and (b) critical size (# of ions) as a function of supersaturation ratio. Curves come from the fit presented in Table 10.1 .....148

## List of Tables

<b>Table 4.1</b> Measured primary nucleation rates at different supersaturation ratios. ....	61
<b>Table 5.1</b> Selected publications utilizing the Poisson-model for extracting nucleation rates from induction time distributions.....	64
<b>Table 5.2</b> Literature value of nucleation kinetic parameter A for various compounds using the stochastic model.....	65
<b>Table 5.3.</b> Magnitude of nucleation rates in literature for various compounds and determination methods. ....	67
<b>Table 5.4</b> Nucleation rates ( $J$ ) and growth time ( $t_g$ ) obtained from the fit of induction times to the stochastic model in equation (5.5).....	73
<b>Table 5.5</b> Confidence intervals of nucleation rates based on Kolmogorov-Smirnov analysis. ....	75
<b>Table 5.6</b> Comparison of predicted primary nucleation rates obtained from two methods: via particle-count approach extrapolated back to stagnant solution and via induction time distribution ( $J_{Ind}$ ). ....	77
<b>Table 5.7</b> Estimated CNT Kinetic Parameter A and Thermodynamic Parameter B obtained from stochastic model and ORM measurement via non-linear regression. ....	78

<b>Table 6.1</b> Fitted nucleation parameters obtained across various scales and techniques. Data points are fitted with classical nucleation theory.....	91
Table 7.1 Details of chemical products.....	97
Table 7.2 Typical microdroplet images at t = 0, 25, 80 min.....	99
<b>Table 7.3</b> Comparison of mean supersaturation at nucleation, nucleation rate, and interfacial energy with no $\sigma$ -oscillations ( $\varepsilon = 0$ ) against that of all data set .....	102
<b>Table 8.1</b> Statistical tests to simultaneously compare the distribution of 6 data sets (3 arrays, 2 cycles each).....	113
<b>Table 8.2</b> Empirical nucleation parameters estimated from various distribution functions <sup>38</sup> .....	115
<b>Table 9.1</b> Numerical values used as input in the evaporation model of pure water droplets taken from Rodriguez-Ruiz et al. <sup>145</sup> .....	131
<b>Table 9.2</b> Numerical values used as input in the CCA evaporation model of saline droplets .....	134
<b>Table 10.1</b> Nucleation kinetic parameters obtained from the fit in Figure 10.2. .	145



# Chapter 1

## Introduction

### 1.1 Motivation

Nucleation is one of the least-understood phenomena in material science.<sup>1-2</sup> Despite the tremendous efforts devoted to this field, there are still several important questions and research gaps that remain unclear. Meanwhile, nucleation is a key step in crystallization processes which is ubiquitous in nature and is a crucial unit operation in the manufacture and purification of products occurring in almost all sorts of industries including foods, pharmaceuticals, cosmetics, fine chemicals, ceramics, metallurgy and electronics.<sup>3-4</sup> In these multi-billion euro industries, nucleation plays a pivotal role.<sup>5-6</sup> Thus, further research on crystal nucleation is of paramount importance. Driven by such motivations, this doctoral thesis seeks to further understand the physics and chemistry of crystal nucleation from both engineering and scientific perspective, with a particular focus on the development of innovative methods in quantifying nucleation kinetics.

### 1.2 Background and Objective

Traditionally, the goal of measuring nucleation kinetics is to design, optimize, and control industrial crystallization processes. With this aim, several approaches on agitated crystallizers have been developed including those of Nyvlt<sup>7</sup>, Kubota<sup>8</sup>, and Sangwal.<sup>9</sup> Later on, Nagy<sup>10</sup> combined Nyvlt's approach with the population balance equation to allow simultaneous determination of nucleation and growth kinetics. Although the methods proposed by Nyvlt, Kubota, Sangwal and Nagy offer fast and simple ways of characterizing nucleation, their parameters are rather empirical which does not correspond to an actual physical quantity that can be interpreted theoretically. To improve on this, Mersmann et al.<sup>11</sup> developed a rather complex model describing various nucleation mechanisms. Similarly, Kashchiev, Borrisova, Hammond and Roberts developed their KBHR<sup>12</sup> model which attempts to predict nucleation parameters with actual physical meanings. However, the complex models require multiple parameters and have tendencies to give physically impossible values especially when some restrictive inequalities are not satisfied. Indeed, studying nucleation kinetics in agitated industrial crystallizer is challenging due to the interplay of hydrodynamics and the presence of foreign surfaces (crystallizer walls, impellers, baffles, sensors, probes) whose influence on

nucleation is not directly quantifiable. This results in the complex coupling of homogeneous primary, heterogeneous primary, and secondary nucleation. Therefore, from an engineering perspective, one of my objectives is to develop a simple and yet reliable method to obtain key nucleation parameters considering the influence of both primary and secondary nucleation.

Recently, the quantification of nucleation kinetics has been geared towards understanding its fundamental mechanisms. In the past, fundamental studies on nucleation were primarily carried out mainly on vapor to liquid experiments<sup>13</sup>. Fortunately, the development of microfluidic technologies has enabled studies of nucleation in solutions, which has been observed to be intrinsically stochastic. This means that identical samples under identical conditions will nucleate at different times. This behavior has its roots in statistical mechanics where the formation of nucleus is treated as a “success” from a series of random fluctuations, thereby making it a “rare” event.<sup>14</sup> Consequently, statistical analysis of multiple experiments is needed to fully elucidate the nucleation kinetics which can be addressed using microfluidic technologies.

With the recent advances in computing power, nucleation has also been studied in molecular level via theoretical simulations notably by molecular dynamics,<sup>15</sup> metadynamics,<sup>16</sup> and Monte Carlo approaches.<sup>17</sup> However, theoretical predictions are still order of magnitudes different from experimental data.<sup>1</sup> Apart from the multiple idealizations and approximations used in simulations, the discrepancy could be partly because simulations are normally carried out at very high supersaturation. This is needed in order to observe a “rare” event within a realistic computational time scale.<sup>18</sup> In bulk solution, this is difficult to achieve experimentally (with a risk of premature precipitation) but fortunately, very small volumes (nanoliter to femtoliter) can withstand very high supersaturations. This is because nucleation time is inversely proportional to the system volume<sup>19</sup> and the formation of clusters in such volume range has the possibility to deplete the supersaturation level.<sup>20</sup> Thus, another goal is to develop a reliable experimental approach in microfluidics that allows extraction of physically meaningful parameters. This is an important step towards achieving reasonable agreement between theory and experiment.

In summary, this thesis aims to develop innovative approaches for quantifying nucleation kinetics both in large-scale agitated crystallizers as well as in picoliter range microfluidic systems.

## 1.3 Structure of the Thesis

Following this introductory chapter, **Chapter 2** presents an extensive literature review of fundamental concepts and background that are essential in understanding the rest of the thesis. This includes the discussion of the thermodynamics of nucleation and the description of existing measurement techniques and mathematical models used in nucleation studies. I also include the principles of microfluidic systems and microdroplet evaporation. **Chapter 3** presents a general description of the materials and techniques used in this research project.

The succeeding chapters are my original research outputs. Each chapter is written in a way that it can stand independently; thus, each chapter has its own set of introduction with literature review, methodology, discussion, and conclusion. For a smooth transition between chapters, a brief description is written at the beginning which explains how each chapter relates to the rest of the thesis.

In **Chapter 4**, I propose a method to quantify primary nucleation kinetics in agitated crystallizers using particle-count approach. This is based on a laser backscattering technique coupled with in situ Raman spectroscopy. Under the assumption that the secondary nucleation rate varies exponentially with agitation rate and that primary nucleation is not severely affected by agitation, my approach involves extrapolation of the particle counts down to zero agitation speed in order to extract the primary nucleation kinetics. The resulting magnitude of nucleation rates are consistent with the KBHR model.

In **Chapter 5**, I compare the nucleation kinetic parameters obtained from the induction time distribution approach of stirred mL-vials against that of the particle-count approach. Results reveal discrepancies of six to seven orders of magnitude. Although differences in fluid dynamics due to agitation and crystallizer geometry may have an effect, this tremendous discrepancy provides strong evidence that primary nucleation rates obtained from such technique may not be used for interpretation of nucleation rates in industrial scale applications.

In **Chapter 6**, I quantify the nucleation kinetics using additional experiments namely, liter-scale conductometry and microliter-scale microscopy which both measure induction time. The results show that the pre-exponential factor  $A$  is highly dependent on the measurement technique and model assumptions while the effective interfacial energy between crystal and solution  $\gamma_{eff}$  is dependent on the supersaturation level and system volume. This chapter highlights that careful attention is needed in interpreting nucleation kinetic parameters acquired from different scales and measurement techniques.



In **Chapter 7**, I make a transition from the industrially oriented agitated crystallizer to a more fundamental study of homogeneous primary nucleation in small volumes. In this chapter, I study the nucleation kinetics of aqueous NaCl using our in-house developed microfluidic setup. Previously, it has been shown that an image analysis procedure based on standard deviation of the gray level pixels can be used to track the microdroplet dynamics and detect diffusive interactions which is marked by oscillations.<sup>21</sup> However, in the context of extracting nucleation parameters from such experiment, there is a need to quantify the influence of such interactions. To do this, I improved the numerical approach for automated detection and characterization of the interactions which allowed the classification of microdroplets as a function of the number of oscillations. Then, I show that failure to account for these interactions in the analysis of kinetic data can lead to severe inaccuracies in the estimated nucleation parameter. I highlight the fact that these interactions would be otherwise unobservable using traditional microscopy techniques. Moreover, with the help of our in-house developed humidity regulation module, I show that diffusion interactions disappear at low relative humidity.

In **Chapter 8**, I develop a novel approach to quantify nucleation kinetics in evaporating arrays of sessile microdroplets using aqueous NaCl as a model system. I demonstrate that by using a deliquescence-efflorescence cycle coupled with the analysis of the gray-level pixel standard deviation of the microdroplet image, one can (1) ascertain the time at which the microdroplet is saturated (2) measure the induction time without assuming a specific value of the evaporation rate. Furthermore, I show that the measurements are reproducible by performing statistical tests.

In **Chapter 9**, I derive an evaporation model for droplets with dissolved solute submerged in a thin layer of oil. This model is needed in order to accurately determine the droplet concentration at any given time. The model accounts for the additional complexity due to the variable diffusion distance due to the presence of oil, the diffusive interactions due to the presence of neighboring droplets, the density change as concentration increases and the water activity change as a function of concentration. By comparing the model predictions to experimental data, I show that different contact-line behaviors, that is, constant contact radius (CCR), constant contact angle, (CCA), or stick-slide (SS) result in almost identical evolution of droplet volume especially within the time scale relevant to crystallization studies. Moreover, I demonstrate for the first time that assuming a constant evaporation rate as well as neglecting the diffusive interactions between droplets can lead to severe discrepancies in the measurement of droplet concentration particularly during nucleation. With my model, one can accurately determine the time evolution of droplet concentration which is important in quantifying crystallization kinetics.

In **Chapter 10**, I show that by combining a modified Poisson distribution analysis together with an accurate evaporation model, one can obtain reliable nucleation kinetic parameters from experiments with increasing supersaturation with time. Using the NaCl-water system, I obtained a pre-exponential factor  $A$  of  $9.30 \times 10^{20} \text{ m}^{-3} \text{ s}^{-1}$  and interfacial energy between crystal and solution  $\gamma$  of  $46.7 \text{ mJ/m}^2$  which are in remarkable agreement with existing experimental and theoretical values. Interesting confinement effects on nucleation is also observed and analyzed. This is in support of the previous findings<sup>20, 22-23</sup> that at very small volume, the formation of the pre-critical cluster depletes the effective supersaturation level of its surrounding, thereby allowing the system to withstand much higher supersaturation. Given the numerous simulation studies on NaCl nucleation, our experimental kinetic parameters based on a stochastic approach can serve as an additional benchmark in validating theoretical predictions. Moreover, this experimental approach and data-treatment protocol can also be extended to study the nucleation of other salts, biological, and pharmaceutical crystals of interest.

Finally in **Chapter 11**, I summarize the key findings in this thesis. Building on these results, I then discuss my perspectives and outlook for future research.

## Chapter 2

### Literature Review

#### 2.1 Fundamentals of Crystallization

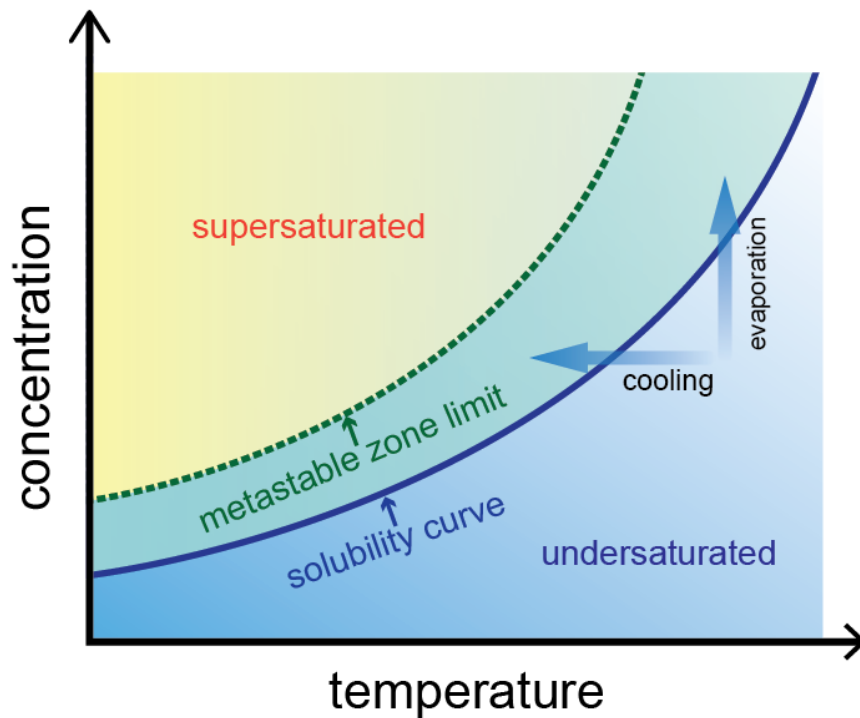
Solution crystallization is referred to as a phase transition in which a crystalline product is obtained from a solution.<sup>24</sup> Solution thermodynamics dictates the maximum amount of solute that can be dissolved in a fixed amount of solvent. Upon reaching this maximum value, the solution is said to be saturated and the amount of solute required to create a saturated solution at a given condition is called the solubility,<sup>25</sup> which is formally defined as the concentration at which the solid solute and liquid solution are at equilibrium.<sup>4</sup> The solubility of solute in solvent can be modeled as a function of temperature by the van't Hoff equation

$$\ln(x_i^{liq} \gamma_i^{liq}) = -\frac{\Delta H_{fus}}{R} \left( \frac{1}{T} - \frac{1}{T_m} \right) \quad (2.1)$$

where  $x_i^{liq}$  is the mole fraction solubility in the liquid phase,  $\gamma_i^{liq}$  is the activity coefficient,  $\Delta H_{fus}$  is the latent heat of fusion,  $T_m$  is the melting point,  $T$  is the absolute temperature, and  $R$  is the universal gas constant.<sup>26</sup>

The different regions of crystallization phase diagram are depicted in **Figure 2.1**. The area below the solubility curve is the undersaturated region where crystals cannot exist in equilibrium,<sup>27</sup> while the area between the solubility curve and the metastable limit curve is the metastable zone (MSZW).<sup>24</sup> Although the metastable region is above the solubility, the driving force is not sufficient to allow spontaneous nucleation to occur although crystal growth may take place.<sup>4</sup> At a supersaturation higher than the metastable zone limit is the region where primary nucleation can occur spontaneously.<sup>27</sup>

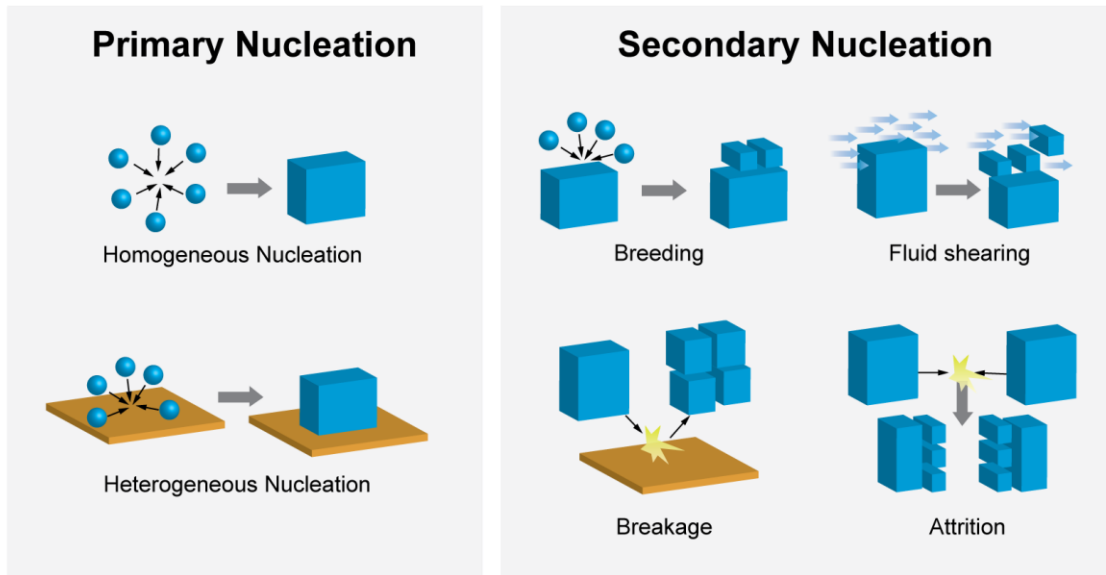
Before crystals can develop, stable nano-sized particles called nuclei must exist in the solution that act as centers of the crystallization.<sup>4</sup> The birth of these nuclei from solution is called nucleation which proceeds to relieve the supersaturation towards equilibrium.<sup>24, 27</sup>



**Figure 2.1** Typical phase diagram of crystallization process showing the solubility curve (blue line) and metastable zone limit (green dotted line).

### 2.1.1 Mechanisms of Nucleation

Nucleation may occur in various mechanisms which can be divided into two main categories - primary and secondary nucleation as illustrated in **Figure 2.2**. Primary nucleation occurs in the system that does not contain any precursor crystal. This can be further classified into (1) homogeneous nucleation in solutions if it is not influenced by impurities (higher free energy barrier) and (2) heterogenous nucleation onto a surface if it occurs due to presence of foreign impurities which lowers the energy barrier.<sup>4, 28</sup> On the other hand, secondary nucleation occurs due to the presence of pre-existing crystals of the same phase that proceeds in various mechanisms such as breeding, fluid-shearing, breakage, and attrition.<sup>29-30</sup>



**Figure 2.2** Schematic illustration of the mechanisms of nucleation. The blue spheres and prisms correspond to the monomer and crystal respectively. The orange plate corresponds to any foreign surface that is not the nucleating crystal.

In nucleation, the fundamental driving force is the difference in chemical potential of the liquid phase  $\mu_L$  and of the bulk crystals  $\mu_C$ . This chemical potential  $\Delta\mu$  is related to the supersaturation ratio  $S$  as <sup>4</sup>

$$\Delta\mu = \mu_L - \mu_C = kT \ln S \quad (2.2)$$

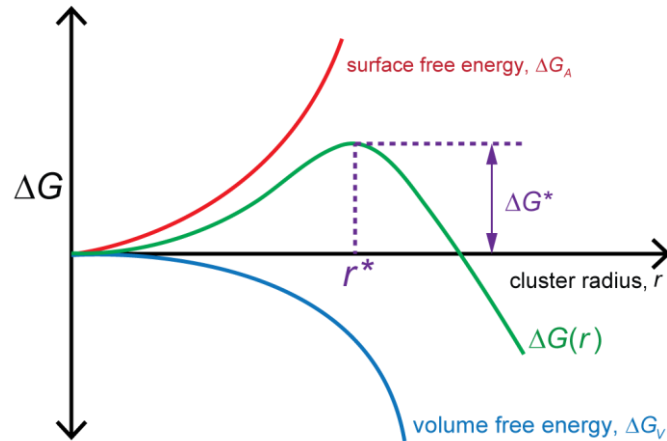
where  $S$  is the ratio of activities (actual vs equilibrium). The activity coefficient of the solute in the supersaturated solution is very close to the activity coefficient of the solute in the saturated solution, so the ratio of the activity coefficients is equal to 1. As a result, the supersaturation ratio can be approximated as the solute concentration  $c$  divided by the solubility  $c_s$ .

## 2.1.2 Classical Nucleation Theory

Classical nucleation theory (CNT) is the most common theoretical model used to describe nucleation,<sup>2</sup> developed by Volmer and Weber,<sup>31</sup> Becker and Döring<sup>32</sup>, and Frenkel.<sup>33</sup> In this section, I will discuss how CNT applies to both homogeneous and heterogeneous nucleation.

### 2.1.2.1 Homogeneous Nucleation

According to CNT, there are two competing energy terms in the formation of nuclei, the volume free energy  $\Delta G_V$  and the surface free energy  $\Delta G_A$ . The volume free energy  $\Delta G_V$  corresponds to the stability gained by the cluster as it aggregates while the surface free energy  $\Delta G_A$  corresponds to the energy penalty for creating a new surface. The typical free diagram of nucleation in the framework of CNT is illustrated in **Figure 2.3**.



**Figure 2.3** Free energy diagram of nucleation as a function of cluster radius  $r$ .

CNT postulates that the change in free energy for the formation of new phase is the sum of  $\Delta G_V$  and  $\Delta G_A$ . Assuming a spherical cluster, this is mathematically written as

$$\Delta G = \Delta G_V + \Delta G_A = -\frac{4}{3}\pi r^3 \rho_s \Delta\mu + 4\pi r^2 \gamma \quad (2.3)$$

Where  $r$  is the cluster radius,  $\Delta\mu$  is the difference in chemical potential between solid and liquid,  $\rho_s$  is the number density of solid (# of molecules or formula units per volume) and  $\gamma$  is the interfacial energy between crystal and solution.

With these two energy terms having opposite signs, there comes a point where the total free energy reaches a maximum,  $\Delta G^*$  and this corresponds to the energy barrier for the formation of nuclei (analogous to activation energy). Therefore, the nucleation rate ( $J$ ), defined as the number of critical nuclei formed per unit time and volume of the bulk solution, can be expressed in terms of the kinetic pre-exponential factor  $A$ , the critical Gibbs free energy  $\Delta G^*$  as,

$$J = A \exp\left(\frac{-\Delta G^*}{kT}\right) \quad (2.4)$$

with  $k$  being the Boltzmann constant, and  $T$  is absolute temperature.<sup>4</sup> To find the critical radius  $r^*$ , we can take the derivative of equation 2.4 with respect to  $r$  and then equate to zero.

$$\frac{d\Delta G}{dr} = -4\pi(r^*)^2 \rho_s \Delta\mu + 8\pi r^* \gamma = 0 \Rightarrow r^* = -\frac{2\gamma}{\Delta\mu \rho_s} \quad (2.5)$$

From equation 2.3 and 2.5, the expression for critical Gibbs free energy for the critical nucleus can be written as

$$\Delta G^* = \frac{4\pi}{3} \gamma (r^*)^2 \quad (2.6)$$

Combining equations, (2.2), (2.4), (2.5), and (2.6), the nucleation rate can be expressed in terms of supersaturation as

$$J = A \exp\left[\frac{-16\pi\gamma^3}{3\rho_s^2 (kT)^3 \ln^2 S}\right] \quad (2.7)$$

At constant temperature, the variables  $\gamma$ ,  $\rho_s$ , and  $T$  remain constant, thus we can combine them as a thermodynamic parameter  $B$  and the CNT equation can be rewritten in a simple form as

$$J = A \exp\left[-\frac{B}{\ln^2 S}\right] \text{ where } B = \frac{-16\pi\gamma^3}{3\rho_s^2 (kT)^3} \quad (2.8)$$

An important implication of CNT is that the rate of nucleation is governed by three primary variables<sup>24</sup> namely temperature  $T$ , supersaturation  $S$ , and interfacial surface tension  $\gamma$  between the nuclei and the solution. The pre-exponential factor

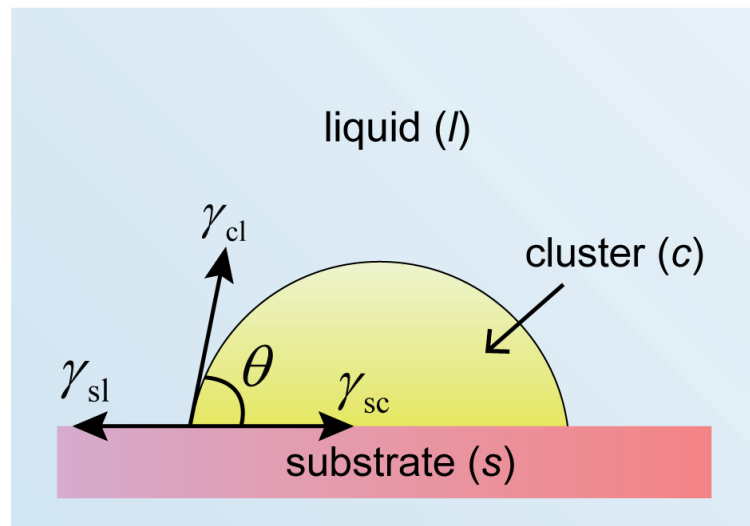
$A$  is related to the Zeldovich factor (correction factor to account for the critical clusters that do not grow to large crystals), attachment frequency  $f^*$  (related to the diffusivity of the monomers to the cluster), and the concentration of nucleation sites  $C_0$  (approximately equal to  $\rho_s$  for homogeneous nucleation).<sup>34</sup>

The relationship between the pre-exponential factor  $A$ , Zeldovich factor  $z$ , attachment frequency  $f^*$ , and concentration of nucleation sites  $C_0$  can be written as

$$A = zf^*C_0 \quad (2.9)$$

### 2.1.2.2 Heterogeneous Nucleation

In the presence of foreign substrate or impurities, the nucleating cluster can form onto the surface through a process known as heterogeneous nucleation as illustrated in **Figure 2.4**.



**Figure 2.4** Schematic illustration of the static equilibrium of three interfacial energies  $\gamma_{sl}$  (substrate-liquid),  $\gamma_{sc}$  (substrate-cluster), and  $\gamma_{cl}$  (cluster-liquid) which are balanced at a contact angle  $\theta$  between the nucleating phase and the substrate.<sup>34</sup>

This phenomenon can be incorporated to the classical nucleation theory equation by multiplying the critical Gibbs' free energy  $\Delta G^*$  by a factor  $\Phi$  (varies between 0 to 1) to obtain the effective energy barrier  $\Delta G_{eff}^*$  as

$$\Delta G_{eff}^* = \Phi \Delta G^* \quad (2.10)$$



The factor  $\Phi$  is a function of the contact angle  $\theta$  of the nucleating cluster to the foreign substrate (**Figure 2.4**) according to

$$\Phi = \frac{1}{4}(2 + \cos \theta)(1 - \cos \theta)^2 \leq 1 \quad (2.11)$$

The value of  $\theta$  is dependent on the interfacial energies between the substrate and liquid  $\gamma_{sl}$ , the substrate and cluster  $\gamma_{sc}$ , and the cluster and liquid phase  $\gamma_{cl}$  according to Young's equation<sup>34</sup> which can be written as

$$\gamma_{sl} = \gamma_{cs} + \gamma_{cl} \cos \theta \quad (2.12)$$

In practice, heterogeneous nucleation is almost inevitable<sup>35</sup> so what we generally extract from nucleation rate measurements is the effective interfacial energy  $\gamma_{\text{eff}}$  instead of the homogeneous interfacial energy  $\gamma$  (between crystal and solution). Since  $\Phi$  varies within 0 to 1, it follows that the effective interfacial  $\gamma_{\text{eff}}$  is bounded as

$$0 < \gamma_{\text{eff}} \leq \gamma \quad (2.13)$$

Due to the lowering of energy barrier, heterogeneous nucleation is generally favored at lower supersaturation while homogeneous nucleation is favored at higher supersaturation.<sup>36</sup>

### 2.1.3 Two-step Nucleation Theory (2-SNT)

As the name implies, the 2-SNT theory has two intermediate states (thus, two energy barriers). The first step is the formation of a stable dense liquid and metastable clusters followed by the second step which is the formation of the solid structured cluster. With this different energetic pathway, the resulting mathematical expression for the nucleation rate may differ and the equation can be found elsewhere<sup>37</sup>. In summary, it postulates an exponential dependence of nucleation rate with respect to supersaturation until a certain critical supersaturation, after which, the nucleation rate either decreases or stabilizes. Although this theory can rationalize the behavior of proteins, the model has more parameters. Consequently, CNT is still the model of choice for nucleation studies in small organic molecules due to its simplicity.

## 2.2 Nucleation Kinetics: Approaches on Data Acquisition and Treatment

### 2.2.1 Deterministic Approach

These methods treat nucleation as a deterministic phenomenon, and thus do not employ probability distribution functions to extract nucleation kinetic data.

#### 2.2.1.1 Nyvlt's Model

Nyvlt's approach allows for estimation of primary nucleation rates by measuring the metastable zone width (maximum undercooling) at different cooling rates. Nyvlt model assumes a power-law relationship between the mass basis nucleation rate and the maximum concentration difference ( $\Delta c_{max}$ ).

$$J = k_m (c_0 - c_s)^m = k_m (\Delta c_{max})^m \quad (2.14)$$

The second assumption is that the mass nucleation rate is related to the variation of solubility with temperature and the cooling rate.

$$J = \left( \frac{dc_s}{dT} \right) \left( \frac{\Delta T}{\Delta t} \right) \quad (2.15)$$

Then, assuming a linear relationship between solubility and temperature, the following approximation can be made

$$\frac{\Delta c_{max}}{\Delta T_{max}} = \frac{dc_s}{dT} \quad (2.16)$$

Combining equations (2.14), (2.15), and (2.16), we get

$$J = k_m (\Delta c_{max})^m = k_m \left[ \Delta T_{max} \left( \frac{dc_s}{dT} \right) \right]^m = \left( \frac{dc_s}{dT} \right) \left( \frac{\Delta T}{\Delta t} \right) \quad (2.17)$$

Solving for the cooling rate  $\Delta T/\Delta t$

$$\left( \frac{\Delta T}{\Delta t} \right) = k_m \left( \frac{dc_s}{dT} \right)^{m-1} (\Delta T_{max})^m \quad (2.18)$$

Taking the logarithm of both sides, the plot of  $\ln(\Delta T/\Delta t)$  against  $\ln(\Delta T_{max})$  would be a straight line whose slope and intercept yields the nucleation order  $m$  and rate constant  $k_m$  can be obtained. The values of  $k_m$  and  $m$  can then be used to calculate the nucleation rate  $J$  at a given supersaturation.

$$\ln\left(\frac{\Delta T}{\Delta t}\right) = \ln k_m + (m - 1) \ln\left(\frac{dc_s}{dT}\right) + m \ln(\Delta T_{max}) \quad (2.19)$$

### 2.2.1.2 Kubota's Model

Kubota's approach is similar to that of Nyvlt except that Kubota relates the nucleation rate to the change in number density ( $N_m/V$ ) instead of using a mass-based nucleation rate. Moreover, while Nyvlt's model interprets MSZW measurements, Kubota's model also allows for interpretation of both MSZW and induction time.

In this model, an empirical power-law relationship between nucleation rate and undercooling is assumed

$$J = k_n(\Delta T)^n \quad (2.20)$$

Then, the number density  $N_m/V$  at time  $t_m$  can be written as

$$\frac{N_m}{V} = \int_0^{N_m} d\left(\frac{N}{V}\right) = \int_0^{t_m} J dt \quad (2.21)$$

where  $N_m$  is the accumulated number  $N$  of grown primary nuclei and  $V$  is the working volume of the crystallizer. Assuming a constant cooling rate  $R = d(\Delta T)/dt$ , we can integrate equation (2.21) as

$$\frac{N_m}{V} = \int_0^{T_{max}} k_n(\Delta T)^n \left(\frac{d\Delta T}{R}\right) = \frac{k_n(\Delta T_{max})^{n+1}}{R(n+1)} \quad (2.22)$$

Rewriting equation (2.22) in terms of the cooling rate  $R$  and taking the logarithm of both sides

$$\ln(R) = \ln \left[ \frac{Vk_n}{N_m(n+1)} \right] + (n+1) \ln(\Delta T_{\max}) \quad (2.23)$$

Thus, plotting  $\ln R$  against  $\ln(\Delta T_{\max})$  yields the nucleation order  $n$  and rate constant  $k_n$  from the slope and intercept respectively.

Kubota defined the induction time  $t_{\text{ind}}$  as the time needed for the number density ( $N_m/V$ ) to reach a certain threshold for detection.

$$\frac{N_m}{V} = \int_0^{t_{\text{ind}}} J dt = \int_0^{t_{\text{ind}}} k_n (\Delta T)^n dt \quad (2.24)$$

Since the experiment is isothermal,  $\Delta T$  is constant with respect to time, so integrating equation (2.24) yields the relationship between induction time  $t_{\text{ind}}$  and undercooling  $\Delta T$  as

$$t_{\text{ind}} = \left( \frac{N_m}{k_n V} \right) (\Delta T)^{-n} \quad (2.25)$$

Thus plotting  $\ln(t_{\text{ind}})$  against  $\ln(\Delta T)$  yields the nucleation order  $n$  and the rate constant  $k_n$  from the slope and intercept respectively. From the values of  $n$  and  $k_n$ , the nucleation rate  $J$  can then be calculated.

### 2.2.1.3 Kashchiev–Borissova–Hammond–Roberts (KBHR) Model

This model postulates two types of nucleation, instantaneous nucleation (IN, all nuclei are generated at the same time) and progressive nucleation (PN, nuclei are generated progressively over time). The model also accounts for the detection limit of the instrument using the dimensionless parameter  $\alpha_{\text{det}}$  defined as the fraction of the minimum volume of detectable crystals to the total volume. The complete derivation is rather complex and has been detailed in the work of Camacho et al<sup>38</sup>. Briefly, the expression for nucleation rate is

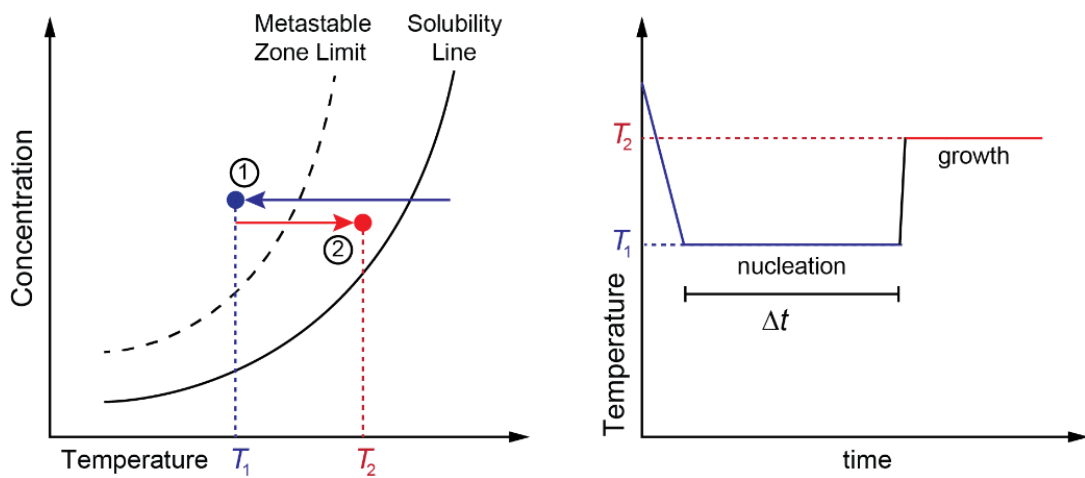
$$J = A \exp \left[ - \frac{b}{(1-u)u^2} \right] \text{ where } u = \frac{\Delta T_c}{T_e}, b = \frac{16\pi\gamma^3}{3kT\rho_s^2\xi^2} \quad (2.26)$$

where  $A$  is the pre-exponential factor,  $b$  is the dimensionless thermodynamic

parameter containing the molecular latent heat of crystallization term  $\xi$ ,  $\Delta T_c$  is the undercooling,  $T_e$  is the equilibrium temperature,  $\gamma$  is the interfacial energy between crystal and solution,  $\rho_s$  is the inverse of molecular volume (number density).

#### 2.2.1.4 Double-Pulse Technique

This method enables direct measurement of the steady-state nucleation rate by decoupling the nucleation and growth processes of crystallization. Its principle is illustrated in Figure 2.5 for systems where solubility increases with temperature.



**Figure 2.5** Principle of double pulse technique (Adapted from Revalor et. al.<sup>39</sup>)

Initially, a supersaturated solution is created by cooling the system to a temperature below the metastable zone limit  $T_1$ , then the temperature is kept constant for a certain period  $\Delta t$  to allow nucleation to occur. Then, the system is heated (or cooled in the case of systems with reverse solubility, i.e. exothermic dissolution) to a temperature within the metastable zone where the nuclei generated are grown to detectable size. Since no spontaneous nucleation can occur in the metastable zone, the steady-state nucleation rate corresponds to the slope of the number of crystals  $\Delta N$  generated (counted via optical microscopy) with respect to the time elapsed in the nucleation pulse  $\Delta t$ .

$$J = \frac{\Delta N}{\Delta t} \quad (2.27)$$

However, this method has few limitations as it would tend to systematically underestimate the nucleation rate<sup>40</sup>. This is because the required critical size

generally increases with temperature. Given that the critical size at  $T_2$  is greater than that of  $T_1$ , some of the nuclei that just reached critical size at  $T_1$  could dissolve at  $T_2$ .

## 2.2.2 Stochastic Approach

These methods use probability distribution functions to treat nucleation data. There are different methods used to acquire such data, either via constant supersaturation or via varying supersaturation experiments. Constant supersaturation experiments are usually performed either via crash-cooling<sup>41</sup> or rapid anti-solvent addition.<sup>42-43</sup> When the desired supersaturation is achieved, the temperature and concentration is held constant and then the induction time is measured. Induction time is generally the “waiting time” for a supersaturated solution to nucleate. On the other hand, varying supersaturation experiments can be done either via slow cooling (to measure metastable zone width at different cooling rates)<sup>44</sup> or via isothermal evaporative crystallization (to measure induction time).<sup>45</sup>

Since nucleation is stochastic, identical samples at identical conditions will have different induction times or metastable zone widths. Thus, numerous independent experiments are needed to obtain representative values of nucleation parameters. In data analysis, the cumulative probability of nucleation  $P(t)$  is normally plotted against time.  $P(t)$  is simply the fraction of the samples that have nucleated after time  $t$  and then a probability distribution function (PDF) is used to fit the data. However, one important question is what mathematical function we should use to fit these data. In this section, I will discuss the different types of distribution functions used in nucleation studies.

### 2.2.2.1 Poisson Distribution

Nucleation can be interpreted as a “rare success” from a series of random fluctuations made by the system to overcome the energy barrier.

From the probability theory, if the probability of success  $p$  remains constant with time and  $n_a$  is the number of successive independent attempts to nucleate, then the probability of forming  $k$  nucleus at a given time interval is given by the binomial distribution written as

$$P_k = \frac{n_a}{k! (n_a - k)!} p^k (1 - p)^{n_a - k} \quad (2.28)$$

The property of binomial distribution also suggests that the mean number of success  $N$  is the product of the number of attempts  $n_a$  and the probability of success  $p$ , written as

$$N = n_a p \quad (2.29)$$

However, the system makes a lot of attempts, and each attempt has a low probability of success. Thus, if we take the limit of  $n_a \rightarrow \infty$  and  $p \rightarrow 0$  while keeping the product  $n_a p$  constant, the binomial distribution reduces to a Poisson distribution<sup>46</sup>, that is,

$$P_k = \lim_{n_a \rightarrow \infty, p \rightarrow 0} \frac{n_a}{k! (n_a - k)!} p^k (1 - p)^{n_a - k} = \frac{(n_a p)^k \exp(-n_a p)}{k!} \quad (2.30)$$

Combining equations (2.29) and (2.30), the probability of forming  $k$  nuclei in a time interval is described by

$$P_k = \frac{N^k \exp(-N)}{k!} \quad (2.31)$$

where  $N$  is the average number of nuclei. Consequently, the probability that the onset of nucleation will be detected at a certain time interval corresponds to the probability that at least one nucleus is formed which can be expressed as

$$P(k \geq 1) = \sum_{i=1}^{\infty} \frac{N^i \exp(-N)}{i!} \quad (2.32)$$

However, notice that the probability of forming at least one nuclei is just the complement of the probability that no nuclei will form. Applying this mathematical concept, equation (2.32) can be simplified as

$$P(k \geq 1) = 1 - P(k = 0) \Rightarrow P(k \geq 1) = 1 - e^{-N} \quad (2.33)$$

In turn, the average number of nuclei  $N$  can be determined as

$$N = JV\Delta t \quad (2.34)$$

where  $J$  is the nucleation rate, i.e. the number of nuclei that appears per unit solution volume per unit time ( $\#/m^3s$ ),  $V$  is the solution volume and  $\Delta t$  is the time interval. This expression relates the probabilistic notion of nucleation to the deterministic classical nucleation theory.

Meanwhile, the formed nuclei must grow to detectable sizes before they can be observed experimentally by measuring equipment which causes a delay in detection called growth time  $t_g$ . Incorporating this lag time, the probability of detecting crystals at a time  $t$  can be expressed as

$$P(t) = 1 - \exp[-J(t - t_g)] \quad (2.35)$$

The cumulative probability distribution described by equation 2.31 can be determined by measuring induction times under equal conditions for a sufficient number of isolated experiments which can be written as

$$P(t) = \frac{M^+(t)}{M} \quad (2.36)$$

where  $M^+(t)$  is the number of isolated experiments that nucleated at a time less than or equal to time  $t$  and  $M$  is the total number of experiments. Thus, the value of the nucleation rate  $J$  by the curve fitting of  $P(t)$  against induction time.

### 2.2.2.2 Distributions for Non-Constant Nucleation Rates

For systems where the effective nucleation rate evolves with time, the Poisson function would not be applicable since it assumes that the probability of nucleation stays constant. For systems with non-steady nucleation rate, other probability distribution are used. To understand these distributions, we will discuss the concept of an effective nucleation rate  $h(t)$  which is related to the cumulative probability function  $P(t)$  as

$$\frac{dP(t)}{dt} = -h(t)P(t) \quad (2.37)$$



By analogy,  $h(t)$  is also known as the hazard function which corresponds to the failure rate in the field of survival data analysis.<sup>41</sup> If  $h(t)$  does not change with time, it leads to a simple exponential cumulative probability function which is mathematically equivalent to the Poisson distribution.

#### 2.2.2.2.1 Gompertz Distribution

If the effective nucleation rate  $h(t)$  increases exponentially with time at rate of  $\lambda$  from an initial rate of  $R_0$ , that is,  $h(t) = R_0 \exp(\lambda t)$ , then it would result in a Gompertz distribution written as

$$P(t) = \exp \left[ \frac{R_0}{\lambda} (1 - \exp(\lambda t)) \right] \quad (2.38)$$

If  $\lambda > 0$ , the nucleation rate increases exponentially with time and if  $\lambda < 0$ , the rate exponentially decreases.

#### 2.2.2.2.2 Weibull Distribution

The Weibull distribution containing two parameters can be written as

$$P(t) = \exp \left[ - \left( \frac{t}{\tau} \right)^\beta \right] \quad (2.39)$$

where  $\tau$  is a parameter related to the median nucleation time  $t_{med}$  as

$$\tau = t_{med} (\ln 2)^{1/\beta} \quad (2.40)$$

If  $\beta > 1$ , the effective nucleation rate increases monotonically with time. Likewise, the rate decreases if  $\beta < 1$ .

## 2.3 Droplet-based Microfluidics in Crystallization Studies

Microfluidics is a system that allows precise manipulation of fluids that are spatially confined in a channel with dimensions on the scale of micrometers. The main advantages of droplet-based microfluidics in crystallization studies are as follows:

- 1) Large numbers of simultaneous independent experiments under identical conditions can be performed using very small quantities of material. This allows for high-throughput screening and optimization of crystallization conditions as well as investigating the stochastic nature of nucleation.
- 2) It offers excellent control of heat and mass transfer due to its high surface-to-volume ratio and miniature scale, allowing rapid mixing and fast temperature control.
- 3) Facile integration of different modules such as online microscopes, spectrometers, diffractometers, and other sensors or external fields. As the appearance of the first nucleus is quickly detectable in microscale, it avoids the detection issues that are present in large-scale experiments where the detection limits of the instrument is taken as an additional parameter.

Given these benefits, microfluidic technology has become an attractive tool and has been extensively used in numerous studies.<sup>47-49</sup> However, conventional setups have some drawbacks.

- 1) Microfluidic chips generally require sophisticated and expensive microfabrication technologies such as soft lithography, stereolithography, or high-resolution 3D printing.<sup>50</sup>
- 2) Conventional chips are made of silicone, hydrogels, elastomers, or polydimethylsiloxane (PDMS) which all have poor solvent compatibility. PDMS devices also suffer from droplet evaporation due to its permeability.<sup>51</sup>
- 3) The need for surfactants which facilitates the formation of an interface and thus stabilizes the emulsion while minimizing the risks of coalescence of

the drops. Unfortunately, surfactants themselves could influence the crystallization behavior.<sup>52</sup>

- 4) The risk of clogging due to precipitates adhering on the channel wall which can obstruct the flow and increase the pressure drop.<sup>47</sup>

### 2.3.1 Principle of Droplet Generation in Microfluidics

The generation of discrete droplets which could serve as independent crystallizers is crucial in microfluidic experiments. Here, we will focus on droplet-based microfluidics based on the generation of monodispersed drops by mixing two immiscible liquids. These drops are isolated from each other by a continuous phase and can thus be considered as a closed system without contact with the outside and therefore can serve as real independent nanocrystallisers. A large number of drops can then be generated to allow the repetition of the experiments and to carry out statistical studies, which is particularly important in the study of nucleation as it is inherently a stochastic process. Ideally, each droplet must be of the same volume (monodispersed), does not coalesce (stable), and equally spaced between each other. To achieve these, it is important to understand the physical principles governing the droplet formation in microfluidics.

#### 2.3.1.1 Relevant Dimensionless Numbers

Although the physical laws of fluid mechanics are the same on a microscopic scale and on a large scale, some macroscopically negligible phenomena become preponderant at the microscopic scale, such as the capillarity force, while others like gravity become negligible. Dimensionless numbers are useful in analyzing the dominating or negligible forces in the system such as viscous forces, inertial forces, gravitational forces, and interfacial forces.

1. **Bond Number** This corresponds to the ratio of gravitational to interfacial forces

$$Bo = \frac{\Delta\rho g D^2}{\sigma} \quad (2.41)$$

where  $\Delta\rho$  is the density difference of the fluids,  $g$  is the acceleration due to gravity,  $D$  is the hydrodynamic diameter,  $\sigma$  is the surface tension. The Bond number can be used to assess whether gravitational forces are insignificant ( $Bo \ll 1$ ).

2. **Capillary Number** This describes the ratio of viscous forces to interfacial surface tension forces

$$Ca = \frac{\mu U}{\sigma} \quad (2.42)$$

where  $\mu$  is the dynamic viscosity of the continuous phase,  $\sigma$  is the surface tension,  $U$  is the average velocity of the two fluids, i.e. if  $q_C$  and  $q_D$  are the volumetric of the two fluids flowing in a channel with a cross section  $A$ , then  $U = (q_C + q_D)/A$ . In terms of droplet velocity  $v_d$  and interfacial tension of the fluid pair  $\gamma_{CD}$ , the expression for  $Ca$  becomes

$$Ca = \frac{\mu_C v_C}{\gamma_{CD}} \quad (2.43)$$

3. **Reynolds Number** This describes the ratio of inertial forces to viscous forces

$$Re = \frac{\rho U D}{\mu} \quad (2.44)$$

Where  $\rho$  is the density,  $U$  is the average velocity of the two fluids,  $D$  is the characteristic hydrodynamic diameter. Reynolds number characterizes the flow pattern as laminar ( $Re < 1000$ ) or turbulent ( $Re > 2100$ ).

4. **Weber Number** This corresponds to the ratio of inertial forces to interfacial forces and is defined as the product of Capillary number and Reynolds number.

$$We = Ca \times Re = \frac{\rho U^2 D}{\sigma} \quad (2.45)$$

The Weber number can be used to assess whether inertial forces are insignificant ( $We \ll 1$ ).

5. **Peclet Number** This is the ratio of convective mass transfer to diffusive mass transfer<sup>53,53</sup>. If  $Pe \ll 1$ , the diffusion rate of the solute is fast enough to avoid a considerable enrichment at the receding surface and thus the system maintains a homogeneous composition. In evaporating microdroplets, this can be expressed mathematically as

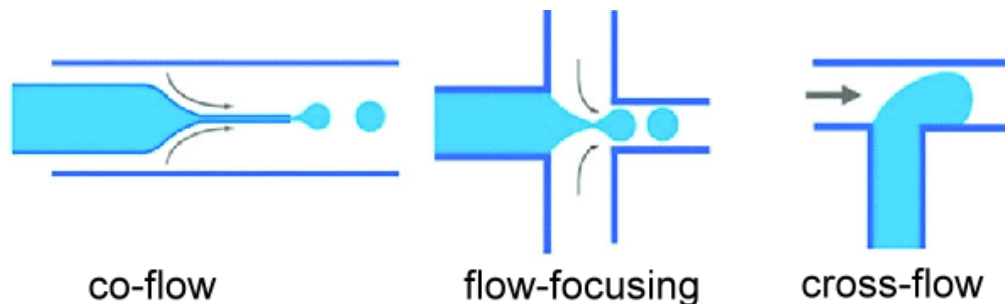
$$\kappa = \frac{1}{A} \frac{dV}{dt} \quad (2.46)$$

$$Pe = \frac{2R\kappa}{D_i} \quad (2.47)$$

Where  $\kappa$  is the evaporation flux (volume loss  $dV/dt$  per unit area  $A$ ),  $R$  is the droplet radius and  $D_i$  is the diffusion coefficient of the solute in the droplet.

### 2.3.1.2 Droplet Generation Design in Microfluidics

There are three common methods of generating droplets namely: co-flow, flow-focusing and cross-flow as illustrated in **Figure 2.6**.



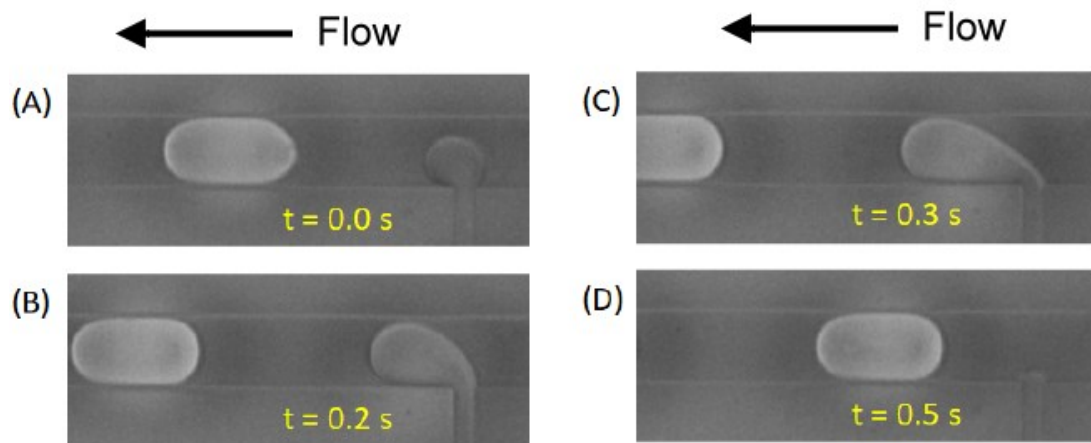
**Figure 2.6** Different designs for droplet generation in microfluidics<sup>54</sup>

1. **Co-flow** In this system, the dispersed phase channel is inserted co-axially with the continuous phase channel, resulting in both dispersed phase and continuous phase fluids flowing in parallel through the channels.
2. **Flow-focusing** Here the dispersed phase flow is pinched perpendicularly by two continuous phase flows, which leads to the rupture of the dispersed phase in drops parallel to its direction of injection

3. **Cross-flow** This system uses a T-junction wherein the continuous phase crosses the dispersed phase flow perpendicularly, leading to the formation of drops perpendicular to the dispersed phase entry.

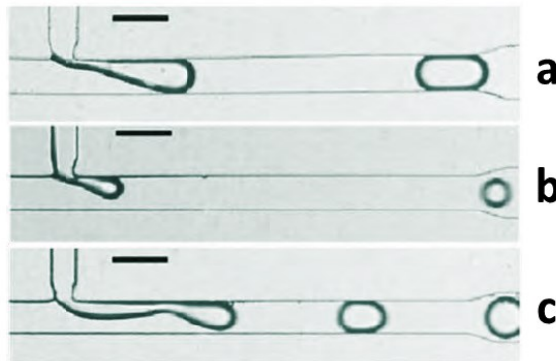
### 2.3.1.3 Droplet Formation in T-junction

While there are different design structures for droplet generation, we will focus our attention on cross-flow system using T-junction. This is perhaps the most popular method because T-junctions are commercially available and can easily be integrated in plug-and-play setups. In T-junctions, two immiscible fluids meet at a 90° angle resulting in the formation of droplets. The stages of droplet formation are illustrated in **Figure 2.7**.



**Figure 2.7** Stages of droplet formation in a T-junction in squeezing regime. (A) At  $t = 0$  s, the droplet begins filling the channel. (B) At  $t = 0.2$  s, the droplet blocks the cross section. (C) At  $t = 0.3$  s, the droplet "neck" gets squeezed. (D) At  $t = 0.5$  s, the interfacial tension could not support the thinning of the "neck" resulting in the detachment of the droplet.<sup>55</sup>

Depending on the value of Capillary number  $Ca$ , different flow regimes can occur as illustrated in **Figure 2.8**.



**Figure 2.8** Three regimes of droplet formation in T-junctions (a) squeezing (b) dripping (c) jetting. Adapted from Zhu et. al.<sup>56</sup>

1. **Squeezing regime** corresponds to a drop that fills the outlet channel before detaching due to the internal pressure drop ( $Ca \ll 0.1$ ). The length of the drop is greater than the diameter of the outlet channel which gives it the name of "plug" (Figure 2.8a).
2. **Dripping regime** is characterized by a drop that does not fill the channel exit before detaching due to the shear stress of the continuous phase. Its size is therefore less than that of the channel width. This regime is observed at  $Ca > 0.01$  (Figure 2.8b).
3. **Jetting regime** corresponds to a flow of the phase dispersed under shape of a wire or a jet. When the interfacial tension is low, the jet is destabilized to form drops which are transported by the flow of the continuous phase. This is observed at very high  $Ca$  values (Figure 2.8c).
4. **Transitional regime** is the intermediate regime between squeezing and jetting. The detachment of the drops is controlled both by the pressure drop and shear stress. Even though most of the authors do not describe this transient regime, a critical value of  $Ca \sim 0.015$  can be defined.

### 2.3.2 Recent Advances in Microfluidics Crystallization

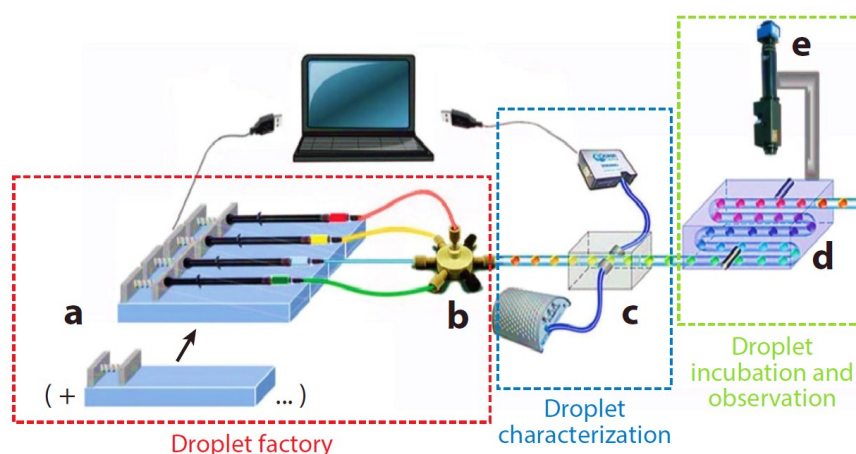
There has been tremendous progress in the use of microfluidics in crystallization as reviewed by Leng<sup>47</sup>, Shi<sup>50</sup>, and Candoni.<sup>57</sup> Indeed, the choice of materials in the fabrication of microfluidic platform is an important consideration. The advantages

and disadvantages of different materials (silicon, glass, ceramics, elastomers, hydrogels, thermoplastics, etc) in terms of mechanical properties, thermal properties, solvent resistance, optical transmissivity, biocompatibility and material cost have been reviewed by Tsao<sup>58</sup> and Niculescu et al.<sup>59</sup> In this section, I will focus on the advances developed in our laboratory to study crystallization fundamentals by taking advantage of cheap and commercially-available materials instead of employing sophisticated fabrication technologies.

### 2.3.2.1 Microfluidic Experiments in Transparent Capillary

As solvent incompatibility limits the diversity of the compounds that can be studied in microfluidics, Ildefonso et al.<sup>51</sup> developed a microfluidic platform consisting of a T-junction made of polyether ether ketone (PEEK) and a Teflon tubing which has been found to be superior to both pure PDMS and mixed PDMS/Teflon device in terms of stability in various solvents namely ethanol, acetone, ethyl acetate, nitrobenzene and acetonitrile. Moreover, this platform enables droplet storage for several weeks without significant evaporation.

To develop a cheaper alternative to the sophisticated microfabrication technologies, Zhang et. al.<sup>52</sup> developed a home-made microfluidic platform built entirely from commercially available modules as illustrated in **Figure 2.9**. This platform has been shown to enable generation of stable monodisperse droplets with uniform spacing and was successfully used to study the crystallization of lysozyme, isonicotinamide, gliclazide and paracetamol.

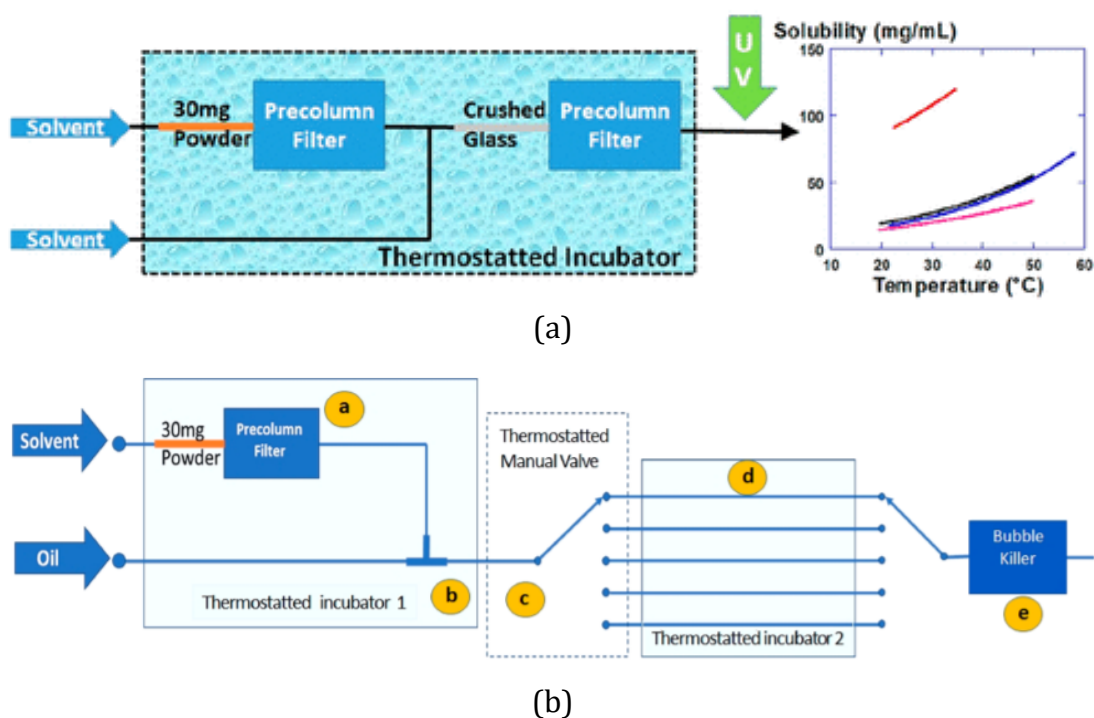


**Figure 2.9** Schematic of the in-house developed microfluidic platform. (a) The droplet factory consists of syringe pumps and (b) multiport junction made of



polyether ether ketone (PEEK) which is resistant to various types of solvent (c) the droplet characterization zone features a UV-VIS-NIR spectrophotometer (190 to 2300 nm). (d,e) The incubation and observation zones are composed of a thermostated bath and xyz-motorized camera with variable zoom capability. Adapted from Candoni et al.<sup>57</sup>

Recently, Peybernes<sup>60</sup> developed a rapid method to measure the solubility and to screen polymorphs directly from powder. The setup is shown in **Figure 2.10**. This is done by passing the solvent through a bed of powder which then rapidly becomes saturated. The solution can then be analyzed by in situ UV-VIS spectroscopy

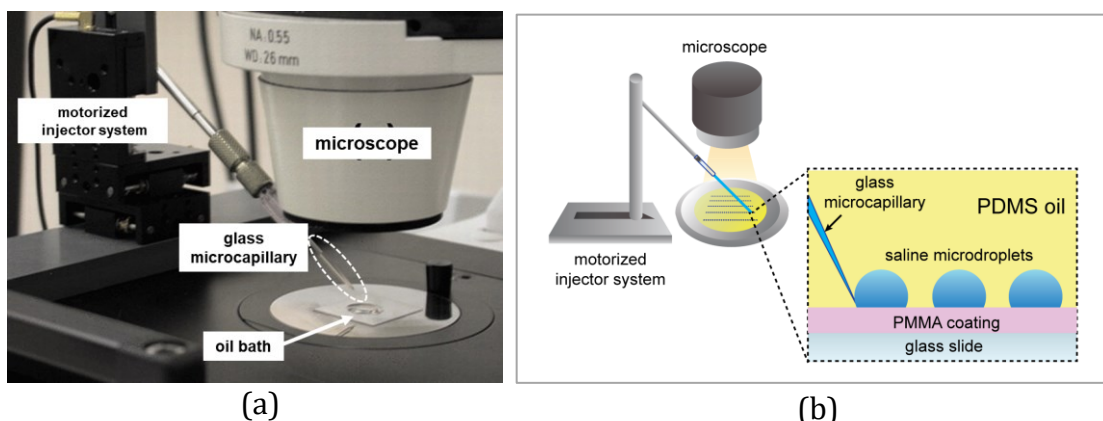


**Figure 2.10** Schematic illustration of the setup for (a) solubility measurement and (b) polymorph screening directly from powder. Adapted from Peybernes et al.<sup>60-61</sup>

These systems are called "closed microfluidics" because the droplets are sealed in the microchannel.<sup>62</sup> Thus, once generated, the droplets are not accessible to external instruments. Moreover, their diameter depends on the size of the capillaries used (commercially available). Hence the droplets are usually in the nanoliter range.

### 2.3.2.2 Evaporative Sessile Microdroplet Experiments

To study nucleation in picoliter to femtoliter volume ranges, Grossier et al<sup>63</sup> developed a simple yet efficient method to generate such microdroplets without the need for surfactants (which can alter fluid-interface properties). This set-up is shown in **Figure 2.11**. The motorized microinjector can move in three directions by 16 nm increments while the glass microcapillary is connected to a pressure-control system. In contrast to microfluidic systems using capillaries, this system is called "open" as droplets are accessible. The size of the droplets (fL-pL) can be adjusted depending on the pressure-drop and the translation speed of the microcapillary across the surface.<sup>63</sup> The setup has been successfully used by Hammadi et al<sup>19</sup> to induce and localize primary nucleation events.

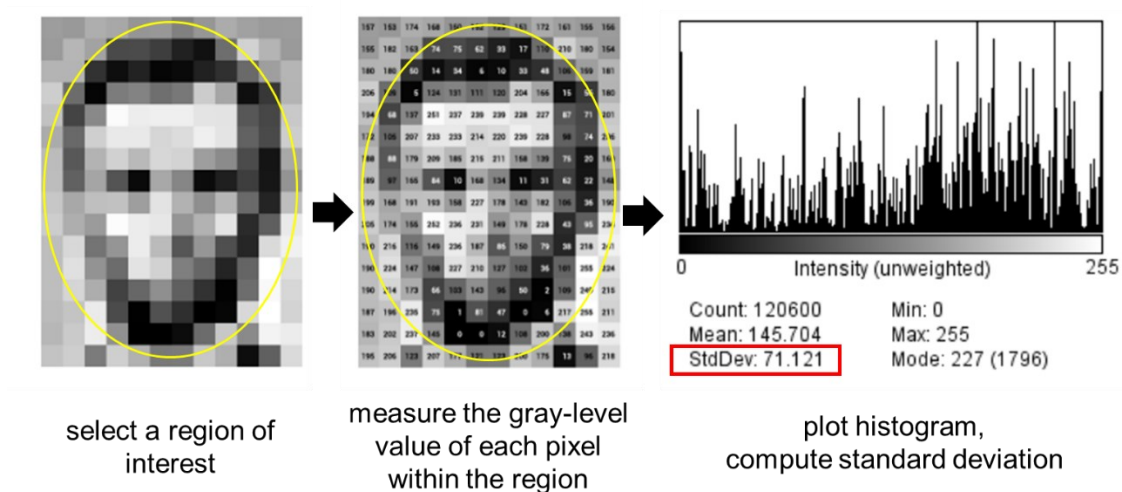


**Figure 2.11.** The image (a) and the schematic diagram (b) of the setup for generating microdroplets on PMMA surface under oil.

### 2.3.2.3 Image Analysis and Application to Crystallization Studies

An important advantage of the setup in **Figure 2.11** is that it allows simultaneous measurement of hundreds of droplets via image analysis. The basic concepts of image analysis and how it can be applied on crystallization studies is thus discussed in this section.

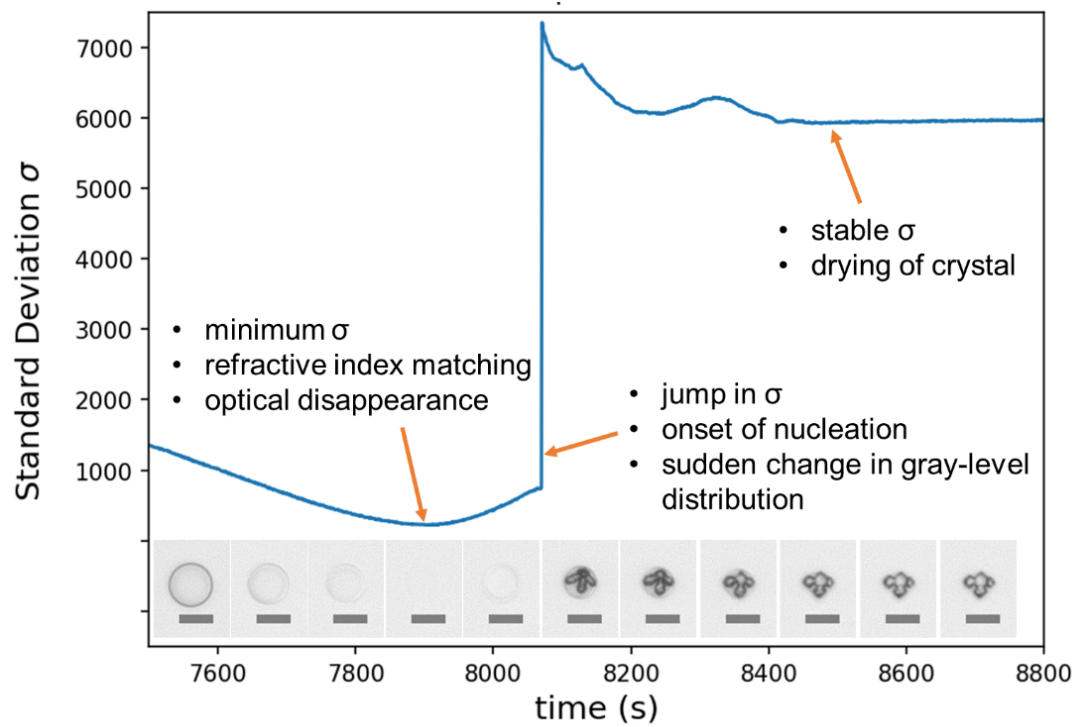
Digital images are made up of 2D array of pixels. For 8-bit gray-scale images, each pixel can have values ranging from 0 (black) to 255 (white). The distribution of pixel values can be analyzed using histograms. Dark images would have more pixels close to zero whereas bright images would have most of them close to 255. The general process of extracting the histogram from a gray-scale image is shown in **Figure 2.12**.



**Figure 2.12** Schematic illustration for obtaining the histogram and extracting the standard deviation of the gray-level pixels.

In a dynamic system (such as an evaporating and nucleating droplet), the histogram of the gray-level pixel evolves with time. To characterize the shape of the histogram, there are several parameters that can be used such as mean, standard deviation, skewness, and kurtosis. In the context of nucleation studies, Grossier et al<sup>21</sup> have shown that the standard deviation  $\sigma$  is a useful parameter in probing microdroplet dynamics as it is very sensitive to changes in refractive index.

To illustrate the usefulness of  $\sigma$  as a tracking parameter, the typical evolution of  $\sigma$  for an evaporating droplet is shown in **Figure 2.13**. Note that the refractive index of the microdroplet is a function of its concentration. When the refractive index of the microdroplet matches that of its environment (PDMS oil in this case), it optically disappears. This corresponds to a minimum in standard deviation  $\sigma$  because the gray levels at this point are relatively uniform (with just few background noise). As the microdroplet continues to evaporate, its refractive index deviates from that of the oil thereby contributing changes to the gray-level histogram. At the onset of nucleation, sudden appearance of black pixels occur which results in a prominent jump in  $\sigma$ -value. Following crystal growth, the solid dries up and the  $\sigma$  stabilizes. Therefore,  $\sigma$  is a useful parameter for tracking the dynamics of evaporation and detecting the onset of nucleation.

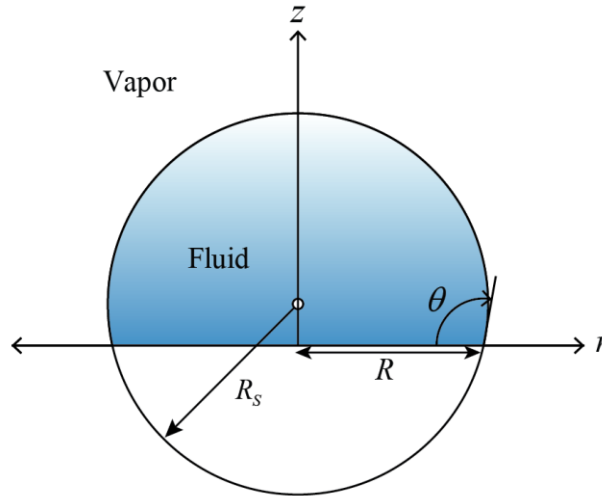


**Figure 2.13** Evolution of the gray-level standard deviation for an evaporating saline microdroplet. The scale bar corresponds to 50  $\mu\text{m}$ .

## 2.4 Principle of Microdroplet Evaporation

In evaporative microdroplet experiments (as in **Figure 2.13**), the evolution of volume with time is an important parameter in quantifying nucleation kinetics as it determines the supersaturation ratio. However, this is not directly measurable by simply tracking the microdroplet radius from the top-view images because microdroplets can also evaporate at constant contact radius mode. Thus, understanding the evaporation of microdroplet is important in such experiments in order to accurately determine the evolution of supersaturation. In this section, I review the basic concepts of microdroplet evaporation, the different contact line behaviors and the existing mathematical models that describe the evaporation rate.

For droplets in  $\mu\text{m}$  range, the gravitational effects are considered negligible (Bond number  $\ll 1$ ), resulting in a spherical cap with radius  $R_s$  and contact radius  $R$ , as in **Figure 2.14**.



**Figure 2.14** Schematic illustration of a sessile droplet with spherical cap radius  $R_s$ , contact radius  $R$ , and contact angle  $\theta$ .

The volume  $V$  is given as<sup>64</sup>

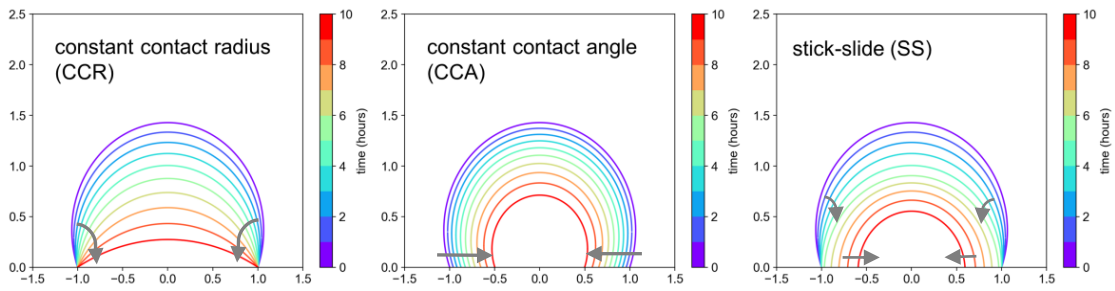
$$V = \frac{\pi R^3 (\sin \theta)(2 + \cos \theta)}{3(1 + \cos \theta)^2} \quad (2.48)$$

By simple trigonometry, the height of the droplet can be expressed in terms of  $R$  and  $\theta$  as

$$h = \sqrt{\frac{R^2(1 - \cos \theta)}{1 + \cos \theta}} \quad (2.49)$$

### 2.4.1 Contact Line Behavior (CCA, CCR, SS mode)

Depending on the nature of the surface, the droplet residing on it shows different behaviors of the contact line and the contact angle as shown in **Figure 2.15**.



**Figure 2.15** Schematic illustration of different contact line behavior.

Hence, the “footprint” on the surface and the volume of the droplet may vary :

1. **Constant Contact Angle (CCA)** In the extreme case of perfectly smooth chemically homogeneous surface, the droplet maintains an equilibrium contact angle, and this is referred to as constant contact angle (CCA) mode. Consequently, the volume decreases due to the continuous decrease in contact radius.<sup>64</sup>
2. **Constant Contact Radius (CCR)** In practice, the droplet will be pinned due to surface roughness so the radius remains constant at some point. In the extreme case where the droplet remains pinned throughout its lifetime, we refer to this as the constant contact radius (CCR) mode. In this mode, the volume decreases due to the continuous decrease in contact angle.
3. **Stick-slide (SS)** As experimental studies suggest,<sup>65</sup> real droplets evaporate in some mixture of CCR and CCA modes. One common observation is the occurrence of CCR mode at the beginning and once the contact angle decreases to a value less than the receding contact angle  $\theta_r$ , it switches to CCA mode. This combination is known as the stick-slide (SS) mode.<sup>65</sup>

## 2.4.2 Evaporation Rate Models

In this section, I review the well-known models that describe the evaporation rate of pure sessile droplets in air under the assumption a diffusion-limited quasi-steady state evaporation in an infinite medium.

### 2.4.2.1 Picknett and Bexon's Model

Picknett and Bexon<sup>65</sup> derived an evaporation model for a sessile droplet with contact radius  $R$  and contact radius  $\theta$  as

$$\frac{dm}{dt} = -2\pi R D M_w (c_s - c_\infty) j(\theta) \quad (2.50)$$

$$j(\theta) = \begin{cases} 8.957 \times 10^{-4} + 0.6333\theta + 0.116\theta^2 - 0.08878\theta^3 + 0.01033\theta^4 & \text{for } \theta \geq 10^\circ \\ 0.6366\theta + 0.09591\theta^2 - 0.06144\theta^3 & \text{for } \theta < 10^\circ \end{cases} \quad (2.51)$$

The factor  $j(\theta)$  serves as a shape factor for different values of contact angle. For a hemispherical droplet,  $j(\theta) = 1$ . The expression is derived from a series expansion which is then approximated using a truncated polynomial expansion.

### 2.4.2.2 Popov's Model

For the same scenario derived by Picknett and Bexon, (that is, diffusion-limited quasi-steady state evaporation of pure liquid in an infinite medium), Popov<sup>66</sup> used an analogy to an equivalent electrostatic problem (in toroidal coordinates) without using a series expansion approach. The analytical solution can be written as

$$\frac{dm}{dt} = -\pi R D M_w (c_s - c_\infty) f(\theta) \quad (2.52)$$

$$f(\theta) = \frac{\sin \theta}{1 + \cos \theta} + 4 \int_0^\infty \frac{1 + \cosh(2\theta\delta)}{\sin(2\pi\delta)} \tanh[(\pi - \theta)\delta] d\delta \quad (2.53)$$

where  $m$  is the mass of the volatile species (in this case, water),  $D$  is the diffusivity of water in the medium,  $M_w$  is the molar mass of water,  $c_s$  and  $c_\infty$  are the concentration of water at saturation and at a point far away from the droplet respectively (in mol/m<sup>3</sup>),  $f(\theta)$  is a shape factor, and  $\delta$  is an arbitrary variable of integration. For hemispherical droplet ( $\theta = 90^\circ$ ),  $f(\theta) = 2$ . This analytical expression is widely used notably by Stauber et al<sup>64</sup> and Nguyen et al.<sup>67</sup>

## Chapter 3

### Materials and Methods

In this chapter, I present a general description of the pertinent chemical products used in the experiments and an introduction to the basic principles of the equipment and instrumentation used.

### 3.1 Model Compounds

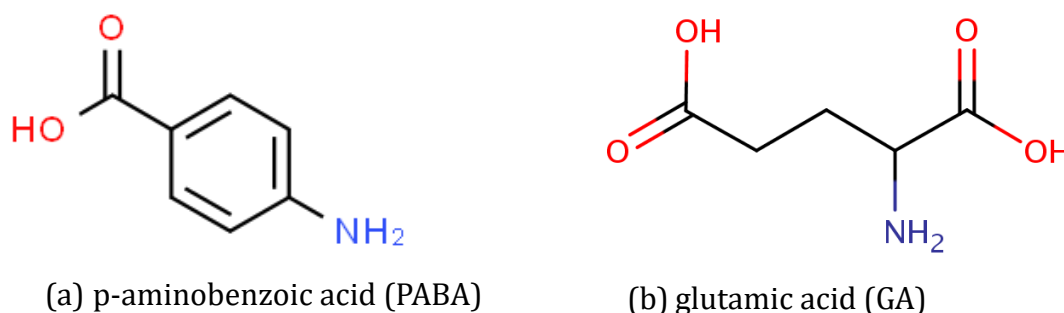
The following were chosen as model compounds in the measurement of nucleation kinetic parameters. This choice is mainly based on the availability of related kinetic studies which allows for comparison.

#### 3.1.1 Para-Aminobenzoic acid (PABA)

Para-aminobenzoic acid, a precursor in the synthesis of folate, crystallizes in two enantiotropic polymorphic forms, the  $\alpha$ -needles and the  $\beta$ -prisms.<sup>68-69</sup> The structure of PABA is shown in **Figure 3.1a**.

#### 3.1.2 Glutamic acid (GA)

Glutamic acid is a proteinogenic amino acid that is usually produced as monosodium glutamate for food additive applications<sup>70-71</sup>. It can either crystallize as the prismatic  $\alpha$ -form or the more stable multishaped  $\beta$ -form (can exist as needle, rod, or plate)<sup>72</sup>. The structure of glutamic acid is shown in **Figure 3.1b**.

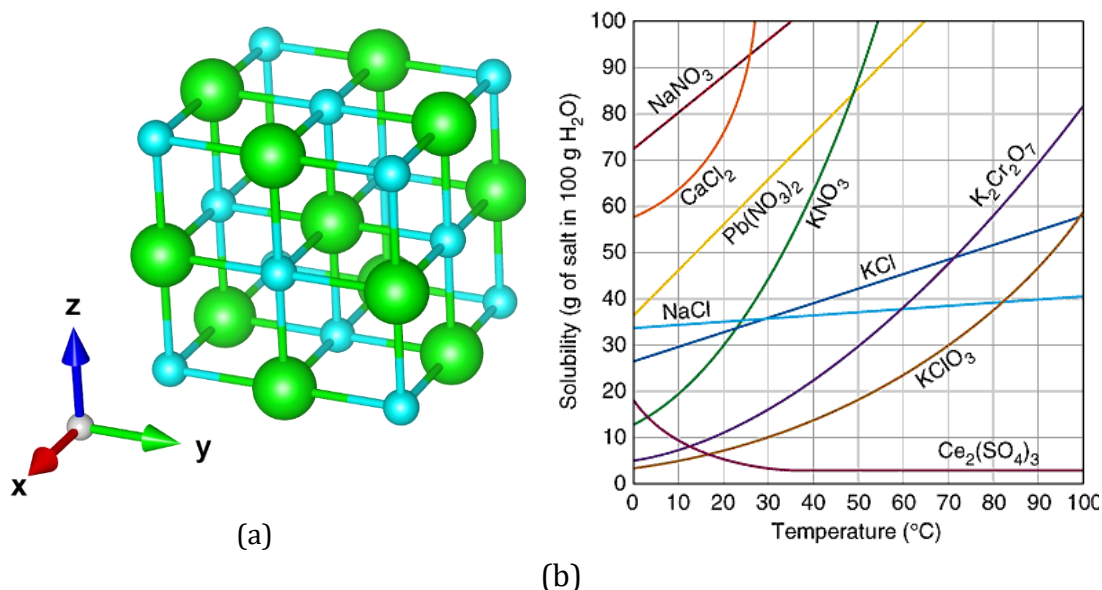


**Figure 3.1** Chemical structure of model compounds (a) PABA and (b) GA.



### 3.1.3 Sodium chloride (NaCl)

Sodium chloride, also known as table salt, crystallizes in a face-centered cubic crystal system (**Figure 3.2a**). It has a density of 2.17 g/mL and a melting point of 804°C. Being the most abundant salt on earth<sup>73</sup>, I have chosen NaCl as a compound of interest due to its influence on metal corrosion<sup>74</sup>, building material degradation<sup>75</sup>, oil well productivity<sup>76</sup>, atmospheric science<sup>77</sup> and so on. Moreover, it is also a well-known model system for nucleation studies and it has a relatively flat solubility line so the effects of temperature heterogeneities can be minimized (**Figure 3.2b**).



**Figure 3.2** (a) Crystal structure of sodium chloride consisting of Na<sup>+</sup>(blue) and Cl<sup>-</sup>(green), (b) Solubility of NaCl in comparison with other salts (adapted from Daniela Feingold et al<sup>78</sup>).

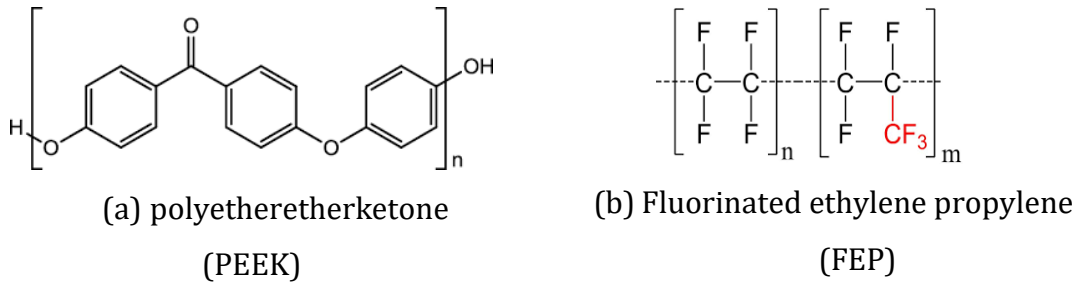
## 3.2 Polymers used in the microfluidic set-up

### 3.2.1 Polyetheretherketone (PEEK)

In generating microdroplets in capillaries, a T-junction is needed where the aqueous phase and continuous phase meet. PEEK (structure shown in **Figure 3.3a**) has been found to be suitable material for the T-junctions as it is compatible with many solvents.<sup>51</sup>

### 3.2.2 Fluorinated ethylene propylene (FEP)

To observe the microdroplets in a capillary, a material that is transparent, water impermeable, and chemically stable to various solvents is needed. FEP (structure shown in **Figure 3.3b**) well fit these criteria making it our standard material for microfluidic capillaries.



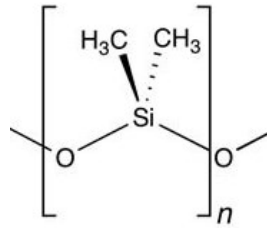
**Figure 3.3** Chemical structure of polymers used in generating microdroplets in capillaries (a) PEEK (b) FEP.

### 3.2.3 Polydimethylsiloxane (PDMS)

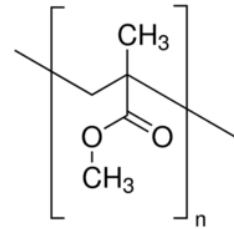
To generate sessile microdroplets, PDMS (structure shown in **Figure 3.4a**) oil is used as a medium where microdroplets are allowed to diffuse (i.e. evaporate). The oil serves to slow down the evaporation rate and to act as a thermal buffer, preventing temperature gradients that might occur due to the endothermic evaporation process. The solubility and diffusivity of water in PDMS oil at ambient conditions are  $30 \text{ mol/m}^3$  and  $8.5 \times 10^{-10} \text{ m}^2/\text{s}$  respectively.<sup>79-80</sup>

### 3.2.4 Polymethylmethacrylate (PMMA)

PMMA (structure shown in **Figure 3.4b**) is used as a coating to glass slides where sessile droplets are generated. PMMA serves to prevent microdroplet spreading and coalescence. The aqueous droplets generated on the interface of PMMA and PDMS have an initial contact angle of greater than  $90^\circ$ .



(a) polydimethylsiloxane (PDMS)



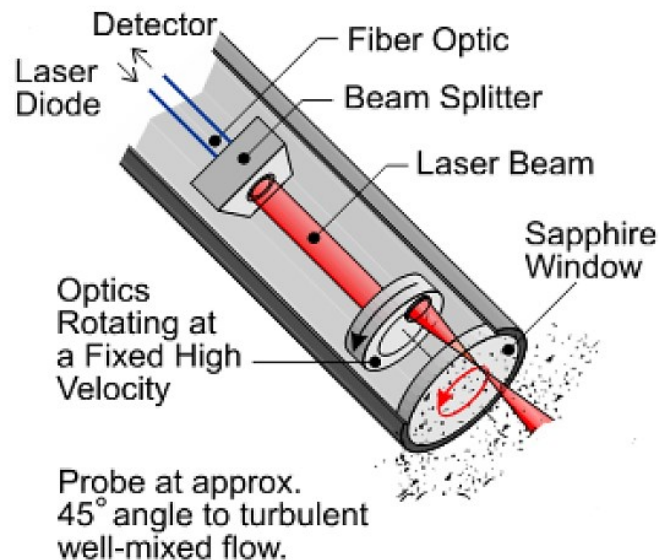
(b) polymethylmethacrylate (PMMA)

**Figure 3.4** Chemical structure of polymers used in sessile microdroplet generation (a) PDMS, (b) PMMA

### 3.3 Process Analytical Tools (PATs)

#### 3.3.1 Optical Reflectance Measurement (ORM)

Optical Reflectance Measurement (ORM) is a widely used real time process monitoring technique based on a laser backscattering<sup>81</sup> where the sensor measures chord length of the particles by moving a laser beam at high velocity through the sample and recording the crossing time. The schematic illustration is shown in **Figure 3.5**. The chord length of each particle traversed by the laser is calculated from the crossing time of the particle.<sup>82-83</sup>



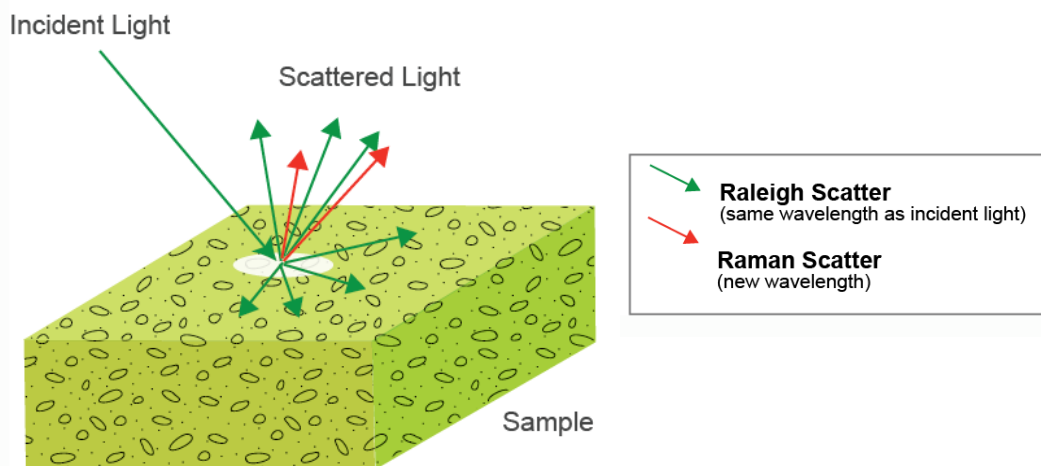
**Figure 3.5** Schematic Illustration of ORM Probe. (adapted from Adlington et al.<sup>84</sup>)

The chord length distribution (CLD) is different from the particle size distribution (PSD), but several methods have been developed to transform CLD to PSD providing detailed information on real-time particle counts and size distribution.<sup>30, 81</sup> Combination of ORM with other PAT tools is often used for obtaining variety of information about the process.

### 3.3.2 In situ Raman spectroscopy

Raman spectroscopy is a light scattering technique in which samples are illuminated by a monochromatic laser source and the scattered light is shifted to various wavelengths due to the interaction of photons with the molecular vibrations of the sample.<sup>85-86</sup> The schematic illustration is shown in **Figure 3.6**. The scattered light at various wavelengths is collected and can be used to provide information on the composition of the sample.<sup>87</sup>

Raman spectroscopy has also been used in crystallization for monitoring solute and solid concentration of single and multiple component suspensions such as polymorphic forms of crystals.<sup>88-90</sup> In this work, Raman spectroscopy was used to monitor real-time solution concentration.



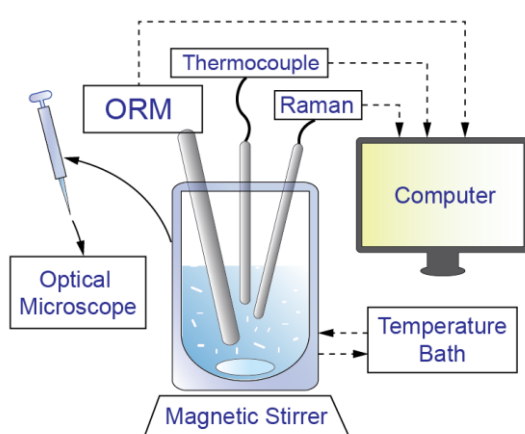
**Figure 3.6** Schematic illustration of Raman spectroscopy (adapted from [www.princetoninstruments.com/](http://www.princetoninstruments.com/))

## 3.4 Experimental Setups

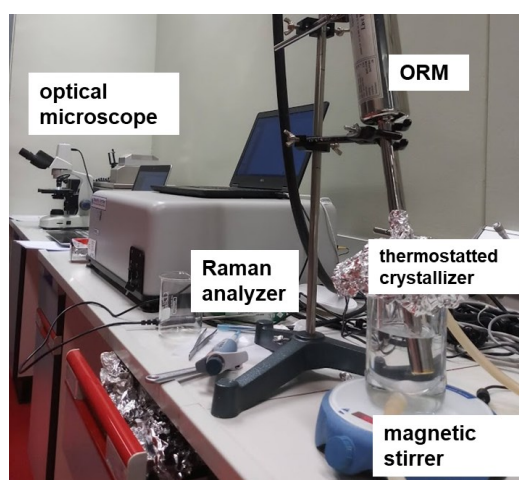
The experiments were done in multiple scales (from L scale down to pL scale). In this section, I describe the experimental techniques used in each scale.

### 3.4.1 Setup for Liter Scale Experiments

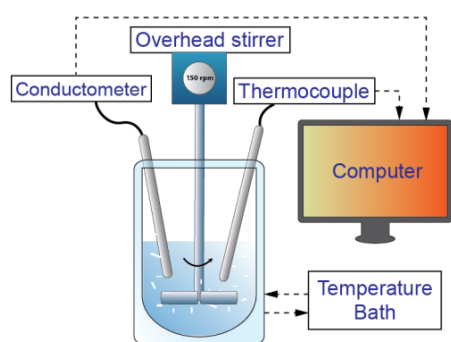
The schematic illustration and image of the liter scale setup is shown in **Figure 3.7** and its corresponding dimensions are detailed in **Figure 3.8**.



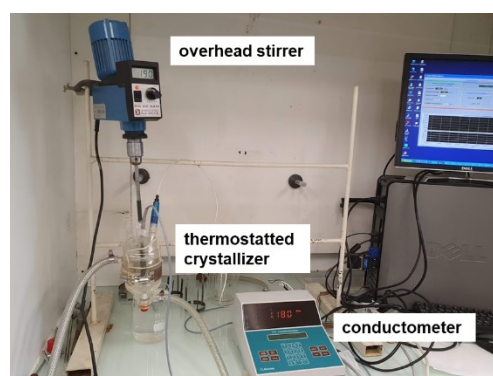
(a)



(b)

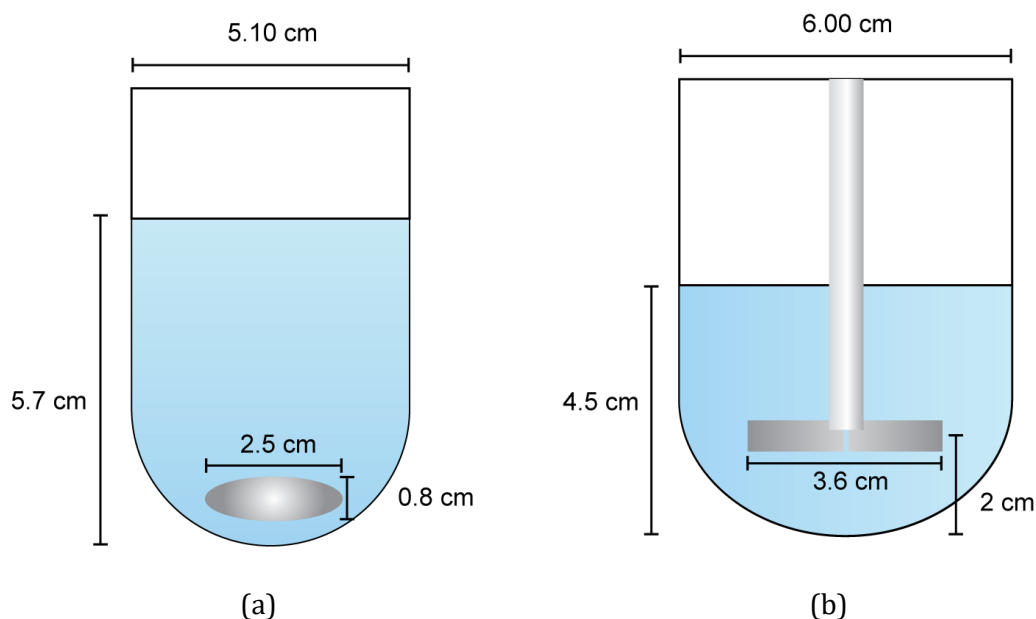


(c)



(d)

**Figure 3.7** (a,b) Schematic diagram and photo of the particle-count approach using optical reflectance measurement and Raman spectroscopy, (c,d) schematic diagram and photo of the conductometry approach for measuring induction time.



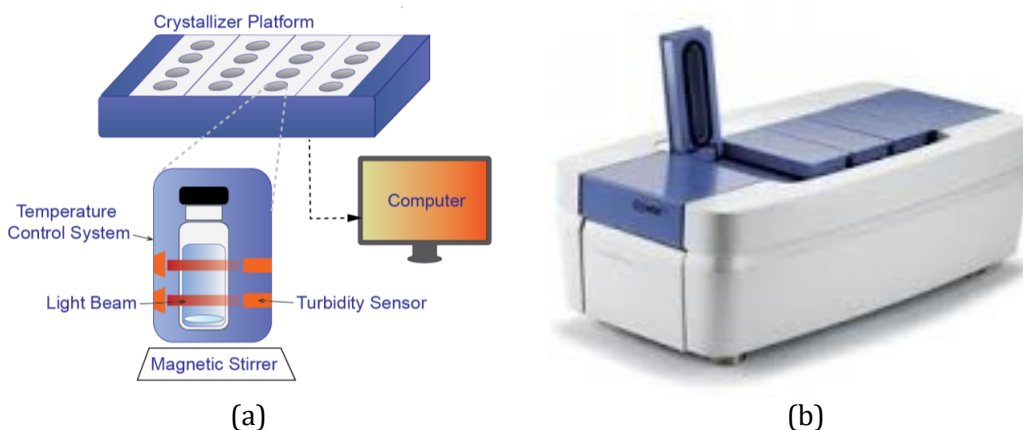
**Figure 3.8** Dimensions of the crystallizer and its agitation system used in (a) particle-count approach (b) solution conductometry. The height of the liquid displayed are prior to the introduction of probes.

For the particle-counting based approach, I used the optical reflectance measurement (3D-ORM IPAS, Sequip S&E GmbH) coupled with in-situ Raman spectroscopy (Kaiser Optical Systems Inc) to track the evolution of number of particles and solution concentration (**Figure 3.7a**) with agitation speeds ranging from 500 to 900 rpm. Although overhead stirrer could offer better mixing, we used a magnetic bar agitation system due to the space limitation imposed by the bulky ORM and Raman probes (**Figure 3.7b**).

Since PABA partially ionizes in solution, I also used another setup which relies on solution conductimetry (Metrohm 712) to determine the onset of nucleation. The system is agitated with an overhead stirrer (150 rpm). The induction time is taken deterministically as the inverse of nucleation rate, that is,  $t_i = 1/(JV)$ .

### 3.4.2 Setup for mL Scale Experiments

For the mL scale experiments, I used a turbidimetry-based crystallizer platform (Crystal16, Technobis). The setup is shown in **Figure 3.9**.



**Figure 3.9** (a) Schematic diagram and (b) photo of a turbidimetric crystallizer platform (Crystal16, Technobis).

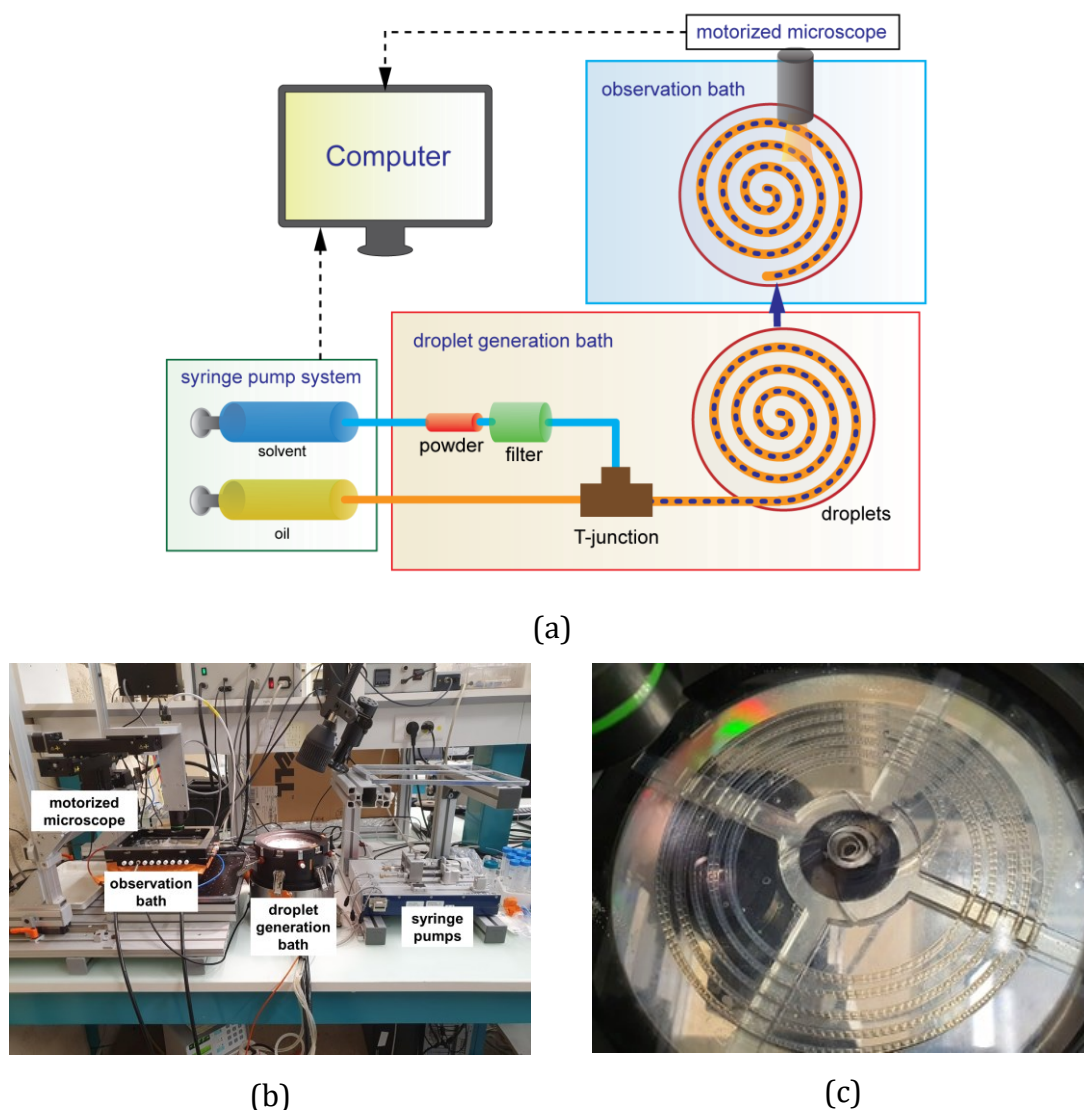
The temperature is controlled with a heater and a Peltier element with an accuracy of  $\pm 0.1$  °C. Each vial contains a magnetic stirrer, with the agitation speed set at 900 rpm. The PTFE-coated stirrer bar was cylindrical and had a length of 7 mm and a diameter of 2 mm. A light beam is passed through the solution, and when the formation of crystals/particles occurs, the transmission of light decreases which marks the onset of nucleation. In these experiments, there is a lag time between the actual start of nucleation and the time at which it is detected. This is taken into account by fitting a parameter  $t_g$  in the plot of cumulative distribution of induction time.

### 3.4.3 Setup for $\mu\text{L}$ Scale Experiments

For the microfluidic experiments, I used two setups: one that involves generating droplets in transparent FEP tubes ( $\mu\text{L}$  to nL scale) and the one that generates smaller sessile microdroplets on a PMMA-coated glass surface immersed in PDMS oil (nL to pL scale).

### 3.4.3.1 Microfluidic Experiment in Capillaries

The microfluidic setup in capillaries (closed microfluidic) is illustrated in **Figure 3.10**.



**Figure 3.10** (a) Schematic illustration of the microfluidic experiment in tubes (b) photo of the experimental setup (c) closer look at the spirally-oriented microfluidic tubes embedded on a 3D-printed polymeric resin template (developed in this thesis).

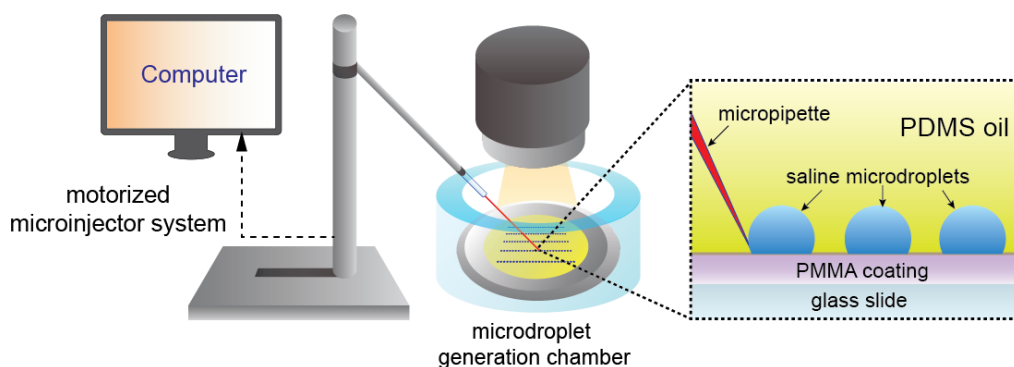
The microfluidic experiments in tubes are designed such that droplets do not evaporate, thereby maintaining a constant supersaturation when temperature is held constant. This is based on the setup developed by Peybernes.<sup>60</sup> The idea is to produce saturated solution on-line directly from powder instead of preparing stock



solutions externally. This minimizes the risk of premature nucleation during solution preparation and diminish the quantity to be held. In the droplet generation bath, automated syringe pumps are used to push the solvent through a powder bed which saturates the fluid. The saturated solution then goes to the PEEK junction where it meets with the continuous phase (oil), thereby generating droplets. The resulting droplets are then sent to the observation bath consisting of a thermostated bath and a xyz-motorized camera (Opto GmbH) with zoom capabilities.

### 3.4.3.2 Setup for Sessile Microdroplet Experiment

The setup for sessile microdroplet experiment (“open microfluidics”) is illustrated in **Figure 3.11**. This setup is designed for evaporative crystallization experiments where hundreds of droplets are monitored simultaneously using image analysis.



**Figure 3.11** Schematic illustration of the setup for sessile microdroplet experiment.

The saline microdroplets were generated on the cover slip by a micropipette with an internal diameter of 0.5  $\mu\text{m}$  (Femtotip Eppendorf). The micropipette is mechanically controlled by a home-made motorized micromanipulator consisting of 3 miniature translation stages (piezo electric, MS30 Mechanics) which allows displacement of the micropipette holder in three dimensions by steps of 16 nm. To avoid microdroplet spreading and coalescence, the glass cover slip is coated with a hydrophobic PMMA resin. For this, glass coverslips (18-mm diameter, cleaned via plasma treatment) were spincoated at 4000 rpm for 1 min (SPIN 150, SPS) with PMMA which were then annealed for 10 min at 170°C. The coverslips were then covered with a 0.8 mm thick layer of PDMS oil. A series of 16-bit images were obtained using an optical microscope (Zeiss Axio Observer D1 equipped with an ANDOR neo sCMOS camera). Images were processed using FIJI software (Image J, NIH, USA).

## Chapter 4

### Measuring Primary Nucleation Rates in Agitated Systems using Particle Count Approach

In liter-scale agitated crystallizers, several techniques have been developed to estimate nucleation parameters, notably those of Nyvlt, Kubota, Sangwal, etc. However, these approaches rely heavily on empirical models (such as the power law model) to correlate nucleation rate against quantities relating to the system metastability such as induction time or metastable zone width (MSZW). Several researchers have pointed out that the physical meaning of induction time and metastable zone width is still questionable<sup>91</sup> and not yet well-understood. These pose doubt on the validity of the nucleation parameters obtained from such methods. In this chapter, I developed a new approach for quantifying primary nucleation rates using in situ optical reflectance measurement (ORM) coupled with in situ Raman spectroscopy. Instead of measuring induction times or MSZW, we monitor the particle counts in the system. Given that the total particle count is the sum of nuclei generated from both primary and secondary nucleation, we assumed that the rate of secondary nucleation varies exponentially with agitation rate. Thus, upon extrapolation to zero agitation rate, the rate of primary nucleation rate can be approximated. The full description of the calibration techniques, measurement protocols, and model assumptions is discussed in this chapter.

*Parts of this chapter were published in*

**Cedeno, R.;** Maosoongnern, S.; Flood, A., Direct Measurements of Primary Nucleation Rates of p-Aminobenzoic Acid and Glutamic Acid and Comparison with Predictions from Induction Time Distributions. *Industrial & Engineering Chemistry Research* 2018, 57 (51), 17504-17515.

## 4.1 Introduction

Nucleation is particularly an important step in crystallization processes as it sets the initial crystal size distribution particularly in the unseeded batch processes often used in the production of high value-added chemicals. In the design of industrial crystallizers, reliable measurement and modeling of process parameters such as nucleation and growth kinetics is necessary for optimal control of final product quality. Although classical theories in crystallization kinetics are well-established, the ability to measure, describe and predict crystallization kinetics remains a challenge due to the large deviations of real systems from ideal behaviors prompting the need to develop alternative models and measurement techniques for both nucleation and growth kinetics.<sup>68</sup> Existing approaches such as those developed by Nyvř, Kubota, and Sangwal rely heavily on empirical models (such as the power law model) to correlate nucleation rate against quantities relating to the system metastability such as induction time or metastable zone width (MSZW). Several researchers have pointed out that the physical meaning of induction time and metastable zone width is still questionable<sup>91</sup> which pose doubt on the validity of the nucleation parameters obtained from such methods.

In this work, instead of measuring induction times or MSZW, I monitor the particle counts in the system for direct quantification of nucleation kinetics. Since the total particle count is the sum of nuclei generated from both primary and secondary nucleation, I assume that the rate of secondary nucleation varies exponentially with agitation rate and that the rate of primary nucleation is a weaker function of hydrodynamics. This is consistent with that of Randolph and Cise<sup>92</sup> who also suggested the use of exponential function for correlating the influence of stirring rate on the total nucleation rate. Although several researchers have recently shown that primary nucleation is influenced by shear rate,<sup>93-95</sup> the order of magnitudes appear to be mildly affected. For instance, Stroobants et al<sup>94</sup> and Forsyth et al<sup>93</sup> observed that increasing the shear rates 10 times would enhance the nucleation rate by about one order of magnitude ( $10^8 \text{ m}^{-3}\text{s}^{-1}$  to  $10^9 \text{ m}^{-3}\text{s}^{-1}$  for lysozyme and  $10^1$  to  $10^2 \text{ m}^{-3}\text{s}^{-1}$  for glycine respectively). Moreover, Nappo et al<sup>95</sup> have shown that the dependence of primary nucleation rate on shear rate is non-monotonic. They observed that at low shear rates, primary nucleation rate increases with increasing shear rate but the opposite trend occurs at high shear rates. This suggests that assuming that primary nucleation is a much weaker function of hydrodynamics than secondary nucleation is reasonable. With this assumption, I develop a method of quantifying nucleation rate by performing particle-count measurements across

several agitation rates. This would allow estimation of primary nucleation by extrapolating the measured rates down to zero agitation. I then compare the extracted primary nucleation rate to that of Turner et al<sup>96</sup> who measured the primary nucleation of the same model compound (*p*-aminobenzoic acid in aqueous/ethanolic system) using the KBHR (Kaschiev-Borrisova-Hammond-Roberts) model.<sup>38</sup>

## 4.2 Materials and Methods

### 4.2.1 Chemicals and Equipment

The compounds *p*-aminobenzoic acid, PABA (TCI, chemical purity > 99%), L-glutamic acid, LGA (TCI, chemical purity > 99%), pure ethanol (TCI, AR grade), and ultrapure water were used as received. The induction time and solubility were measured using the multiple-crystallizer setup called Crystal16 (Technobis, Amsterdam) which measures light transmissivity through standard HPLC vials. Particle count measurements were carried out in a 250 mL jacketed glass crystallizer connected to a water-cooled temperature control system (Julabo F32,  $\pm 0.01$  °C) with an egg-shaped PTFE-coated magnetic stirrer (25x8 mm) magnetic stirrer. The crystallization process was monitored in real time via 3-Fold Dynamical Optical Reflectance Measurement (3D-ORM IPAS, Sequip S&E GmbH) which employs laser backscattering to measure chord-length distributions from which particle size distributions (PSD) and particle counts per volume can be obtained upon calibration. The concentration profile was monitored via time-resolved in-situ Raman Spectroscopy (Kaiser Optical Systems Inc).

### 4.2.2 Solubility Measurement

Both PABA and LGA exhibit polymorphism and are known to crystallize in either  $\alpha$  or  $\beta$  forms.<sup>97-98</sup> Since solubilities of different polymorphic forms vary, only the  $\alpha$ -form of both compounds was considered in this work since this was found to form exclusively in the conditions employed in the nucleation measurements. The solubility of  $\alpha$ -PABA in 30 wt% ethanol-water mixture was measured as a function of temperature using the Crystal16 by preparing 1 mL solutions with varying concentrations in 16 vials with magnetic stirring (900 rpm) and heating rates set at 0.2 °C/min; this was found to be a suitable heating rate for solubility experiments since it gave equivalent solubilities to lower heating rates, for instance 0.1 °C/min. As the temperature is increased, the transmissivity of light through each sample

reaches a maximum at a certain temperature (the clear point) in which the sample becomes a clear solution. The clear point is taken as the saturation temperature and was measured for three trials for each concentration. The solubility of the metastable  $\alpha$ -LGA in water was taken from literature<sup>99</sup>.

### **4.2.3 Calibration of in-situ Raman Spectroscopy**

Raman spectra were collected in-situ via immersion fiber-optic probe (305 mm x 12.7 mm) connected to a 785-nm RamanRXN1 analyzer (Kaiser Optical Systems Inc., MI, USA) with exposure time set at 10 seconds per scan. The Raman spectra was calibrated starting from pure solvent followed by incremental addition of known amounts of solute at constant temperature (30°C for PABA). Upon addition of solute, new peaks were observed corresponding to the characteristic peaks of the solutes. The ratio of the characteristic peak area of the solute to that of the solvent was chosen as a reference for the calibration curve. In principle, the presence of suspended particles during nucleation could interfere with the reference peaks. To determine whether a multivariate calibration model (such as principal component or partial least squares regression) is necessary, we determined the influence of suspended solids on the reference relative peak area by incremental addition of solids on a saturated solution.

### **4.2.4 Calibration of In-situ 3D ORM**

3D ORM is based on diffuse reflection of an incident light beam at the surfaces and edges of particles enabling measurement of the chord length distribution (CLD) which is related to the particle size distribution (PSD). In contrast to the stationary focal point of focused-beam reflectance measurement (FBRM), 3D ORM features a dynamic focal point providing better quantitative capability<sup>100</sup>. The probe used in this work has a laser beam intensity of 10 mW with a 4 $\mu$ m single-mode fiber and rotating optics with tangential velocity of 2m/s. A threshold value of 0.02 and size window of 1-10 $\mu$ m (fine mode) were set to maximize detection of early nuclei.

Note that the counts per seconds (CPS) measured by ORM represents the number of detections within a small region of fluid surrounding the tip of the probe and not the actual number density of crystals. Thus, there is a need to correlate the number of particles detected by the probe to the actual number of particles per volume in the system. To do this, a 100 mL saturated solution was prepared and then a known amount of solute was incrementally added leading to an increase in the number of

detected particles. Since the solution is at equilibrium, the added seed crystals are not expected to dissolve nor grow. Assuming the system is well-mixed and with the known mass of added crystals, the total number of crystal per unit volume  $N_T$  can be calculated by the following equation

$$N_T = \frac{M_T}{V_S \rho_c k'_v L_{3,0}^{CLD}} \quad (4.1)$$

where  $V_S$  is the solution volume,  $M_T$  is the total mass of crystals,  $\rho_c$  is the crystal density,  $L_{3,0}^{CLD}$  is the mean crystal volume based on the chord-length distribution (CLD) and  $k'_v$  is a modified shape factor relating the measured third moment,  $L_{3,0}^{CLD}$  to the actual average crystal volume.

Note that several mathematical frameworks have been developed for converting CLD to PSD<sup>101</sup>, however for simplicity, we assume that the ratio of the third moment of normalized PSD to that of CLD is constant which we define as the modified volumetric shape factor  $k'_v$  written as

$$k'_v = \frac{L_{3,0}^{PSD}}{L_{3,0}^{CLD}} \quad (4.2)$$

This is under the assumption that the shape of the distribution does not change significantly with time, i.e. the standard deviation of the distribution is constant.

To evaluate  $k'_v$ , optical micrographs (Xenon VR790) of over 500 randomly-selected crystals were analyzed. We modeled the needle-shaped PABA as very long cylinder and the characteristic length  $L_c$  is taken as the length of a cube that has equivalent volume as a needle with length  $L$  and width  $w$ , which can be calculated as:

$$L_c = \left( \frac{\pi w^2 L}{4} \right)^{1/3} \quad (4.3)$$

On the other hand, the prismatic LGA was taken as regular prisms. A histogram with respect to  $L_c$  was then normalized and fitted to a log-normal distribution

$$P(L_c) = \frac{1}{\sqrt{2\pi}\sigma L_c} \exp \left[ -0.5 \left( \frac{\ln L_c - \ln L_m}{\sigma} \right)^2 \right] \quad (4.4)$$

where  $L_m$  and  $\sigma$  are the parameters corresponding to the median and standard deviation respectively. The  $L_m$  and  $\sigma$  of CLD was also obtained in a similar manner.

A calibration curve was then obtained by relating the calculated  $N_T$  to its corresponding counts per second. Since the number of crystals detected per second depends on agitation rate, calibration was performed for different stirring speeds.

#### 4.2.5 Crystallization Process Monitoring

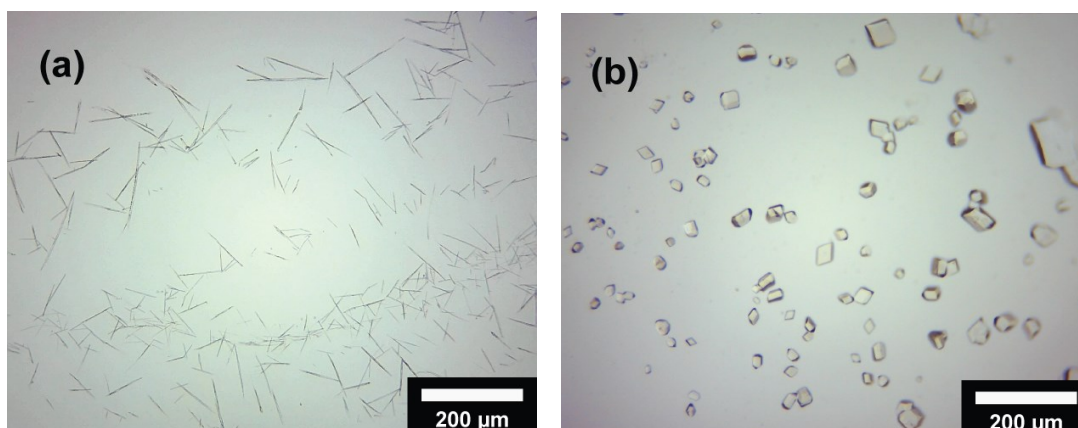
Experiments were carried out in a 250 mL jacketed glass crystallizer with egg-shaped PTFE-coated magnetic stirrer (25x8 mm,700rpm) placed in the bottom of the vessel, with the vessel connected to a water-cooled thermostat. A known mass of PABA was dissolved in 100 g of 30 wt% EtOH-water mixture at a temperature 10°C above saturation for 20 minutes to ensure complete dissolution. It was then crash cooled to 30°C in such a way that the onset of nucleation occurs only after the stable final temperature is established. The evolution of particle count and average crystal volume  $L_{3,0}$  was monitored by 3D-ORM while the supersaturation ratio  $S$  is monitored by in-situ Raman spectroscopy. A similar procedure was performed for LGA, except that the final temperature is set to 25°C and the solvent used is pure water.

### 4.3 Results and Discussion

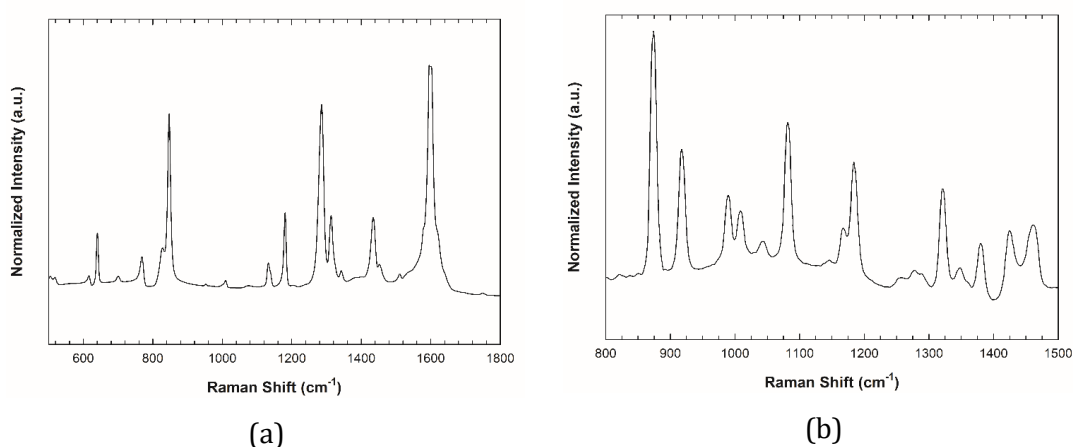
#### 4.3.1 Identification of Polymorphs

As mentioned earlier, both para-aminobenzoic acid (PABA) and L-glutamic acid (LGA) and are known to crystallize in either  $\alpha$  or  $\beta$  forms. The images and Raman spectra of our crystallized PABA and LGA are shown in **Figure 4.1** and **Figure 4.2** respectively.

Since the nucleation rate of different polymorphs varies, measurements were done in conditions where only one type of polymorph is nucleating, i.e. concomitant nucleation was avoided. For PABA in H<sub>2</sub>O/EtOH solution, only the stable needle-shaped  $\alpha$ -form was found to nucleate at 30°C for all supersaturations employed, and no polymorphic transformation was observed (**Figure 4.1a**). In the case of LGA in water, nucleation at 25°C results exclusively in the metastable prismatic  $\alpha$ -form, as shown by optical microscopy (**Figure 4.1b**). However, it is known to undergo a gradual solvent-mediated transformation to the stable  $\beta$ -form as observed in other studies.<sup>72, 102</sup> The nucleated crystal powder was further characterized by Raman Spectroscopy (**Figure 4.2**) which confirms the absence of  $\beta$ -form for both PABA and LGA.



**Figure 4.1** Optical micrographs of crystal samples of (a) PABA and (b) LGA used in polymorph identification and determination of particle-size distribution.

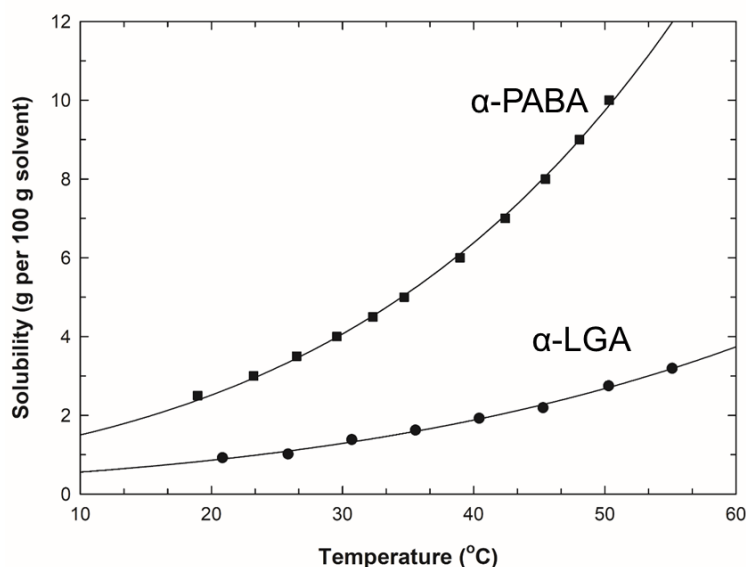


**Figure 4.2** Raman Spectra of dried powder obtained after nucleation of (a) PABA and (b) LGA. In (a), the absence of strong peak at  $1700\text{ cm}^{-1}$  (characteristic peak of  $\beta$ -form)<sup>103</sup> confirms that it is  $\alpha$ -form. In (b), the absence of peak at  $1130\text{ cm}^{-1}$  (characteristic peak of  $\beta$ -form)<sup>104</sup> confirms that it is  $\alpha$ -form.

### 4.3.2 Solubility Data

A plot of experimental solubility of both model compounds ( $\alpha$ -PABA and  $\alpha$ -LGA) in their respective solvents from  $20^\circ\text{C}$  to  $60^\circ\text{C}$  is shown in **Figure 4.3**. It shows an excellent fit to the van't Hoff equation which was used to calculate initial supersaturation ratios at the chosen operating temperature. All nucleation experiments for PABA were carried out at  $30^\circ\text{C}$  where the solubility is  $4.060\text{ g per }100\text{ g solvent}$ , while LGA was nucleated at  $25^\circ\text{C}$  where the solubility is  $1.056\text{ g per }100\text{ g solvent}$ .



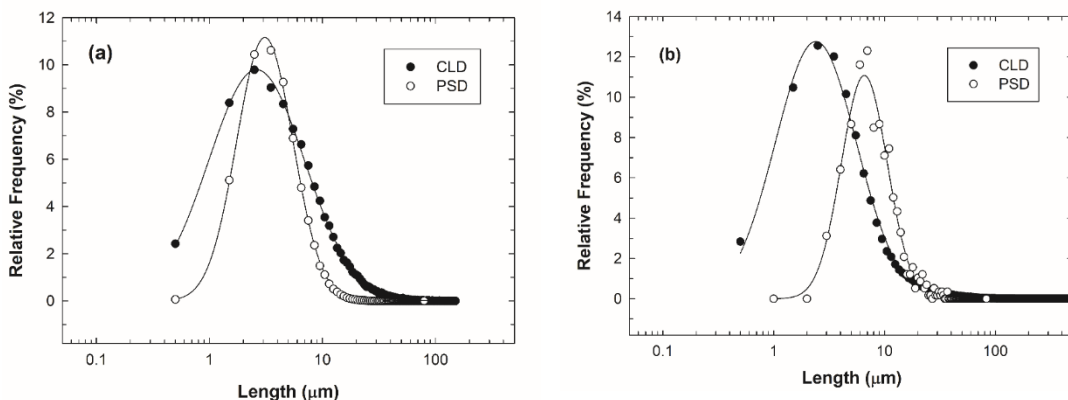


**Figure 4.3** Temperature-dependent solubilities of  $\alpha$ -PABA in 30 wt% aqueous ethanol (■) and  $\alpha$ -LGA in water (●). The solid lines are the fit of the van't Hoff equation. Each point in PABA solubility line is an average of three measurements while that of LGA is based on Scholl et al<sup>102</sup>.

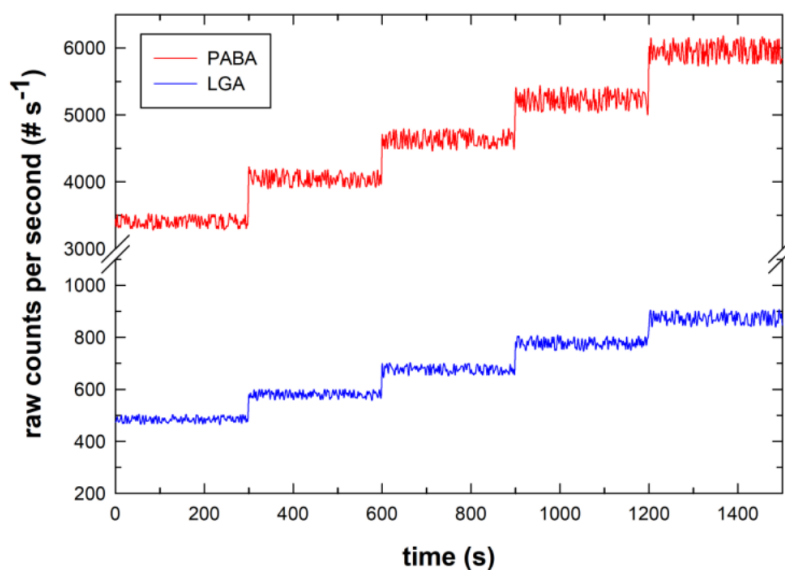
### 4.3.3 Calibration Curves of ORM

The particle size distribution based on the microscope images are shown in **Figure 4.4**. The CLD from the 3D-ORM and the PSD from optical microscope (**Figure 4.1**) are well-represented by a log-normal distribution (**Figure 4.4**) with  $R^2 > 0.96$  from which the distribution parameters median  $L_m$  and standard deviation  $\sigma$  was estimated. Using equation S4, these parameters lead to modified volumetric shape factor  $k'_v = 0.0144$  for the needle-shaped PABA and  $k'_v = 0.550$  for prismatic LGA. With a known  $k'_v$ , the count per second was correlated to the actual number density using equation (4.1) which leads to a calibration curve of PABA in **Figure 4.6**. It is important to note that changes in agitation speed have an effect on the fluid dynamics near the tip of the ORM probe, and therefore differences in the number of counts measured per second even for a constant crystal number density. For this reason, the ORM was calibrated for agitator speeds between 500 and 900 rpm. A similar procedure was done for LGA. With the calibration curve, the number of crystals per volume (number density) can be monitored in real time. To check for the influence of breakage and agglomeration during calibration, the plot the raw particle counts against time. If breakage and agglomeration were dominant, the plot the raw counts should have a positive slope and negative slope respectively in each

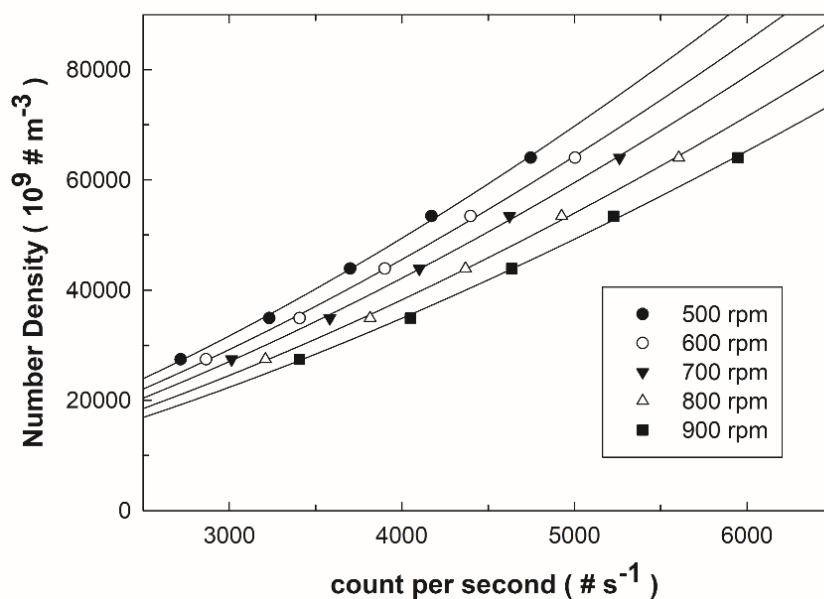
incremental addition of crystals. However, Figure 4.5 (raw counts vs time) shows a stable particle count suggesting that breakage and agglomeration are negligible during calibration.



**Figure 4.4** Particle Size Distribution (PSD) ( $\circ$ ) and Chord Length distribution (CLD) ( $\bullet$ ) of (a) PABA and (b) LGA. The length is in logarithmic scale



**Figure 4.5** Raw counts per second during the calibration of PABA (red) and LGA (blue) at 900 rpm. The steady counts across each incremental addition of seeds suggests a negligible breakage/agglomeration during calibration.



**Figure 4.6** Calibration curve relating ORM counts per second to actual number density of PABA at 500 rpm (●), 600 rpm (○), 700 rpm (▼), 800 rpm (△), 900 rpm (■).

#### 4.3.4 Validation of ORM Measurement by Raman Spectroscopy

In the Raman spectra of PABA (**Figure 4.7a**), the peak between 879 cm<sup>-1</sup> to 881 cm<sup>-1</sup> are associated with the vibrations of intramolecular C–C bonds in ethanol molecules<sup>105</sup> while the strong peak between 1600 cm<sup>-1</sup> and 1615 cm<sup>-1</sup> is due to C–C stretching.<sup>106</sup> Its intensity is positively correlated to an increase in solute concentration. The ratio of baseline integrated peak area of PABA to that of ethanol (using a two-point base line correction) was chosen as reference for the calibration curve. From **Figure 4.7b**, it is evident that there is almost zero correlation ( $R^2=0.047$ ) between the amount of suspended solids to the relative peak area, however, the presence of solids shifts the relative peak area up by around 22 a.u. above that of without solids regardless of the solid concentration.

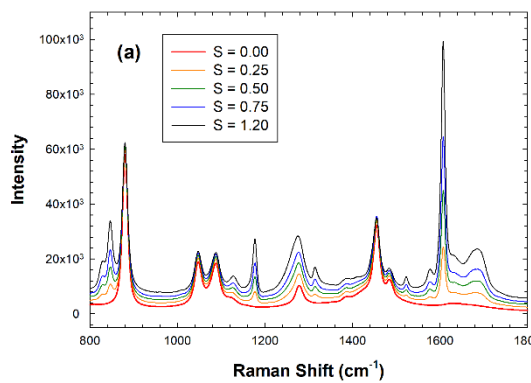
With this information, the calibration curve for systems with and without suspended solids was obtained (shown in **Figure 4.7c**) which allowed real-time monitoring of solution concentration. Note that the concentration profile can also be estimated from in-situ ORM data using the mass balance which can be written as

$$S = S_0 - \frac{N\rho k'_v L_{3,0}^{CLD}}{c^*} \quad (4.5)$$

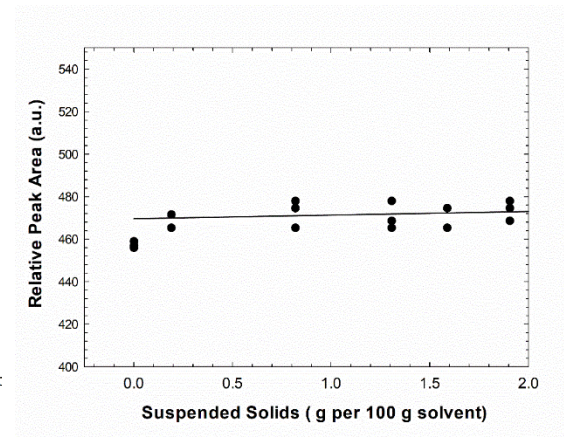
The close agreement between the supersaturation profile from Raman spectroscopy with that calculated from in-situ ORM data (**Figure 4.7d**) confirms the validity of our methods used in interpreting the chord-length distributions and the successful calibration of particle counts with respect to actual number density.

#### 4.3.5 Total Nucleation Rates from in-situ ORM

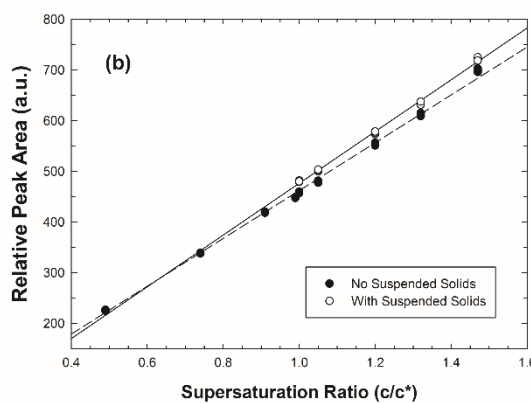
The evolution of number density (particle count per volume) with time of PABA and LGA is shown in **Figure 4.8a** and **Figure 4.8b** respectively. As expected, solutions at higher initial supersaturation ratios start to nucleate at an earlier time and exhibit a faster increase in the number of particles due to the higher driving force for nucleation. Their trajectories resemble an S-shape or sigmoidal curve. This autocatalytic behavior suggests that secondary nucleation is occurring in our system. To obtain the nucleation rate for each supersaturation, we took the moving-average slope of the change in number density over time which were plotted in **Figure 4.8c** and **Figure 4.8d**. The peaks were taken as the representative nucleation rate which corresponds to the maximum slope of the number density.



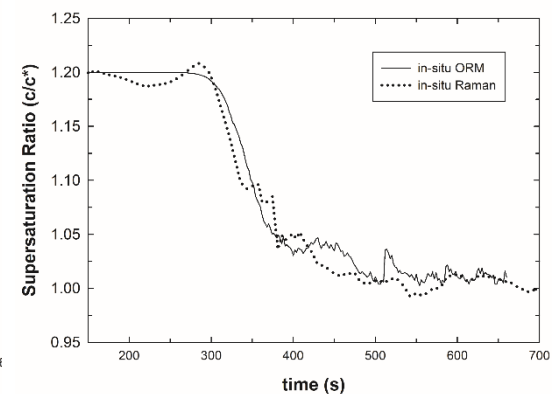
(a)



(b)



(c)

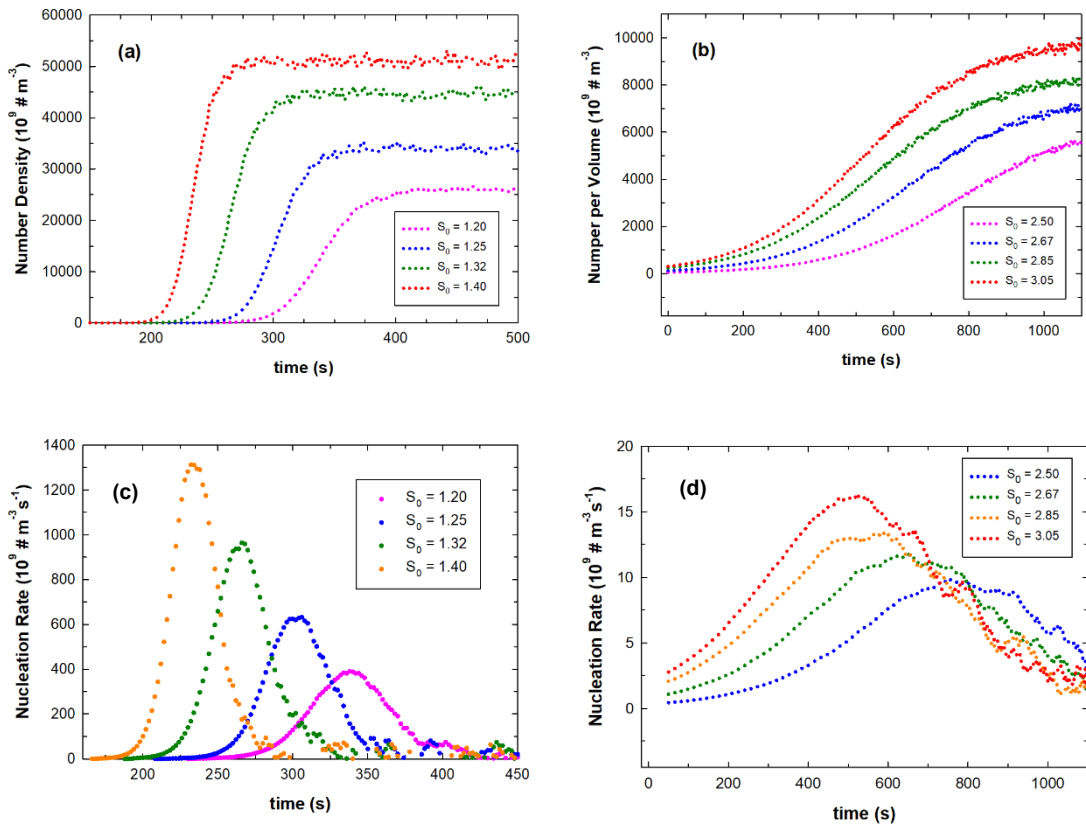


(d)

**Figure 4.7** (a) Raman spectra of solvent (red) and PABA solution at  $S = 0.25$  (orange),  $0.5$  (green),  $0.75$  (blue),  $1.20$  (black); (b) Effect of suspended solids on the reference peak area. A negligible correlation ( $R^2 < 0.05$ ) can be observed, however the presence of solids shifts the reference peak area of clear solution up by around 22 a.u. (c) Correlation between supersaturation ratio and relative peak area in clear solution ( $\bullet$ ) and with suspended solids ( $\circ$ ). (d) Comparison of supersaturation profile of PABA at  $S_0 = 1.20$  obtained from in situ Raman spectroscopy (dotted line) against that obtained from in situ ORM (solid line).

### 4.3.6 Estimation of Primary Nucleation Rate

As mentioned above, the measured nucleation rates via ORM in stirred system represents the total nucleation rate, i.e. the sum of both primary and secondary nucleation. While both may occur simultaneously, it is well-known that secondary nucleation is highly dependent on agitation rate. At higher speeds, crystal collisions onto the crystallizer walls, baffles, impeller, and other crystals occur at a much higher frequency resulting in more chances for breakage, breeding, and attrition which consequently enhances secondary nucleation. Conversely, the effect of secondary nucleation is expected to drop at lower agitation speeds leading to a predominance of primary nucleation in near-stagnant suspensions.



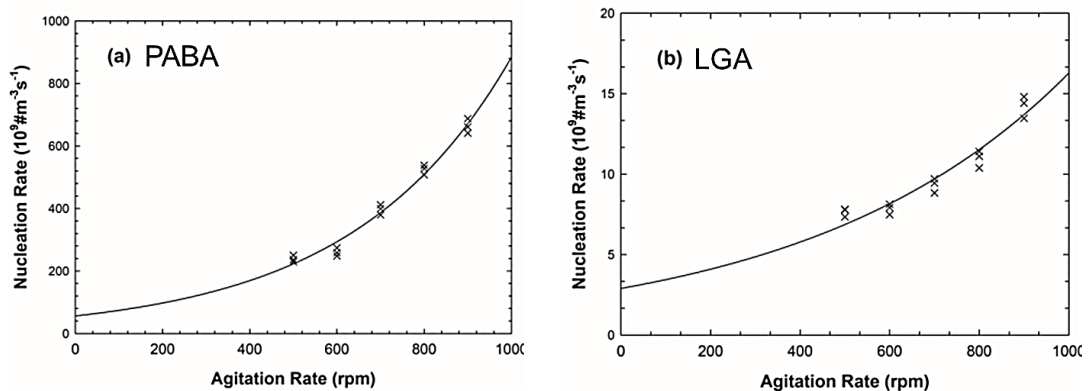
**Figure 4.8** Evolution of number density of (a) PABA and (b) LGA. Evolution of nucleation rate for (c) PABA and (d) LGA.

Thus, we can estimate the primary nucleation rate by performing experiments at different agitation speeds and extrapolating nucleation rate data to zero agitation rate, where the effect of secondary nucleation approaches zero. Note that at agitator speeds lower than 500 rpm, particles tend to settle with a layer of clear

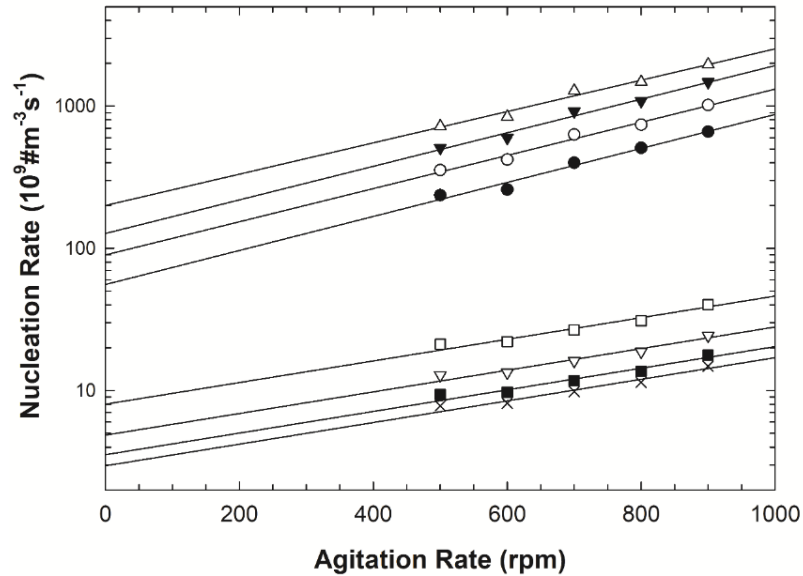
solution on top, indicating that the system is not well-mixed. Hence, we performed the experiments only above 500 rpm, otherwise number counts from the ORM measurements could not be relied upon. However, by measuring nucleation rates for a range of agitator speeds, nucleation rates could be reliably extrapolated to low shear rates.

The reproducibility of this approach was first evaluated for PABA ( $S_0=1.20$ ) and LGA ( $S_0=2.50$ ) in Figure 4.9 which showed a relative standard error of around 10% for the extrapolated nucleation rate.

The effect of agitation rate on the measured nucleation rate for other supersaturation ratios is shown in **Figure 4.10** and upon exponential extrapolation to zero rpm the estimated primary nucleation rate for PABA at  $S=1.2$  and LGA at  $S = 2.50$  were found to be  $5.6 \times 10^{10} \# \text{ m}^{-3}\text{s}^{-1}$  and  $3.0 \times 10^9 \# \text{ m}^{-3}\text{s}^{-1}$  respectively.



**Figure 4.9** Reproducibility of nucleation rates measured by ORM of (a) PABA at  $S_0 = 1.20$  and (b) LGA at  $S_0 = 2.50$  across different agitation rates. The solid line is a fit to an exponential function  $y = y_0 e^{kx}$ . For PABA, a relative standard error of 9.75% was obtained for  $y_0$  and 4.39% for  $k$  while for LGA, the relative standard error is 10.55% for  $y_0$  and 7.87% for  $k$ . Note that the nucleation rate here is in linear scale while that in Figure 4.10 is in logarithmic scale which displays a straight line for an exponential curve.



**Figure 4.10** Effect of agitation rate on the measured nucleation rate of PABA at  $S_0 = 1.20$  (●),  $1.25$  (○),  $1.32$  (▼),  $1.40$  (△) and LGA at  $S = 2.50$  (×),  $2.67$  (■),  $2.85$  (▽),  $3.05$  (□). Note that the nucleation rate is in logarithmic scale where an exponential curve appears linear.

Notice from **Figure 4.10** that on a logarithmic scale, nucleation rate varies linearly with agitation rate implying an exponential relationship. In principle, agitation increases the shear stress and frequency of collisions of crystals onto other crystals, crystallizer, and impeller resulting in more pronounced breakage, attrition, and other mechanisms of secondary nucleation. The theoretical relationship between secondary nucleation rate and agitation rate is rather complex and has mainly been described by empirical equations such as power law, polynomial and exponential functions. For convenience, a two-parameter estimator is generally preferable. While power-law and linear function could also somehow fit the trend for the total nucleation rate, both would imply that in stagnant solutions (zero rpm), nucleation rate would assume zero and negative values respectively, which is obviously unphysical. Again, we only carried out the experiments above 500 rpm since lower agitation rates resulted in settling of particles implying a non-uniform spatial distribution of particles in the crystallizer wherein laser-backscattering results can't be relied upon. This prevented us from confirming experimentally whether the exponential regime holds true in lower agitation rates using the current technique.



Nevertheless, notice that for both PABA and LGA, the total nucleation rate at 500 rpm and 600 rpm are close to each other as shown in Figure 4.9, indicating the likely formation of an asymptote towards lower agitation rates. Having almost equivalent nucleation rates for two different agitation rates imply that the nucleation rate is no longer a strong function of agitation rate around this regime, in other words, the increase in number of particles is becoming independent of the main driving force for secondary nucleation. Although the experimental data points below 500 rpm is inaccessible in the current technique, it is highly unlikely that a sudden shift in trend would occur below 500 rpm because as shown in Figure 4.9, the nucleation rate appears to be on the process of converging to some finite value. Moreover, Randolph and Cise<sup>40</sup> also suggested the use of exponential function for correlating the influence of stirring rate on the total nucleation rate. Altogether, this experimental evidence and literature support justify our assumption that the exponential fit is the most appropriate from 0 to 900 rpm and that an exponential extrapolation to stagnant conditions is a reasonable approximation of primary nucleation rate.

Considering that the main driving force for secondary nucleation is agitation, we further assume that the rate of secondary nucleation approaches zero at near-stagnant conditions. Thus, a simple empirical model accounting for the effect of agitation on the total nucleation rate can be written as

$$J_{tot} = J_p \exp(k_2 \omega) \quad (4.6)$$

where  $J_{tot}$  is the total nucleation rate,  $J_p$  is the primary nucleation rate,  $\omega$  is the agitation rate,  $k_2$  is a parameter describing the dependence of total nucleation rate on agitation rate. This means  $k_2$  should be higher for crystals that are more prone to breakage and attrition (such as needle, brittle crystals). Hence, we postulate that the extrapolated nucleation rate at zero rpm denoted as  $J_p$  represents a reasonable estimate of primary nucleation rate at that specific supersaturation. Note further that this formulation assumes that primary nucleation rate does not change significantly with agitation rate which is in accordance with the classical nucleation theory.

**Table 4.1** Measured primary nucleation rates at different supersaturation ratios.

	supersaturation ratio	primary nucleation rate ( $\pm 10\%$ )
PABA	1.20	$5.60 \times 10^{10}$
	1.25	$9.00 \times 10^{10}$
	1.32	$1.30 \times 10^{11}$
	1.40	$2.00 \times 10^{11}$
LGA	2.50	$3.00 \times 10^9$
	2.67	$3.50 \times 10^9$
	2.85	$4.90 \times 10^9$
	3.05	$8.00 \times 10^9$

The measured nucleation rates are listed in **Table 4.1** whose magnitudes are between  $10^9$  to  $10^{10}$ . To compare with literature, Turner et al<sup>96</sup> measured the nucleation rates of PABA using the KBHR framework and found that the concentration of instantaneously created nucleation sites  $C_0$  is in the order of  $10^{10} \text{ m}^{-3}$ . If we interpret this in terms of classical nucleation theory,  $C_0$  is related to the pre-exponential CNT parameter as  $A=zf^*C_0$  where  $z$  is the Zeldovich factor and  $f^*$  is the attachment frequency. If we conservatively assume  $z=1$  and  $f^*=1 \text{ s}^{-1}$ , this would lead to a magnitude of  $10^{10}$  for the pre-exponential factor  $A$  which is consistent with our results. Note that the KBHR approach<sup>38</sup> is based on a completely different yet well-established theoretical view of primary nucleation. Thus, its agreement of magnitude order with our particle-count approach provides an evidence supporting the validity of our newly developed protocol.

## 4.4 Conclusion

In this chapter, I developed a protocol to measure primary nucleation rates by monitoring particle counts (based on optical reflectance measurement coupled with in-situ Raman spectroscopy), with the following assumptions: (1) the rate of secondary nucleation approaches zero at zero agitation speed (2) the rate of secondary nucleation increases exponentially with increasing agitation speed. I applied these assumptions in the analysis of kinetic data obtained from various agitation speeds using *p*-aminobenzoic acid in water-ethanol mixture as a model system. Upon extrapolation to zero agitation, I obtained an order of magnitude of  $10^{10}$  for the pre-exponential factor  $A$  which is in agreement with the KBHR approach. Our particle-count based approach along with our empirical treatment of secondary nucleation could be useful in quantifying nucleation kinetics in the context of industrial applications where the interplay between hydrodynamics and secondary nucleation is important.

## Chapter 5

### Nucleation Kinetics in Agitated Systems: Particle Counts vs Induction Time Approach

In Chapter 4, an approach for measuring primary nucleation rate in liter-scale agitated crystallizer via particle-count approach was presented and the order of magnitudes of nucleation rates were in good agreement with KBHR method. However, there is also another approach for agitated systems based on induction time distribution of temperature-cycled mL-scale vials. This has been used extensively in the literature; however, there has been no experimental validation of this approach with other techniques.

In this chapter, I compared the nucleation kinetic parameters obtained from induction time distribution approach against that of particle-count approach. Results reveal discrepancies of six to seven orders of magnitudes. Although differences in fluid dynamics due to agitation and crystallizer geometry may have an effect, this tremendous discrepancy provides strong evidence that primary nucleation rates obtained from such technique may not be used for interpretation of nucleation rates in industrial scale applications.

*Parts of this chapter were published in:*

**Cedeno, R.**; Maosoongnern, S.; Flood, A., Direct Measurements of Primary Nucleation Rates of p-Aminobenzoic Acid and Glutamic Acid and Comparison with Predictions from Induction Time Distributions. *Industrial & Engineering Chemistry Research* 2018, 57 (51), 17504-17515.

## 5.1 Introduction

Convenient methods in quantifying nucleation kinetics especially in agitated systems is important for industrial scale-up of crystallization processes. Recently, a medium-throughput method to extract nucleation rates from the induction time distribution in multiple stirred mL volumes was developed by Jiang et. al.<sup>107</sup> based on the mathematical approach of Toshev et. al.<sup>108</sup> which assumes that the formation of at least one nucleus is a rare-event described by a Poisson distribution.<sup>3, 109-110</sup> This stochastic model has been used extensively in estimating nucleation parameters as exemplified by numerous publications utilizing the model.

**Table 5.1** Selected publications utilizing the Poisson-model for extracting nucleation rates from induction time distributions.

Year	Author	Compound	Technique	Detection
2003	Pino-Garcia <sup>111</sup>	vanillin in water/2-propanol solution	Reactors	Turbidity
2010	Goh <sup>45</sup>	lysozyme and paracetamol	Microfluidic system	Microscopy
2011	Jiang <sup>112</sup>	L-histidine, m-aminobenzoic acid	Crystallizer Platform	Turbidity
2012	Teychene <sup>113</sup>	Eflucimibe	Microfluidic system	Microscopy
2012	Chen <sup>114</sup>	paracetamol and glycine	Microfluidic system	Microscopy
2013	Kulkarni <sup>109</sup>	Isonicotinamide	Crystallizer Platform	Turbidity
2015	Lu <sup>115</sup>	aspirin and ibuprofen	microfluidic drop-based platform	stereomicroscopy
2017	Capellades <sup>116</sup>	glycine and L-arginine	Crystallizer Platform	Turbidity
2017	Stojakovic <sup>117</sup>	Paracetamol	Crystallizer Platform	Turbidity
2017	Patel <sup>118</sup>	benzocaine & 1,1'-bi-2-naphthol	Crystallizer Platform	Turbidity
2018	Nappo <sup>95</sup>	p-aminobenzoic acid	Double-pulse method	Microscopy

In response to the growing popularity of this approach, Xiao et. al.<sup>119</sup> and Maggioni et. al.<sup>14</sup> quantified the inherent uncertainties associated in such method via statistical analysis while Kubota<sup>17</sup> investigated the influence of solution volume on the stochasticity of nucleation via Monte Carlo simulations where it was shown that the stochasticity apparently disappears at larger volumes. Moreover, Maggioni and Mazzotti<sup>120</sup> pointed out some issues regarding the assumptions made in the stochastic model and subsequently developed two model modifications accounting for the interplay between stochastic nucleation and deterministic crystal growth. Surprisingly, the question as to whether the nucleation rates obtained via stochastic model can be used in scale-up and design of industrial crystallizers has not been fully investigated.

**Table 5.2** Literature value of nucleation kinetic parameter A for various compounds using the stochastic model.

Compound	A ( $\text{m}^{-3}\text{s}^{-1}$ )	Ref
m-ABA in 50% EtOH-water	$8.70 \times 10^5$	(112)
L-histidine in water	$3.63 \times 10^4$	
isonicotanamide in EtOH	$6.60 \times 10^4$	(109)
diprophylline RII in IPA	$5.76 \times 10^2$	(121)
diprophylline RI in DMF	$4.99 \times 10^2$	
p-aminobenzoic acid in acetonitrile	$3.63 \times 10^4$	(69)
p-aminobenzoic acid in 2-propanol	$1.09 \times 10^4$	
p-aminobenzoic acid in ethyl acetate	$2.05 \times 10^4$	
benzoic acid in toluene	$6.18 \times 10^4$	
p-aminobenzoic acid in water	$2.06 \times 10^5$	(122)
paracetamol in water	$2.00 \times 10^3$	(123)
	$1.3 \times 10^2$	(124)
adipic acid in water	$2.80 \times 10^6$	(125)

It is evident from literature that for organic compounds, the magnitude of nucleation rates predicted by the stochastic model typically ranges from  $10^2$  to  $10^6$   $\text{m}^{-3}\text{s}^{-1}$  (Table 5.2) whereas conventional methods yield values around  $10^8$  to  $10^{17}$   $\text{m}^{-3}\text{s}^{-1}$  (Table 5.3). The huge disparity has commonly been attributed to the occurrence of predominant secondary nucleation, particularly breakage and attrition. While it is true that secondary nucleation occurs in agitated systems, other model-based approach such as those proposed by Nyvlt, Kubota, and

Kashchiev also predict primary nucleation rates in the range of  $10^8$ - $10^{11}$   $\text{m}^{-3}\text{s}^{-1}$ . Note that all these model-based approaches postulate an assumed relationship between the nucleation rate and induction time or metastable zone widths, which we will refer to as indirect measurement. The disagreement between the indirect approaches shows the need to quantify nucleation rate via direct measurement which does not rely heavily on model assumptions. These direct methods physically quantify the evolution of number of particles which include in-line video microscopy (IVM) and laser-backscattering. However, the issue with direct measurement lies on its inability to distinguish between primary and secondary nuclei which prevents the straight-forward experimental validation of models for primary nucleation in agitated systems.

To overcome this, Li et. al.<sup>30</sup> simultaneously fitted the expressions for primary and secondary nucleation to experimental data under the population balance framework which resulted in five kinetic parameters describing the total nucleation rate data. This however yielded primary nucleation rate with confidence intervals within six orders of magnitude. We also believe that in this approach, the ratio of primary to secondary nucleation strongly depends on the functional form of expressions used for fitting experimental data (in their case, a logarithmic function was used for primary and power-law function for secondary) to the population balance equation.

Hence, this chapter aims to determine whether the magnitude of nucleation rates obtained from the stochastic model is comparable with direct measurements via direct particle-counting approach using *p*-aminobenzoic acid (PABA) and L-glutamic acid (LGA) as model compounds.

**Table 5.3.** Magnitude of nucleation rates in literature for various compounds and determination methods.

Compound	J (m <sup>-3</sup> s <sup>-1</sup> )	nucleation	method	Ref
benzoic acid in water-ethanol	10 <sup>7</sup> -10 <sup>9</sup>	total	direct, FBRM, Population Balance	126
L-glutamic acid in water	10 <sup>8</sup>	primary	indirect, FBRM, Kaschiev model	71
paracetamol in water-ethanol	10 <sup>10</sup> -10 <sup>11</sup>	primary	indirect, FBRM, MSZW, Nyvlt & Kubota model	127
	10 <sup>9</sup> -10 <sup>11</sup>	primary	indirect, FBRM, induction time, Nyvlt & Kubota model	128
	10 <sup>19</sup>	total	direct FBRM, population balance	129
	10 <sup>-1</sup> -10 <sup>5</sup>	primary*	direct FBRM, population balance	30
	10 <sup>7</sup> -10 <sup>8</sup>	secondary*		
RDX in $\gamma$ -butyrolactone	10 <sup>8</sup>	total	direct, FBRM	130
L-asparagine monohydrate in water-2-propanol	10 <sup>10</sup>	total	direct, Coulter Multisizer	131
$\gamma$ -DL-methionine in water	10 <sup>8</sup> -10 <sup>11</sup>	total	direct, droplet-based method	132
H <sub>4</sub> EDTA in water	10 <sup>15</sup>	total	direct, stopped-flow technique,	133
salicylic acid	10 <sup>9</sup> -10 <sup>17</sup>	total	direct, microscopy, population Balance	134
p-aminobenzoic acid in ethanol	10 <sup>8</sup> -10 <sup>9</sup> §	primary	indirect, metastable zone width, KBHR model	96
p-aminobenzoic acid in acetonitrile	10 <sup>9</sup> -10 <sup>10</sup> §	primary		
p-aminobenzoic acid in water	10 <sup>10</sup> §	primary		

\*In Ref (30), the expressions for primary and secondary nucleation were added to fit experimental data. Thus, the ratio of primary to secondary is not observed experimentally. §In Ref(96), the concentration of instantaneously nucleated crystallites  $C_0$  (m<sup>-3</sup>) is shown here instead of J.  $C_0$  is related to the pre-exponential CNT parameter as  $A=zf^*C_0$  where  $z$  is the Zeldovich factor and  $f^*$  is the attachment frequency.

Direct methods are those that measure particle counts from instrumental data. Indirect methods involves correlating nucleation rate with induction time or metastable zone widths as employed in Kaschiev's, Nyvlt's, Kubota's, and KBHR's approaches.



## 5.2 Materials and Methods

### 5.2.1 Chemicals and Equipment

The compounds p-aminobenzoic acid, PABA (TCI, chemical purity > 99%), L-glutamic acid, LGA (TCI, chemical purity > 99%), pure ethanol (TCI, AR grade), and ultrapure water were used as received. The induction time and solubility were measured using the multiple-crystallizer setup called Crystal16 (Technobis, Amsterdam) which measures light transmissivity through standard HPLC vials.

### 5.2.2 Induction Time Measurement

Induction time ( $t_i$ ) is defined as the period between the point of constant supersaturation and the instance of detection of crystals. The induction times were obtained using the Crystal16 for four different initial supersaturation ratios ( $S_0=c_0/c^*$ ) of PABA ( $S_0=1.20, 1.26, 1.33, 1.40, T = 30^\circ\text{C}$ ) and LGA ( $S_0 = 2.50, 2.67, 2.85, 3.05, T = 25^\circ\text{C}$ ). For each supersaturation ratio, a 50-mL solution ( $\pm 0.0005$  mL) was prepared in a stirred beaker by dissolving the corresponding amount of PABA ( $\pm 0.0005$  g) in the solvent which was then heated to  $10^\circ\text{C}$  above the saturation temperature for at least 20 minutes to ensure complete dissolution of solute particles. A pipet ( $\pm 2.5$   $\mu\text{L}$ ) was used to dispense 1 mL of clear solution into 1.8 mL HPLC vial which was then loaded into the Crystal16 setup and stirred for 20 minutes. The solution was then cooled down quickly ( $5^\circ\text{C}/\text{min}$ ) and maintained at  $30^\circ\text{C}$ . The point at which the temperature inside the vessel reached  $30^\circ\text{C}$  was taken as time zero. After some time, light transmission starts to decrease which marks the onset of detectable nucleation. The difference between this time and time zero was taken as the induction time. Then, samples were reheated at a rate of  $0.5^\circ\text{C}/\text{min}$  up to  $50^\circ\text{C}$  to dissolve all crystals forming a clear solution. This heat-cool-hold cycle was done 7 times per vial to obtain up to 112 induction time measurements for each supersaturation ratio. All induction time measurements in this work are based on a 900-rpm stirring speed to ensure complete mixing.

### 5.2.3 Extraction of Nucleation Rate from Induction Time

In the stochastic model, the probability of forming  $k$  nuclei in a time interval can be described by the Poisson distribution which can be written as<sup>112</sup>

$$P_k = \frac{N^k \exp(-N)}{k!} \quad (5.1)$$

where  $N$  is the average number of nuclei and  $i$  is the random variable corresponding to the number of nuclei formed. Consequently, the probability that the onset of nucleation will be detected at a certain time interval corresponds to the probability that at least one nucleus is formed which can be expressed as

$$P(k \geq 1) = \sum_{k=1}^N \frac{N^k \exp(-N)}{k!} \quad (5.2)$$

However, notice that the probability of forming at least one nucleus is just the complement of the probability that no nuclei will form. Applying this mathematical concept, equation (5.2) can be simplified as

$$P(k \geq 1) = 1 - P(k = 0) \Rightarrow P(k \geq 1) = 1 - e^{-N} \quad (5.3)$$

In turn, the average number of nuclei  $N$  can be determined as

$$N = JV\Delta t \quad (5.4)$$

where  $J$  is the nucleation rate, i.e. the number of nuclei that appears per unit solution volume per unit time ( $\#/m^3s$ ),  $V$  is the solution volume and  $\Delta t$  is the time interval.

Meanwhile, the formed nuclei must grow to detectable sizes before they can be observed experimentally by measuring equipment which causes a delay in detection called growth time  $t_g$ . Incorporating this lag time to equations (5.3) and (5.4), the probability of detecting crystals at a time  $t$  can be expressed as

$$P(t) = 1 - \exp[-J(t - t_g)] \quad (5.5)$$

The cumulative probability distribution described by equation (5.5) can be determined by measuring induction times under equal conditions for sufficient number of isolated experiments which can be written as

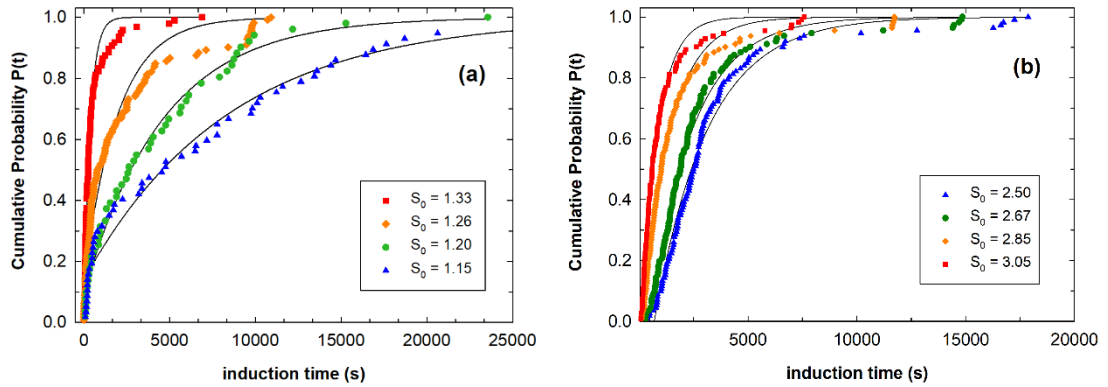
$$P(t) = \frac{M^+(t)}{M} \quad (5.6)$$

where  $M^+(t)$  is the number of isolated experiments that nucleated at a time less than or equal to time  $t$  and  $M$  is the total number of experiments. Thus, the value of the nucleation rate  $J$  by the curve fitting of  $P(t)$  against induction time.

## 5.3 Results and Discussion

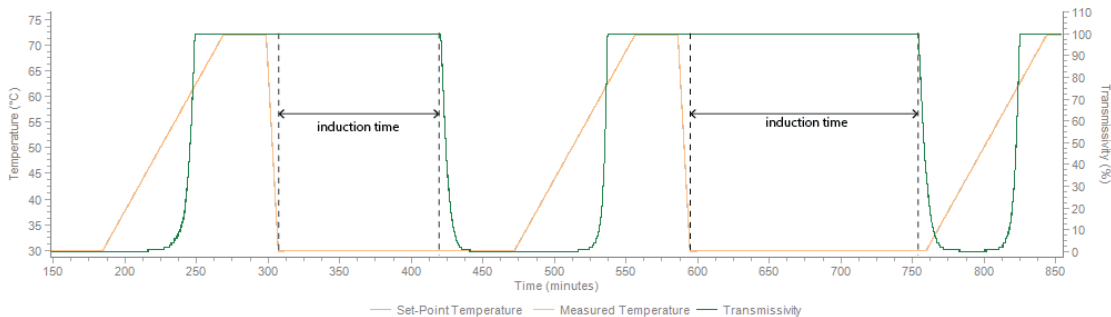
### 5.3.1 Nucleation Rates from Induction Time Probability Distribution

The induction time distributions of PABA and LGA for four different supersaturations are shown in **Figure 5.1a** and **Figure 5.1b** respectively.



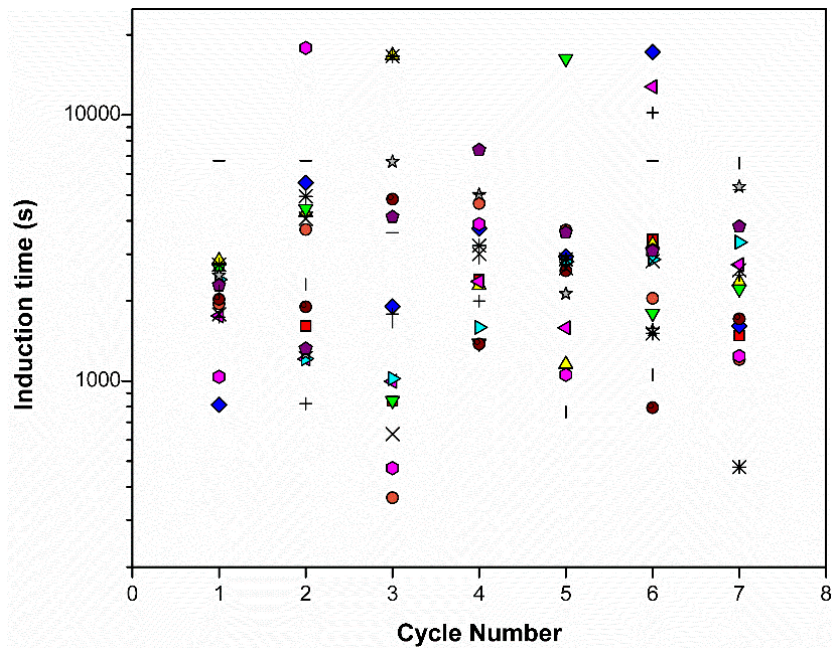
**Figure 5.1** Experimentally obtained cumulative probability distribution  $P(t)$  of induction time for PABA (a) at supersaturation ratios  $S = 1.20$  (blue  $\blacktriangle$ ),  $1.25$  (green  $\bullet$ ),  $1.32$  (orange  $\blacklozenge$ ),  $1.40$  (red  $\blacksquare$ ) and LGA (b) at supersaturation ratios  $S = 2.50$  (blue  $\blacktriangle$ ),  $2.67$  (green  $\bullet$ ),  $2.85$  (orange  $\blacklozenge$ ),  $3.05$  (red  $\blacksquare$ ).

The results reveal large variations of induction times ranging from close to zero to over 7 hours, even at identical conditions, which is indicative of the stochastic nature of nucleation in small volumes. As expected, the variability of induction time is higher in lower supersaturations since the probability of nuclei formation is lower due to the lower driving force. To check whether thermal history due to temperature cycling (**Figure 5.2**) has any influence on induction time, a plot of induction times for different cycles is shown in **Figure 5.3** for LGA at  $S=2.50$ .



**Figure 5.2** Typical temperature profile used in induction time measurements via Crystal16. The excellent agreement between set-point temperature (gray) and the measured temperature inside the vial (orange) suggests an accurate temperature control. A sample data for the evolution of transmissivity (green) for LGA is shown.

A mean  $R^2$  value of 0.123 between induction time and cycle number was obtained suggesting that the temperature cycle has essentially no influence on induction time. Furthermore, it is evident that samples with relatively short or long induction time in one cycle do not retain this behavior in the next cycles thereby providing evidence that the temperature and time used for dissolution in each cycle are sufficient to eliminate the “memory effect”. A similar behavior was observed for both LGA and PABA at different supersaturations.



**Figure 5.3** Scatter plot of induction time against cycle number for LGA ( $S_0 = 2.50$ ). The squared correlation coefficient  $R^2$  of induction time with respect to cycle number was calculated for each vial. The average  $R^2$  for the 16 vials was found to be 0.123 suggesting that induction time is not significantly influenced by cycle number. Different symbols in each cycle represents different vials. The vials with short induction time in one cycle do not necessarily have short induction time in the next cycles. This supports that the “memory effect” does not have considerable influence in the conditions employed. A similar behavior was observed for both LGA and PABA at different supersaturations.

**Table 5.4** Nucleation rates ( $J$ ) and growth time ( $t_g$ ) obtained from the fit of induction times to the stochastic model in equation (5.5).

	$S_0$	$J$ ( $m^{-3}s^{-1}$ )	Std. Error ( $m^{-3}s^{-1}$ )	$t_g$ (s)	Std. Error (s)	$R^2$
PABA	1.20	118.7 (151.0)	4.3 (5.40)	-1273.5 (82.0)	143.49 -	0.9727
	1.25	216.6 (224.0)	5.40 (5.25)	-464.5 (63.0)	54.26 -	0.9879
	1.32	506.7 (697.3)	18.3 (26.4)	-283.7 (5.0)	31.19 -	0.9596
	1.40	2733.0 (2927)	67.1 (50.8)	-9.9 (4.0)	4.03 -	0.9809
LGA	2.50	407.4 (339.7)	7.6 (7.0)	694.1 (364.0)	22.74	0.9808
	2.67	503.8 (440.2)	7.6 (6.7)	472.5 (282.0)	14.53	0.9883
	2.86	777.2 (751.2)	7.7 (5.5)	139.5 (112.0)	5.91	0.9957
	3.05	1293.0 (1292.0)	14.3 (9.7)	84.5 (84.0)	3.96	0.9947

Following the method proposed by the group of ter Horst<sup>44</sup>, the nucleation rate  $J$  and growth time  $t_g$  can be extracted from the induction time distributions by non-linear regression. The growth time is defined as the time required for the nuclei to grow to detectable size. Note that for PABA, the growth time assumes a negative value when treated as a parameter in non-linear regression (**Table 5.4**). This is probably due to the fact that the experimental values do not conform well with the Poisson distribution, as shown by its Kolmogorov-Smirnov (KS) number (**Table 5.5**) being greater than the critical value of 1.358 ( $\alpha=0.05$ ), particularly at lower supersaturations. This suggests that the onset of nucleation cannot always be modelled as a Poisson process. Unreasonable values of  $t_g$  have also been observed in other studies on isonicotinamide in ethanol<sup>44</sup>, PABA in water<sup>122</sup>, benzoic acid in toluene<sup>69</sup>, and L-histidine in water<sup>107</sup> which further suggest that the model assumptions may be invalid for nucleation for some systems.

The usual approach to circumvent this negative  $t_g$  values is to set the growth time as the minimum induction time (results shown as enclosed in parenthesis in **Table 5.4**). However, we believe that this is statistically inappropriate because the smallest measurable induction time is a much stronger function of the number of points measured than the physical description of growth time itself (i.e. small numbers of measurements will give a high  $t_g$  and infinitely large numbers of measurements will give  $t_g$  values approaching zero).

In **Table 5.4**, observe that the relative standard error of the estimated parameters is small (<5%) under the protocols of non-linear regression which suggests a good fit of the data to the model. However, a more detailed description of the inherent uncertainties associated with this nucleation rates has been subject to scrutiny in recent papers<sup>119-120, 135</sup> and Kolmogorov-Smirnov (KS) analysis has been shown to be appropriate for both hypothesis testing and quantifying confidence intervals.<sup>135-136</sup>

### 5.3.2 Confidence Intervals of Estimated Parameters

Kolmogorov-Smirnov analysis allows for comparison of cumulative probability distributions derived from experiment  $P(t)$  against that predicted by Poisson distribution  $P^*(t)$ . If we denote  $D$  as the maximum absolute difference between the corresponding  $P(t)$  and  $P^*(t)$  and  $n$  as the number of independent experiments, then the KS number can be defined as  $D\sqrt{n}$ . If the KS number is greater than the critical value  $C$  (1.358 for  $\alpha = 0.05$ ), then we can conclude that  $P(t)$  is likely not following a Poisson distribution. As suggested by Maggioni and co-workers<sup>9</sup>, the confidence interval of  $J$  can be written as

$$J(1 + \eta^-) \leq J \leq J(1 + \eta^+) \text{ such that } \frac{\eta}{(1+\eta)^{1+\frac{1}{n}}} = \pm \frac{C}{\sqrt{n}} \quad (5.7)$$

where  $\eta^-$  and  $\eta^+$  are the values of  $\eta$  by equating to negative and positive value of  $C$  respectively. Note that this would result in asymmetric confidence intervals, i.e. the distance from the estimated value to the upper bound is higher compared to its lower bound counterpart.

The result of this statistical analysis is tabulated in **Table 5.5**. Notice that the first three supersaturations of PABA have KS numbers greater than the critical value 1.358, suggesting that the Poisson distribution does not well-represent the experimental distribution.

**Table 5.5** Confidence intervals of nucleation rates based on Kolmogorov-Smirnov analysis.

	S	J (m <sup>-3</sup> s <sup>-1</sup> )	KS number	95% Confidence Interval	
				Lower Limit	Upper Limit
PABA	1.20	151.0	2.09	105.1	215.8
	1.25	224.0	1.41	157.8	318.1
	1.32	697.3	1.46	491.1	990.1
	1.40	2927.0	1.07	2003.5	4275.8
LGA	2.50	339.7	1.27	239.3	482.3
	2.57	440.2	0.88	310.0	625.0
	2.85	751.2	0.85	529.1	1066.6
	3.05	1292.0	0.64	910.7	1835.9

Moreover, KS number is found to be relatively higher for lower supersaturation than in higher supersaturation. Having an experimentally measured curve that does not fit a Poisson distribution at 95% confidence may indicate that the assumptions in the induction time model are not valid for some conditions particularly at lower supersaturations. It is also worth noting that the confidence intervals deviate by around 40% from the estimated value and are much higher than the confidence intervals based on standard errors from non-linear regression. Thus, the choice of statistical technique must be clearly indicated when reporting confidence intervals. Overall, despite the wide confidence intervals obtained from KS analysis, the upper and lower bounds are found to lie on similar order of magnitude as the estimated value.

To determine whether these magnitude of nucleation rates can be used in the actual design of industrial crystallization processes, the nucleation rates of PABA and LGA were measured with a direct measurement of particle counts using in-situ ORM.



### 5.3.3 Comparing Nucleation Kinetic Parameters

The comparison of predicted primary nucleation rates obtained from the two methods (particle count approach vs induction time distribution) are shown in **Table 5.6**. Observe in that the magnitude of nucleation rate  $J$  from particle-count approach is in the order of  $10^9$  while that of the induction time distribution approach is in the order of  $10^3$ . Indeed, the nucleation rates predicted by the induction time distributions appear very low; if we take a solution of PABA at  $S=1.2$  as an example, only 10 nuclei would form in a 1-mL solution after 24 hours if the nucleation rate is taken as  $119 \text{ \# m}^{-3}\text{s}^{-1}$ .

Furthermore, the differences become more evident when we analyze the nucleation rates based on Classical Nucleation Theory (CNT)<sup>137</sup> which states that the primary nucleation rate  $J$  can be expressed as a function of supersaturation as

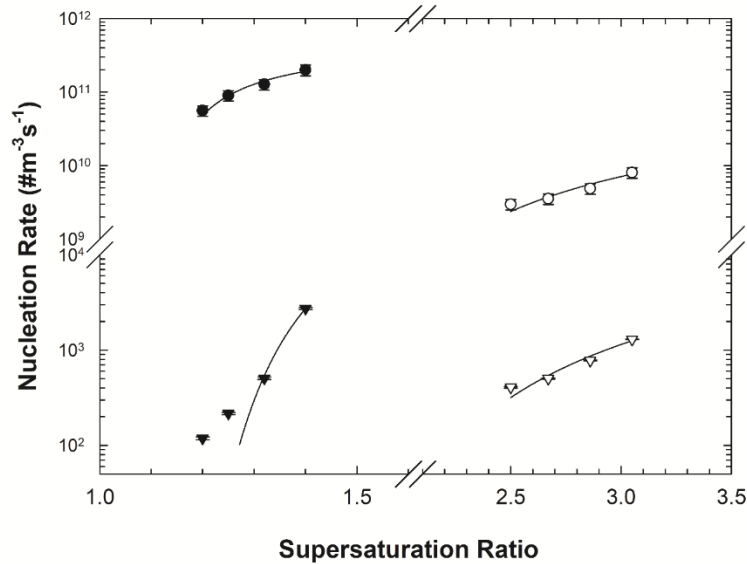
$$J(S) = AS \exp\left(-\frac{B}{\ln^2 S}\right) \quad (5.8)$$

where  $A$  is a kinetic parameter which is a function of attachment frequency, concentration of nucleation sites, and Zeldovich factor, while  $B$  is a thermodynamic parameter which is related to the interfacial energy between crystal and solution and molecular volume<sup>121, 138</sup>.

**Table 5.6** Comparison of predicted primary nucleation rates obtained from two methods: via particle-count approach extrapolated back to stagnant solution and via induction time distribution ( $J_{Ind}$ ).

	$S_0$	$J_p$ ( $\# \text{ m}^{-3}\text{s}^{-1}$ )	Rel. Std. Error (%)	$J_{Ind}$ ( $\# \text{ m}^{-3}\text{s}^{-1}$ )	Rel. Std. Error (%)
PABA	1.20	$56 \times 10^9$	9.8	119	3.6
	1.25	$90 \times 10^9$		217	2.5
	1.32	$130 \times 10^9$		507	3.6
	1.40	$200 \times 10^9$		2733	2.5
LGA	2.50	$3.0 \times 10^9$	10.6	407	1.9
	2.67	$3.5 \times 10^9$		504	1.5
	2.85	$4.9 \times 10^9$		777	1.0
	3.05	$8.0 \times 10^9$		1293	1.1

The parameters A and B can be estimated by non-linear regression in **Figure 5.4** whose results are shown in **Table 5.7**. Notice that from both the stochastic model and ORM measurement, the parameter B is of similar magnitude which agrees to the formulation of B as a thermodynamic property.



**Figure 5.4** Estimation of CNT parameters of PABA from induction time distributions ( $\blacktriangledown$ ) and from *in situ* ORM ( $\bullet$ ) and of LGA from induction time distributions ( $\triangledown$ ) and from *in situ* ORM ( $\circ$ ) by fitting to equation (5.7) by non-linear least square regression.

**Table 5.7** Estimated CNT Kinetic Parameter A and Thermodynamic Parameter B obtained from stochastic model and ORM measurement via non-linear regression.

Method		PABA	Std. Error	LGA	Std. Error
Induction Time	A ( $\text{m}^{-3}\text{s}^{-1}$ )	$5.46 \times 10^4$	$3.43 \times 10^4$	$4.70 \times 10^3$	$2.24 \times 10^3$
	B	0.0377	0.070	3.03	0.542
Particle Counts	A ( $\text{m}^{-3}\text{s}^{-1}$ )	$2.28 \times 10^{11}$	$3.10 \times 10^{10}$	$1.894 \times 10^{10}$	$9.94 \times 10^9$
	B	0.0579	0.010	2.51	0.589

These results suggest that the stochastic model can predict surface energies that are reasonably consistent with other measurement technique. On the other hand, the kinetic parameter A obtained from such model ( $10^3$  to  $10^4 \text{ #m}^{-3}\text{s}^{-1}$ ) is several orders of magnitude lower than that obtained via ORM measurement ( $10^{10}$  to  $10^{11} \text{ #m}^{-3}\text{s}^{-1}$ ).

In literature, the theoretical order of magnitude of the kinetic parameter  $A$ <sup>36, 139</sup> ranges from  $10^{15}$  to  $10^{25} \text{ #m}^{-3}\text{s}^{-1}$  which is much closer to what we have obtained via in-situ ORM measurements. In a review, the value of A is given as  $10^{30} \text{ #m}^{-3}\text{s}^{-1}$  ‘plus or minus a few orders of magnitude’ for homogeneous primary nucleation, and  $10^{10}$  to  $10^{20}$  for heterogeneous primary nucleation<sup>140</sup>. Furthermore, experimental studies on  $\alpha$ -L-glutamic acid<sup>141</sup>,  $\gamma$ -DL-methionine<sup>132</sup>, benzoic acid<sup>142</sup> and L-asparagine monohydrate<sup>143</sup> also revealed A values of around  $10^7$  to  $10^{13} \text{ #m}^{-3}\text{s}^{-1}$ . The group of ter Horst<sup>144</sup> made a review of previous studies involving homogeneous and heterogeneous nucleation of both ionic and molecular compounds, and found A values from experiments were of the order  $10^{17}$  –  $10^{38} \text{ #m}^{-3}\text{s}^{-1}$  for ionic compounds, and  $10^{11}$  –  $10^{28} \text{ #m}^{-3}\text{s}^{-1}$  for molecular compounds. Recent studies using microfluidics to measure nucleation have found similar values for A; values in the range of  $10^8$  –  $10^{16}$  were quoted for lysozyme.<sup>51</sup> This data suggests that although the stochastic model may be used to estimate surface energies, we believe that it predicts values of the pre-exponential factor A that are too small for industrial applications. What is not clear is whether the discrepancy is due to the assumptions in the model being invalid, or whether it is due to the conditions in which the nucleation occurs in small scale induction time experiments being substantially different to the conditions experienced in larger scale experiments. This may cause a distinct difference in the number of

heterogeneous nucleation sites available, thus substantially changing the preexponential factor and the kinetics of the nucleation.

Nevertheless, we believe that the difference in scale (1 mL vs 100 mL) alone does not explain the six orders of discrepancies presented herein. The influence of scale-up factors such as energy dissipation rate, turbulence, and mixing collisions are mainly attributable to secondary nucleation rate rather than primary nucleation. As justified earlier, our proposed method of extrapolating to zero agitation essentially removes the effect of secondary nucleation allowing us to estimate the primary nucleation rate. It is worth noting that primary nucleation, a first-order phase transition, occurs at the molecular level and is generally assumed to be very insensitive to macroscopic fluid dynamics (such as velocity and shear stress distribution, formation of turbulent eddies, etc.), which is why classical theories for both homogeneous and heterogeneous nucleation do not include terms related to fluid dynamics. As mentioned, there is some recent evidence of the effect of shear on primary nucleation<sup>95</sup> but this effect has been shown to be positive for some values of shear and negative for others, and thus, could not be responsible for *ca* 6 orders of magnitude differences in rates of primary nucleation.

The reason for this huge discrepancy could then be due to the intrinsic assumptions of the stochastic model of nucleation. Note however that this contribution does not intend to invalidate the assumptions of the stochastic model entirely, nor propose a relevant model modification, but mainly show that its predictions inconsistent with other techniques at larger scales even if the effect of secondary nucleation is made to approach zero as shown in this work. Nonetheless, we will mention some possibilities which could explain the observed discrepancy. A detailed discussion of the assumptions used in the probabilistic approach and their corresponding issues have been presented by Bhamidi and co-workers<sup>6</sup>. The group of Mazzotti has also shown that it is not possible to obtain independent information about both nucleation and growth kinetics from induction time measurement alone as this results in fitted parameters being correlated<sup>145</sup>. Another possibility for the difference between predicted and experimental primary nucleation rates is that the model assumes that there is effectively no relaxation time for the molecules in the mixture to attain a state suitable for the nucleation event to occur. Potentially there is a lag time before the first attempt at nucleation can occur, thus increasing the value of the parameter  $t_g$ . In fact, it was found in some cases that this nucleation delay time is much longer than both nucleation time and growth time<sup>146</sup>, in contrary to the model assumptions.

In addition, the Poisson model is mathematically applicable if and only if the formation of each nuclei is completely independent of each other and all nuclei are formed with equal probabilities across the time interval. However, several experimental studies indicate that nucleation proceeds deterministically after the formation of the first nucleus.<sup>120</sup> The observed influence of the earlier nuclei to the succeeding nuclei has led the group of ter Horst<sup>147</sup> to conclude the occurrence of single nucleus mechanism (SNM) which postulates that the entire crystal population subsequently originates from the first stochastically-formed single crystal. Although this theory is well-supported by experiments whereby pure polymorphic form appear under conditions of concomitant polymorphism,<sup>147</sup> this would imply that the conventional definition of primary nucleation i.e. the number of stable nuclei formed from solution per volume per time, will not be a measurable quantity from an industrial perspective if the second nuclei is assumed to originate from the first nuclei.

## 5.4 Conclusion

In this chapter, I compared the nucleation kinetic parameters obtained from L-scale particle-count approach against the mL-scale induction time approach using *p*-aminobenzoic acid (PABA) and L-glutamic acid (LGA) as model compounds. The results show that the induction time approach results in kinetic prefactors in the order of  $10^3$ - $10^4$   $\text{m}^{-3}\text{s}^{-1}$  which is about 6 orders of magnitudes lower than that obtained from particle-count approach. Although the stochastic model has been used extensively in literature for quantifying crystallization kinetics, these results provide strong evidence that nucleation rates obtained from such model may not be used as reference for scale up and design of industrial crystallizers and we suggest limiting its use to estimating interfacial surface energies rather than extracting numerical values of nucleation rates. It is possible that the variation of induction times may only describe the stochasticity of the onset of nucleation and may not carry sufficient information to describe nucleation kinetics quantitatively, particularly in the context of industrial applications.

## **Chapter 6**

### **Quantifying Nucleation Kinetics: A Multi-scale Comparison**

In the previous chapter, I have shown that two different methods for the same compound-solvent system can result in nucleation parameters that have differences of 6-7 orders of magnitude. I have shown that methods based on induction time give inherently low values of the pre-exponential factor  $A$  but interestingly, both methods give relatively similar value of the thermodynamic parameter  $B$  which is related to the effective interfacial energy  $\gamma_{\text{eff}}$  between crystal and solution. To further shed light into this huge discrepancy in the kinetic factor  $A$ , in this chapter, I quantified the nucleation kinetics using additional experiments namely, liter-scale conductometry and microliter-scale microscopy which both measure induction time. The results show that  $A$  is highly dependent on the measurement technique and model assumptions while  $\gamma_{\text{eff}}$  is dependent on the supersaturation level and system volume. This chapter highlights that careful attention is needed in interpreting nucleation kinetic parameters acquired from different scales and measurement techniques.

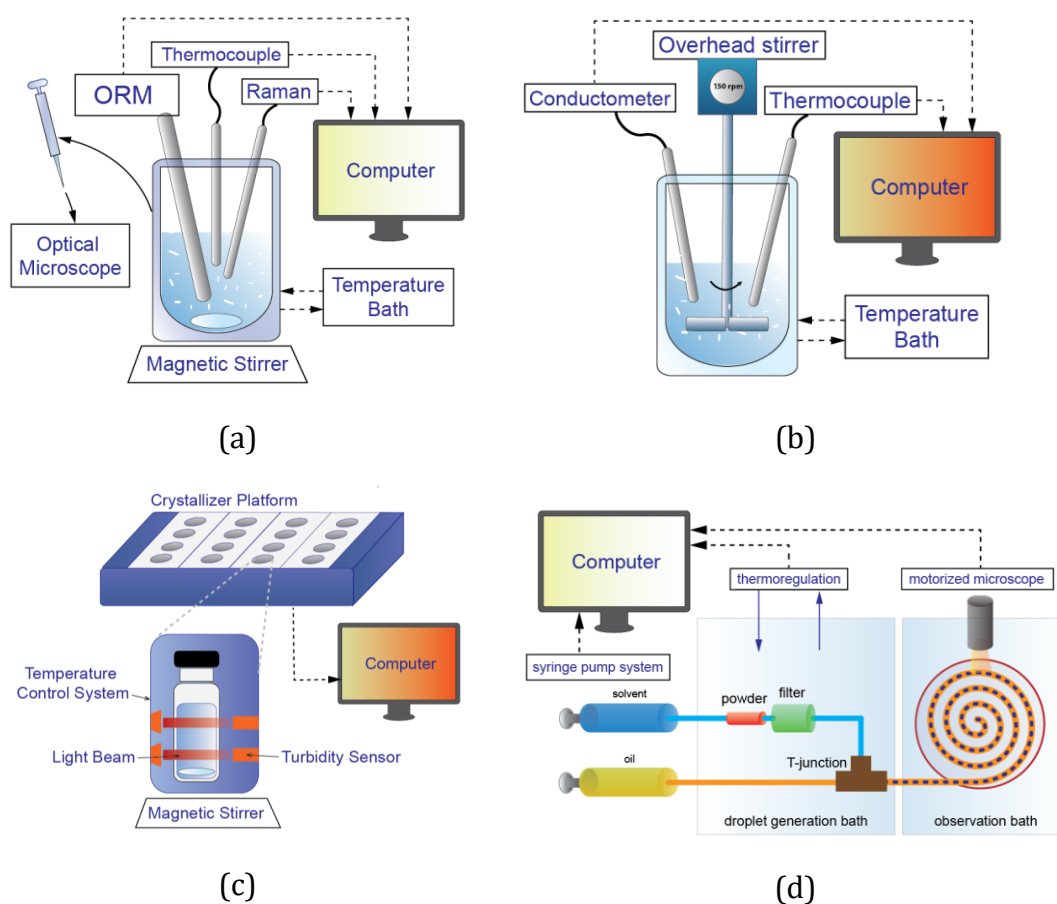
## 6.1 Introduction

Reliable quantification of nucleation kinetics is key in the design and scale-up of industrial crystallization processes. For this reason, several methods in quantifying nucleation kinetics have been developed across different scales. For instance, in large-volume agitated systems ( $\sim 1\text{L}$ ), the use of process-analytical technology such as laser backscattering has been widely used in estimating nucleation parameters based on particle counts, induction time or metastable widths. In 1-mL scale, a turbidimetry-based crystallizer platform has been employed to extract nucleation parameters from induction time distributions. In  $\mu\text{L}$  to nL scale, microfluidics approaches have been successfully employed to obtain such parameters either by induction time distributions or double-pulse techniques. Note that some of the results in L (particle count approach) and mL scale crystallizer (induction time approach) were already presented in chapter 4 and 5.

Given that each of these methods mentioned above are based on very different volumes, fluid dynamics, instrumental techniques, and model assumptions, it remains unclear whether the kinetic parameters obtained from each method have comparable magnitudes. Consequently, whether we could reasonably use a kinetic parameter obtained from one technique to describe the kinetics occurring in a different scale is still an unresolved question. To address this, we present a multiscale study where we quantify the nucleation kinetics of a pharmaceutical compound across  $\mu\text{L}$ , mL, and L scales and across various data treatment procedures. We then rationalize the observed discrepancies in terms of nucleation principles, model assumptions, hydrodynamics, and instrumental limitations. Our findings will not only shed valuable insights on the fundamentals of nucleation but may also guide researchers and industries in deciding which experimental protocol and data treatment are appropriate for their specific purpose.

## 6.2 Material and Methods

With p-aminobenzoic acid (PABA) in 30% by weight ethanol-water mixture as model system, we performed nucleation rate measurements using various techniques at different scales. As an overview, a schematic illustration of each setup is shown in **Figure 6.1**.

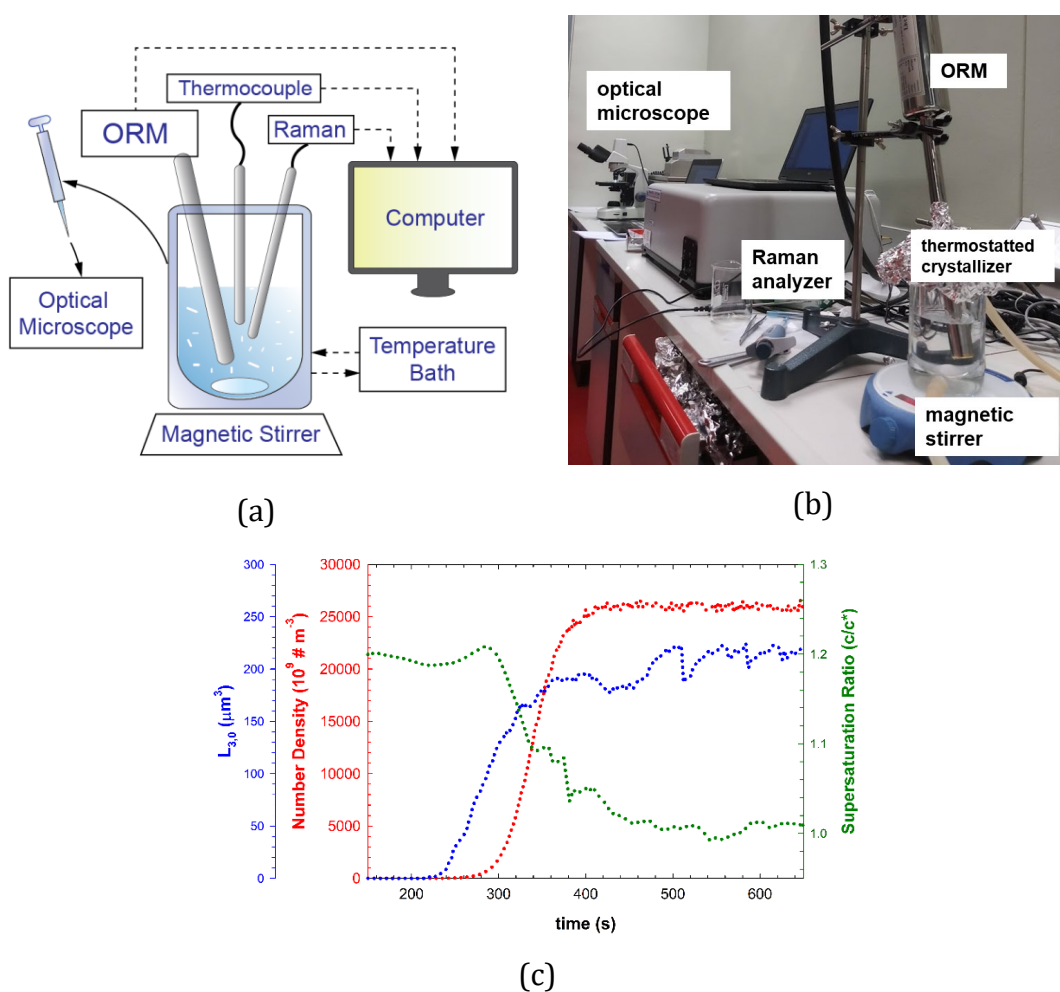


**Figure 6.1** Overview of the experimental setup across different scales (a) liter-scale particle count approach (b) liter-scale deterministic induction time approach (c) mL scale probabilistic induction time approach (d)  $\mu\text{L}$  scale probabilistic induction time approach



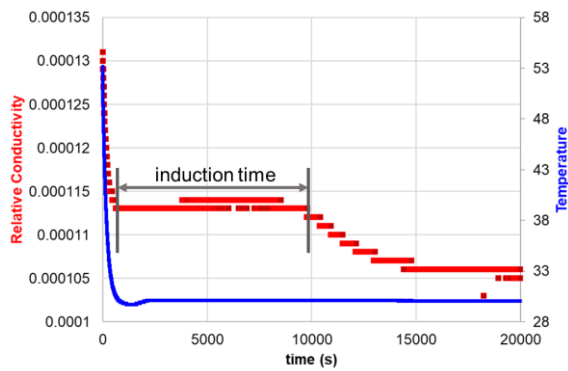
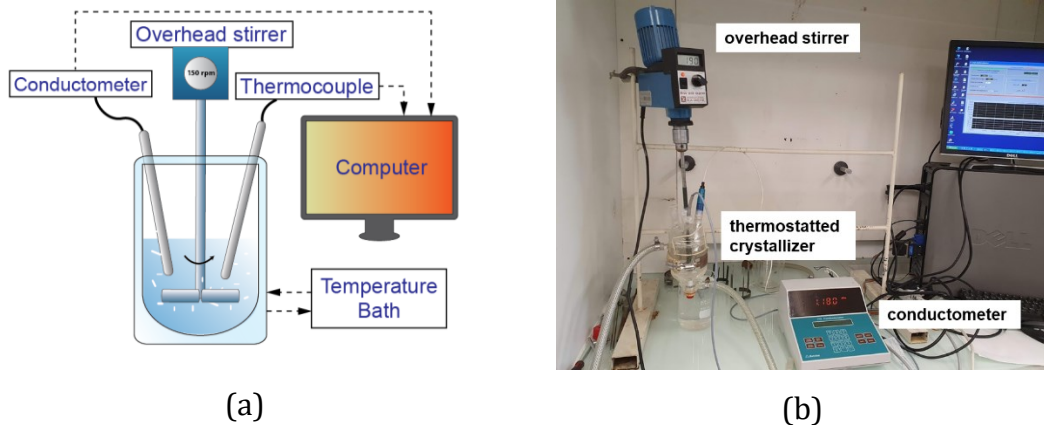
## 6.2.1 Liter Scale

**(a) Particle Count Approach.** I used optical reflectance measurement (ORM) coupled with in-situ Raman spectroscopy to track the evolution of number of particles and solution concentration. The setup is shown in **Figure 6.2**. In the estimation of primary nucleation rate, we empirically assumed that the rate of secondary nucleation varies exponentially with agitation speed. Thus, upon extrapolating the nucleation rate to zero agitation, we extract the primary nucleation rate. A detailed description of this process is presented in Chapter 4.



**Figure 6.2** (a) Schematic diagram of the experimental setups for liter-scale particle count approach (b) Photograph of the induction time measurement setup (c) Typical evolution of calibrated quantities: crystal size ( $L_{3,0}$ ), number density, and supersaturation ratio.

**(b) Deterministic Induction Time Approach.** Since PABA partially ionizes in solution, we used a solution conductometer to determine the onset of nucleation. The setup is shown in **Figure 6.3**. The system is agitated with an overhead stirrer. The induction time is taken deterministically as the inverse of nucleation rate, that is,  $t_i = 1/(JV)$ .



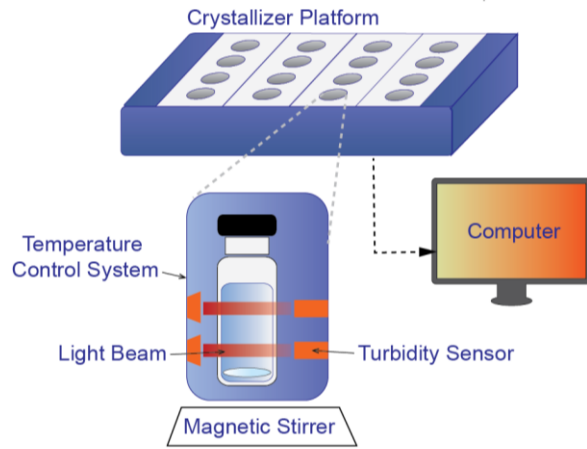
**Figure 6.3** (a) Schematic illustration of the L-scale induction time measurement setup via solution conductometry (b) Photograph of the setup (c) Typical evolution of relative conductivity and temperature. The time elapsed between the attainment of the final temperature and the onset of sustained decrease in conductivity is taken as the induction time.

## 6.2.2 Milliliter Scale

**(a) Probabilistic Induction Time Approach.** I used a commercial crystallizer platform Crystal16 that determines the onset of nucleation from the increase of system turbidity. A total of 112 induction times were obtained which were then fitted with Poisson distribution function as suggested by Jiang et al.<sup>112</sup> A detailed description of this process is presented in Chapter 5.

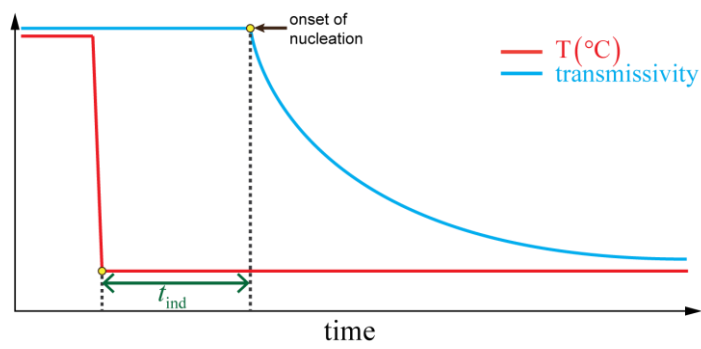
(b) KBHR approach. I compared our results to that of Turner et al<sup>96</sup> who reported the concentration of nucleation sites and interfacial energy between PABA crystal and water.

Both approaches uses the setup in **Figure 6.4a** (based on transmissivity of light to detect crystals) but they employ different mathematical treatment and temperature profile as illustrated in **Figure 6.5**. In induction time approach, the system is cooled quickly to a final temperature which is then kept constant while waiting for the nucleation event (isothermal experiment). Then, the distribution of induction time is fitted with a probability distribution (in this work, Poisson distribution). On the other hand, KBHR approach is deterministic and employs a polythermal experiment to measure the undercooling  $\Delta T_c$  across various cooling rates. The full description of the model is given by Camacho et al.<sup>148</sup>



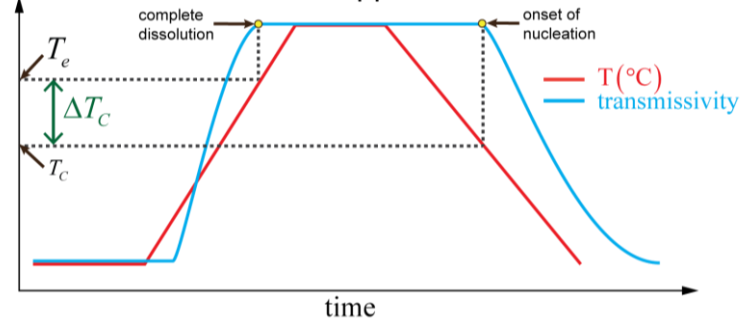
(a)

induction time approach



(b)

KBHR approach

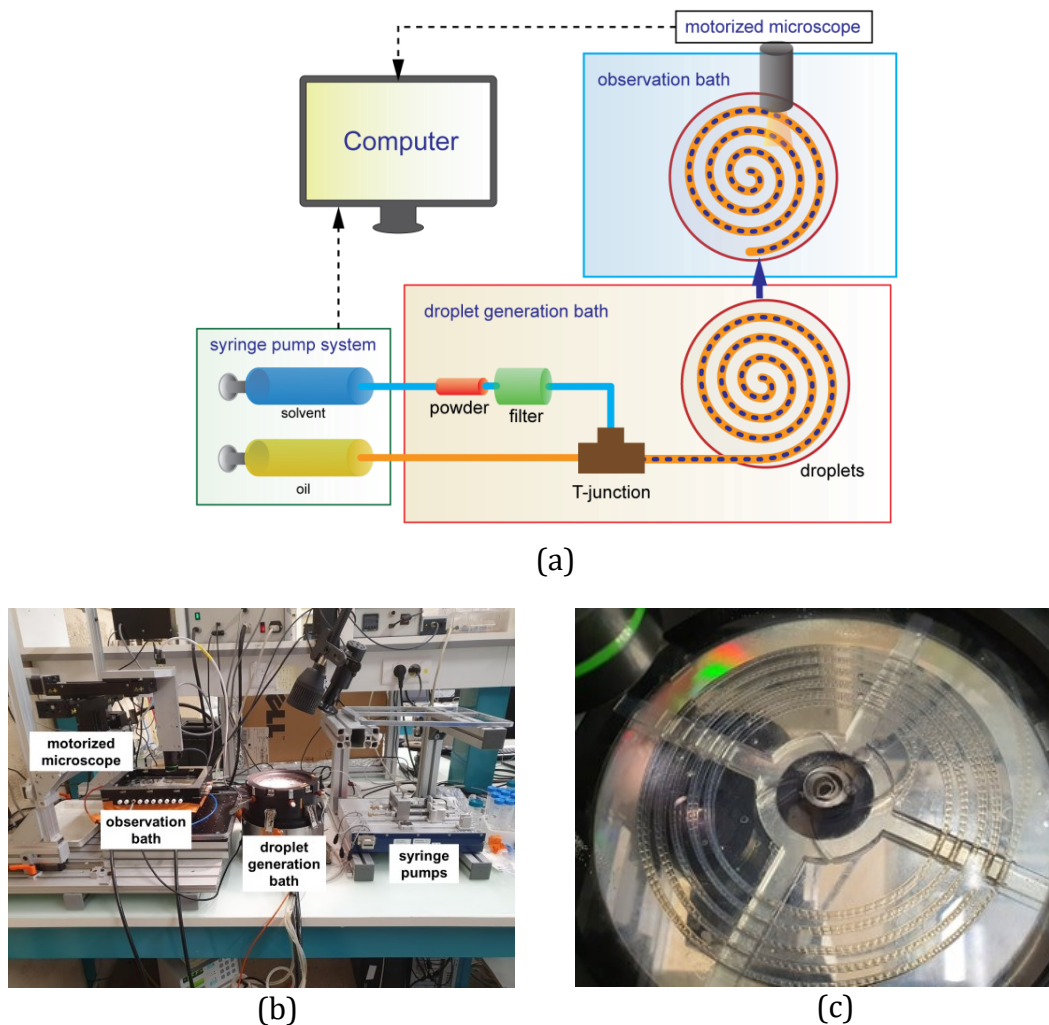


(c)

**Figure 6.4** (a) Schematic illustration of the setup, (b) typical temperature profile and evolution of transmissivity in induction time approach and (c) KBHR approach.

### 6.2.3 Submicroliter Scale

The microfluidic setup is based on the work of Peybernes<sup>61</sup> which is illustrated in **Figure 6.5**. This allows the production of monodisperse supersaturated droplets directly from powder in a thermostatic bath.



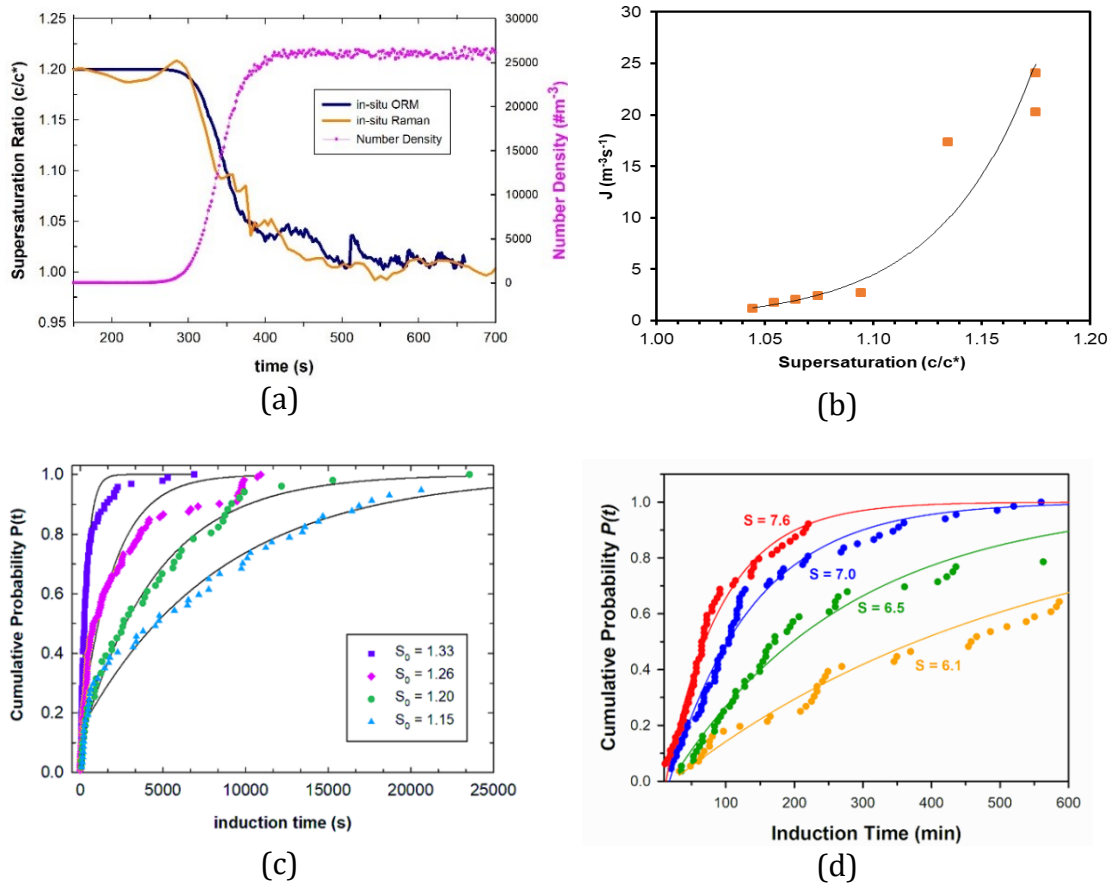
**Figure 6.5** (a) Schematic illustration of the microfluidic setup (b) Image of the microfluidic setup (c) Image of the portable spiral template containing droplets that facilitates the transfer from the generation bath to the observation bath.

Briefly, the solvent flows through the 30-mg powder bed (1-mm inner diameter, 10 cm long) which is connected to a 500-nm filter. Due to the miniature scale, the solvent that passes through the powder bed rapidly reaches equilibrium and so the liquid that comes out from the filter is always saturated.<sup>60</sup> Saturated droplets are then generated by cross-flowing in a T-junction with the continuous phase (GPL106 oil, Kryptox®). Then, supersaturation is generated by quickly transferring

the spiral template (containing droplets) to the observation bath at a much lower temperature (around 10°C). The droplets are then monitored using an xyz-motorized microscope (Opto GmbH). The induction time of 80 droplets (570 nL) were measured by analyzing the time-stamped image sequence.

### 6.3 Results and Discussion

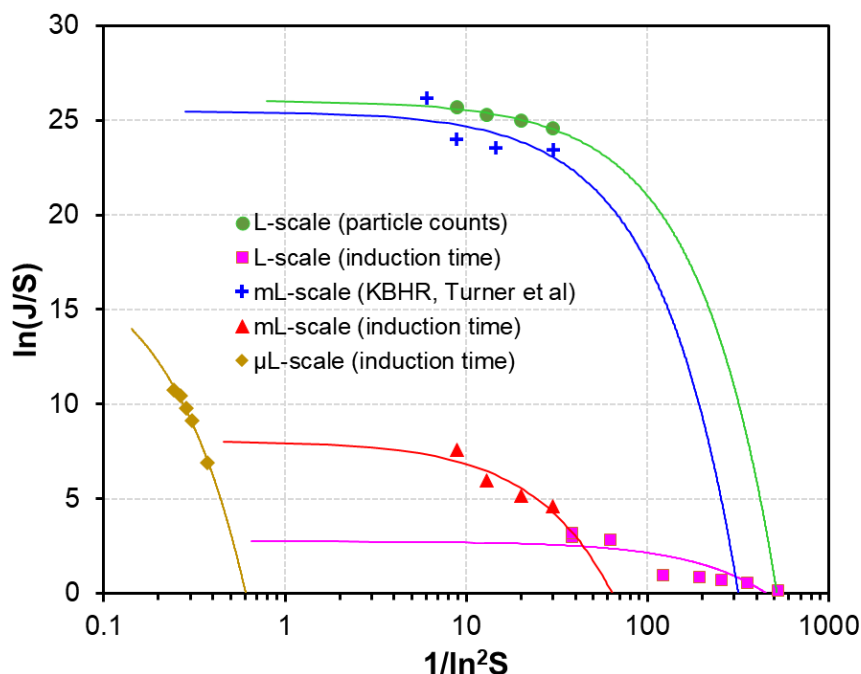
**Figure 6.6** shows the results of the nucleation rate measurement corresponding to each experimental method (shown in Figure 6.1).



**Figure 6.6** Results of nucleation rate measurement corresponding to each experimental method in Figure 6.1. (a) evolution of number density and supersaturation in the liter scale particle count approach (b) nucleation rate as a function of supersaturation based on induction time approach in the liter scale (c) cumulative probability of nucleation as a function of induction time for mL scale (d) cumulative probability of nucleation as a function of induction time in μL scale.

In the liter scale particle-count approach (**Figure 6.6a**), we track the evolution of the number density and supersaturation as a function time. The supersaturation obtained from laser backscattering (via mass balance with particle size and number density) agrees well with Raman spectroscopy measurements, validating our calibration protocol. The experiments were performed at different supersaturations and different agitation rates following the procedure in Chapter 4. In liter scale deterministic induction time approach, we calculated the nucleation rates using  $J = 1/Vt_i$  where  $V$  is the solution volume and  $t_i$  is the induction time and were plotted as a function supersaturation in **Figure 6.6b**. The data points are qualitatively consistent with the fit of classical nucleation theory. Both mL scale (**Figure 6.6c**) and  $\mu$ L scale (**Figure 6.6d**) use the same data treatment which is fitting the induction time distribution with Poisson function from which nucleation rate can be estimated. Notice that in  $\mu$ L scale, very high supersaturation is required since the probability of nucleation is low in small volumes.

Now, we compare the nucleation kinetics obtained across different scales and techniques. In **Figure 6.7**, we see that methods based on induction time results in relatively low nucleation rates compared to KBHR approach and particle counts.



**Figure 6.7** Nucleation rates obtained across various scales and techniques. Data points are fitted with classical nucleation theory.

The estimated kinetic parameters together with additional literature values are summarized in **Table 6.1**. Notice that methods based on induction time have consistently low magnitudes of kinetic pre-exponential factor (less than  $10^6 \text{ m}^{-3}\text{s}^{-1}$ ) while other methods such as that of the particle-count approach and the KBHR analysis are consistent at  $10^{11} \text{ m}^{-3}\text{s}^{-1}$  regardless of the scale. This supports the findings in Chapter 5 which implied that induction time approaches in agitated systems may not be used as reference for industrial scale applications as they inherently give low values of the kinetic prefactor.

**Table 6.1** Fitted nucleation parameters obtained across various scales and techniques. Data points are fitted with classical nucleation theory.

Scale	$A \text{ (m}^{-3}\text{s}^{-1}\text{)}$	$\gamma_{\text{eff}} \text{ (mJ/m}^2\text{)}$	Measured Quantity	Model
L	$2.3 \times 10^{11}$	2.04	Particle Counts (laser backscattering)	Exponential 2° Nucleation vs Agitation
L	44	1.70	Induction Time (conductometry)	$t_i = 1/JV$
mL	$5.5 \times 10^4$	1.76	Induction time (turbidimetry)	Poisson
mL (Sullivan et al.) <sup>69</sup>	$\sim 10^4$	1.33-2.24	Induction time (turbidimetry)	Poisson
mL (Turner et al.) <sup>96</sup>	$\sim 10^{11}$	1.13-2.71	MSZW (turbidimetry)	KBHR
$\mu\text{L}$	$9.4 \times 10^6$	13.7	Induction time (microscopy)	Poisson
$\mu\text{L}$ (Nappo et al) <sup>95</sup>	$\sim 10^5$	-	Induction time (microscopy)	Poisson

On the other hand, all the methods investigated seem to give relatively consistent values of the effective interfacial energy  $\gamma_{\text{eff}}$  between crystal and solution except for the  $\mu\text{L}$  scale which is done at a much higher supersaturation ratio (**Figure 6.7**). The high value of  $\gamma_{\text{eff}}$  is indicative of a high thermodynamic barrier for nucleation. This could be explained by the fact that nucleation in microfluidics require very high supersaturation, thus making homogeneous nucleation the predominant mechanism. This is also because the use of miniature volumes minimizes the presence of impurities and foreign surfaces which can act as heterogeneous



nucleation sites (which can lower the energy barrier). In contrast, if we compare the methods based on induction time, notice that as the volume decreases, the pre-exponential factor  $A$  increases. This can be rationalized from the increase in surface to volume ratio which can favor the heterogeneous mechanism leading to higher pre-exponential factor. As a result, there is a complex interplay between the supersaturation level, the influence of purities, and the surface-to-volume ratio which all impact the measured kinetic parameter.

Overall, as demonstrated by our experimental results in conjunction with literature values, the values of nucleation parameters can be highly sensitive to the measured quantity and the volume scale. The discrepancy could be due to the limitation of the models used in correlating induction time with nucleation rate. Another possibility is the interplay of hydrodynamics (agitation efficiency, presence of turbulence, spatial homogeneity, etc) and heterogeneous nucleation (at the surface of impellers, stirrer bars, baffles, crystallizer walls, etc). The influence of these interfering factors is not well understood nor directly quantifiable. Thus, careful attention must be done in using them as reference in the scale up and design of industrial crystallizers.

## 6.4 Conclusion

In this chapter, I have performed multiple comparison of nucleation kinetics across different scales (L, mL,  $\mu$ L) and measurement techniques (particle counts, deterministic induction time, probabilistic induction time) using *p*-aminobenzoic acid in water/ethanol as a model system. Upon comparing my results together with literature data, I have shown that measurements across different scales and techniques can lead to significantly different values of nucleation kinetic parameters. The pre-exponential factor  $A$  is highly dependent on the measurement technique and model assumptions while the effective interfacial energy  $\gamma_{eff}$  between crystal and solution is dependent on the supersaturation level and system volume. This suggests that in the design of industrial crystallizers, careful attention must be done in terms of the transferability and scalability of kinetic data. Aside from the differences in the model assumptions, I hypothesize that the observed discrepancies could be due to two practical reasons: (1) limitations of existing models in correlating induction time and nucleation rate (2) differences in foreign surfaces and fluid dynamics. In agitated systems, the influence of the foreign surfaces (impellers, crystallizer walls, baffles, analytical probes, impurities) which could act as heterogeneous nucleation sites are not well-characterized. Moreover, the impact of fluid dynamics on nucleation mechanisms is currently not well-understood quantitatively. This highlights that more research is needed to fully understand the influence of interfering variables (fluid dynamics, surfaces, etc) in order to compare nucleation kinetic measurements obtained across different scales and techniques. Consequently, if we intend to study the fundamentals of nucleation, an experiment that minimizes the interference of hydrodynamics, impurities, and uncharacterized surfaces would be needed. This can be achieved using stagnant microfluidics, which will be the subject of the next three chapters.

## Chapter 7

### Probing Nucleation in Microdroplets via Image Analysis: Effect of Diffusive Interactions

In the previous chapters, I have focused on the quantification of nucleation kinetics in the context of industrial crystallizers where agitation is required. I have shown that careful attention must be made in the interpretation of scalability and transferability of kinetic data. This is partly due to the influence of fluid dynamics (agitation speed, turbulence) and foreign surfaces (crystallizer walls, impellers, baffles) which results in a complex interplay of homogeneous nucleation, heterogeneous nucleation, and secondary nucleation. Thus, if we intend to study homogeneous primary nucleation at a more fundamental level, there is a need to minimize the effect of other interfering mechanisms. This can be achieved using stagnant microfluidic systems. Studies have shown that in microdroplets surrounded by hydrophobic surfaces, nucleation tends to occur at the center and not on the droplet-oil interface, thereby promoting the homogeneous nucleation mechanism. In this chapter, I studied the nucleation kinetics of aqueous NaCl using our in-house developed microfluidic setup. To investigate the effect of diffusive interactions between microdroplets, I improved the existing numerical approach for automated detection and characterization of the interactions via image analysis. This allowed the classification of each microdroplets in terms of number of interactions. I also highlight that this method can detect minuscule diffusion-mediated interactions, which would be otherwise unobservable using traditional microscopy techniques. Furthermore, I show that failure to account for these interactions in the analysis of kinetic data can lead to severe inaccuracies in the estimated nucleation parameter. Moreover, with the help of our in-house developed humidity regulation module, I show that diffusion interactions disappear at low relative humidity.

*Parts of this chapter are in preparation for submission to **Crystal Growth & Design** as:*

**Cedeno, R.;** Grossier, R.; Lagaize, M.; Candoni, N.; Flood, A.; Veessler, S.,  
Nucleation in Sessile Microdroplets: New Approach for Measuring Induction  
Time.

## 7.1 Introduction

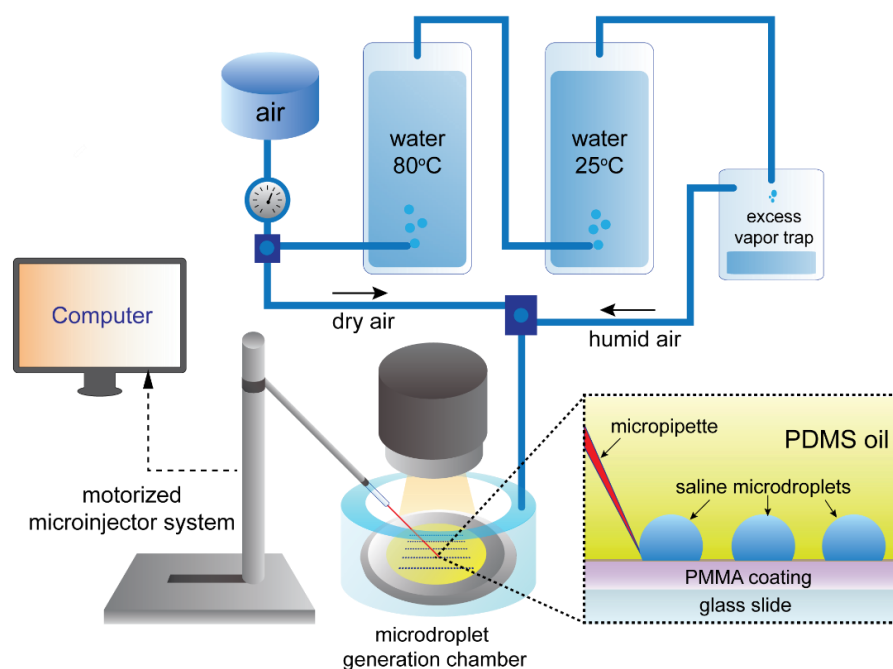
The complex interplay of homogeneous, heterogeneous, and secondary nucleation makes it difficult to study the fundamental aspects of primary nucleation in agitated systems where the effect of hydrodynamics and foreign surfaces are not directly quantifiable. Moreover, nucleation is inherently stochastic, that is, a statistical analysis of numerous independent experiments is needed in quantifying nucleation kinetics. To study primary nucleation at a more fundamental level, we address the aforementioned issues by developing a microfluidic setup allowing facile generation of monodisperse arrays of sessile microdroplets, immersed in an oil film, which can serve as evaporative microcrystallizers.<sup>63</sup> Our previous work has shown that the standard deviation of the grey-level pixels  $\sigma$  is a useful parameter in probing the microdroplet dynamics, particularly the onset of nucleation.<sup>21</sup> It has also been illustrated that although spatial heterogeneity in evaporation rates exists among droplets, a reproducible statistical distribution of nucleation times can be obtained upon appropriate normalization.

While the experimental protocol described is a promising approach for nucleation studies, it has been observed that droplets can interact with other droplets. This is because when one droplet crystallizes, water diffuses to the neighboring droplet due to differences in chemical potentials. This leads to nucleation events that are not completely independent from each other. In this work, we show that by analyzing the oscillations in the  $\sigma$ -curves, we can account for these diffusion-driven interactions leading to reliable measurement of induction time distributions. Here, we also demonstrate that failure to account for these diffusive interactions can lead to large errors in the estimated nucleation kinetic parameters. However, given that the droplets that are affected by such interfering interaction must be excluded, the statistical quality of the measured independent nucleation events is reduced. To address this, we incorporated a humidity regulation module to our setup. We show that by lowering the relative humidity, the diffusive interactions disappear allowing the use of all the droplet population for analysis.

## 7.2 Materials and Methods

### 7.2.1 Details of Instrumentation

The setup used in the microdroplet generation together with its humidity control module is illustrated in **Figure 7.1**.



**Figure 7.1** Schematic diagram of the microdroplet generation system with humidity control module.

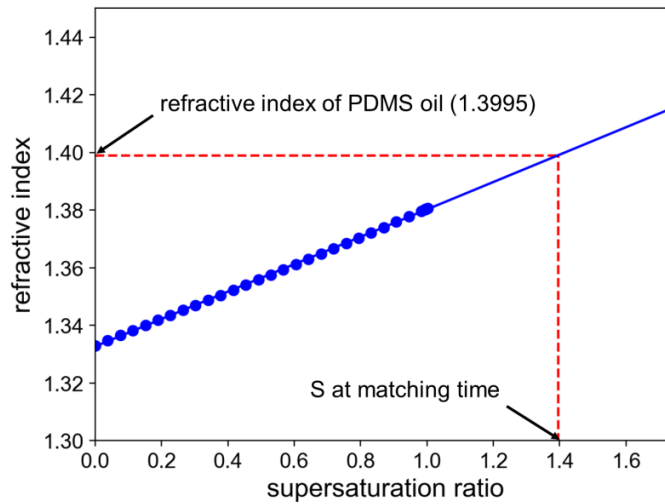
To avoid microdroplet spreading and coalescence, we coated the glass cover slip with a hydrophobic PMMA resin. For this, glass coverslips (18-mm diameter, cleaned via plasma treatment) were spincoated at 4000 rpm for 1 min (SPIN 150, SPS) with PMMA which were then annealed for 10 min at 170°C. The coverslips were then covered with a 0.8 mm thick layer of PDMS oil. The saline microdroplets were generated on the cover slip by a micropipette with an internal diameter of 0.5  $\mu\text{m}$  (Femtotip Eppendorf). The micropipette is mechanically controlled by a home-made motorized micromanipulator consisting of 3 miniature translation stages (piezo electric, MS30 Mechnics) which allows displacement of the micropipette holder in three dimensions by steps of 16 nm. A series of 16-bit images were obtained using an optical microscope (Zeiss Axio Observer D1 equipped with an ANDOR neo sCMOS camera). Images were processed using FIJI software (Image J, NIH, USA) which calculates  $\sigma$  for each region containing microdroplets. A detailed description of this procedure has been presented previously<sup>63</sup> while the details of the chemical products are shown in **Table 7.1**

**Table 7.1** Details of chemical products

Product	Vendor	Properties
Sodium chloride, NaCl	R.P Normapur ®	Purity = 99.5% Refractive index = 1.5442
Polymethylmethacrylate, PMMA	ALLRESIST GmbH	Molecular weight= 950,000 g/mol Refractive index = 1.395
Polydimethylsiloxane, PDMS oil	Alfa Aesar	Molecular weight = 1250 g/mol Viscosity = 10 cSt Refractive index = 1.3990
Ultrapure water	via Milli-Q Purifier	resistivity = 18.2 M $\Omega$ ·cm TOC value < 5 ppb

### 7.2.2 Microdroplet Generation

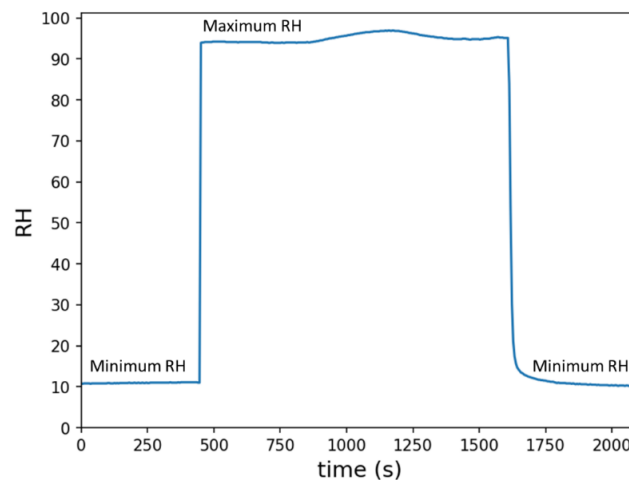
We generated arrays of 20 pL microdroplets on a polymethylmethacrylate (PMMA) surface, with droplets submerged in 0.8 mm thick polydimethylsiloxane (PDMS) oil (10 cSt) using the method described in Ref<sup>63</sup>. The saline droplets (initially at 4.9 M NaCl) were allowed to evaporate at a relative humidity (RH) of 63%. Sessile microdroplets were then observed under a transmission optical microscope. Snapshots were taken every 4 s for 80 minutes and images were analyzed using the procedure of Grossier et al<sup>21</sup>. Briefly, the standard deviation of the gray-level pixels  $\sigma$  of the microdroplet image is probed. This parameter is related to the absolute difference in refractive index between the droplet and the oil  $|\Delta n|$  which in turn is a function of droplet's solute concentration. When  $|\Delta n| = 0$  (oil and droplet refractive index match, which occurs when the supersaturation ratio  $S = 1.395$  for aqueous NaCl solutions as shown in **Figure 7.2**), the droplet optically disappears and this corresponds to a minimum  $\sigma$ . Concentrations lower or higher than  $S = 1.395$  would therefore lead to an increase in  $\sigma$ . At nucleation, a sudden change in refractive index occurs leading to a highly observable “jump” in the  $\sigma$ -curve. Thus, it can be efficiently used to measure induction time.



**Figure 7.2** Refractive index as a function of supersaturation ratio. The refractive index of the droplet matches that of the PDMS oil at  $S = 1.395$ .

### 7.2.3 Humidity Regulation

Air is pumped and passes through a series of water bath (80°C and 25°C) and then the excess vapor is collected in a vessel (**Figure 7.1**). To assess the speed at which the humidity can be changed in our humidification system, we measured the RH in the microdroplet generation chamber with “dry” air (directly obtained from compressed air pipelines) and our humid air as shown in **Figure 7.3**. This suggests that our humidity control system can almost instantaneously change the RH of our microdroplet generation chamber (negligible lag period). We also show we can maintain a reasonably stable RH as needed.



**Figure 7.3** Assessment of the humidity regulation module showing a minimum and maximum RH of 10% and 95% respectively.


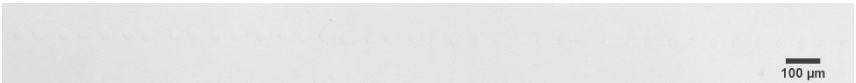

### 7.2.4 Numerical Detection of Oscillations

In the time interval between matching time  $t_m$  and nucleation time  $t_n$ , we applied a Savitzky-Golay smoothing filter to remove tiny oscillations due to random noise. To obtain the number of oscillations, we used the signal-processing algorithm of Du et al<sup>149</sup>.

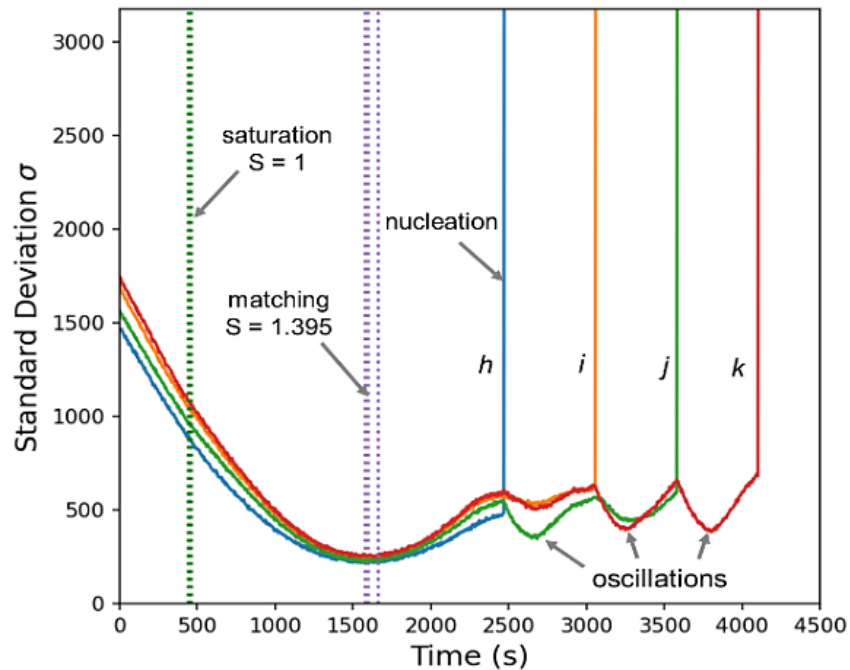
## 7.3 Results and Discussion

The typical microdroplet images for specific times are shown in **Table 7.2** and the plot of  $\sigma$  with time of four representative microdroplets is shown in **Figure 7.4**. As the monodisperse microdroplets evaporate, their concentration increases until the supersaturation ratio reaches 1.395 where the refractive index of the droplet matches that of the oil making it optically disappear. This point (at 25 min) corresponds to the minimum in the  $\sigma$ -curve (**Figure 7.4**). As it continues to evaporate, its concentration departs from  $S = 1.395$  so  $\sigma$  starts to increase until a sudden “jump” occurs indicating the occurrence of nucleation.

Table 7.2 Typical microdroplet images at  $t = 0, 25, 80$  min.

time (min)	S	Microdroplet Image
0	0.80	
25	1.395	
80	--	



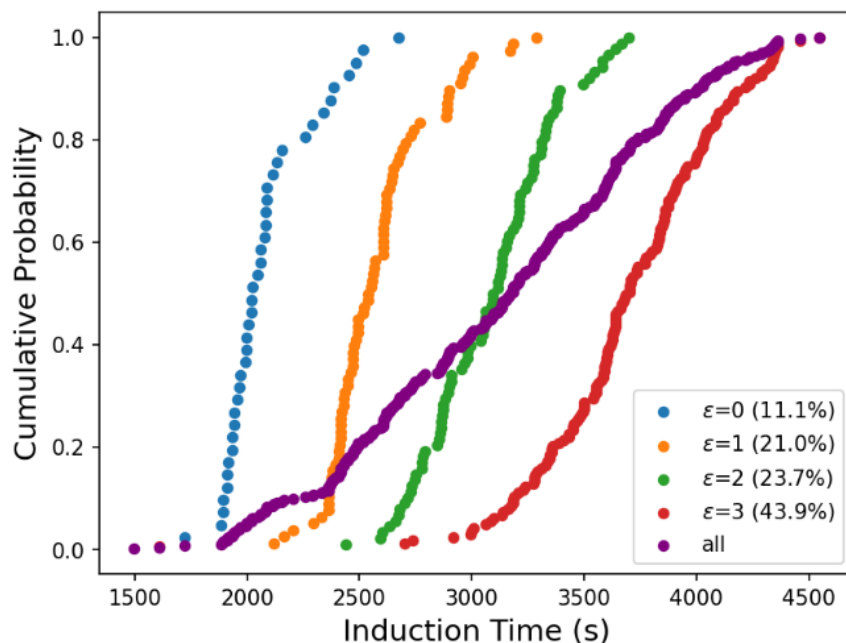


**Figure 7.4** Evolution of  $\sigma$  of 4 neighbouring microdroplets denoted as droplet  $h,i,j,k$

### 7.3.1 Effect of Diffusive Interactions

Due to the stochasticity of nucleation, droplets are not expected to nucleate at the same time. However, we have observed that induction time tends to systematically increase due to the presence of oscillations (waves) in the  $\sigma$  curve prior to nucleation. This oscillations are in fact due to the oscillations in droplet concentration because of the diffusion of water from already nucleated droplets nearby<sup>21</sup>. For instance, in the four consecutive droplets in **Figure 7.4**, droplet  $k$  has 3 oscillations prior to nucleation, and it is the slowest while droplet  $h$  with no oscillation is the fastest.

To verify this trend, we plot the cumulative probability distribution of 370 microdroplets as a function of induction time in **Figure 7.5**



**Figure 7.5** Cumulative probability of nucleation as a function of induction time, classified according to number of sigma-oscillations, for the all arrays (370 microdroplets).

We clearly see that more oscillations lead to longer induction time. For nucleation kinetic studies, only droplets with no oscillations must be considered for analysis to obtain a meaningful distribution of independent nucleation events. This suggests that when one fails to account for these interactions, one would end up with a completely different curve (the purple curve in **Figure 7.5**) which would result in inaccurate estimation of kinetic parameters. For example, the mean induction time for independent droplets (75 out of 370) is 44 min while that of the entire sample is around 59 min.

To exemplify the importance of accounting the diffusive interactions, let's assume a constant evaporation rate.<sup>150</sup> Under this assumption, we calculated the mean supersaturation at nucleation  $S_n$  and the nucleation rate  $J$  and the results are shown in **Table 7.3**. The calculated supersaturation ratio at nucleation would then be 2.35 for independent droplets (no oscillations), and would be 5.07 if we analyze the entire sample; this is an unphysically large value of  $S$ . In reality however, the evaporation rate is not constant due to the reduction of water activity at high concentrations.

**Table 7.3** Comparison of mean supersaturation at nucleation, nucleation rate, and interfacial energy between crystal and solution with no  $\sigma$ -oscillations ( $\varepsilon = 0$ ) against that of all data set

	$\varepsilon = 0$ (unperturbed)	all data set
Mean S at nucleation, $S_n$	2.35	5.07
Nucleation Rate, $J$	$6 \times 10^{10} \text{ m}^{-3}\text{s}^{-1}$	$8 \times 10^{10} \text{ m}^{-3}\text{s}^{-1}$

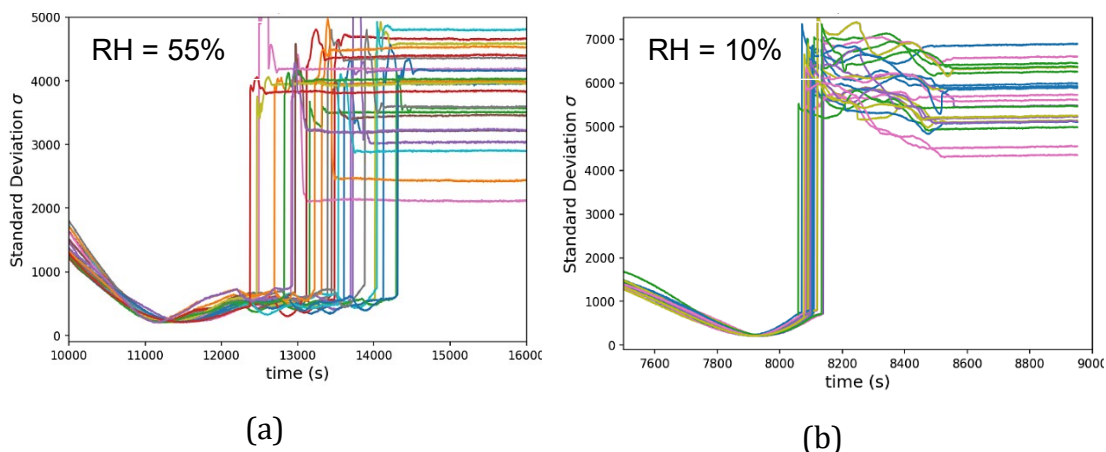
Nevertheless, the large discrepancy in the measured mean induction time and the predicted supersaturation ratio illustrates the significance of accounting the diffusive interactions in the data treatment. Since the change in volume due to water diffusion is too small compared to the optical resolution, these interactions are unobservable in traditional microscopy techniques however as we show here, it can be easily detected as oscillations in our  $\sigma$ -curve analysis. With our image analysis protocol, this is clearly visible leading to a reliable induction time distribution measurement.

### 7.3.2 Eliminating Diffusive Interactions

As mentioned earlier, due to diffusive interactions, some of data points must be eliminated in the analysis which consequently reduces the statistical quality of the estimated nucleation parameter. For instance, in the example shown, only 11% of the microdroplets are usable for the subsequent analysis. Therefore, there is a need to eliminate the interfering diffusion-mediated interactions. In principle, this can be addressed by maximizing the separation distance between droplets. However, with our current setup, although the droplet size can be controlled by adjusting the injection pressure and the translation speed of the micropipette, there is no direct option to control the separation distance of each droplet. One plausible option would be to generate large droplets with very low concentrations so it would have to considerably decrease in size before nucleation (thereby increasing separation distance at nucleation). However, as more water needs to diffuse from the droplet to the oil medium, this could introduce a considerable change in local humidity whose impact on evaporation rate is not easily quantifiable.

Our solution is to lower the relative humidity RH which increases the driving force for evaporation. The idea is that when water diffuses out of the nucleated microdroplet, the low RH at the oil-air interface would enhance the diffusion upward (into the air) thereby preventing the accumulation of water in the oil phase. In other words, the driving force for evaporation would be high enough to prevent water vapor from diffusing to neighboring droplets. To verify this, we

performed a similar with experiment but at different RH. If the diffusive interactions were absent, there should be no observable oscillations in the  $\sigma$ -curve prior to nucleation. Thus, we compared the  $\sigma$ -curves for experiments at 55% RH and at 10% RH in **Figure 7.6**. Indeed, the result confirms the successful elimination of the diffusion-mediated interactions.



**Figure 7.6** Evolution of  $\sigma$  for 25 randomly selected microdroplets that corresponds to different relative humidity RH (a) RH = 55% and (b) RH = 10%. The  $\sigma$  oscillations prior to nucleation disappear at low relative humidity.

Note that this has an important implication. By eliminating the interfering interactions, there will be no need to discard data points so all the experimental points can be used for subsequent analysis.

## 7.4 Conclusion

In this chapter, I investigated the diffusive interactions of saline microdroplets under PDMS oil. I have shown that diffusion-mediated interactions between evaporating microdroplets must be accounted for in estimating nucleation kinetic parameters, that is, only the population of droplets that are not affected by such interaction must be used in the analysis. Failure to account for diffusive interactions can result in severe inaccuracies in the measured nucleation kinetic parameters. However, this procedure consequently reduces the number of usable droplets because majority of the microdroplets would have to be excluded (90%). To address this, I have shown that the interfering interactions can be achieved by lowering the relative humidity to 10%. As a result, 100% of the microdroplet population can be used for the quantification of nucleation kinetics.

## Chapter 8

### Nucleation in Sessile Microdroplets: Measuring Induction Time via Deliquescence-Efflorescence Cycle

In the previous chapter, I have demonstrated that failure to account for diffusive interactions can lead to huge errors in nucleation parameter estimation; fortunately, its interference can be eliminated by lowering the relative humidity. In order to quantify nucleation kinetics in these systems, induction time must be defined properly. For crash cooling experiments, induction time is measured by setting the time zero as the point in which the final temperature is achieved. Similarly, for antisolvent experiments, the time zero is set at the time at which the final supersaturation is reached. However, for evaporative crystallization, the final supersaturation is not fixed since it evolves continuously with time. Thus, to measure induction time, the time zero must be defined at the point in which the solution is saturated and thus has the possibility to nucleate. Otherwise, the measured induction time would be highly sensitive to the arbitrarily chosen initial concentration, i.e. more dilute starting solution would systematically take more time to reach the nucleation zone. Indeed, in evaporating system, induction time must be taken as the difference between the time to reach the nucleation point  $t_n$  and the time to reach the saturated solution  $t_{sat}$ . However, in the image analysis approach presented in the previous chapter, the time at which the microdroplet reaches saturation is experimentally inaccessible (without assuming a model of evaporation rate). In this chapter, I address this by developing a new protocol for measuring induction time via deliquescence-efflorescence cycle.

*Parts of this chapter are in preparation for submission to **Crystal Growth & Design** as:*

**Cedeno, R.;** Grossier, R.; Nerini, D.; Lagaize, M.; Candoni, N.; Flood, A.; Veessler, S., Nucleation in Sessile Microdroplets: New Approach for Measuring Induction Time.

## 8.1 Introduction

Nucleation is the step that determines how long we must wait before the appearance of a stable crystal cluster in a supersaturated solution.<sup>41</sup> This “waiting time” is referred to as induction time which is a function of the nucleation rate and the system volume. Most induction time measurements are carried out at constant supersaturation for the sake of simplicity of data interpretation and modeling.<sup>41</sup> However, in reality, most nucleation processes occur at varying supersaturation, either by cooling, antisolvent, or evaporative crystallization.<sup>45</sup> Thus, a thorough understanding of the nucleation kinetics of such systems is important.

Due to the stochastic nature of nucleation, a statistical analysis of numerous independent induction times is needed to quantify nucleation kinetics. This can be addressed by using droplet microfluidics which allows multiple simultaneous independent experiments with a very small amount of material.<sup>57</sup> In the context of experiments with time-varying supersaturation, induction time can be defined as the “waiting time” starting from the moment the solution exceeds the saturated state<sup>45</sup> since nucleation cannot occur in undersaturated systems. For this reason, the time evolution of system concentration is required in the data treatment. In large volumes, this is done conveniently by measuring the temperature or concentration profile using standard probes and process-analytical tools. Unfortunately, in evaporative microdroplet experiments the determination of concentration and the time at which the system is saturated often requires assuming a specific value of evaporation rate which depends on the complex interplay of several factors such as humidity, droplet size, contact angle, etc.<sup>67, 151</sup>

Previously, we have shown that a simple and efficient digital-image processing method based on the standard deviation of the grey-level pixels of a single microdroplet and its immediate vicinity (denoted as  $\sigma$ ) is useful in probing the microdroplet dynamics, particularly the onset of nucleation<sup>21, 152</sup>. In order to conveniently quantify nucleation kinetics in these systems, other issues must be addressed. First, each droplet is generated sequentially so the initial time for each droplet is different leading to additional complications in the data analysis. Second, considering that induction time  $t_{\text{ind}}$  is the “waiting time” for nucleation in a supersaturated solution, it can be defined as the difference between the time to reach the nucleation point  $t_n$  and the time to reach the saturated solution  $t_{\text{sat}}$ .

$$t_{\text{ind}} = t_n - t_{\text{sat}} \quad (8.1)$$

However, in the previous protocol, the time at which the microdroplet becomes saturated  $t_{\text{sat}}$  is experimentally inaccessible, yet it is needed in defining induction time.

In this chapter, I develop a new approach to measure induction time by performing a deliquescence-efflorescence cycle. Then using our measured induction times, we show that our estimated interfacial energy  $\gamma$  (between crystal and solution) for NaCl-brine system is consistent with literature values.

## 8.2 Materials and Methods

As described in our previous work,<sup>21</sup> we used the gray-level pixel standard deviation  $\sigma$  of the microdroplet image to track the microdroplet dynamics. Following this approach, we employed a mechanically controlled micropipette to generate arrays of monodisperse aqueous NaCl microdroplets (1.7 M) on the surface of a PMMA-coated glass slide immersed in a 0.4mm-thick layer of PDMS oil (10 cSt).

As mentioned, the time at which nucleation occurs can be easily measured but the time at which the solution is saturated could not be accessed experimentally. To address this, our approach here takes advantage of the deliquescent nature of NaCl. In principle, when the prevailing relative humidity RH is less than the deliquescence point  $RH_0$  (75% for NaCl at 25°C), water evaporates from the droplet. Conversely, when  $RH > RH_0$ , NaCl crystals would absorb water until complete dissolution (saturated solution) which is observable in the  $\sigma$ ,  $t$ -curve.

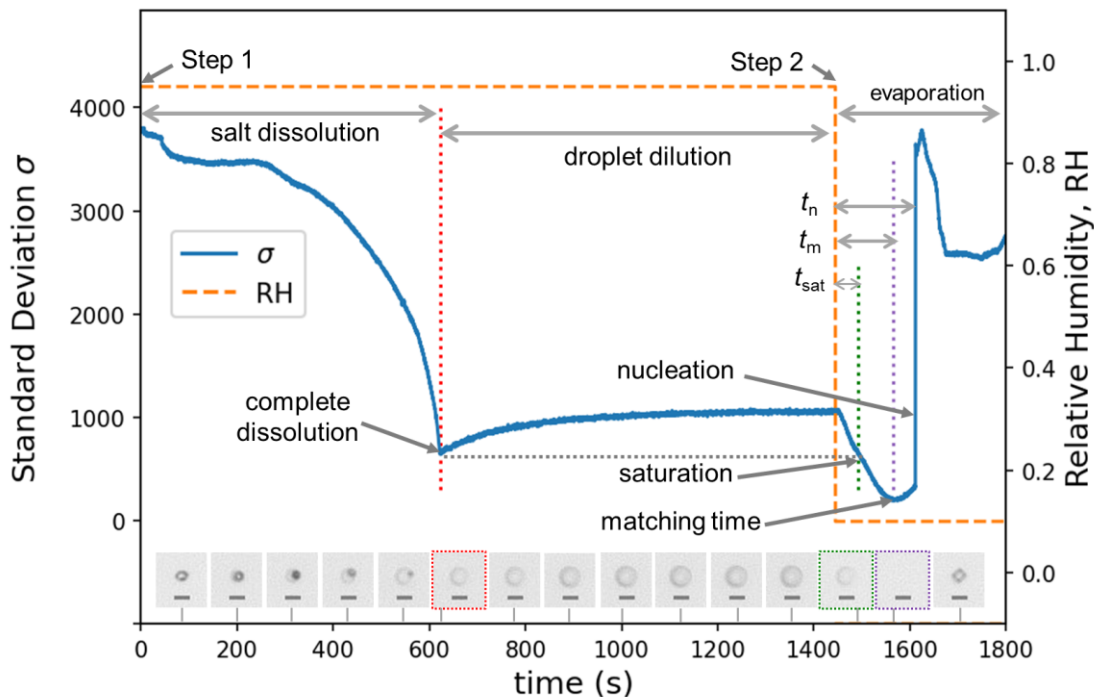
To measure the induction time, we performed three steps. In the preliminary step, we generated monodisperse arrays of undersaturated NaCl microdroplets which were then allowed to evaporate at 10% RH until crystallization. Then in Step 1, we raised RH to 95% so crystals could absorb moisture until complete dissolution. We then let the microdroplets absorb more water to make it undersaturated. Finally, in Step 2, we decreased RH to 10% to allow microdroplets to evaporate and eventually crystallize.

Although it is possible to directly generate undersaturated microdroplets to begin the nucleation experiment<sup>153</sup>, we decided to employ crystallization-dissolution steps for two reasons. First, with direct generation, droplets are formed sequentially so each droplet would have had different initial time that needs to be accounted for. Second, crystallization-dissolution steps allow us to measure the exact time at which the droplet is saturated, information which is essential to calculate the induction time.

## 8.3 Results and Discussion

### 8.3.1 Analysis of $\sigma$ -curves

The typical time evolution of the grey-level pixel standard deviation  $\sigma$  of microdroplets starting from Step 1 is shown in **Figure 8.1**.



**Figure 8.1** Typical time evolution of the  $\sigma$ -curve (in blue) during an experiment where the RH (in orange) is stepped to create a cycle of deliquescence and efflorescence. The corresponding images in each specific time points are shown (scale bar = 20  $\mu\text{m}$ ).

From the perspective of image analysis,  $\sigma$  is a sophisticated function of multiple parameters. Since we are dealing with simple circular microdroplets, we interpret  $\sigma$  as a function of two main factors: refractive index difference  $|\Delta n|$  between the microdroplet and oil (a function of microdroplet concentration) and microdroplet size. When  $|\Delta n| = 0$ , (i.e. oil and microdroplet refractive index match), the droplet optically disappears and this corresponds to a minimum  $\sigma$ : this is the standard deviation of the optical noise of the system (matching time in Figure 2a). For the NaCl-water system at ambient conditions, this occurs at a supersaturation ratio  $S$  of 1.395. Concentrations lower or higher than  $S = 1.395$  would therefore lead to an increase in  $\sigma$ . When microdroplets increase in size, more pixels could “contribute” to the histogram which also leads to an increase in  $\sigma$ .

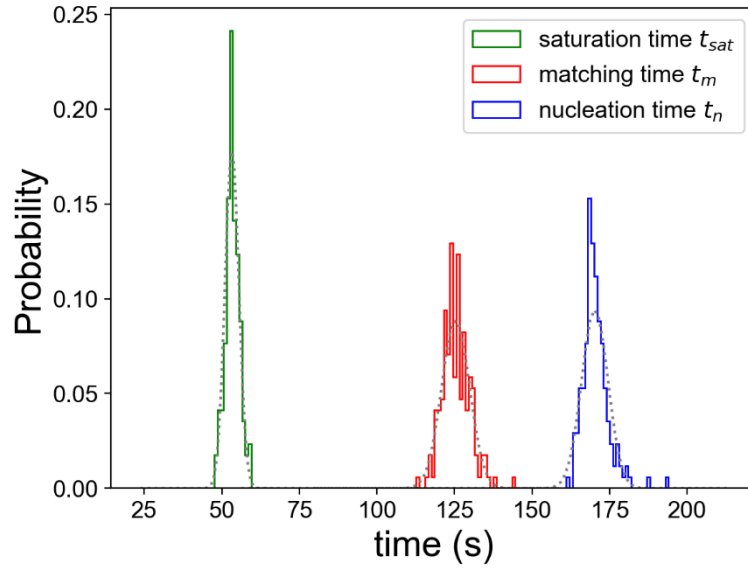


Since solid crystals generally have higher refractive index (appear darker) than liquids, the conversion of NaCl crystal to saturated solution leads to a decrease in  $|\Delta n|$  and thus a decrease in  $\sigma$  until complete dissolution. Note that within the time interval before complete dissolution, the liquid is in equilibrium with the solid phase so the bulk solution concentration remains saturated.<sup>154</sup> This suggests that the refractive index matching ( $|\Delta n| = 0$ ) cannot occur before complete dissolution.

When all solids have dissolved, the microdroplet concentration decreases (causing an increase in the  $|\Delta n|$ ) and its size increases as it continues to absorb more moisture: both of these lead to a rise in  $\sigma$ . As a result, the point of complete dissolution corresponds to the first cusp in the  $\sigma$ -plot (marked by a red vertical line in **Figure 8.1**). From this point, the resulting saturated microdroplet continues to absorb water and undergoes dilution thus becoming undersaturated. Note that for this experiment, it is important to choose an oil that has a refractive index higher than that of the saturated solution to ensure the formation of cusp at complete dissolution.

In Step 2, the undersaturated microdroplet started to evaporate until it reforms a saturated solution. At first glance, the determination of  $t_{\text{sat}}$  is not straightforward since it does not correspond to any peak, maxima, or minima in  $\sigma$ -curves during the evaporation step. To circumvent this, we take advantage of the presence of a cusp in  $\sigma$ -plot occurring at complete dissolution (step 1) in which the solution is at equilibrium. We, thus, use this value of  $\sigma$  as an indicator of droplet's concentration to approximate  $t_{\text{sat}}$  during step 2 (marked by a dashed green line in **Figure 8.1**). This is because the two parameters that determine the  $\sigma$ -value (droplet size and  $|\Delta n|$ ) must be equivalent since the concentration and the geometry of the droplet are essentially the same. After which, evaporation continued until the refractive index of the drop matched that of the oil (the minima in the  $\sigma$ -curve marked by a purple dashed line in **Figure 8.1**). Eventually, it nucleated which led to a sudden change in refractive index. This corresponds to a jump in the  $\sigma$ -curve which then reaches a plateau.

Since nucleation is stochastic, we performed a similar procedure to 175 independent microdroplets and the resulting histogram of saturation time, matching time, and nucleation time is shown in **Figure 8.2**.



**Figure 8.2** Histograms of saturation time  $t_{sat}$ , matching time  $t_m$ , and nucleation time  $t_n$  fitted with Gaussian curves.

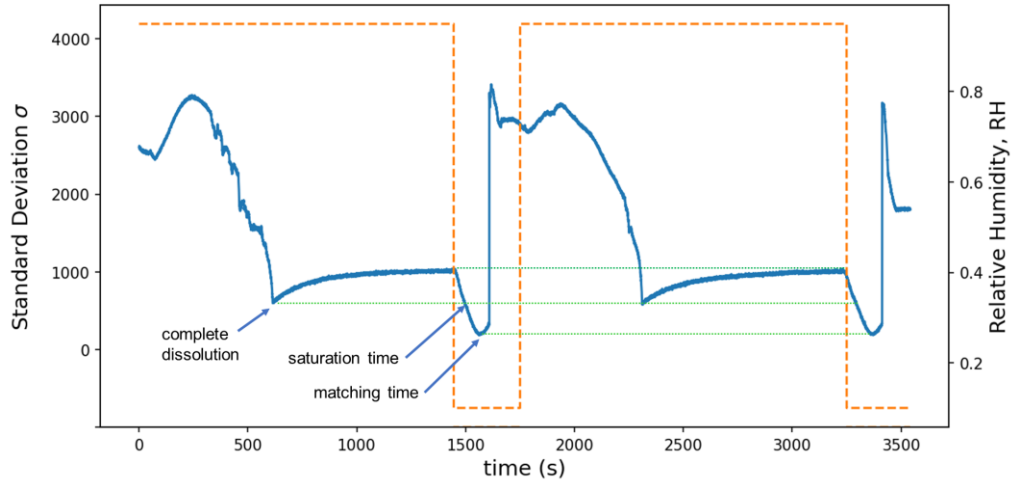
In evaporative crystallization where supersaturation varies with time, it is more convenient to analyze the distribution of supersaturation ratios during the onset of nucleation<sup>6</sup> as it has more tangible physical meaning than the induction time itself. To do this, a commonly used assumption is that the evaporation rate remains constant so that the volume decreases linearly with time<sup>45</sup>. Since volume is inversely proportional to supersaturation, we can calculate the supersaturation ratio at nucleation  $S_n$  using the values of saturation time  $t_{sat}$ , matching time  $t_m$ , and nucleation time  $t_n$ , by simple linear extrapolation with equilibrium supersaturation ( $S_{sat} = 1$ ) and matching time supersaturation ( $S_m = 1.395$ ). Note that this is just an approximation since in principle, water activity decreases as the salt concentration increases.

$$\frac{\left(\frac{1}{S_n} - \frac{1}{S_{sat}}\right)}{t_n - t_{sat}} = \frac{\left(\frac{1}{S_m} - \frac{1}{S_{sat}}\right)}{t_m - t_{sat}} \quad (8.2)$$

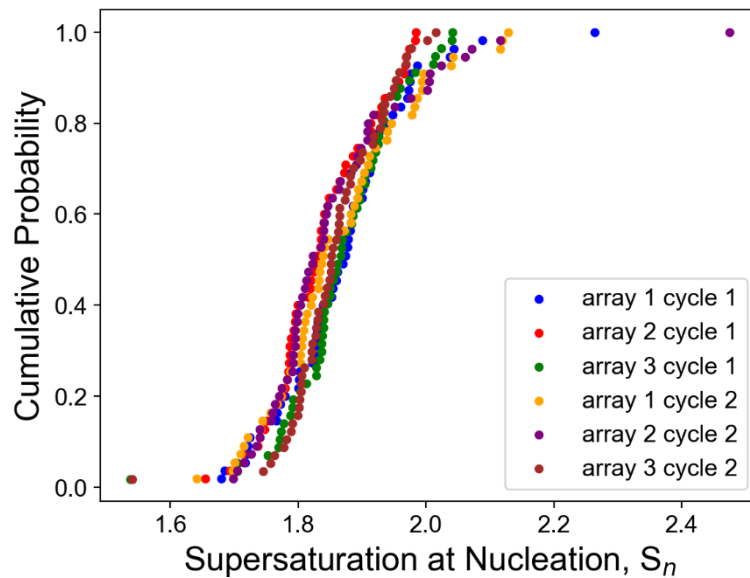
### 8.3.2 Assessment of Reproducibility

To verify the reproducibility of our method, we repeated the same procedure for a second cycle i.e., after the induction time measurement in the first cycle, the crystals were redissolved by deliquescence and then recrystallized. The humidity profile and the evolution of  $\sigma$  for a typical microdroplet is shown in **Figure 8.3** which confirms the reproducibility of using  $\sigma$  as an indicator of droplet concentration.

With this two-cycle experiment, we plot the cumulative distribution of supersaturation ratio of three different arrays of microdroplets in **Figure 8.4**.



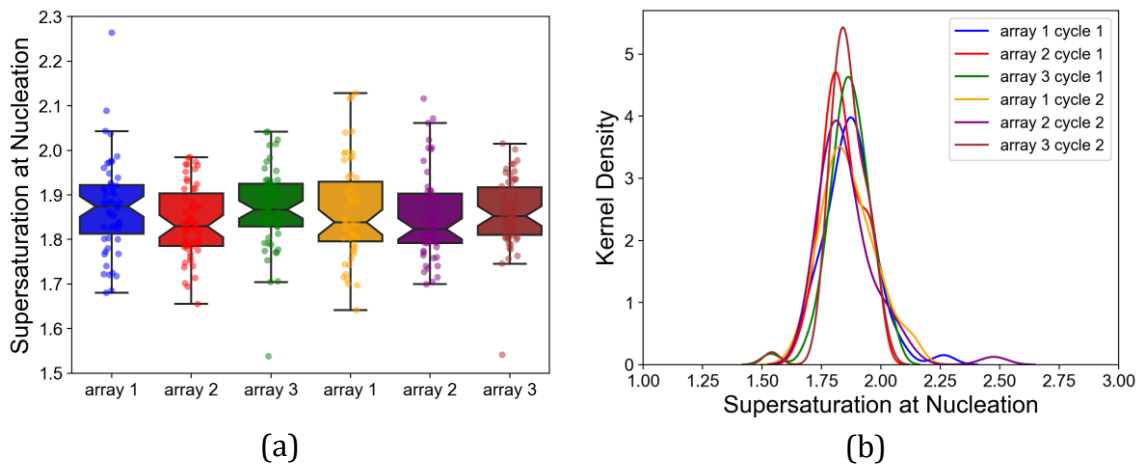
**Figure 8.3** Evolution of  $\sigma$ -curve in a two-cycle experiment. Observe that the  $\sigma$ -value for complete dissolution and matching time for both cycles are the same which confirms the validity of using  $\sigma$  as a “calibration reference” for measuring the saturation time.



**Figure 8.4** Cumulative probability distribution as a function of the dimensionless induction time. Each array contains around 56 microdroplets.

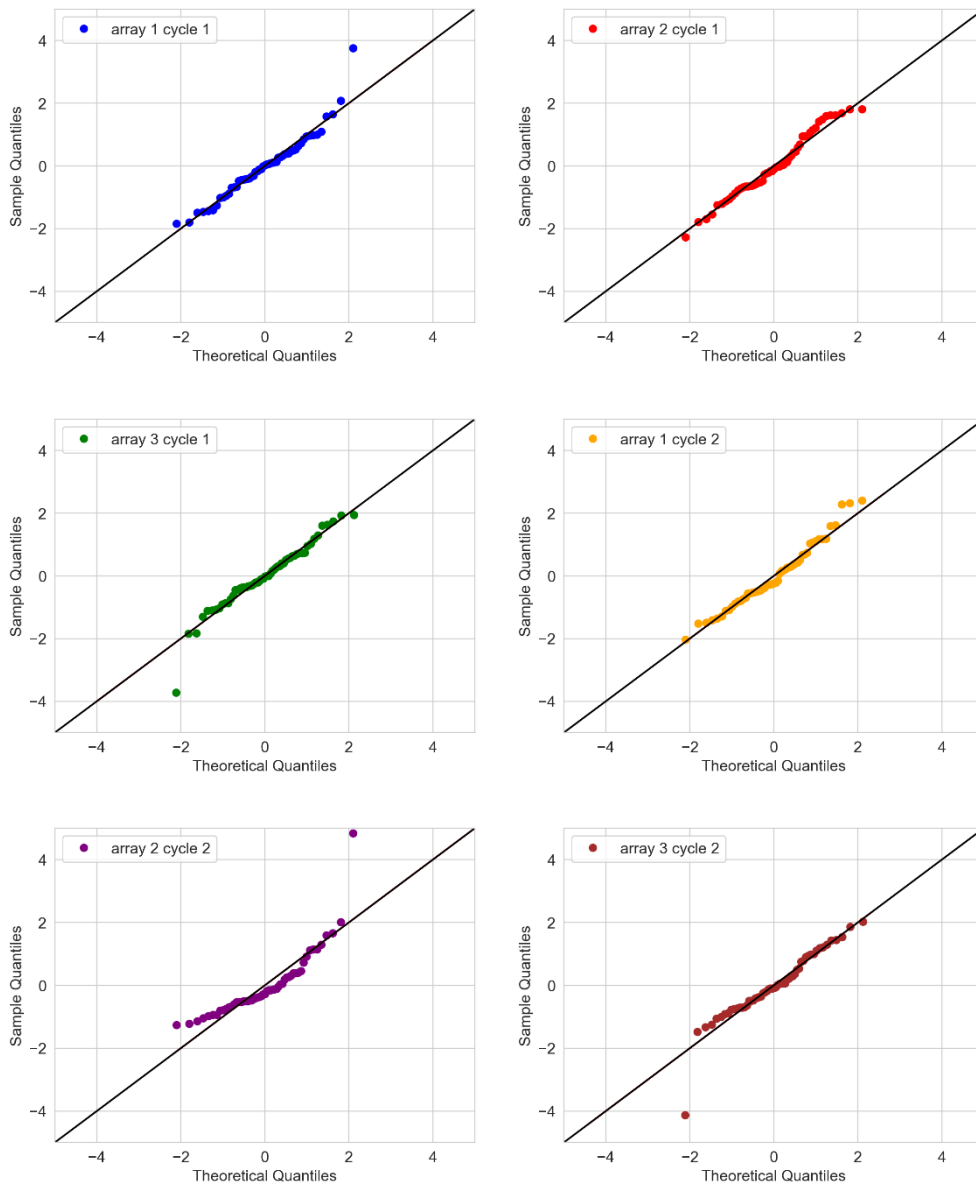
### 8.3.3 Statistical Analysis

To determine whether each curve in **Figure 8.4** can be aggregated to form a larger distribution, statistical analysis must be performed. In general, we can aggregate multiple data sets if they exhibit relatively identical distribution. To establish this, first, we will use graphical approaches followed by a more formal statistical testing. We show the notched box plot in **Figure 8.5a** and the kernel density plot in **Figure 8.5b**.



**Figure 8.5** Cumulative probability distribution as a function of the dimensionless induction time. Each array contains around 56 microdroplets.

The notched box plot (**Figure 8.5a**) shows that the 95% confidence interval for the median saturation at nucleation is consistent at around 1.8 to 1.9 range. Moreover, the kernel density plot (**Figure 8.5b**) shows a unimodal gaussian-like distribution. This is also supported by the Q-Q plot shown in **Figure 8.6**. Apart from the presence of few outliers and slight deviation from normality (notably in array2 cycle 2), most of the data points lie close to the 45° line which is a characteristic of a normal distribution.



**Figure 8.6** QQ-plot of the supersaturation at nucleation. If most of the data points lie close to the 45° line, the distribution tends to follow a normal distribution.

To test the hypothesis of whether the six different curves in **Figure 8.4** have identical distribution, we can either use a parametric test such as one-way ANOVA (assumes normal distribution) or non-parametric test such as Anderson-Darling<sup>155-156</sup> and Kruskal-Wallis<sup>157-158</sup> (no distributional assumptions). Although the distributions appear normally distributed graphically (**Figure 8.5b** and **Figure 8.6**), some of the datasets do not pass the standard Shapiro-Wilk normality test<sup>159</sup>

due to the presence of some outliers. However, with about 60 data points per set, we can also take advantage of the central limit theorem. This postulates that at large sample sizes (more than 30), the standard parametric tests (generally more powerful than nonparametric tests) are robust to departures from normality.<sup>160</sup> Therefore, I decided to use both parameteric and non-parametric statistical tests to compare the 6 data sets.

As a pre-requisite for ANOVA, the equality of variance has been tested via Levene test ( $p$ -value = 0.153) which satisfies the homoscedasticity assumption. The results are then tabulated in **Table 8.1** which all showed a  $p$ -value greater than 0.05, suggesting that the distributions are statistically identical. Note that technically, failure to reject the null hypothesis does not exactly mean that the null hypothesis is true. It just implies that there is no sufficient evidence to conclude that a significant difference exists. However, for practical purposes, a simplified interpretation is given in **Table 8.1**.

**Table 8.1** Statistical tests to simultaneously compare the distribution of 6 data sets (3 arrays, 2 cycles each)

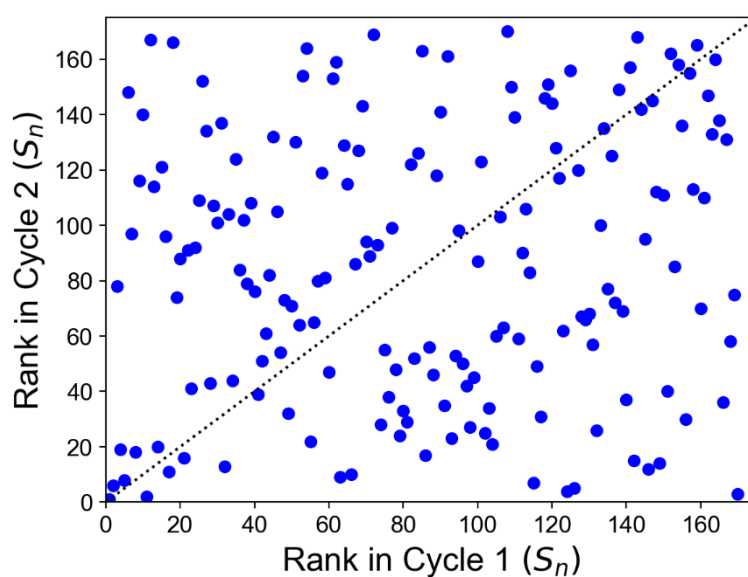
Test	Statistic	$p$ -value	Interpretation
Levene	1.625	0.153	data sets have equal variances
one-way ANOVA	0.7986	0.551	data sets have equal means
Anderson-Darling	1.371	0.093	data sets have the same distribution
Kruskal-Wallis	7.412	0.192	data sets have the same distribution

In summary, the consistent results across multiple statistical tests provide strong evidence that the experimental data across different arrays and cycles are reproducible, and thus can be aggregated together.

### 8.3.4 Checking for Possible Influence of Impurities

In primary nucleation studies, possible sources of artifacts include the presence of impurities (in the droplet or on the substrate) which can act as heterogeneous nucleation sites. With such impurities, nucleation tends to occur at a lower supersaturation than usual. To check whether such phenomenon occur in our system, we compared the results of the first and second cycle. If impurities are present, microdroplets that nucleated at a low supersaturation ratio in the first cycle would retain this behavior in the second cycle. Otherwise, there would be no correlation between the behavior of each droplet in the first and second cycles.

To facilitate visualization, we plot the rank of the microdroplet's  $S_n$  (supersaturation at nucleation) in cycle 1 against cycle 2 in **Figure 8.7**. If impurities played a huge impact, the data points must lie close to the diagonal line. However, we see a random behavior and a negligible correlation (Spearman  $R = 0.121$ ,  $p$ -value = 0.115) between two cycles. This confirms that nucleation events are truly independent and are not influenced by impurities. Moreover, this suggests that the “memory effect” due to solution history<sup>161</sup> does not occur in our experiments.



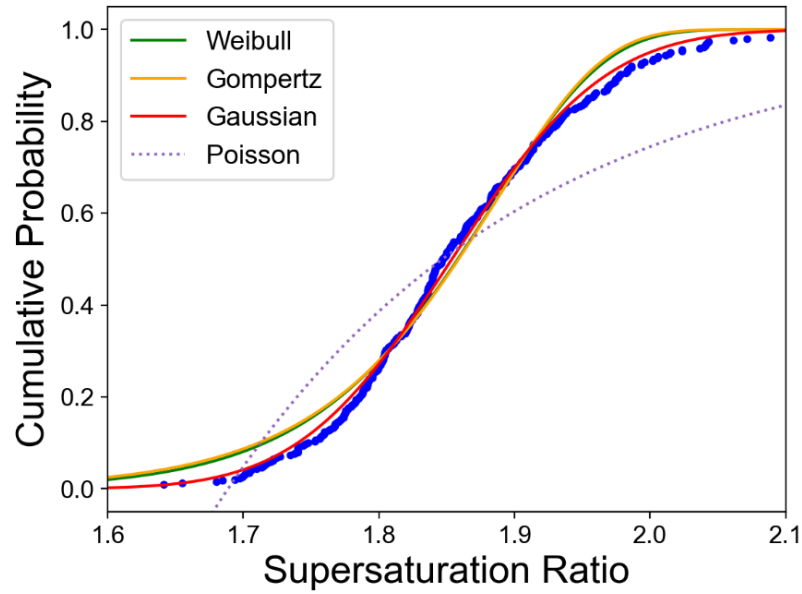
**Figure 8.7** Correlation between rank of microdroplets in terms of supersaturation at nucleation. The microdroplet that nucleated at the lowest supersaturation is ranked 1 and the one that nucleated at the highest supersaturation is ranked 175.

### 8.3.5 Nucleation Kinetic Parameter Estimation

To extract useful information regarding nucleation kinetics, we plot the combined cumulative probability distribution (350 data points) of supersaturation ratio during nucleation in **Figure 8.8**. We then fitted our data with the various probability functions that are commonly used in constant supersaturation experiments<sup>41</sup>. We see that nucleation occurs at a supersaturation ratio ranging from 1.65 to 2.10. This is in agreement with that of the microcapillary experiment of Desarnaud et al.<sup>73</sup> who reported a metastability limit of  $S = 1.6$  for aqueous NaCl under confinement.

Although our experiments are performed with increasing supersaturation with time, we see in **Figure 8.8** that functions such as Weibull, Gompertz, and Gaussian

fit well with our sigmoidal experimental data. The fitted parameters are listed in **Table 8.2**. From these fits, we can qualitatively infer some physical mechanisms involved in the nucleation process. From the Weibull fit, the fact that  $\beta > 1$  shows that the effective nucleation rate monotonically increases with increasing supersaturation. Moreover, the excellent fit of the Gompertz and Gaussian functions suggests that the nucleation rate increases exponentially with supersaturation and the induction times are normally distributed. On the other hand, the Poisson distribution fails to describe the data set because it assumes a time-invariant nucleation rate which is physically not the case in our experiments.



**Figure 8.8** Distribution of dimensionless induction time for unperturbed droplets fitted with Weibull, Gompertz, Gaussian, and Poisson distribution functions (Weibull and Gompertz coincide).

**Table 8.2** Empirical nucleation parameters estimated from various distribution functions<sup>41</sup>

Function	CDF	Fitted parameter	R <sup>2</sup>
Weibull	$P(t) = 1 - \exp\left[-\left(\frac{S_n}{\tau}\right)^\beta\right]$	$\tau = 1.89 (\pm 0.03\%)$ $\beta = 23.7 (\pm 1.13\%)$	0.9863
Gompertz	$P(t) = 1 - \exp\left[-\left(\frac{R_0}{\lambda}\right)(e^{\lambda S_n} - 1)\right]$	$R_0 = 3.28 \times 10^{-11}$ ( $\pm 29\%$ ) $\lambda = 12.8 (\pm 1.24\%)$	0.9839
Gaussian	$P(t) = 0.5 \left[1 + \operatorname{erf}\left(\frac{(S_n - \mu)}{\sigma_s \sqrt{2}}\right)\right]$	$\mu = 1.85 (\pm 0.01\%)$ $\sigma_s = 0.0891 (\pm 0.52\%)$	0.9968
Poisson	$P(t) = 1 - \exp[-\kappa(S_n - S_0)]$	$\kappa = 4.39 (\pm 3.02\%)$ $S_0 = 1.69 (\pm 0.24\%)$	0.7840



To interpret our measured induction time distribution deterministically in terms of classical nucleation theory,<sup>162</sup> we can use the mean supersaturation ratio at nucleation of 1.85 obtained from the Gaussian fit. In the literature<sup>1</sup>, the commonly quoted value of the pre-exponential factor  $A$  for NaCl in brine is  $10^{30} \text{ m}^{-3}\text{s}^{-1}$ . Using this value along with classical nucleation theory, we obtained  $\gamma = 75.5 \text{ mJ/m}^2$ .

For literature comparison, the electrodynamic levitator experiment of Na *et al*<sup>163</sup> resulted in  $\gamma = 87 \text{ mJ/m}^2$  which is 15% higher than our obtained value. However, note that in their experiment, the induction times measured are very short (in the order of 1 s) which could be sensitive to the temporal resolution of the detection technique. Ours are in the span of 120 s which was made possible by immersing the droplet in an oil bath. On the other hand, the theoretical calculations of Zimmerman *et. al.*<sup>164</sup> showed  $\gamma$  of NaCl-water system ranging from 41 to 63 mJ/m<sup>2</sup>.

## 8.4 Conclusion

In this work, we developed a novel approach to quantify nucleation kinetics in evaporating arrays of sessile microdroplets using aqueous NaCl as a model system. We showed that by using a deliquescence-efflorescence cycle coupled with the analysis of the gray-level pixel standard deviation of the microdroplet image, one can (1) ascertain the time at which the microdroplet is saturated (2) measure the induction time of unperturbed droplets without assuming a specific value of the evaporation rate. Multiple statistical tests suggest that the measurements from different arrays and cycles have the same distribution and thus can be aggregated together. Fittings of various distributions suggests that while nucleation rate in evaporating microdroplets increases exponentially with time, the induction times follow a normal distribution.

Although the induction times were obtained without assuming a value of evaporation rate, the nucleation at supersaturation cannot be obtained without an evaporation model. To obtain the interfacial energy between crystal and solution from classical nucleation theory, we thus approximated the system by assuming a linear decrease in volume with time. This led to a mean supersaturation ratio at nucleation of 1.85 with a nucleation rate of  $J = 4.1 \times 10^{12} \text{ m}^{-3}\text{s}^{-1}$  and an interfacial energy of  $\gamma = 75.5 \text{ mJ/m}^2$  which is consistent with literature values. Note that the value of  $\gamma$  reported here is just an approximation, since in reality the evaporation rate is not constant due to changes in water activity. Moreover, we used a deterministic view as opposed to the stochastic view of nucleation in the calculation. Thus, in the next chapters, the modeling of evaporation and the use of stochastic approach to obtain a more accurate  $\gamma$  will be my focus. Overall, the new experimental method and data-treatment procedure presented herein is a promising approach that can be adapted to study the crystallization behavior of other salts, pharmaceuticals, or biological crystals of interest.

## Chapter 9

# Modeling the Evaporation Dynamics of Sessile Saline Microdroplets

In the previous chapter, I have shown that a deliquescence-efflorescence cycle is a viable approach to measure the induction time in evaporating microdroplets. However, in the estimation of supersaturation ratio at nucleation, it was assumed that the volume decreases linearly with time, i.e. the evaporation rate is constant. Although this assumption is reasonable for dilute droplets, the evaporation rate should decrease with time since the water activity decreases as the salt concentration increases (Raoult's law). Moreover, it has been shown that the droplet arrays evaporate slower than an isolated droplet because of the contribution of the neighboring droplets to the local relative humidity. Additionally, the height of the oil medium as well as the effect of evolving solution density must be taken into account. Thus, to accurately obtain the supersaturation at nucleation, a reliable mathematical treatment that accounts for these additional complications is much needed, yet it is currently lacking. In this chapter, I addressed this by deriving phenomenological models to describe the evaporation of microdroplets considering the interplay of the additional complexities mentioned.

*Parts of this chapter are in preparation for submission to **Langmuir** as:*

**Cedeno, R.**; Grossier, R.; Candoni, N.; Flood, A.; Veessler, S., Evaporation Dynamics of Sessile Saline Droplets in Oil.

## 9.1 Introduction

Droplet evaporation on surfaces is ubiquitous in nature and plays a key role in a wide range of industrial and scientific applications<sup>165</sup> such as inkjet printing<sup>166</sup>, nanostructure fabrication<sup>167</sup>, DNA chip manufacturing<sup>168</sup>, crystallization studies<sup>22</sup>, biomedical diagnostics<sup>169</sup>, as well as virus spreading<sup>170</sup> and testing<sup>171</sup>. However, this seemingly “simple” process is governed by the complex interplay of many physical phenomena such as evaporative mass transfer<sup>172</sup>, heat conduction and convection, thermal-hydrodynamic instabilities, viscous and inertial flows, surface-tension-driven flows, contact-line pinning and depinning and buoyancy effects.<sup>173</sup>

Given its complexity and practical significance, numerous experimental and theoretical investigations have been devoted to better understand the underlying physics of sessile droplet evaporation as described by Larson in his review paper<sup>173</sup>. Many of these studies dealt with the evaporation of either pure liquid droplets<sup>65, 174</sup> or those with suspended colloidal particles which can lead to the so-called “coffee-ring effect”.<sup>175-176</sup> However, the evaporation of droplets containing dissolved salts has been rarely investigated. For instance, Takistov et al.<sup>177</sup>, Shin et. al.<sup>178</sup>, Zhang et. al.<sup>179</sup>, and Zhong et. al.<sup>180</sup> showed that the resulting patterns and morphologies of the dried salt droplets depend on the wettability of the surface, i.e. crystal rings would form on hydrophilic surfaces while single crystals at the center of the droplet are likely to form on hydrophobic surfaces. This suggests that surrounding salt droplets with hydrophobic surfaces is a promising approach for studying homogeneous primary nucleation.

In the context of crystallization studies, we need to ensure spatial homogeneity of droplet temperature and composition. However, in microliter droplets, it has been shown that various internal and Marangoni flows can lead to temperature and concentration gradients<sup>181-182</sup>. To address this, we reduce the droplet size down to picoliter range<sup>63</sup> and we reduce the evaporation rate by immersing the droplet in oil under regulated humidity. The oil bath also serves as a thermal buffer which minimizes temperature gradients due to evaporation. To extract nucleation parameters from such experiments<sup>21</sup>, it is crucial to determine how the volume, and so supersaturation of microdroplets, evolve with time. In modeling the evaporation rate, Soulié et. al.<sup>150</sup> reported that the droplet volume varies linearly with time within the early stages of evaporation. Given that the later stages of evaporation are crucial for the analysis of nucleation, we need a model that works even for the later stages. Since we are dealing with arrays of concentrated salt

droplets immersed in a bath of oil, there are additional phenomena that need to be accounted for: First, the varying diffusion distance due to the presence of oil surrounding the droplet must be taken as an additional parameter. Second, the separation distance of neighboring droplets must be accounted for.<sup>183</sup> Third, the density of the droplet changes as water evaporates. Fourth, the equilibrium concentration at the interface varies with time because water activity decreases as solute concentration increases (Raoult's law).<sup>66</sup> In this work, we derive expressions describing the evaporation dynamics that account for these four additional phenomena based on well-established mass transfer equations. We then validate our model with experimental data obtained in a previous work<sup>152</sup>. Moreover, we highlight that (1), surprisingly, different contact-line behavior such as constant contact angle (CCA), constant contact radius (CCR), and stick-slide (SS) leads to comparable evolution of droplet volume within the time of nucleation (2) failure to account for diffusive interactions between droplets nor the changes in colligative properties can lead to significant overestimation of droplet concentration.

## 9.2 Modeling

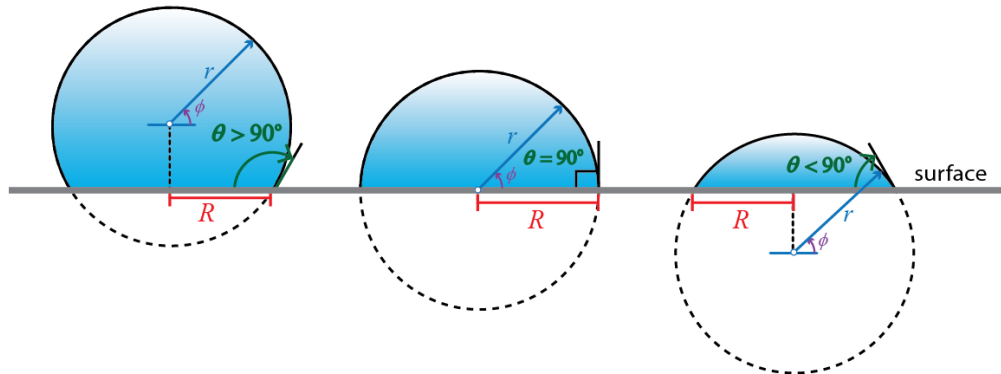
When a droplet is deposited onto a surface, it rapidly conforms to a quasi-equilibrium geometry with contact radius  $R$ , and contact angle  $\theta$ , which determine the droplet volume  $V_d$ . The shape of the droplet is either spherical or flattened, depending on the value of  $R$  compared to the capillary length  $L_c$  which characterizes the ratio of the interfacial energy between the droplet and the medium  $\gamma_{(\text{droplet}/\text{medium})}$  to gravitational effects.  $L_c$  can be calculated as

$$L_c = \sqrt{\frac{\gamma_{(\text{droplet}/\text{medium})}}{\Delta\rho \times g}} \quad (9.1)$$

where  $\Delta\rho$  is the density difference between the solution and the surrounding medium and  $g$  is the gravitational acceleration. In our case, the droplet is either pure water or saline solution and the medium is PDMS oil. If the droplet size is much less than  $L_c$ , then the droplet assumes a spherical cap geometry. For the PDMS-water system<sup>184</sup>, the capillary length is in the millimeter range. Since  $R$  is in the micrometer range, (much smaller than  $L_c$ ), the gravity is negligible compared to the interfacial energy between droplet and oil and so the droplets can be assumed to be a spherical cap. Thus, the droplet volume  $V_d$  can be calculated as<sup>64</sup> (see section 2.4 of Chapter 2)

$$V_d = \pi R^3 g(\theta) \text{ with } g(\theta) = \frac{\sin\theta(\cos\theta+2)}{3(1+\cos\theta)^2} \quad (9.2)$$

In the following section, we derive expressions for the diffusion-controlled evaporation of saline microdroplet with contact radius  $R$  and constant contact angle  $\theta$  immersed in a PDMS oil bath with thickness  $h$ . The different cases ( $\theta > 90^\circ$ ,  $\theta = 90^\circ$ ,  $\theta < 90^\circ$ ) are shown in **Figure 9.1**. Recall that we define  $r$  as the radial distance from the center of the equivalent spherical cap at an angle of  $\phi$  with the equatorial line.



**Figure 9.1.** Illustration of microdroplet showing the equivalent spherical cap at different values of contact angle  $\theta$ .

For simplicity, we will first consider the case where  $\theta=90^\circ$  (hemispherical droplet) which exhibits uniform evaporation flux over the surface area. Later on, we will incorporate a widely-used shape factor<sup>174, 185</sup> denoted as  $f(\theta)$  to obtain a general expression for any value of  $\theta$ .

### 9.2.1 Influence of oil thickness on the evaporation rate

Since the droplet is submerged in an oil bath ( $R \ll h$ ), we assume an isothermal system so that temperature-dependent quantities such as solubility and diffusivity remain constant. With the continuity equation in spherical coordinates, the molar flux of water vapor  $N(r)$  as a function of radial distance  $r$  is

$$\frac{1}{r^2} \frac{d}{dr} (r^2 N) = 0 \Rightarrow N(r) = \frac{C_1}{r^2} \quad (9.3)$$

where  $C_1$  is a constant of integration that will be evaluated later. Assuming negligible convective transport, Fick's equation can be simplified as

$$N = -D \frac{dc}{dr} \quad (9.4)$$

where  $D$  is the diffusivity of water in oil and  $c$  is the molar concentration of water. Combining equations (9.3) and (9.4),

$$\frac{dc}{dr} = -\frac{C_1}{D} \left( \frac{1}{r^2} \right) \quad (9.5)$$

Since the diffusion distance varies at any angle (with respect to the horizontal), the radial distance from the droplet center to the oil-air interface is  $r = \frac{h}{\sin \phi}$ . To facilitate integration, we express the boundary conditions in terms of  $R$ . We can write  $\frac{h}{\sin \phi} = R + \frac{h-R \sin \phi}{\sin \phi}$ . Given that  $h \gg R \sin \phi$ , we can approximate  $\frac{h}{\sin \phi} \approx R + \frac{h}{\sin \phi}$ . Integrating equation (9.5) with boundary conditions  $c(R) = c_s$  and  $c\left(R + \frac{h}{\sin \phi}\right) = c_\infty$ , we obtain

$$\int_{c_s}^{c_\infty} dc = -\frac{C_1}{D} \int_{r=R}^{r=R+\frac{h}{\sin \phi}} \left(\frac{1}{r^2}\right) dr \Rightarrow C_1 = D(c_\infty - c_s) \left(\frac{1}{R} - \frac{1}{R + \frac{h}{\sin \phi}}\right)^{-1} \quad (9.6)$$

Combining equations (9.3), and (9.6), we can write the molar flux as

$$N(r, \phi) = D(c_\infty - c_s) \left(\frac{1}{R} - \frac{1}{R + \frac{h}{\sin \phi}}\right)^{-1} \left(\frac{1}{r^2}\right) \quad (9.7)$$

Now, we can express the rate of change in droplet volume as the mass flux of water vapor integrated over the droplet surface area  $A$ .

$$\frac{dm}{dt} = \int^A M_w N(r, \phi) dA \quad (9.8)$$

The differential surface area  $dA$  can be written as a function of the differential angle  $d\phi$  as

$$dA = (2\pi r \cos \phi)(rd\phi) \quad (9.9)$$

Combining equations (9.7), (9.8) and (9.9) and integrating  $\phi$  from 0 to  $\pi/2$  (because we consider the case of hemispherical droplet where  $\theta = \pi/2$ ), we get

$$\frac{dm}{dt} = \int_0^{\pi/2} M_w D(c_\infty - c_s) \left(\frac{1}{R} - \frac{1}{R + \frac{h}{\sin \phi}}\right)^{-1} \left(\frac{1}{r^2}\right) (2\pi r \cos \phi)(rd\phi) \quad (9.10)$$

$$\frac{dm}{dt} = -(2\pi R) D M_w (c_s - c_\infty) \left(1 + \frac{R}{2h}\right) \quad (9.11)$$



Note that this is similar to that of Popov<sup>66</sup> for pure droplets directly evaporating in air. By comparison, if we substitute  $\theta = \pi/2$  in the shape factor expression (equation 4 in the main text), we obtain  $f(\theta) = 2$  (via numerical integration), *i.e.*

$$f\left(\frac{\pi}{2}\right) = \frac{\sin\left(\frac{\pi}{2}\right)}{1 + \cos\left(\frac{\pi}{2}\right)} + 4 \int_0^\infty \frac{1 + \cosh(2(0.5\pi)\varepsilon)}{\sin(2\pi\varepsilon)} \tanh\left[\left(\pi - \frac{\pi}{2}\right)\varepsilon\right] d\varepsilon = 2 \quad (9.12)$$

Furthermore, note that  $\left(1 + \frac{R}{2h}\right) \approx 1$  since  $R \ll h$ . Thus, we incorporate the shape factor  $f(\theta)$  for any contact angle  $\theta$  as

$$\frac{dm}{dt} = -\pi R D M_w (c_s - c_\infty) \left(1 + \frac{R}{2h}\right) f(\theta) \quad (9.13)$$

The relative humidity  $RH$  is defined as water vapor concentration divided by the concentration at saturation  $c_s$  (in this case, the solubility of water in oil). Thus, we can write

$$(c_s - c_\infty) = c_s (RH_s - RH_\infty) \quad (9.14)$$

where  $RH_s$  and  $RH_\infty$  are the relative humidity at the droplet-oil interface (saturated) and oil-air interface, respectively. For pure water droplets,  $RH_s$  is always equal to 1. As a result, equation (9.13) can be written as

$$\frac{dm}{dt} = -\pi R D M_w c_s (RH_s - RH_\infty) \left(1 + \frac{R}{2h}\right) f(\theta) \quad (9.15)$$

Note that  $m$  is the mass of the volatile component (in this case, water). Using the definition of density, we can write  $m = \rho_w V$  where  $\rho_w$  and  $V$  are the density and volume of pure water respectively. Since  $\rho_w$  is constant,  $\frac{dm}{dt} = \rho_w \frac{dV}{dt}$ . We can then combine the constant terms as  $K = \frac{D M_w c_s}{\rho_w}$ . Thus, equation (9.15) can be re-written as

$$\frac{dV}{dt} = -\pi R K (RH_s - RH_\infty) \left(1 + \frac{R}{2h}\right) f(\theta) \quad (9.16)$$

Note that this is valid for isolated droplets (*i.e.*, no neighbors).

## 9.2.2 Considering the presence of neighboring droplet

Several studies,<sup>186-187</sup> have shown that the presence of neighboring droplets slow down the evaporation process relative to isolated sessile droplets due to the

contribution of the neighboring droplets to the local relative humidity. To account for this behavior, we adapt the theoretical model of Hatte et al.<sup>183</sup> In simple terms, the effective relative humidity  $RH_{eff}$  is approximated from the prevailing relative humidity at the oil-air interface  $RH_{\infty}$  using a correction factor  $\epsilon$  defined as

$$\epsilon = \frac{1 - RH_{eff}}{1 - RH_{\infty}} = \frac{A_c}{2\pi R_0 f(\theta_0) A \bar{L}_a + A_c} \quad (9.17)$$

where  $A_c$  is the surface area of the vapor field,  $R_0$  and  $f(\theta_0)$  are the initial contact radius and shape factor respectively, and  $\bar{L}_a$  is the average vapor accumulation length (Refer to equation 8.8 of Hatte et al.<sup>183</sup>). Accordingly,  $A_c$  is the cross-sectional area of the half-cylindrical region surrounding the microdroplets with enhanced local vapor concentration. This is a function of the distance between the centers of the droplets  $L$ , the initial contact radius  $R_0$ , the instantaneous contact radius  $R$ , the initial contact angle  $\theta_0$  and the instantaneous contact angle  $\theta$  as

$$A_c = 4R_0 \left( L - \frac{R}{\sin \theta} \right) \sqrt{\pi \left( 1 + \frac{1}{\sin \theta_0} \right)} \quad (9.18)$$

$$\bar{L}_a = \frac{\alpha R_0}{\sin \theta_0} \quad (9.19)$$

where  $\alpha$  is a constant. Note that in the original derivation of Hatte et al.<sup>183</sup>, we substituted  $\lambda = 2L - D_e$  (see their Figure 6a) and  $D_e = 2R/\sin \theta$  (spherical cap geometry). We also let  $\alpha = 2K\beta$  where  $K$  and  $\beta$  are empirical parameters which have been shown to follow  $K\beta \approx 0.5$ . For simplicity, we combined this giving a single parameter ( $\alpha \approx 1$ ).

Thus, for droplets with neighbors, we replace  $RH_{\infty}$  by  $RH_{eff}$  in equation (9.16) which leads to

$$\frac{dV}{dt} = -\pi R K (RH_s - RH_{eff}) \left( 1 + \frac{R}{2h} \right) f(\theta) \quad (9.20)$$

### 9.2.3 Considering the evolution of droplet density as water evaporates

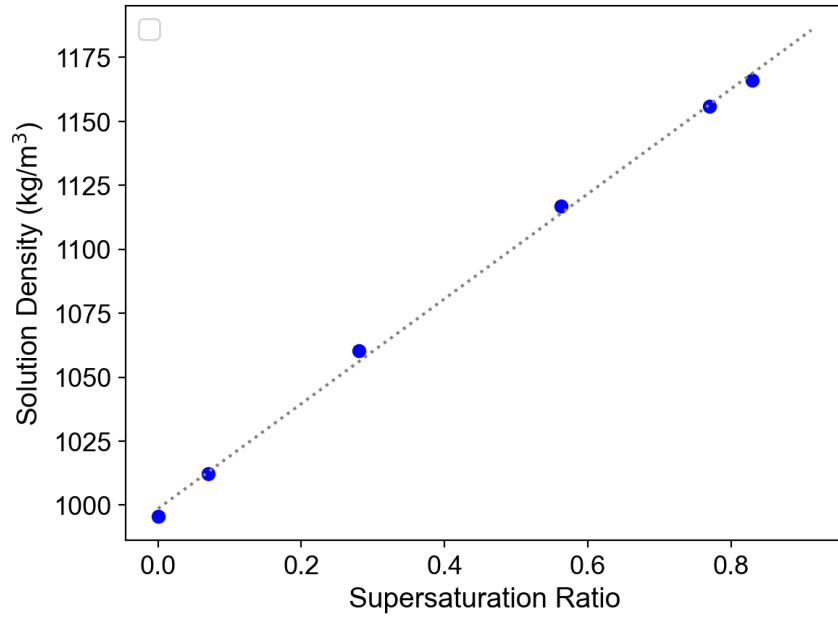
Note that we defined  $V$  as the volume of pure water (the volatile component) and  $R$  as the radius of the entire droplet. However, the total volume of the droplet  $V_d$  is a function of the volume occupied by both water and salt ions. To relate the volume

of pure water  $V$  to the droplet volume  $V_d$ , we employ experimental data on the solution density change as a function of NaCl supersaturation ratio ( $S = c/c^*$ ) as shown in **Figure 9.2**. We then use a simple linear function with  $b_1$  (slope) as the dimensionless coefficient of density increase relating the density of pure water  $\rho_w$  and the density  $\rho$  at any  $S$ .

$$\rho = \rho_w(1 + b_1S) \quad (9.21)$$

Given that the droplet mass is the sum of water mass and NaCl mass ( $m_d = m_w + m_{\text{NaCl}}$ ), we can write

$$\frac{m_w + m_{\text{NaCl}}}{V_d} = \frac{m_w}{V} (1 + b_1S) \Rightarrow \frac{1 + \left(\frac{m_{\text{NaCl}}}{m_w}\right)}{V_d} = \frac{1 + b_1S}{V} \quad (9.22)$$



**Figure 9.2.** Variation of aqueous NaCl density as a function of supersaturation ratio.<sup>188</sup> The regression line is  $y = 998(1+0.205x)$  with  $R^2 = 0.9984$ .

We can express  $m_{\text{NaCl}}/m_w$  in terms of  $S$  using the solubility of NaCl in water  $c_{eq}$  (in mol/kg water) and NaCl molar mass  $M_{\text{NaCl}}$  (kg/mol)

$$\frac{m_{\text{NaCl}}}{m_w} = c_{eq}M_{\text{NaCl}}S \quad (9.23)$$

Thus, the droplet volume  $V_d$  is related to the volume of pure water  $V$  as

$$V_d = \left( \frac{1 + c_{eq}M_{\text{NaCl}}S}{1 + b_1S} \right) V \quad (9.24)$$

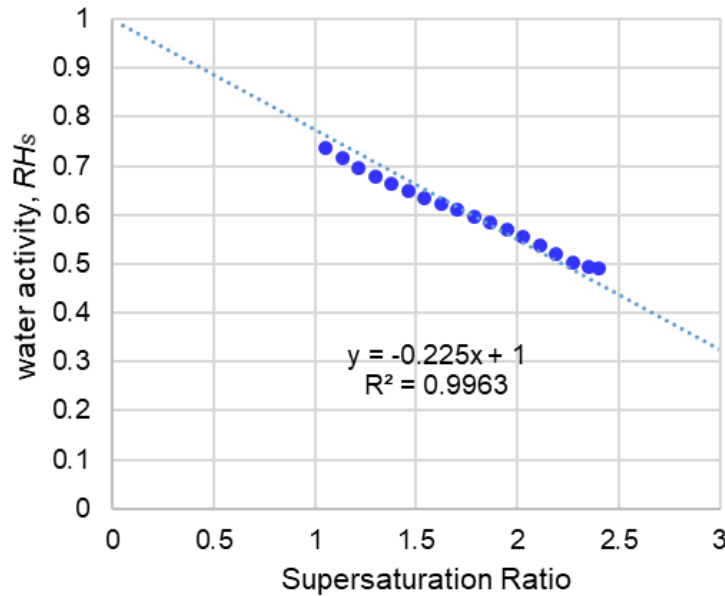
Observe that for pure droplet ( $S=0$ ),  $V_d = V$ . We can now express the droplet radius  $R$  in terms of  $V$  using the equation for the volume of spherical cap along with the density changes.

$$R = \left( \frac{V_d}{\pi g(\theta)} \right)^{\frac{1}{3}} = \left[ \frac{V(1 + c_{eq} M_{\text{NaCl}} S)}{(1 + b_1 S) \pi \cdot g(\theta)} \right]^{\frac{1}{3}} \text{ with } g(\theta) = \frac{\sin \theta (\cos \theta + 2)}{3(1 + \cos \theta)^2} \quad (9.25)$$

This expression for  $R$  will be used in equation (9.20).

### 9.2.4 Dependence of water activity on solute concentration

To account for the change in water activity due to the presence of salt, we express the decrease in water activity as a linear function with slope  $b_2$  fitted from experimental data of An et al, as shown in **Figure 9.3**.<sup>189</sup>



**Figure 9.3.** Variation of water activity (numerically equal to the equilibrium relative humidity,  $RH_s$ ) as a function of supersaturation ratio. The data were taken from Table 6 of An et al.<sup>189</sup>

Thus, in equation (9.20), the saturation relative humidity  $RH_s$  is expressed as

$$RH_s = 1 - b_2 S \quad (9.26)$$

where  $b_2$  is the coefficient of vapor pressure lowering fitted from experimental data of An et al.<sup>189</sup> Since the total mass of the salt is constant, we can write  $S_0 V_0 = SV$  so all equations containing  $S$  can be expressed in terms of  $V$ .

### 9.2.5 Models for Contact Line Behavior

The contact line behavior (how the contact radius and contact angle evolve with time) generally depends on the nature of the surface where the sessile microdroplet is situated. In the extreme case of perfectly smooth chemically homogeneous surface, the droplet maintains an equilibrium contact angle, and this is referred to as constant contact angle (CCA) mode. Consequently, the volume decreases due to the continuous decrease in contact radius.<sup>64</sup> In practice, the droplet will be pinned due to surface roughness so the radius remains constant at some point. In the extreme case where the droplet remains pinned throughout its lifetime, we refer to this as the constant contact radius (CCR) mode. In this mode, the volume decreases due to the continuous decrease in contact angle. As experimental studies suggest,<sup>65</sup> real droplets evaporate in some mixture of CCR and CCA modes. One common observation is the occurrence of CCR mode at the beginning and once the contact angle decreases to a value less than the receding contact angle  $\theta_r$ , it switches to CCA mode. This combination is known as the stick-slide (SS) mode.<sup>65</sup> In this work, we consider all three cases (CCA, CCR, and SS models) in analyzing the experimental data.

Mathematically, we can then incorporate the contact-line behavior by modeling the behavior of the contact angle  $\theta$ .

For constant contact angle (CCA), the change in contact angle with time is simply,

$$\frac{d\theta}{dt} = 0 \quad (9.27)$$

For constant contact radius (CCR) mode, the change in contact angle with time can be obtained by taking the derivative of  $V = f(\theta, R)$  where  $R$  is constant (see **Figure 9.1**)

$$V = \pi R^3 g(\theta) \Rightarrow \frac{dV}{dt} = \pi R^3 \frac{d}{dt} [g(\theta)] \text{ with } g(\theta) = \frac{\sin \theta (\cos \theta + 2)}{3(1 + \cos \theta)^2} \quad (9.28)$$

$$\frac{d}{dt} [g(\theta)] = \frac{d}{dt} \left( \frac{\sin \theta (\cos \theta + 2)}{3(1 + \cos \theta)^2} \right) = \frac{1}{(1 + \cos \theta)^2} \frac{d\theta}{dt} \quad (9.29)$$

Combining equations (9.28) and (9.29), we can obtain the change in contact angle as

$$\frac{d\theta}{dt} = \frac{1}{V} \frac{dV}{dt} (1 + \cos \theta)^2 g(\theta) \quad (9.30)$$

Therefore, the time evolution of  $V$  and  $\theta$  can be obtained from the numerical solution of equation (9.20) through (9.26) solved simultaneously with either equation (9.27) for CCA and equation (9.30) for CCR. For stick-slide mode (SS), the

evaporation follows CCR mode, that is, the initial contact angle  $\theta_0$  decreases until it reaches the receding contact angle  $\theta_r$ , where it suddenly shifts to the CCA model<sup>64</sup>. The full SS model can be written as

$$\frac{d\theta}{dt} = \begin{cases} \frac{1}{V} \frac{dV}{dt} (1 + \cos \theta)^2 g(\theta) & \text{for } \theta_r \leq \theta \leq \theta_0 \\ 0 & \text{for } 0 < \theta < \theta_r \end{cases} \quad (9.31)$$

For the numerical solution of the SS model, the final condition of the CCR part is used as the initial condition of the CCA part.

## 9.3 Materials and Methods

To determine the applicability of our models, we compared the experimental results of our previous works to the numerical solution of the derived equations for CCA, CCR, and SS respectively. This gives the time evolution of droplet volume and contact angle which can then be used to calculate the contact radius  $R$  and droplet height  $H$ . For pure water droplets we used the data of Rodriguez-Ruiz et al.<sup>152</sup> who tracked the evolution of contact radius and droplet height from a series of lateral images of droplets acquired using a side-view microscope. With simple trigonometry,  $R$  and  $H$  allow calculation of contact angle  $\theta$  and droplet volume  $V_d$ . Although the use of side-view microscope gives direct access to geometric parameters of the microdroplets, it only permits measurement of 3-4 droplets at a time.

For saline droplets, we used another approach based on the analysis of gray-level pixel standard deviation<sup>21</sup> of 170 bottom-view droplet images as discussed in Chapter 8. This gives three characteristic times namely the saturation time (droplet is saturated), matching time (refractive index of droplet equals that of the oil), and nucleation time. Although the use of the bottom-view microscope only gives the droplet volume and concentration at some specific times, it allows simultaneous measurement of hundreds of droplets, which is useful for studying the stochastic nature of nucleation.

## 9.4 Results and Discussion

Herein, the performance of the newly derived models (Section 9.2) is tested against the existing experimental data<sup>152</sup> (for pure microdroplets) and my own experiments (for saline microdroplets).

### 9.4.1 Model Predictions for Pure Microdroplets

For water droplets with no dissolved solutes, the numerical values used as input in the evaporation model are taken from Rodriguez-Ruiz et al.<sup>152</sup> The experimental parameters, symbol, values, and units are tabulated in **Table 9.1**.

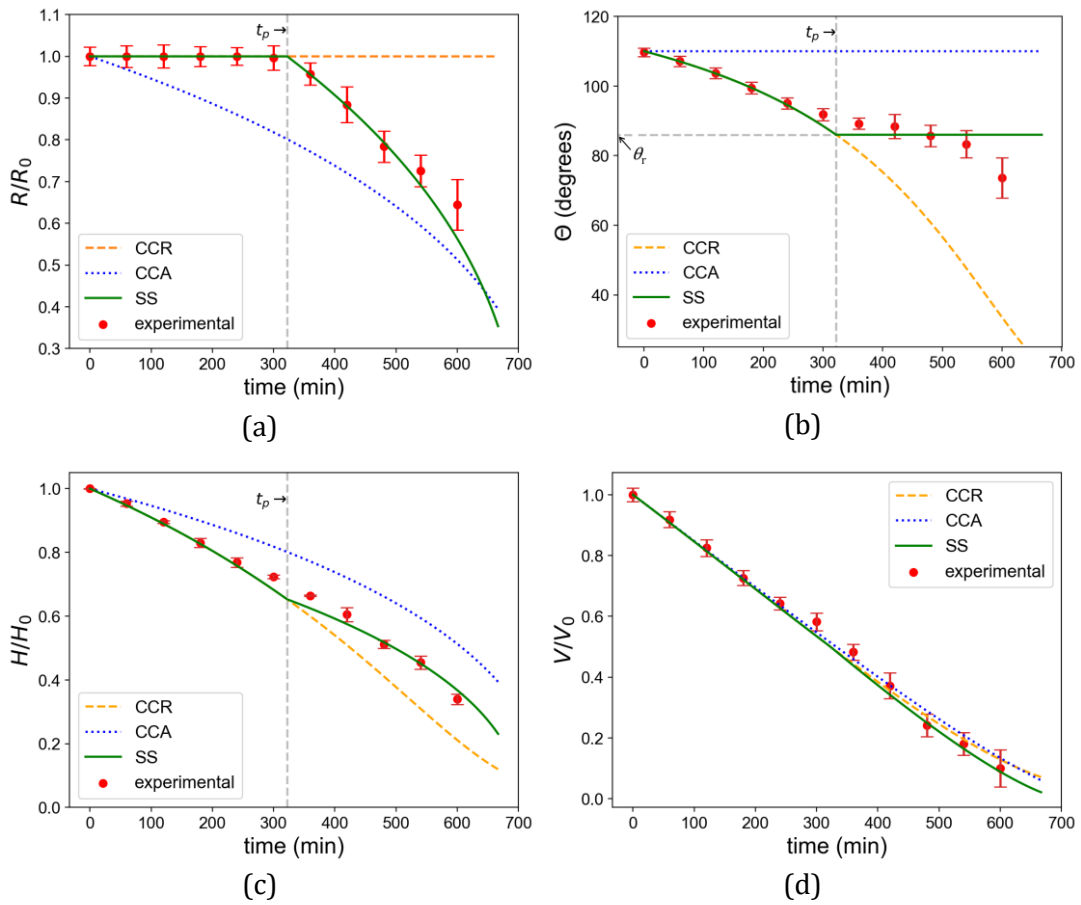
**Table 9.1** Numerical values used as input in the evaporation model of pure water droplets taken from Rodriguez-Ruiz et al.<sup>152</sup>

Experimental Parameter	Symbol	Value	
initial radius	$R_0$	25.7	$\mu\text{m}$
initial contact angle	$\theta_0$	110	degrees
initial volume	$V_0$	64.6	pL
receding angle (for SS)	$\theta_r$	86	degrees
oil height	$h$	0.40	mm
ambient temperature	$T$	298	K
rel. humidity at evaporation step	$RH_\infty$	60	%
distance between droplet centers	$L$	65	$\mu\text{m}$
Literature Data			
solubility of water in paraffin oil <sup>152</sup>	$c_s$	2.95	$\text{mol/m}^3$
diffusivity of water in paraffin oil <sup>190</sup>	$D$	$8.5 \times 10^{-10}$	$\text{m}^2/\text{s}$
density of pure water <sup>188</sup>	$\rho_w$	997	$\text{kg/m}^3$

In **Figure 9.4**, we compared the experimental geometric parameters obtained for pure water droplets by Rodriguez-Ruiz et. al.<sup>152</sup>, with the predictions of three contact line behavior models (CCR, CCA, and SS).

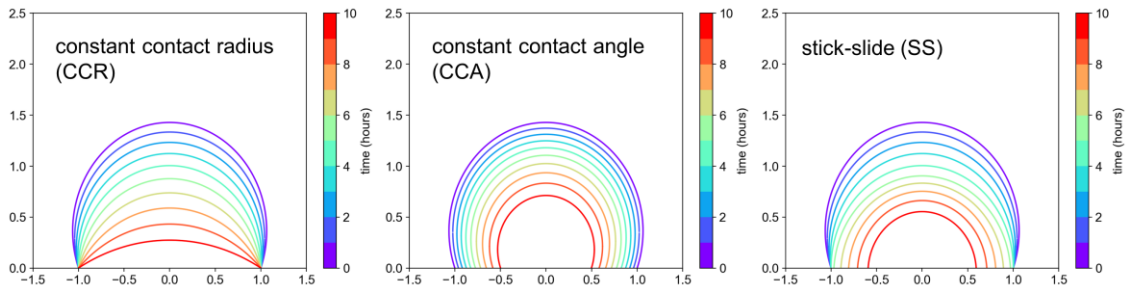
**Figure 9.4a** suggests that the normalized contact radius  $R/R_0$  is constant until a certain time of pinning  $t_p$ , then  $R/R_0$  decreases. Meanwhile, **Figure 9.4b** shows that  $\theta$  decreases until this threshold at  $t_p$ , after which,  $\theta$  becomes constant. This indicates that the system undergoes a stick-slide (SS) mode, i.e. CCR followed by CCA. In our system, we found that the time of pinning  $t_p$  corresponds to a contact angle of around  $86^\circ$  (**Figure 9.4b**). Thus we assume a receding contact angle of  $86^\circ$  for our system and we use this value for the stick-slide (SS) model in equation (9.31). Upon comparing the experimental points with the model predictions, it is clear that our stick-slide (SS) model well captures the evolution of the microdroplet's geometric parameters (i.e. contact angle, contact radius, height, and volume).





**Figure 9.4.** Model predictions of three contact line behavior models (CCR, CCA, SS) in comparison with experimental data obtained for pure water droplets by Rodriguez-Ruiz et. al.<sup>152</sup> Time evolution of (a) normalized contact radius, (b) Contact angle of the microdroplets with the substrate (c) normalized microdroplet height, and (d) Volume contraction. Error bars represent standard errors based on 3 replicates.

To visualize the evolution of droplet shape, we used the numerical solution of **Figure 9.4a-c** to simulate the geometry of the droplet at discrete time points as shown in **Figure 9.5**. We see that the final droplet shape is highly dependent on the contact-line behavior.

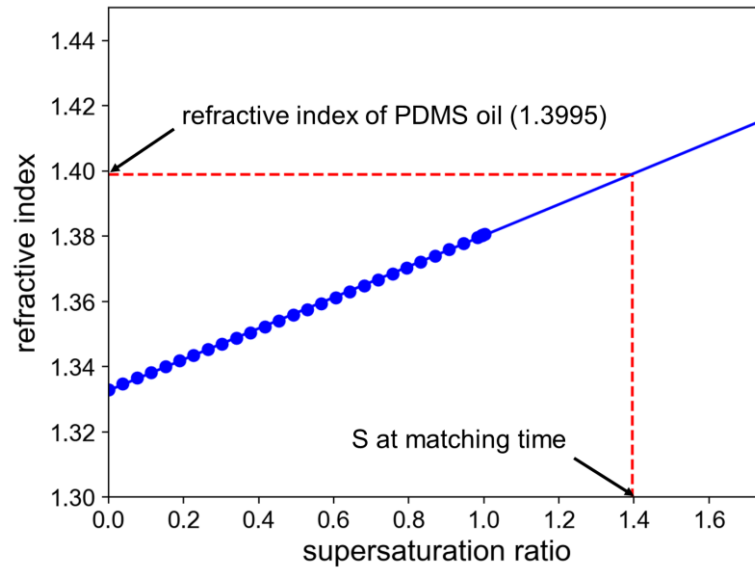


**Figure 9.5.** Predicted evolution of microdroplet shape (pure water) for CCR, CCA, and SS models at discrete time points (every 1 hour). X,Y axis (lengths) are in terms of  $R/R_0$ .

However, in the context of crystallization studies, the most important parameter to obtain from the evaporation modeling is the evolution of droplet volume in which the solution concentration depends on. Thus, regardless of the droplet shape, the excellent agreement of the CCR, CCA, and SS in terms of droplet volume (**Figure 9.4d**) indicates that we can just choose one of these three contact-line behavior models to calculate the droplet concentration. Thus, we have chosen CCA to describe the evaporation rate in saline droplets as this is the simplest case mathematically. Note that, even though the SS model works better in predicting geometric parameters, we currently do not have an experimental value of the receding angle  $\theta_r$  for saline droplets needed in SS model.

#### 9.4.2 Model Predictions for Saline Microdroplets

Using the CCA model, we thus extend our analysis to microdroplets containing dissolved salt (NaCl). As mentioned, this is based on bottom-view images from an inverted optical microscope which allow us to measure experimental points corresponding to the time at which the solution is saturated ( $S=1$ ) and the time at which the refractive index of the droplet matches that of the oil ( $S=1.395$ ) (shown in **Figure 9.6**).



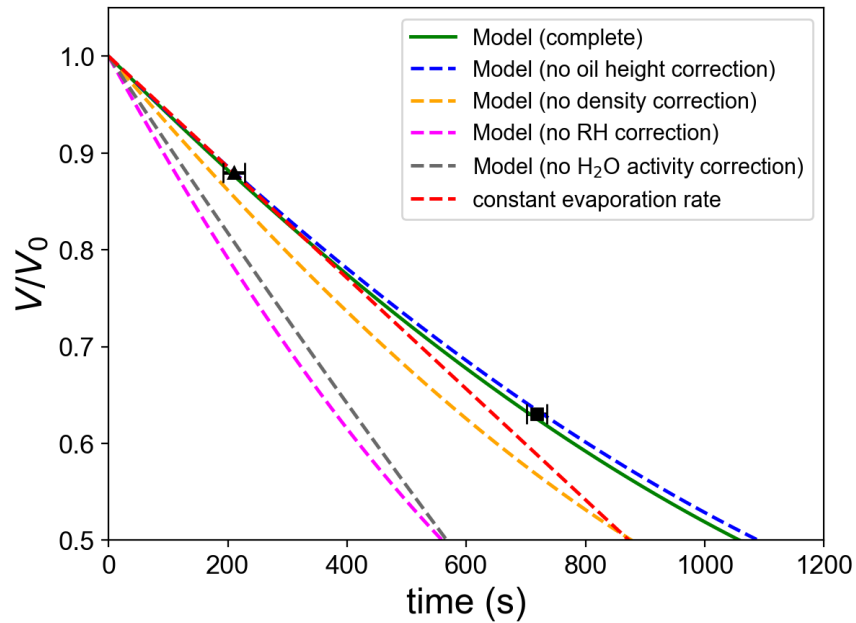
**Figure 9.6.** Variation of the refractive index<sup>188</sup> with supersaturation ratio.

Numerical values used as input in the CCA evaporation model of saline droplets are presented in **Table 9.2**.

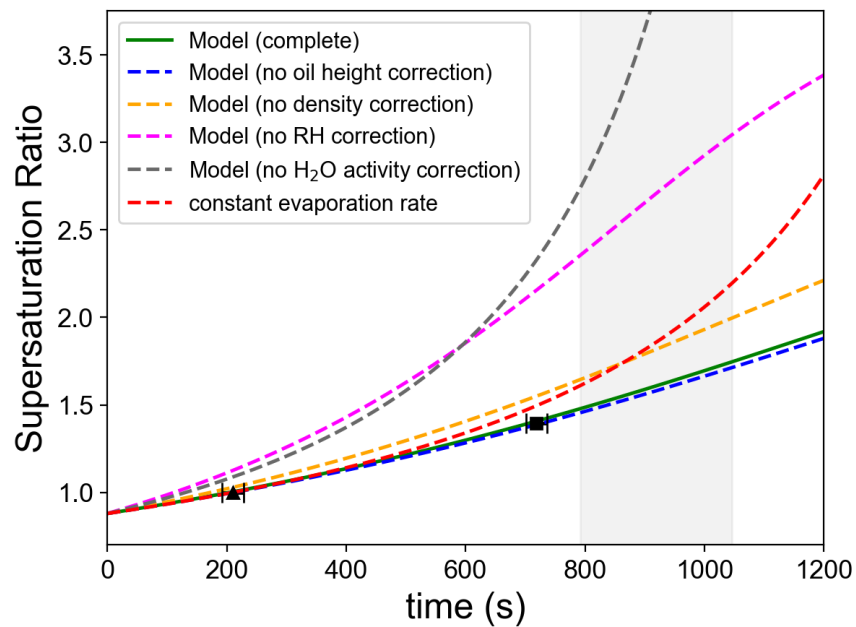
**Table 9.2** Numerical values used as input in the CCA evaporation model of saline droplets

Experimental Parameter	Symbol	Value	
initial radius	$R_0$	26.1	$\mu\text{m}$
contact angle	$\theta$	110	degrees
initial volume	$V_0$	66.93	pL
radius at saturation	$R_s$	25	$\mu\text{m}$
oil height	$h$	0.40	mm
ambient temperature	$T$	298	K
rel. humidity at evaporation step	$RH_\infty$	10	%
distance between droplet centers	$L$	100	$\mu\text{m}$
Literature Data			
solubility of water in PDMS oil <sup>79</sup>	$c_s$	30	$\text{mol}/\text{m}^3$
diffusivity of water in PDMS oil <sup>80</sup>	$D$	$8.5 \times 10^{-10}$	$\text{m}^2/\text{s}$
coefficient of density change <sup>188</sup>	$b_1$	0.205	-
coefficient of water activity lowering <sup>189</sup>	$b_2$	0.225	-
solubility of NaCl in water <sup>191</sup>	$c_{eq}$	6.14	$\text{mol}/\text{kg}$
molar mass of NaCl	$M_{\text{NaCl}}$	0.0584	$\text{kg}/\text{mol}$
diffusivity of NaCl in water <sup>192</sup>	$D_i$	$1.47 \times 10^{-9}$	$\text{m}^2/\text{s}$
density of pure water <sup>188</sup>	$\rho_w$	997	$\text{kg}/\text{m}^3$

**Figure 9.7** compares the prediction of the droplet volume and the supersaturation ratio in the CCA model for saline microdroplets ( $V_0 = 67$  pL and  $S_0 = 0.88$ ) with experimental data, in particular by issuing various hypotheses of simplification.



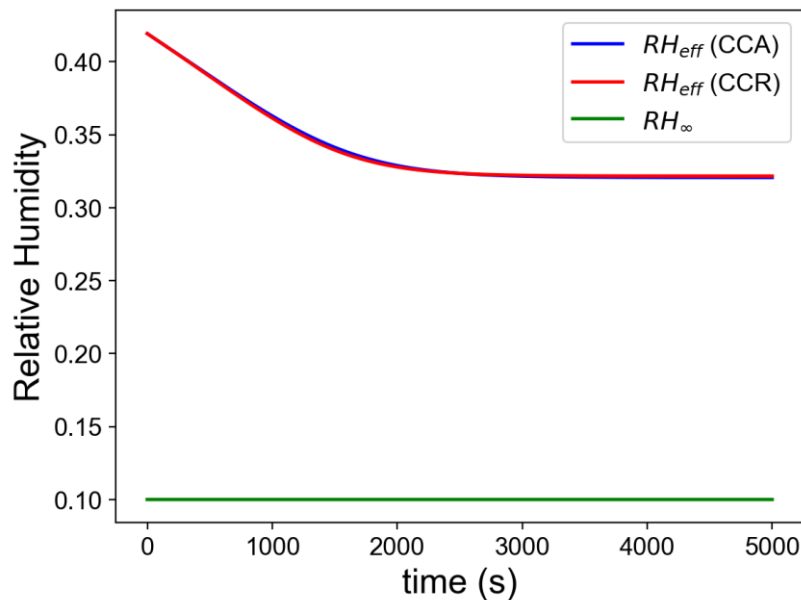
(a)



(b)

**Figure 9.7.** Model predictions (CCA) for saline microdroplets ( $V_0 = 67$  pL and  $S_0 = 0.88$ ) in terms of (a) droplet volume and (b) supersaturation ratio in comparison with experimental data. The error bars at saturation time ( $S=1$ ) and matching time ( $S=1.395$ ) represent the standard deviation of the distribution of data points (190 droplets). The grey area corresponds to the time range where nucleation occurs.

In **Figure 9.7a**, we see that neglecting the oil height correction can slightly overestimate the predicted volume. This is because without the oil height parameter, the droplet is considered to evaporate in an infinite medium of oil thereby hindering evaporation. Without density correction, the evaporation rate is significantly misestimated because the volume occupied by the NaCl in the droplet is not accounted which then affects the surface area to volume ratio. Remarkably, failure to correct for the relative humidity (due to the presence of neighboring droplet) and the changes in water activity (Raoult's law) led to a drastic overestimation of evaporation rate. This is because both cases directly affect the driving force for evaporation. The relationship between the effective relative humidity  $RH_{eff}$  and the prevailing humidity above the oil  $RH_{\infty}$  is shown in **Figure 9.8** where  $RH_{eff}$  decreases and then reaches equilibrium as the droplets become very small.



**Figure 9.8.** Evolution of the effective relative humidity  $RH_{eff}$  for CCA and CCR against the humidity above the oil  $RH_{\infty}$ .

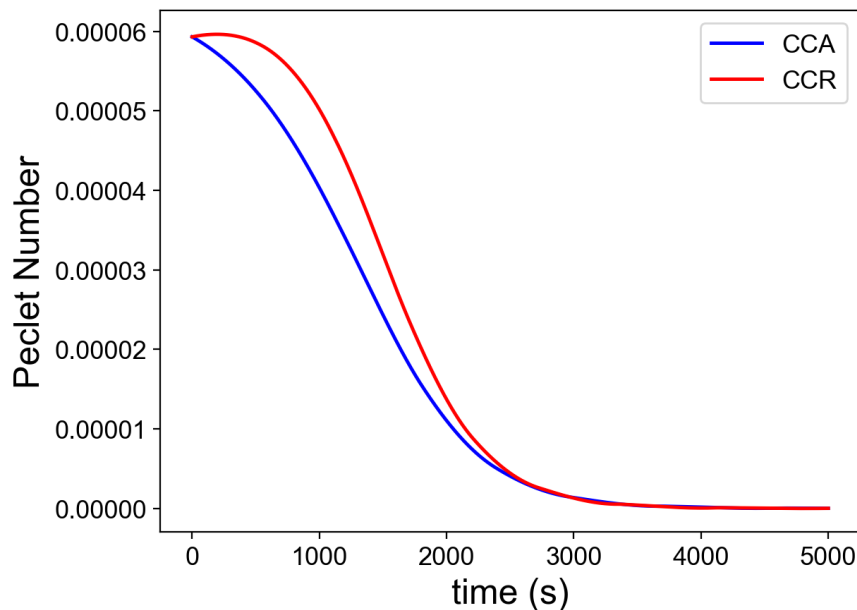
Therefore, we incorporated the four corrections concerning the oil height, the density, the relative humidity and the changes in water activity to the well-established mass transfer equations and we obtain a “complete CCA model” (**Figure 9.7**), which is able to predict the two experimental points with excellent accuracy.

Finally, to verify whether the saline droplets have a homogeneous composition throughout the evaporation process, we use the Peclet number (Pe) which is the ratio of convective mass transfer to diffusive mass transfer<sup>53</sup>. If  $Pe < 1$ , the diffusion

rate of the solute is fast enough to avoid a considerable enrichment at the receding surface and thus the system maintains a homogeneous composition. In microdroplets, Pe can be expressed mathematically as

$$Pe = \frac{2R\kappa}{D_i} \text{ with } \kappa = \frac{1}{A} \frac{dV}{dt} \quad (9.32)$$

Where  $\kappa$  is the evaporation flux (volume loss  $dV/dt$  per unit area  $A$ ),  $R$  is the droplet radius and  $D_i$  is the diffusion coefficient of the solute in the droplet. Peclet number is plotted as a function of time in **Figure 9.9**. We found that the maximum Pe is in the order of  $10^{-4}$  suggesting a uniform droplet concentration.

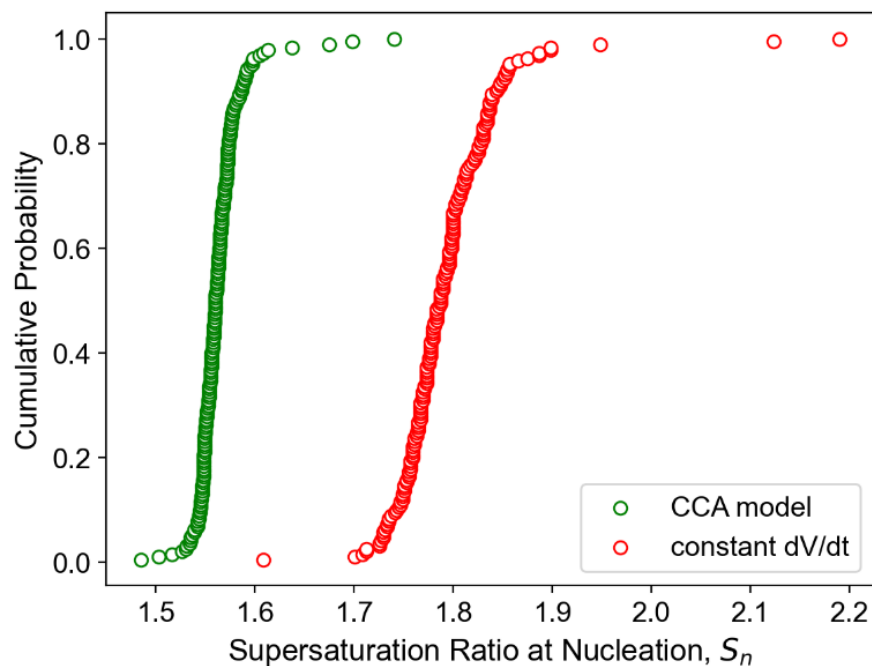


**Figure 9.9.** Evolution of Peclet number for CCA and CCR models. (If Peclet number  $\ll 1$ , the microdroplet is considered to have homogeneous composition)

### 9.4.3 Implications on Crystallization Studies

In the context of crystallization studies, droplets are not expected to nucleate at the same time even though they have identical concentration due to the stochastic nature of nucleation. Our experimental results demonstrate this with nucleation events spanning from 800s to 1050s (grey area in **Figure 9.7b**). In principle, these nucleation times can be used to estimate the interfacial energy between crystal and solution for NaCl-water system if we know the supersaturation ratio at nucleation  $S_n$ . To do this, several reports assumed a linear evaporation rate (neglecting changes in water activity) to calculate the droplet concentration as a function of time<sup>151, 193-194</sup>. Here we highlight that this approximation can lead to inaccurate values of droplet concentration particularly in later stages where nucleation

occurs. For instance, using our “complete CCA model”, the supersaturation at nucleation  $S_n$  ranges from  $S = 1.50$  to  $1.75$  (**Figure 9.7b**). This is consistent with the results of Desarnaud et. al.<sup>73</sup> who showed a metastability limit of  $S = 1.60$  for NaCl-water system using microcapillary experiments. However, if we assume a constant evaporation rate by extrapolating  $t = 0$  and  $t =$  saturation time (dashed red curve in **Figure 9.7b**), the predicted range of  $S_n$  would be up to 40% higher (ranges from 1.75 to 2.50). This discrepancy would have a huge consequence particularly in crystallization studies. To illustrate this, we plot the cumulative probability distribution as a function of supersaturation at nucleation  $S_n$  in **Figure 9.10**. The constant evaporation rate assumption clearly overestimates  $S_n$  resulting in unreasonably large values of supersaturation. Furthermore, if diffusive interactions and changes in water activity were not accounted for, much larger deviations could be obtained. All of these can lead to inaccurate values of nucleation kinetic parameters. Thus, we highlight the need for accurate modeling of evaporation rate of sessile droplets in the context of nucleation studies.



**Figure 9.10.** Cumulative probability distribution of supersaturation ratio at nucleation  $S_n$  based on two evaporation models.

## 9.5 Conclusion

In this chapter, I studied the evaporation dynamics of sessile picoliter droplets in oil until crystallization using NaCl-water as a model system. Although there are existing evaporation models for the evaporation of pure sessile droplets in air, they are not directly applicable in our system due to the additional phenomena that require further consideration. Thus, starting from well-established mass transfer equations, I derived new expressions applicable for droplets with dissolved solute submerged in a thin layer of oil. The model accounts for the additional complexity due to (i) variable diffusion distance due to the presence of oil (ii) diffusive interactions due to the presence of neighboring droplets (iii) density change as concentration increases (iv) water activity change as a function of concentration. By comparing our model predictions to experimental data, we showed that different contact-line behavior (CCR, CCA, or SS) results in almost identical evolution of droplet volume especially within the time scale relevant to crystallization studies. With this information, I analyzed the evaporation rate of saline droplets using the CCA model and using NaCl-water as a model system, I demonstrated for the first time that assuming a constant evaporation rate as well as neglecting the diffusive interactions between droplets can lead to severe discrepancies in the measurement of droplet concentration particularly during nucleation. This indicates that crystallization studies in literature that had used this assumption may be subject to large errors (in the example presented here, 40%). With our “complete CCA model”, one can accurately determine the time evolution of droplet concentration which is important in quantifying crystallization kinetics. Moreover, given the importance of evaporation dynamics in a wide array of scientific and practical applications, the models and new insights presented herein would be of great value to many fields of interest.



## **Chapter 10**

### **Modeling the Nucleation Kinetics of Aqueous NaCl with Modified Poisson Distribution**

Nucleation kinetic studies based on induction time are usually carried out at constant supersaturation to facilitate data treatment. In literature, induction time distribution are usually fitted with Poisson distribution since the driving force for nucleation is constant and so the effective nucleation rate is invariable with time. However, for evaporative crystallization (which is ubiquitous in nature), supersaturation evolves with time, rendering the Poisson function unapplicable. Although other empirical distributions such as Weibull, Gompertz, and Gumbell can describe the time-dependence of effective nucleation rate<sup>41</sup>, the fitting parameters do not carry physical information that can be interpreted in terms of classical nucleation theory (CNT). To address this, I explore the use of a modified Poisson distribution compatible with CNT which considers the time-dependence of the nucleation driving force.

In this chapter, I demonstrate that by combining the induction time measurement approach and the evaporation model developed in the previous chapters, together with the modified Poisson distribution, one can obtain accurate nucleation kinetic parameters that are of excellent agreement with theoretical predictions.

*Parts of this chapter are in preparation for submission as*

**Cedeno, R.;** Grossier, R.; Candoni, N.; Flood, A.; Veessler, S.,  
Nucleation Kinetics of Aqueous NaCl via Stochastic Approach

## 10.1 Introduction

Nucleation in solutions has been a subject of numerous investigations due to its significance in material synthesis, pharmaceutical purification, biomineralization, and climate modeling<sup>180</sup>. Sodium chloride, being the most abundant salt on earth<sup>73</sup>, is of particular interest due to its influence on metal corrosion<sup>74</sup>, building material degradation<sup>75</sup>, oil well productivity<sup>76</sup>, atmospheric science<sup>77</sup> and so on. Thus, fundamental understanding of its nucleation kinetics is of paramount importance yet it remains poorly understood from both experimental and theoretical perspective.<sup>1</sup> Up to date, there are only few experimental studies that quantitatively measure the nucleation kinetic parameters of NaCl in brine. These include experiments which employ an efflorescence chamber<sup>195</sup>, electrodynamic levitator<sup>163</sup>, and microcapillaries<sup>73</sup>; all of which treated nucleation deterministically. However, nucleation is inherently stochastic rather than deterministic. In fact, with *in situ* electron microscopy, Nakamuro et al.<sup>196</sup> have captured atomically-resolved images of NaCl nucleation. They observed that a critical cluster must have at least 48 NaCl units and that the nucleation periods follow a normal distribution spanning from 2 to 10 s (but the statistical relevance is not well-established). This is a strong evidence for the stochasticity of NaCl nucleation yet surprisingly, there are no existing experimental studies that measure its kinetic parameters using the stochastic view of nucleation.

In this work, we address this by measuring the primary nucleation kinetic parameters of aqueous NaCl in confined microdroplets with a stochastic model.<sup>21, 152</sup> We demonstrate that by combining the deliquescence-efflorescence cycle for measuring induction time in Chapter 8, the evaporation model derived in Chapter 9, and together with inhomogeneous Poisson probability distribution<sup>45</sup> and classical nucleation theory, one can obtain a reliable estimate of nucleation kinetic parameters which are consistent with theoretical and literature values. To the best of our knowledge, this is the first work to utilize a probabilistic approach in the simultaneous estimation of pre-exponential factor and interfacial energy between crystal and solution in NaCl-water system.

## 10.2 Theory and Modeling

### 10.2.1 Classical Nucleation Theory for Ionic Systems

Classical Nucleation theory expresses the primary nucleation rate  $J$  as the product of the pre-exponential factor  $A$  and an exponential factor containing the free energy cost of forming a critical nucleus  $\Delta G^*$  and thermal energy  $kT$ .

$$J = A \exp\left(-\frac{\Delta G^*}{kT}\right) \quad (10.1)$$

An important difference between the treatment of ionic systems and molecular systems is in the expression of chemical potential difference between solid and liquid.<sup>73</sup> For ionic systems, it is a function of the number of ions forming one formula unit  $\nu$  (2 for NaCl), and the mean ionic activity coefficient of the solute  $\gamma_{\pm}$ . These leads to the following expression for  $\Delta G^*$

$$\Delta G^* = \frac{4}{3}\pi\gamma(R_c)^2 \text{ with } R_c = \frac{2\gamma}{\nu kT\rho_s \ln\left(\frac{\gamma_{\pm}m}{\gamma_{\pm 0}m_0}\right)} \quad (10.2)$$

with interfacial energy  $\gamma$  between crystal and solution, critical radius  $R_c$ , number density of formula units in the solid  $\rho_s$  ( $2.27 \times 10^{28} \text{ m}^{-3}$  for NaCl), and  $m$  and  $m_0$  are the molalities at nucleation and saturation respectively<sup>73</sup>. The ionic activity coefficient is often modeled as a function of molality using the modified Debye-Huckel equation<sup>1</sup>.

$$\log_{10} \gamma_{\pm} = -\frac{a\sqrt{m}}{1 + b\sqrt{m}} + cm \quad (10.3)$$

with empirical fitting parameters  $a$ ,  $b$ , and  $c$ .

### 10.2.2 Modified Poisson Distribution Function

In the stochastic view of nucleation, the probability distribution of the nucleation times must be analyzed. In the context of microdroplets, it is normally assumed that the time it takes for a nucleus to grow to detectable size is negligible<sup>45</sup>.

Thus, for constant supersaturation experiments, the cumulative probability of obtaining a droplet with at least one nucleus after time  $t$  is a function of nucleation rate  $J$  and droplet volume  $V$  given as

$$P(t) = 1 - \exp(-JVt) \quad (10.4)$$

In the case of evaporating droplet, both the supersaturation and the volume vary with time. As suggested by Goh et. al.,<sup>45</sup> the cumulative probability distribution function becomes

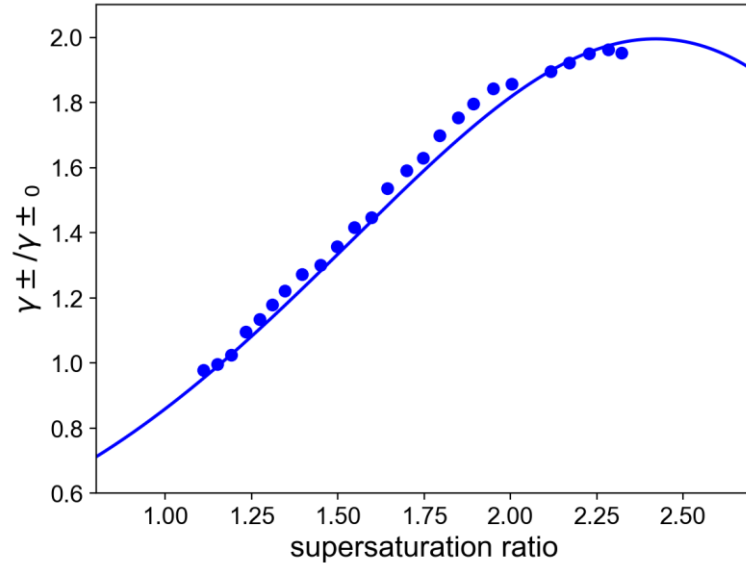
$$P(t) = 1 - \exp \left[ - \int_{t_{\text{sat}}}^{t_{\text{nuc}}} J(t)V(t)dt \right] \quad (10.5)$$

In equation (10.5),  $J(t)$  can be expressed as a function of supersaturation  $S(t)$  by combining with equations (10.1) through (10.3). To determine supersaturation  $S(t)$  and volume  $V(t)$ , we can use the evaporation model developed in Chapter 9 which describe the volume and concentration variation with time.

To account for the variation of the ionic activity coefficient with concentration, we referred to the experimental results of Na et al.<sup>163</sup> The ratio of activity coefficients  $\gamma_{\pm}/\gamma_{\pm 0}$  is calculated from the ratio of activities  $a/a_0$  as follows

$$\frac{a}{a_0} = \frac{\gamma_{\pm}m}{\gamma_{\pm 0}m_0} \quad (10.6)$$

where  $a$  is the solution activity at a molality  $m$ ,  $a_0$  is the solution activity at saturation, and  $m_0$  is the molality at saturation. The plot of  $\gamma_{\pm}/\gamma_{\pm 0}$  against the supersaturation ratio ( $m/m_0$ ) is shown in **Figure 10.1**.



**Figure 10.1.** Ratio of ionic activity coefficients  $\gamma_{\pm}/\gamma_{\pm 0}$  based on the experimental data of Na et al.<sup>163</sup>

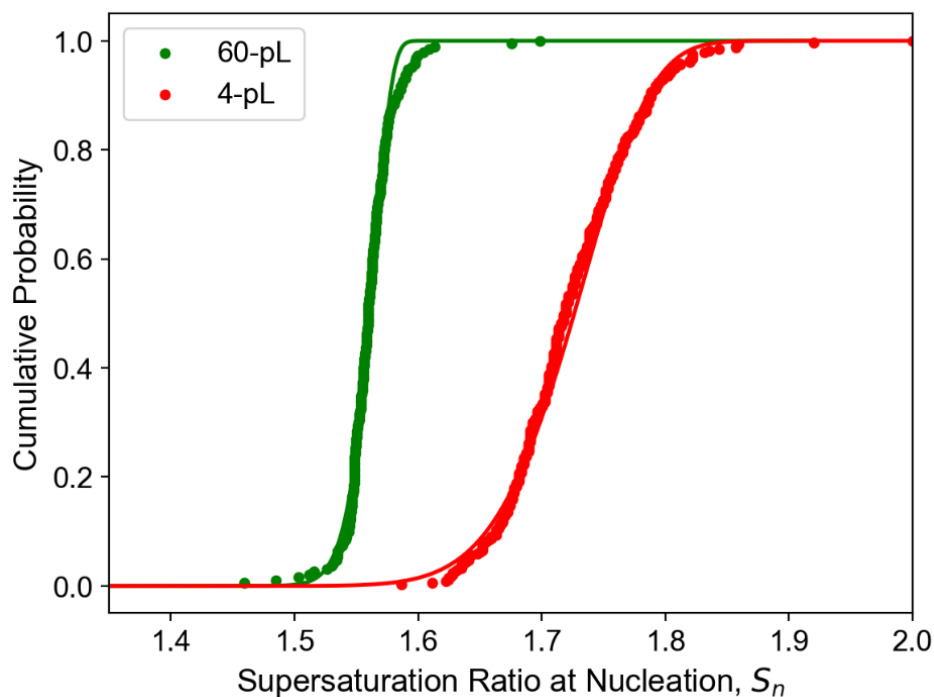
By minimizing the squared residuals between the observed and predicted cumulative probabilities in equation (10.5), one can extract the important nucleation parameters  $A$  (pre-exponential factor) and  $\gamma_{\text{eff}}$  (effective interfacial energy between crystal and solution). Note that prior to curve fitting, we non-dimensionalize the induction times following the procedure of Grossier et al<sup>21</sup>.

## 10.3 Results and Discussion

### 10.3.1 Kinetic Parameter Estimation

To check the applicability of the modified Poisson distribution in describing our experimental data, we fitted it with the distribution of supersaturation ratio at nucleation for two different microdroplet sizes of 60 and 4pL as shown in **Figure 10.2**. Indeed, the model well captures the sigmoidal nature of the distribution which supports the validity of our approach. Unlike the use of empirical distributions such as Weibull, Gompertz, Gumbell etc (whose parameters cannot be interpreted in terms of classical nucleation theory), this method allows the extraction of physical quantities describing the nucleation kinetic as listed in **Table 10.1**.

For the 60 pL experiment, we obtained an interfacial energy between crystal and solution of  $\gamma = 46.7 \text{ mJ/m}^2$  ( $\pm 0.54\%$ ). Interestingly, an atomistic simulations performed by the group of Peters<sup>164</sup> yielded an interfacial energy of  $\gamma = 47 \text{ mJ/m}^2$ , a remarkable agreement between theory and experiment.



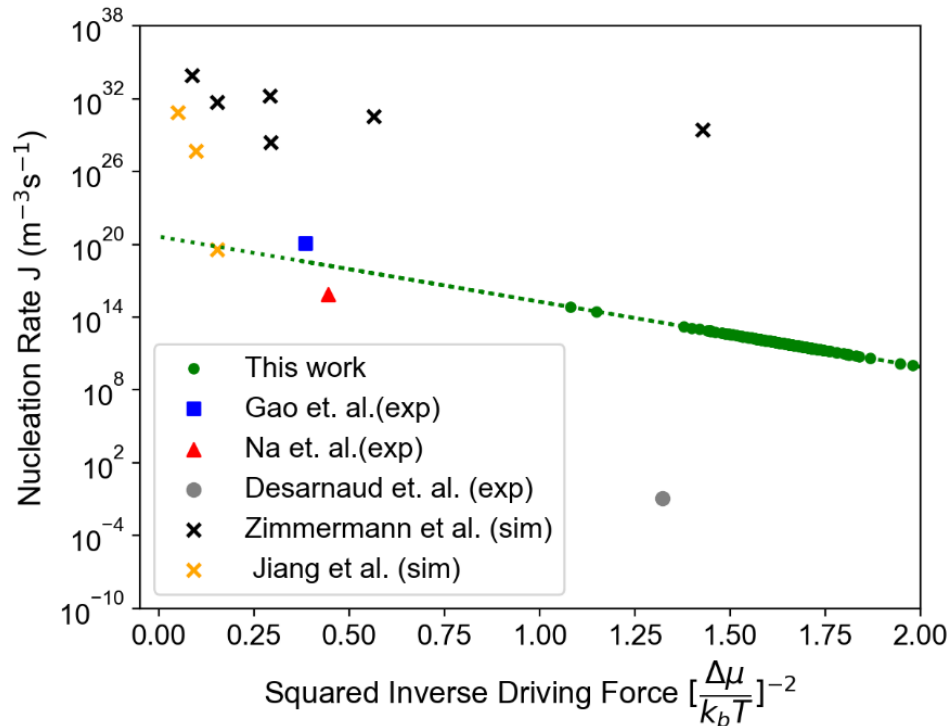
**Figure 10.2** Fitting of the modified Poisson distribution (eq. 10.5) with the experimental distribution of supersaturation ratio at nucleation for microdroplets with volumes  $\sim 60 \text{ pL}$  and  $\sim 4 \text{ pL}$  (measured at saturation).

**Table 10.1** Nucleation kinetic parameters obtained from the fit in Figure 10.2.

	60 pL	4 pL
Average $S$ at nucleation, $\bar{S}_n$	1.56	1.72
Pre-exponential Factor ( $\text{m}^{-3}\text{s}^{-1}$ )	$9.30 \times 10^{20} (\pm 1.47\%)$	$1.12 \times 10^{17} (\pm 0.39\%)$
Interfacial energy ( $\text{mJ/m}^2$ )	$46.7 (\pm 0.48\%)$	$39.6 (\pm 0.27\%)$

### 10.3.2 Comparison with Literature

For further comparison with other literature data, we use the results for the 60 pL as it is not significantly impacted by the confinement effect which requires a particular mathematical treatment.<sup>20</sup> We then plotted our experimental results together with literature values in **Figure 10.3**.



**Figure 10.3** Comparison of our experimental results (dashed green line is via extrapolation of CNT from the 60-pL experiment) to relevant experimental literature data (exp) and theoretical simulations (sim). Experiments were based on efflorescence chamber (Gao et. al.)<sup>195</sup>, spherical void electrodynamic levitator trap (Na. et. al.)<sup>163</sup>, and microcapillaries (Desarnaud et. al.)<sup>73</sup> while the simulations were based on forward flux sampling (Jiang et. al.)<sup>197</sup> and seeded atomistic simulations (Zimmerman et. al.)<sup>1, 164</sup>

In **Figure 10.3**, one can see that the magnitude of our measured nucleation rate is very close to that of Gao et. al.<sup>195</sup> (efflorescence chamber experiment) and Na. et. al.<sup>163</sup> who used an electrodynamic levitator trap, a setup that aimed to minimize all possible heterogeneous nucleation sites. Although they reported an interfacial energy between crystal and solution  $\gamma = 87 \text{ mJ/m}^2$ , they calculated it from the average induction time while taking  $A = 10^{30} \text{ m}^{-3}\text{s}^{-1}$  as a fixed value (taking induction time as deterministic rather than stochastic). Interestingly, when similar

calculation procedure is used (average induction time and  $A = 10^{30} \text{ m}^{-3}\text{s}^{-1}$ ), we obtained a value of effective interfacial energy between crystal and solution  $\gamma_{\text{eff}}$  of  $64 \text{ mJ/m}^2$  and  $76 \text{ mJ/m}^2$  for the 60 pL and 4 pL microdroplet respectively.

Thus, the discrepancy in the measured interfacial energy is likely due to two main reasons. First, their approach assumes nucleation as a deterministic process (based on average induction time) while our treatment considers its inherent probabilistic nature which is eminent in small volumes. Second, we did not assume any pre-defined value of the pre-exponential factor in the parameter estimation. In the experimental work of Gao et. al.<sup>195</sup> where they measured mean efflorescence time, they also fixed the prefactor at a value of  $2.8 \times 10^{38} \text{ m}^{-3}\text{s}^{-1}$ .

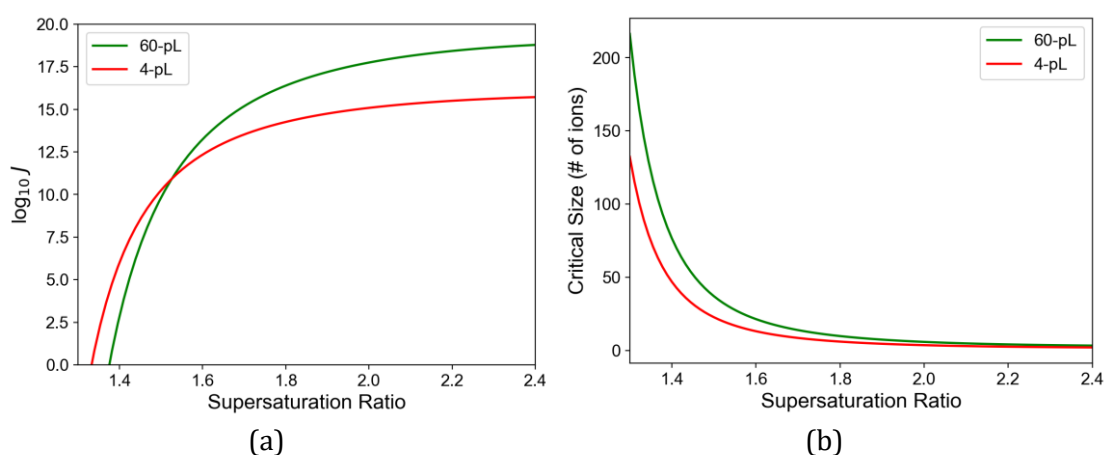
Furthermore, in the microcapillary experiments of Desarnaud et. al.<sup>73</sup>, they reported  $J = 0.004 \text{ m}^{-3}\text{s}^{-1}$  at  $S \approx 1.6$  but they fixed the value of  $\gamma$  at  $80 \text{ mJ/m}^2$ . Thus, to the best of our knowledge, our work is the first experimental work that employed a probabilistic approach to measure the interfacial energy between crystal and solution for NaCl-water system without assuming a fixed value of pre-exponential factor. This suggests that the commonly accepted experimental value of  $A$  and  $\gamma$  for NaCl crystallization may need to be re-examined. Given that the current theoretical simulations generally overestimate the experimental nucleation rates, our findings can serve as an additional benchmark leading to new insights which could bridge the gap between theory and experiments.

### 10.3.3 Observing Confinement Effects

Comparing the results for two microdroplet sizes, it is evident that the confinement effect plays a role. This is consistent with the fact that smaller volume can withstand higher degree of metastability and requires a higher supersaturation to nucleate<sup>20</sup>. In such confined environment, the formation of the pre-critical cluster depletes the effective supersaturation level of its surrounding.<sup>20</sup> This is reflected in the lower pre-exponential factor  $A$  for the 4 pL microdroplet by 3 orders of magnitude. Recall that the kinetic prefactor is related to the attachment frequency which depends on the diffusivity of the monomers to the cluster surface. Thus, as the effective monomer concentration is reduced, the attachment frequency also decreases. Surprisingly, the effective interfacial energy between crystal and solution  $\gamma_{\text{eff}}$  is lower for the smaller volume. As it is more difficult to form the critical nuclei in smaller volumes, one would intuitively expect a higher energy barrier. However, this could be rationalized in terms of heterogeneous nucleation



mechanism. This is supported by the plot of nucleation rate and critical size (from the fit presented in Table 10.1) as a function of supersaturation ratio in **Figure 10.4**. Higher supersaturation  $S$  generally favors homogeneous nucleation while lower  $S$  tends to favor heterogeneous mechanism. Thus, at lower  $S$ , the 4 pL microdroplet nucleates faster due to the lower energy barrier and high surface area to volume ratio (**Figure 10.4a**). However, at higher supersaturation, the homogeneous mechanism dominates while the energy barrier converges (**Figure 10.4b**), so the 4 pL microdroplet nucleates slower due to lower monomer attachment rates. Overall, we highlight that these interesting finite-size effects are clearly observable in our experimental approach and data treatment which would not be observed in bulk solution experiments. Overall, the data treatment of our experiments with CNT model allows us to have a better understanding of nucleation, providing kinetic and thermodynamic information on the NaCl/water system.



**Figure 10.4** Comparison of 60-pL and 4-pL microdroplet in terms of (a) nucleation rate ( $J$  in  $\text{m}^{-3}\text{s}^{-1}$ ) and (b) critical size (# of ions) as a function of supersaturation ratio. Curves come from the fit presented in Table 10.1

## 10.4 Conclusion

In this chapter, I proposed an approach to extract the nucleation kinetic parameters from the induction time distribution of evaporating sessile microdroplets, using NaCl-water as a model system. I showed that by combining a modified Poisson distribution analysis together with an accurate evaporation model, one can obtain reliable nucleation kinetic parameters (both kinetic and thermodynamic). For the experimental condition where I expect to have predominant homogeneous nucleation, I obtained a pre-exponential factor  $A$  of  $9.30 \times 10^{20} \text{ m}^{-3}\text{s}^{-1}$  and an interfacial energy between crystal and solution  $\gamma$  of  $46.7 \text{ mJ/m}^2$ . This is in remarkable agreement with existing experimental and theoretical values for NaCl-water system. Moreover, we are able to unravel experimentally the confinement effect when decreasing experimental volume from 60 to 4pL as well as a modification of nucleation mechanism from homogeneous to heterogeneous.

Given the numerous simulation studies on NaCl nucleation, our experimental kinetic parameters based on stochastic approach can serve as an additional benchmark in validating theoretical predictions. Moreover, our experimental approach and data-treatment protocol can also be extended to study the nucleation of other salts, biological, and pharmaceutical crystals of interest.

# Chapter 11

## Concluding Remarks and Perspective

Given the profound importance of nucleation in both industrial and scientific perspective, this thesis has shed light into the measurement and modeling of nucleation kinetics across different scales, techniques, and viewpoints.

### 11.1 Notable Findings

The key findings and advancements that I have achieved in this thesis can be summarized as follows.

#### 11.1.1. In Agitated crystallizers

In the context of industrial agitated crystallizers, a new method for treating primary and secondary nucleation was developed using in situ laser-backscattering (to monitor particle count) and Raman spectroscopy (to monitor solution concentration). Assuming that primary nucleation is a much weaker function of hydrodynamics, and that secondary nucleation varies exponentially with agitation rate, I proposed an extrapolation method for estimating primary nucleation kinetic parameters. The approach was tested on model systems *p*-aminobenzoic acid (in water/ethanol) and glutamic acid (in water). Indeed, an exponential dependence of the total nucleation rate with the agitation rate was experimentally observed. The order of magnitudes of extrapolated primary nucleation rates obtained were in agreement with the KBHR method which supports the validity of our approach.

To shed light into the interpretation of kinetic data, a multi-scale comparison of nucleation kinetics was performed across various techniques using *p*-aminobenzoic acid in water/ethanol as a model system. The results from the L-scale (particle-count and solution conductometry), the mL-scale (turbidimetry), and the  $\mu$ L-scale (in situ microscopy) revealed that the kinetic parameters are highly sensitive to the choice of technique and model assumptions. This suggests that in the interpretation of nucleation data in published literature, careful attention must be paid to the transferability of kinetic data especially in the scale-up and design of industrial crystallizers. This highlights that more research is needed to fully understand the influence of interfering variables (fluid dynamics, foreign surfaces, etc) in order to compare nucleation kinetic measurements obtained across different scales and techniques.

### **11.1.2. In microfluidics with evaporative pL-sized droplets**

To study homogeneous primary nucleation at a more fundamental level, I employed microfluidic techniques which aims to minimize the interference of heterogeneous and secondary nucleation. We used our in-house developed microfluidic setup to generate picoliter-sized sessile droplets, which can serve as microcrystallizers, and we performed induction time measurements using NaCl-water system. The droplets have been found to interact with each other via water diffusion dynamics. I have shown that failure to account for diffusion-mediated interactions can lead to severe errors in the measured nucleation parameters. Fortunately, these interactions can be eliminated by lowering the relative humidity, which provokes droplets evaporation.

To properly define induction time in our evaporative microcrystallizers, I developed an approach utilizing deliquescence-efflorescence cycles which allows the experimental determination of saturation time. The proposed method resulted in statistically reproducible induction time distribution. Possible effects of system impurities have been shown to be negligible.

To accurately measure the supersaturation ratio during nucleation, I developed an evaporation model that mathematically accounts for the additional complexities in our setup: (1) effect of oil thickness (2) influence of neighboring microdroplets (3) reduction of in water activity (4) evolution of microdroplet density. The model shows excellent agreement with the experimental data for both pure and saline microdroplets. Moreover, I show that simply assuming a constant evaporation can lead to large discrepancies in nucleation parameters.

To extract accurate nucleation kinetic parameters from our microdroplet experiment, I combined the deliquescence-efflorescence approach and the derived evaporation model together with a modified Poisson distribution which accounts for the time-dependence of the driving force. The resulting kinetic parameters, notably the interfacial energy between crystal and solution, are in excellent agreement with existing theoretical simulations. This is also the first report of nucleation kinetic parameters for NaCl-water system that considers the stochastic nature of nucleation, thereby serving as an additional benchmark in validating theoretical predictions. Additionally, the protocol allows the investigation of interesting finite-size effects on nucleation which is not possible in bulk solution studies. Moreover, it allows the experimental analysis of the interplay between heterogeneous and homogeneous mechanisms in confined environments.

## **11.2 Perspective**

In the scope of my thesis, I mainly focused on the quantification of nucleation kinetic parameters both from both industrial and fundamental point of view. Despite the considerable advances in the field, the full understanding of nucleation is far from complete. For further studies, here are my recommendations.

### **11.2.1 Influence of interfering variables in Agitated Crystallizers**

To further understand the effect of hydrodynamics on nucleation in the case of agitated crystallizers, computational fluid dynamics can be employed to understand the spatio-temporal aspects of nucleation with respect to shear rate and turbulence which may cause localized fluctuations of concentration and temperature. The effect of various agitation systems (overhead stirrer, magnetic stirrer, etc) as well as the turbulence induced by the probes/baffles must also be examined in detail to further understand the impact of hydrodynamics on nucleation kinetic measurements.

The surface area of the crystallizer, baffles, and impellers that are in contact with the solution can be investigated to determine how it influences the nucleation mechanism. A model that contains a scaling factor which accounts for the contact area of foreign surfaces can be developed. Other approaches to decouple primary and secondary nucleation can be useful.

### **11.2.1 Evaporative microdroplet experiments**

The evaporation model can be further tested for other solutes and medium. It can also be extended for multicomponent systems which contain a mixture of volatile and non-volatile species. For droplets directly evaporating in air, the enthalpy of vaporization and the change of temperature-dependent properties such as diffusivity and solubility must be taken as an additional parameter.

The influence of evaporate rate on the measured kinetic parameters, can be investigated by controlling the relative humidity. Some researchers argue that kinetic pre-exponential factors cannot be reliably obtained from experiments with time-varying supersaturation<sup>6</sup>. This can be refuted if the measured kinetic parameter would be shown to be independent with the rate of change of supersaturation.

Using the set-up developed, we can confirm the existing models of the confinement effect. Moreover, a threshold criterion which tells whether the confinement effect is significant or not for a given droplet size and nucleating compound must be developed.

For non-deliquescent compounds, a side-way in situ camera which allows real-time acquisition of droplet volume would be useful to measure the time at which the microdroplet is saturated.

## References

1. Zimmermann, N. E. R.; Vorselaars, B.; Espinosa, J. R.; Quigley, D.; Smith, W. R.; Sanz, E.; Vega, C.; Peters, B., NaCl nucleation from brine in seeded simulations: Sources of uncertainty in rate estimates. *The Journal of Chemical Physics* **2018**, *148* (22), 222838.
2. Karthika, S.; Radhakrishnan, T. K.; Kalaichelvi, P., A Review of Classical and Nonclassical Nucleation Theories. *Cryst. Growth Des.* **2016**, *16* (11), 6663.
3. Brandel, C.; ter Horst, J. H., Measuring induction times and crystal nucleation rates. *Faraday Discuss.* **2015**, *179*, 199-214.
4. Mullin, J. W., *Crystallization*. Elsevier Science: 2001.
5. Myerson AS, G. R., Allan SM, Crystal Growth and Nucleation. *Handbook of Industrial Crystallization* **2002**, *2nd ed*, 30.
6. Bhamidi, V.; Kenis, P. J. A.; Zukoski, C. F., Probability of Nucleation in a Metastable Zone: Induction Supersaturation and Implications. *Crystal Growth & Design* **2017**, *17* (3), 1132-1145.
7. Nývlt, J., Kinetics of nucleation in solutions. *J. Cryst. Growth* **1968**, 3-4 (Supplement C), 377-383.
8. Kubota, N., A new interpretation of metastable zone widths measured for unseeded solutions. *J. Cryst. Growth* **2008**, *310*, 629.
9. Sangwal, K., Novel Approach to Analyze Metastable Zone Width Determined by the Polythermal Method: Physical Interpretation of Various Parameters. *Cryst. Growth Des.* **2009**, *9* (2), 942.
10. Nagy, Z. K.; Fujiwara, M.; Braatz, R. D., Modelling and control of combined cooling and antisolvent crystallization processes. *J. Process Control* **2008**, *18*, 856.
11. Kim, K. J.; Mersmann, A., Estimation of Metastable Zone Width in Different Nucleation Processes. *Chem. Eng. Sci.* **2001**, *56* (7), 2315.
12. Kashchiev, D.; Borissova, A.; Hammond, R. B.; Roberts, K. J., Dependence of the Critical Undercooling for Crystallization on the Cooling Rate. *The Journal of Physical Chemistry B* **2010**, *114* (16), 5441-5446.
13. Peters, F. In *Nucleation and growth rates from shock tube experiments*, Atmospheric Aerosols and Nucleation, Berlin, Heidelberg, 1988//; Wagner, P. E.; Vali, G., Eds. Springer Berlin Heidelberg: Berlin, Heidelberg, 1988; pp 535-537.
14. Maggioni, G. M.; Mazzotti, M., Stochasticity in Primary Nucleation: Measuring and Modeling Detection Times. *Crystal Growth & Design* **2017**, *17* (7), 3625-3635.
15. Salvalaglio, M.; Perego, C.; Giberti, F.; Mazzotti, M.; Parrinello, M., Molecular-dynamics simulations of urea nucleation from aqueous solution. *Proc. Natl. Acad. Sci. U. S. A.* **2015**, *112*, E6.
16. Salvalaglio, M.; Tiwary, P.; Maggioni, G. M.; Mazzotti, M.; Parrinello, M., Overcoming time scale and finite size limitations to compute nucleation rates from small scale well tempered metadynamics simulations. *J. Chem. Phys.* **2016**, *145*, 211925.
17. Kubota, N., Monte Carlo simulation of induction time and metastable zone width; stochastic or deterministic? *J. Cryst. Growth* **2018**, *485*, 1-7.
18. Sosso, G. C.; Chen, J.; Cox, S. J.; Fitzner, M.; Pedevilla, P.; Zen, A.; Michaelides, A., Crystal Nucleation in Liquids: Open Questions and Future Challenges in Molecular Dynamics Simulations. *Chem. Rev.* **2016**, *116* (12), 7078-7116.
19. Hammadi, Z.; Grossier, R.; Zhang, S.; Ikni, A.; Candoni, N.; Morin, R.; Veessler, S., Localizing and inducing primary nucleation. *Faraday Discuss.* **2015**, *179* (0), 489-501.

20. Grossier, R.; Veessler, S., Reaching One Single and Stable Critical Cluster through Finite-Sized Systems. *Crystal Growth & Design* **2009**, *9* (4), 1917-1922.
21. Grossier, R.; Tishkova, V.; Morin, R.; Veessler, S., A parameter to probe microdroplet dynamics and crystal nucleation. *AIP Advances* **2018**, *8* (7), 075324.
22. Hammadi, Z.; Candoni, N.; Grossier, R.; Ildefonso, M.; Morin, R.; Veessler, S., Small-volume nucleation. *C. R. Phys.* **2013**, *14*, 192.
23. Grossier, R.; Hammadi, Z.; Morin, R.; Veessler, S., Predictive Nucleation of Crystals in Small Volumes and Its Consequences. *Phys. Rev. Lett.* **2011**, *107* (2), 025504.
24. Nanev, C. N.; Nishinaga, T., Theory of nucleation. *Handbook Of Crystal Growth, Volume 1 A, Fundamentals: Thermodynamics And Kinetics* **2015**, 315-358.
25. Kashchiev, D., *Nucleation: Basic Theory with Applications*. 2000.
26. Barton, A. F., *CRC Handbook of Solubility Parameters and Other Cohesion Parameters*. 1991; p 278.
27. Myerson, A., *Handbook of Industrial Crystallization*. Elsevier Science: 2002.
28. Georgieva, D. G.; Kuil, M. E.; Oosterkamp, T. H.; Zandbergen, H. W.; Abrahams, J. P., Heterogeneous nucleation of three-dimensional protein nanocrystals. *Acta Crystallogr. D* **2007**, *63*, 564-570.
29. Kadam, S. S.; Kramer, H. J. M.; ter Horst, J. H., Combination of a Single Primary Nucleation Event and Secondary Nucleation in Crystallization Processes. *Cryst. Growth Des.* **2011**, *11*, 1271.
30. Li, H.; Kawajiri, Y.; Grover, M. A.; Rousseau, R. W., Modeling of Nucleation and Growth Kinetics for Unseeded Batch Cooling Crystallization. *Industrial & Engineering Chemistry Research* **2017**, *56* (14), 4060-4073.
31. Volmer, M.; Weber, A., *Z. Phys. Chem.* **1926**, *119*, 277.
32. Becker, R.; Döring, W., *Ann. Phys.* **1935**, *24* (719), 752.
33. Frenkel, J., *J. Chem. Phys.* **1939**, *7* (7), 538.
34. Meldrum, F. C.; O'Shaughnessy, C., Crystallization in Confinement. *Adv. Mater.* **2020**, *32* (31), 2001068.
35. Ildefonso, M.; Candoni, N.; Veessler, S., Heterogeneous Nucleation in Droplet-Based Nucleation Measurements. *Crystal Growth & Design* **2013**, *13* (5), 2107-2110.
36. Kashchiev, D.; Rosmalen, G., Review: Nucleation in solutions revisited. *Cryst. Res. Technol.* **2003**, *38* (7-8), 555-574.
37. Vekilov, P. G., The Two-Step Mechanism of Nucleation of Crystals in Solution. *Nanoscale* **2010**, *2* (11), 2346.
38. Camacho, D. M.; Roberts, K. J.; More, I.; Lewtas, K., Solubility and Nucleation of Methyl Stearate as a Function of Crystallization Environment. *Energy & Fuels* **2018**, *32* (3), 3447-3459.
39. Revalor, E.; Hammadi, Z.; Astier, J.-P.; Grossier, R.; Garcia, E.; Hoff, C.; Furuta, K.; Okustu, T.; Morin, R.; Veessler, S., Usual and unusual crystallization from solution. *J. Cryst. Growth* **2010**, *312* (7), 939-946.
40. Dixit, N. M.; Kulkarni, A. M.; Zukoski, C. F., Comparison of experimental estimates and model predictions of protein crystal nucleation rates. *Colloids and Surfaces A: Physicochemical and Engineering Aspects* **2001**, *190* (1), 47-60.
41. Sear, R. P., Quantitative studies of crystal nucleation at constant supersaturation: experimental data and models. *CrystEngComm* **2014**, *16* (29), 6506-6522.
42. Kodera, T.; Kobari, M.; Hirasawa, I., Experimental Estimation of Primary and Secondary Nucleation Kinetics of Antisolvent Crystallization As Measured by Induction Time. *Organic Process Research & Development* **2019**, *23* (12), 2724-2732.



43. Kaskiewicz, P. L.; Xu, G.; Lai, X.; Warren, N. J.; Roberts, K. J.; Morton, C.; Dowding, P.; George, N., Isothermal by Design: An Accelerated Approach to the Prediction of the Crystallizability of Slowly Nucleating Systems. *Organic Process Research & Development* **2019**, *23* (9), 1948-1959.
44. Kulkarni, S.; Kadam, S.; Meekes, H.; Stankiewicz, A.; ter Horst, J., Crystal Nucleation Kinetics from Induction Times and Metastable Zone Widths. *Cryst. Growth Des.* **2013**, *13*, 2435.
45. Goh, L.; Chen, K.; Bhamidi, V.; He, G.; Kee, N. C.; Kenis, P. J.; Zukoski, C. F., 3rd; Braatz, R. D., A Stochastic Model for Nucleation Kinetics Determination in Droplet-Based Microfluidic Systems. *Cryst. Growth Des.* **2010**, *10* (6), 2515-2521.
46. Jacob, P., Probability and Statistics for Engineers and Scientists (9th Edition). *CHANCE* **2013**, *26* (3), 53-53.
47. Leng, J.; Salmon, J. B., Microfluidic Crystallization. *Lab Chip* **2009**, *9* (1), 24.
48. Laval, P.; Salmon, J. B.; Joanicot, M., A microfluidic device for investigating crystal nucleation kinetics. *J. Cryst. Growth* **2007**, *303*, 622.
49. Shim, J.; Cristobal, G.; Link, D. R.; Thorsen, T.; Fraden, S., Using Microfluidics to Decouple Nucleation and Growth of Protein Crystals. *Cryst. Growth Des.* **2007**, *7*, 2192.
50. Shi, H.-h.; Xiao, Y.; Ferguson, S.; Huang, X.; Wang, N.; Hao, H.-x., Progress of crystallization in microfluidic devices. *Lab on a Chip* **2017**, *17* (13), 2167-2185.
51. Ildefonso, M.; Candoni, N.; Veessler, S., A Cheap, Easy Microfluidic Crystallization Device Ensuring Universal Solvent Compatibility. *Org. Process Res. Dev.* **2012**, *16*, 556.
52. Zhang, S.; Gerard, C. J. J.; Ikni, A.; Ferry, G.; Vuillard, L. M.; Boutin, J. A.; Ferte, N.; Grossier, R.; Candoni, N.; Veessler, S., Microfluidic platform for optimization of crystallization conditions. *J. Cryst. Growth* **2017**, *472*, 18-28.
53. Boel, E.; Koekoekx, R.; Dedroog, S.; Babkin, I.; Vetrano, M. R.; Clasen, C.; Van den Mooter, G., Unraveling Particle Formation: From Single Droplet Drying to Spray Drying and Electrospraying. *Pharmaceutics* **2020**, *12* (7), 625.
54. Li, W.; Zhang, L.; Ge, X.; Xu, B.; Zhang, W.; Qu, L.; Choi, C.-H.; Xu, J.; Zhang, A.; Lee, H.; Weitz, D. A., Microfluidic fabrication of microparticles for biomedical applications. *Chem. Soc. Rev.* **2018**, *47* (15), 5646-5683.
55. Rossi, D.; Gavriilidis, A.; Kuhn, S.; Candel, M. A.; Jones, A. G.; Price, C.; Mazzei, L., Adipic Acid Primary Nucleation Kinetics from Probability Distributions in Droplet-Based Systems under Stagnant and Flow Conditions. *Crystal Growth & Design* **2015**, *15* (4), 1784-1791.
56. Zhu, P.; Wang, L., Passive and active droplet generation with microfluidics: a review. *Lab on a Chip* **2017**, *17* (1), 34-75.
57. Candoni, N.; Grossier, R.; Lagaize, M.; Veessler, S., Advances in the Use of Microfluidics to Study Crystallization Fundamentals. *Annual Review of Chemical and Biomolecular Engineering* **2019**, *10* (1), 59-83.
58. Tsao, C. W., Polymer Microfluidics: Simple, Low-Cost Fabrication Process Bridging Academic Lab Research to Commercialized Production. *Micromachines (Basel)* **2016**, *7* (12).
59. Niculescu, A.-G.; Chircov, C.; Bîrcă, A. C.; Grumezescu, A. M., Fabrication and Applications of Microfluidic Devices: A Review. *International Journal of Molecular Sciences* **2021**, *22* (4), 2011.
60. Peybernès, G.; Grossier, R.; Villard, F.; Letellier, P.; Lagaize, M.; Candoni, N.; Veessler, S., Microfluidics Setup Rapidly Measures Solubility Directly from Powder. *Organic Process Research & Development* **2018**.

61. Peybernes, G.; Grossier, R.; Villard, F.; Letellier, P.; Candoni, N.; Veesler, S., Microfluidics Platform for Polymorph Screening Directly from Powder. *Crystal Growth & Design* **2020**, *20* (6), 3882-3887.
62. Zhang, Q.; Feng, S.; Lin, L.; Mao, S.; Lin, J.-M., Emerging open microfluidics for cell manipulation. *Chem. Soc. Rev.* **2021**, *50* (9), 5333-5348.
63. Grossier, R.; Hammadi, Z.; Morin, R.; Magnaldo, A.; Veesler, S., Generating nanoliter to femtoliter microdroplets with ease. *Appl. Phys. Lett.* **2011**, *98* (9), 091916.
64. Stauber, J. M.; Wilson, S. K.; Duffy, B. R.; Sefiane, K., On the lifetimes of evaporating droplets with related initial and receding contact angles. *Physics of Fluids* **2015**, *27* (12), 122101.
65. Picknett, R. G.; Bexon, R., The evaporation of sessile or pendant drops in still air. *J. Colloid Interface Sci.* **1977**, *61*, 336.
66. Popov, Y. O., Evaporative deposition patterns: Spatial dimensions of the deposit. *Physical Review E* **2005**, *71* (3), 036313.
67. Nguyen, T. A. H.; Nguyen, A. V., On the lifetime of evaporating sessile droplets. *Langmuir* **2012**, *28*, 1924.
68. Toroz, D.; Rosbottom, I.; Turner, T. D.; Corzo, D. M.; Hammond, R. B.; Lai, X.; Roberts, K. J., Towards an understanding of the nucleation of alpha-para amino benzoic acid from ethanolic solutions: a multi-scale approach. *Faraday Discuss.* **2015**, *179*, 79-114.
69. Sullivan, R.; Davey, R.; Sadiq, G.; Dent, G.; Back, K.; ter Horst, J.; Toroz, D.; Hammond, R., Revealing the Roles of Desolvation and Molecular Self-Assembly in Crystal Nucleation from Solution: Benzoic and p-Aminobenzoic Acids. *Cryst. Growth Des.* **2014**, *14*, 2689.
70. Ault, A., The Monosodium Glutamate Story: The Commercial Production of MSG and Other Amino Acids. *J. Chem. Educ.* **2004**, *81* (3), 347.
71. Schöll, J.; Vicum, L.; Müller, M.; Mazzotti, M., Precipitation of L-Glutamic Acid: Determination of Nucleation Kinetics. *Chemical Engineering & Technology* **2006**, *29* (2), 257-264.
72. Shi, H.; Li, F.; Huang, X.; Wang, T.; Bao, Y.; Yin, Q.; Xie, C.; Hao, H., Screening and Manipulation of L-Glutamic Acid Polymorphs by Antisolvent Crystallization in an Easy-to-Use Microfluidic Device. *Industrial & Engineering Chemistry Research* **2020**, *59* (13), 6102-6111.
73. Desarnaud, J.; Derluyn, H.; Carmeliet, J.; Bonn, D.; Shahidzadeh, N., Metastability Limit for the Nucleation of NaCl Crystals in Confinement. *The Journal of Physical Chemistry Letters* **2014**, *5* (5), 890-895.
74. Han, J.; Carey, J. W.; Zhang, J., Effect of sodium chloride on corrosion of mild steel in CO<sub>2</sub>-saturated brines. *J. Appl. Electrochem.* **2011**, *41* (6), 741-749.
75. Shen, Y.; Linnow, K.; Steiger, M., Crystallization Behavior and Damage Potential of Na<sub>2</sub>SO<sub>4</sub>-NaCl Mixtures in Porous Building Materials. *Crystal Growth & Design* **2020**, *20* (9), 5974-5985.
76. Qazi, M. J.; Liefferink, R. W.; Schlegel, S. J.; Backus, E. H. G.; Bonn, D.; Shahidzadeh, N., Influence of Surfactants on Sodium Chloride Crystallization in Confinement. *Langmuir* **2017**, *33* (17), 4260-4268.
77. Schulz, M.; de Leeuw, G.; Balkanski, Y. In *Sea-salt aerosol source functions and emissions*, Emissions of Atmospheric Trace Compounds, Dordrecht, 2004//; Granier, C.; Artaxo, P.; Reeves, C. E., Eds. Springer Netherlands: Dordrecht, 2004; pp 333-359.
78. Lide, D. R.; Haynes, W., *CRC Handbook of Chemistry and Physics*. 2010.
79. Watson, J. M.; Baron, M. G., The behaviour of water in poly(dimethylsiloxane). *Journal of Membrane Science* **1996**, *110* (1), 47-57.

80. Randall, G. C.; Doyle, P. S., Permeation-driven flow in poly(dimethylsiloxane) microfluidic devices. *Proceedings of the National Academy of Sciences of the United States of America* **2005**, *102* (31), 10813-10818.
81. Li, H.; Grover, M.; Kawajiri, Y.; Rousseau, R. W., Development of an empirical method relating crystal size distributions and FBRM measurements. *Chem. Eng. Sci.* **2013**, *89*, 142.
82. Larsen, P. A.; Rawlings, J. B.; Ferrier, N. J., An algorithm for analyzing noisy, in situ images of high-aspect-ratio crystals to monitor particle size distribution. *Chem. Eng. Sci.* **2006**, *61*, 5236.
83. Kempkes, M.; Eggers, J.; Mazzotti, M., Measurement of particle size and shape by FBRM and in situ microscopy. *Chem. Eng. Sci.* **2008**, *63* (19), 4656.
84. Adlington, N. K.; Black, S. N.; Adshead, D. L., How To Use the Lasentec FBRM Probe on Manufacturing Scale. *Org. Process Res. Dev.* **2013**, *17*, 557.
85. Cornel, J.; Lindenberg, C.; Mazzotti, M., Quantitative application of in situ ATR-FTIR and raman spectroscopy in crystallization processes. *Ind. Eng. Chem. Res.* **2008**, *47* (14), 4870.
86. De Beer, T.; Burggraeve, A.; Fonteyne, M.; Saerens, L.; Remon, J. P.; Vervaet, C., Near infrared and Raman spectroscopy for the in-process monitoring of pharmaceutical production processes. *Int. J. Pharm.* **2011**, *417*, 32.
87. Qu, H.; Alatalo, H.; Hatakka, H.; Kohonen, J.; Louhi-Kultanen, M.; Reinikainen, S. P.; Kallas, J., Raman and ATR FTIR spectroscopy in reactive crystallization: Simultaneous monitoring of solute concentration and polymorphic state of the crystals. *J. Cryst. Growth* **2009**, *311*, 3466.
88. Simone, E.; Saleemi, A. N.; Nagy, Z. K., In situ monitoring of polymorphic transformations using a composite sensor array of Raman, NIR, ATR-UV/Vis spectroscopy, FBRM and PVM, for an intelligent decision support system. *Org. Process Res. Dev.* **2014**.
89. Saerens, L.; Dierickx, L.; Lenain, B.; Vervaet, C.; Remon, J. P.; Beer, T. D., Raman spectroscopy for the in-line polymer–drug quantification and solid state characterization during a pharmaceutical hot-melt extrusion process. *Eur. J. Pharm. Biopharm.* **2011**, *77*, 158.
90. Wang, F.; Wachter, J. A.; Antosz, F. J.; Berglund, K. A., An Investigation of Solvent-Mediated Polymorphic Transformation of Progesterone Using in Situ Raman Spectroscopy. *Org. Process Res. Dev.* **2000**, *4*, 391.
91. Gherras, N.; Fevotte, G., Comparison between approaches for the experimental determination of metastable zone width: A case study of the batch cooling crystallization of ammonium oxalate in water. *J. Cryst. Growth* **2012**, *342* (1), 88-98.
92. Randolph, A. D.; Cise, M. D., Nucleation kinetics of the potassium sulfate-water system. *AIChE J.* **1972**, *18* (4), 798-807.
93. Forsyth, C.; Burns, I. S.; Mulheran, P. A.; Sefcik, J., Scaling of Glycine Nucleation Kinetics with Shear Rate and Glass–Liquid Interfacial Area. *Crystal Growth & Design* **2016**, *16* (1), 136-144.
94. Stroobants, S.; Callewaert, M.; Krzek, M.; Chinnu, S.; Gelin, P.; Ziemecka, I.; Lutsko, J. F.; De Malsche, W.; Maes, D., Influence of Shear on Protein Crystallization under Constant Shear Conditions. *Crystal Growth & Design* **2020**, *20* (3), 1876-1883.
95. Nappo, V.; Sullivan, R.; Davey, R.; Kuhn, S.; Gavriilidis, A.; Mazzei, L., Effect of shear rate on primary nucleation of para-amino benzoic acid in solution under different fluid dynamic conditions. *Chem. Eng. Res. Des.* **2018**, *136*, 48-56.
96. Turner, T. D.; Corzo, D. M. C.; Toroz, D.; Curtis, A.; Dos Santos, M. M.; Hammond, R. B.; Lai, X.; Roberts, K. J., The influence of solution environment on the nucleation kinetics and crystallisability of para-aminobenzoic acid. *Phys. Chem. Chem. Phys.* **2016**, *18* (39), 27507-27520.

97. Di Profio, G.; Curcio, E.; Ferraro, S.; Stabile, C.; Drioli, E., Effect of supersaturation control and heterogeneous nucleation on porous membrane surfaces in the crystallization of L-glutamic acid polymorphs. *Cryst. Growth Des.* **2009**, *9*, 2179-2186.
98. Ono, T.; ter Horst, J. H.; Jansens, P. J., Quantitative measurement of the polymorphic transformation of L-glutamic acid using in-situ Raman spectroscopy. *Cryst. Growth Des.* **2004**, *4*, 465.
99. Mo, Y.; Dang, L.; Wei, H., L-Glutamic Acid Polymorph Control Using Amino Acid Additives. *Industrial & Engineering Chemistry Research* **2011**, *50* (18), 10385-10392.
100. Peda, S.; Crumeyrolle-Smieszek, M.; Stollberg, C.; Ay, P., *Interpretation of fbrm and 3d orm smf data via simulated nucleation and crystal growth* Proceedings of International Workshop on Industrial Crystallization, BIWIC 2010: 2010; Vol. 14, p 1-55.
101. Worlitschek, J.; Hocker, T.; Mazzotti, M., Restoration of PSD from chord length distribution data using the method of projections onto convex sets. *Part. Part. Syst. Charact.* **2005**, *22*, 81.
102. Scholl, J.; Bonalumi, D.; Vicum, L.; Mazzotti, M., In Situ Monitoring and Modeling of the Solvent-Mediated Polymorphic Transformation of L -Glutamic Acid. *Cryst. Growth Des.* **2006**, *6*, 881.
103. Hao, H.; Barrett, M.; Hu, Y.; Su, W.; Ferguson, S.; Wood, B.; Glennon, B., The Use of in Situ Tools To Monitor the Enantiotropic Transformation of p-Aminobenzoic Acid Polymorphs. *Organic Process Research & Development* **2012**, *16* (1), 35-41.
104. Schöll, J.; Bonalumi, D.; Vicum, L.; Mazzotti, M.; Müller, M., In Situ Monitoring and Modeling of the Solvent-Mediated Polymorphic Transformation of L-Glutamic Acid. *Crystal Growth & Design* **2006**, *6* (4), 881-891.
105. Dolenko, T. A.; Burikov, S. A.; Dolenko, S. A.; Efitorov, A. O.; Plastinin, I. V.; Yuzhakov, V. I.; Patsaeva, S. V., Raman Spectroscopy of Water–Ethanol Solutions: The Estimation of Hydrogen Bonding Energy and the Appearance of Clathrate-like Structures in Solutions. *The Journal of Physical Chemistry A* **2015**, *119* (44), 10806-10815.
106. Xia, Y.; Xiujuan, W.; Bun, C. C., In situ monitoring of solid-state transition of p-aminobenzoic acid polymorphs using Raman spectroscopy. *Journal of Raman Spectroscopy* **2009**, *40* (8), 870-875.
107. Jiang, S.; ter Horst, J., Crystal Nucleation Rates from Probability Distributions of Induction Times. *Cryst. Growth Des.* **2011**, *11*, 256.
108. Toshev, S.; Milchev, A.; Stoyanov, S., On some probabilistic aspects of the nucleation process. *J. Cryst. Growth* **1972**, *13-14* (Supplement C), 123-127.
109. Kulkarni, S. A.; Kadam, S. S.; Meekes, H.; Stankiewicz, A. I.; ter Horst, J. H., Crystal Nucleation Kinetics from Induction Times and Metastable Zone Widths. *Crystal Growth & Design* **2013**, *13* (6), 2435-2440.
110. Kubota, N., Analysis of the effect of volume on induction time and metastable zone width using a stochastic model. *J. Cryst. Growth* **2015**, *418*, 15-24.
111. Pino-García, O.; Rasmuson, Å. C., Primary Nucleation of Vanillin Explored by a Novel Multicell Device. *Industrial & Engineering Chemistry Research* **2003**, *42* (20), 4899-4909.
112. Jiang, S.; ter Horst, J. H., Crystal Nucleation Rates from Probability Distributions of Induction Times. *Crystal Growth & Design* **2011**, *11* (1), 256-261.
113. Teychené, S.; Biscans, B., Microfluidic Device for the Crystallization of Organic Molecules in Organic Solvents. *Crystal Growth & Design* **2011**, *11* (11), 4810-4818.
114. Chen, K.; Goh, L.; He, G.; Kenis, P. J. A.; Zukoski, C. F.; Braatz, R. D., Identification of nucleation rates in droplet-based microfluidic systems. *Chem. Eng. Sci.* **2012**, *77* (Supplement C), 235-241.

115. Lu, J.; Litster, J. D.; Nagy, Z. K., Nucleation Studies of Active Pharmaceutical Ingredients in an Air-Segmented Microfluidic Drop-Based Crystallizer. *Crystal Growth & Design* **2015**, *15* (8), 3645-3651.
116. Capellades, G.; Kiil, S.; Dam-Johansen, K.; Mealy, M. J.; Christensen, T. V.; Myerson, A. S., Effect of Air Injection on Nucleation Rates: An Approach from Induction Time Statistics. *Crystal Growth & Design* **2017**, *17* (6), 3287-3294.
117. Stojaković, J.; Baftizadeh, F.; Bellucci, M. A.; Myerson, A. S.; Trout, B. L., Angle-Directed Nucleation of Paracetamol on Biocompatible Nanoimprinted Polymers. *Crystal Growth & Design* **2017**, *17* (6), 2955-2963.
118. Patel, M. A.; Nguyen, B.; Chadwick, K., Predicting the Nucleation Induction Time Based on Preferred Intermolecular Interactions. *Crystal Growth & Design* **2017**, *17* (9), 4613-4621.
119. Xiao, Y.; Tang, S. K.; Hao, H.; Davey, R. J.; Vetter, T., Quantifying the Inherent Uncertainty Associated with Nucleation Rates Estimated from Induction Time Data Measured in Small Volumes. *Crystal Growth & Design* **2017**, *17* (5), 2852-2863.
120. Maggioni, G.; Mazzotti, M., Modelling the stochastic behaviour of primary nucleation. *Faraday Discuss.* **2015**, *179*, 359.
121. Brandel, C.; ter Horst, J., Measuring induction times and crystal nucleation rates. *Faraday Discuss.* **2015**, *179*, 199.
122. Sullivan, R. Molecules, Clusters and Crystals: The Crystallisation of p-aminobenzoic acid from Solution. University of Manchester, United Kingdom, 2015.
123. Kadam, S. S.; Kulkarni, S. A.; Coloma Ribera, R.; Stankiewicz, A. I.; ter Horst, J. H.; Kramer, H. J. M., A new view on the metastable zone width during cooling crystallization. *Chem. Eng. Sci.* **2012**, *72*, 10.
124. Steendam, R. R. E.; Keshavarz, L.; Blijlevens, M. A. R.; de Souza, B.; Croker, D. M.; Frawley, P. J., Effects of Scale-Up on the Mechanism and Kinetics of Crystal Nucleation. *Crystal Growth & Design* **2018**, *18* (9), 5547-5555.
125. Rossi, D.; Gavriilidis, A.; Kuhn, S.; Candel, M.; Jones, A.; Price, C.; Mazzei, L., Adipic Acid Primary Nucleation Kinetics from Probability Distributions in Droplet-Based Systems under Stagnant and Flow Conditions. *Cryst. Growth Des.* **2015**, *15*, 1784.
126. Gary Morris; Graham Power; Steven Ferguson; Mark Barrett; Guangyang Hou; Glennon, B., Estimation of Nucleation and Growth Kinetics of Benzoic Acid by Population Balance Modeling of a Continuous Cooling Mixed Suspension, Mixed Product Removal Crystallizer. *Organic Process Research & Development* **2015**, *19* (12), 1891-1902.
127. Mitchell, N. A.; Frawley, P. J.; Ó'Ciardhá, C. T., Nucleation kinetics of paracetamol-ethanol solutions from induction time experiments using Lasentec FBRM®. *J. Cryst. Growth* **2011**, *321* (1), 91-99.
128. Mitchell, N. A.; Frawley, P. J., Nucleation kinetics of paracetamol-ethanol solutions from metastable zone widths. *J. Cryst. Growth* **2010**, *312* (19), 2740-2746.
129. Nagy, Z. K.; Fujiwara, M.; Woo, X. Y.; Braatz, R. D., Determination of the kinetic parameters for the crystallization of paracetamol from water using metastable zone width experiments. *Ind. Eng. Chem. Res.* **2008**, *47*, 1245.
130. Jun-Woo, K.; Jungwook, K.; Keun-Deuk, L.; Kee-Kahb, K., Evaluation of nucleation rate by in-situ focused beam reflectance measurement in an unseeded batch cooling crystallization. *Cryst. Res. Technol.* **2013**, *48* (12), 1097-1105.
131. Lindenberg, C.; Mazzotti, M., Continuous precipitation of L-asparagine monohydrate in a micromixer: Estimation of nucleation and growth kinetics. *AIChE J.* **2011**, *57* (4), 942-950.
132. Wantha, L.; Flood, A. E., Nucleation Kinetics of the  $\gamma$ -Polymorph of DL-Methionine. *Chemical Engineering & Technology* **2012**, *35* (6), 1024-1030.

133. Roelands, C. P. M.; Roestenberg, R. R. W.; ter Horst, J. H.; Kramer, H. J. M.; Jansens, P. J., Development of an Experimental Method to Measure Nucleation Rates in Reactive Precipitation. *Crystal Growth & Design* **2004**, *4* (5), 921-928.
134. Blandin, A. F.; Mangin, D.; Nallet, V.; Klein, J. P.; Bossoutrot, J. M., Kinetics identification of salicylic acid precipitation through experiments in a batch stirred vessel and a T-mixer. *Chem. Eng. J.* **2001**, *81* (1), 91-100.
135. Maggioni, G. M.; Bosetti, L.; dos Santos, E.; Mazzotti, M., Statistical Analysis of Series of Detection Time Measurements for the Estimation of Nucleation Rates. *Crystal Growth & Design* **2017**, *17* (10), 5488-5498.
136. Little, L. J.; Sear, R. P.; Keddie, J. L., Does the  $\gamma$  Polymorph of Glycine Nucleate Faster? A Quantitative Study of Nucleation from Aqueous Solution. *Crystal Growth & Design* **2015**, *15* (11), 5345-5354.
137. Erdemir, D.; Lee, A. Y.; Myerson, A. S., Nucleation of crystals from solution: classical and two-step models. *Acc. Chem. Res.* **2009**, *42*, 621.
138. Davey, R.; Back, K.; Sullivan, R., Crystal nucleation from solutions - transition states, rate determining steps and complexity. *Faraday Discuss.* **2015**, *179*, 9.
139. Vekilov, P. G., Nucleation. *Cryst. Growth Des.* **2010**, *10*, 5007.
140. Lewis A.; Seckler, M.; Kramer, H.; Rosmalen, G., Industrial Crystallization: Fundamentals and Applications. *Cambridge University Press, Cambridge UK* **2015**, 76-77.
141. Lindenberg, C.; Mazzotti, M., Effect of temperature on the nucleation kinetics of  $\alpha$  l-glutamic acid. *J. Cryst. Growth* **2009**, *311* (4), 1178-1184.
142. Morris, G.; Power, G.; Ferguson, S.; Barrett, M.; Hou, G.; Glennon, B., Estimation of Nucleation and Growth Kinetics of Benzoic Acid by Population Balance Modeling of a Continuous Cooling Mixed Suspension, Mixed Product Removal Crystallizer. *Organic Process Research & Development* **2015**, *19* (12), 1891-1902.
143. Lenka, M.; Sarkar, D., Determination of metastable zone width, induction period and primary nucleation kinetics for cooling crystallization of l-asparaginohydrate. *J. Cryst. Growth* **2014**, *408*, 85-90.
144. Roelands, C. P. M.; ter Horst, J. H.; Kramer, H. J. M.; Jansens, P. J., Analysis of Nucleation Rate Measurements in Precipitation Processes. *Crystal Growth & Design* **2006**, *6* (6), 1380-1392.
145. Maggioni, G. M.; Mazzotti, M., Stochasticity in Primary Nucleation: Measuring and Modeling Detection Times. *Cryst. Growth Des.* **2017**, *17*, 3625.
146. Sun, W.; Booth, S.; Myerson, A.; Hughes, C.; Pan, H.; Coquerel, G.; Brandel, C.; Meekes, H.; Mazzotti, M.; Fabian, L., Time and Space Resolved Methods: General Discussion. *Faraday Discuss.* **2015**, *179*, 247.
147. Kulkarni, S.; Meekes, H.; ter Horst, J., Polymorphism Control through a Single Nucleation Event. *Cryst. Growth Des.* **2014**, *14*, 1493.
148. Camacho Corzo, D. M.; Borissova, A.; Hammond, R. B.; Kashchiev, D.; Roberts, K. J.; Lewtas, K.; More, I., Nucleation Mechanism and Kinetics from the Analysis of Polythermal Crystallisation Data: Methyl Stearate from Kerosene Solutions. *CrystEngComm* **2014**, *16* (6), 974.
149. Du, P.; Kibbe, W. A.; Lin, S. M., Improved peak detection in mass spectrum by incorporating continuous wavelet transform-based pattern matching. *Bioinformatics* **2006**, *22* (17), 2059-2065.
150. Soulié, V.; Karpitschka, S.; Lequien, F.; Prené, P.; Zemb, T.; Moehwald, H.; Riegler, H., The evaporation behavior of sessile droplets from aqueous saline solutions. *Phys. Chem. Chem. Phys.* **2015**, *17* (34), 22296-22303.

151. Talreja, S.; Kim, D. Y.; Mirarefi, A. Y.; Zukoski, C. F.; Kenis, P. J. A., Screening and optimization of protein crystallization conditions through gradual evaporation using a novel crystallization platform. *J. Appl. Crystallogr.* **2005**, *38* (6), 988-995.
152. Rodríguez-Ruiz, I.; Hammadi, Z.; Grossier, R.; Gómez-Morales, J.; Veessler, S., Monitoring Picoliter Sessile Microdroplet Dynamics Shows That Size Does Not Matter. *Langmuir* **2013**, *29* (41), 12628-12632.
153. Grossier R.; Magnaldo A.; veessler S, Ultra-fast crystallization due to Confinement. *J. Crystal Growth* **2010**, *312*, 487-489.
154. McGraw, R.; Lewis, E. R., Deliquescence and efflorescence of small particles. *The Journal of Chemical Physics* **2009**, *131* (19), 194705.
155. Scholz, F. W.; Stephens, M. A., K-Sample Anderson–Darling Tests. *Journal of the American Statistical Association* **1987**, *82* (399), 918-924.
156. Babu, G. J.; Feigelson, E. D. In *Astrostatistics: Goodness-of-Fit and All That!*, July 01, 2006; 2006; p 127.
157. BRESLOW, N., A generalized Kruskal-Wallis test for comparing K samples subject to unequal patterns of censorship. *Biometrika* **1970**, *57* (3), 579-594.
158. Fan, C.; Zhang, D.; Zhang, C.-H., On Sample Size of the Kruskal-Wallis Test with Application to a Mouse Peritoneal Cavity Study. *Biometrics* **2011**, *67* (1), 213-224.
159. Wijekularathna, D. K.; Manage, A. B. W.; Scariano, S. M., Power analysis of several normality tests: A Monte Carlo simulation study. *Communications in Statistics - Simulation and Computation* **2019**, 1-17.
160. Ghasemi, A.; Zahediasl, S., Normality tests for statistical analysis: a guide for non-statisticians. *International journal of endocrinology and metabolism* **2012**, *10* (2), 486-489.
161. Kuhs, M.; Zeglinski, J.; Rasmuson, Å. C., Influence of History of Solution in Crystal Nucleation of Fenoxycarb: Kinetics and Mechanisms. *Crystal Growth & Design* **2014**, *14* (3), 905-915.
162. Davey, R. J.; Back, K. R.; Sullivan, R. A., Crystal nucleation from solutions - transition states, rate determining steps and complexity. *Faraday Discuss.* **2015**, *179* (0), 9-26.
163. Na, H.-S.; Arnold, S.; Myerson, A. S., Cluster formation in highly supersaturated solution droplets. *J. Cryst. Growth* **1994**, *139* (1), 104-112.
164. Zimmermann, N. E. R.; Vorselaars, B.; Quigley, D.; Peters, B., Nucleation of NaCl from Aqueous Solution: Critical Sizes, Ion-Attachment Kinetics, and Rates. *JACS* **2015**, *137* (41), 13352-13361.
165. Zang, D.; Tarafdar, S.; Tarasevich, Y. Y.; Dutta Choudhury, M.; Dutta, T., Evaporation of a Droplet: From physics to applications. *Physics Reports* **2019**, *804*, 1-56.
166. Yoo, H.; Kim, C., Experimental studies on formation, spreading and drying of inkjet drop of colloidal suspensions. *Colloids Surf., A* **2015**, *468*, 234.
167. Chen, J.; Liao, W.-S.; Chen, X.; Yang, T.; Wark, S. E.; Son, D. H.; Batteas, J. D.; Cremer, P. S., Evaporation-Induced Assembly of Quantum Dots into Nanorings. *ACS Nano* **2009**, *3* (1), 173-180.
168. Dugas, V.; Broutin, J.; Souteyrand, E., Droplet evaporation study applied to DNA chip manufacturing. *Langmuir* **2005**, *21*, 9130.
169. Sefiane, K., On the Formation of Regular Patterns from Drying Droplets and Their Potential Use for Bio-Medical Applications. *Journal of Bionic Engineering* **2010**, *7*, S82-S93.
170. Bhardwaj, R.; Agrawal, A., Likelihood of survival of coronavirus in a respiratory droplet deposited on a solid surface. *Physics of Fluids* **2020**, *32* (6), 061704.
171. Zhang, J.; Mahalanabis, M.; Liu, L.; Chang, J.; Pollock, N.; Klapperich, C., A disposable microfluidic virus concentration device based on evaporation and interfacial tension. *Diagnostics* **2013**, *3*, 155.

172. Semenov, S.; Starov, V. M.; Velarde, M. G.; Rubio, R. G., Droplets evaporation: Problems and solutions. *The European Physical Journal Special Topics* **2011**, *197* (1), 265.
173. Larson, R. G., Transport and deposition patterns in drying sessile droplets. *AIChE J.* **2014**, *60* (5), 1538-1571.
174. Stauber, J. M.; Wilson, S. K.; Duffy, B. R.; Sefiane, K., Evaporation of droplets on strongly hydrophobic substrates. *Langmuir* **2015**, *31*, 3653.
175. Deegan, R. D.; Bakajin, O.; Dupont, T. F.; Huber, G.; Nagel, S. R.; Witten, T. A., Capillary flow as the cause of ring stains from dried liquid drops. *Nature* **1997**, *389*, 827.
176. Li, Y.; Diddens, C.; Segers, T.; Wijshoff, H.; Versluis, M.; Lohse, D., Evaporating droplets on oil-wetted surfaces: Suppression of the coffee-stain effect. *Proceedings of the National Academy of Sciences* **2020**, *117* (29), 16756-16763.
177. Takhistov, P.; Chang, H., Complex Stain Morphologies. *Ind. Eng. Chem. Res.* **2002**, *41*, 6256.
178. Shin, B.; Moon, M. W.; Kim, H. Y., Rings, Igloos, and Pebbles of Salt Formed by Drying Saline Drops. *Langmuir* **2014**, *30*, 12837.
179. Zhang, J.; Borg, M. K.; Sefiane, K.; Reese, J. M., Wetting and evaporation of salt-water nanodroplets: A molecular dynamics investigation. *Physical Review E* **2015**, *92* (5), 052403.
180. Zhong, X.; Ren, J.; Duan, F., Wettability Effect on Evaporation Dynamics and Crystalline Patterns of Sessile Saline Droplets. *The Journal of Physical Chemistry B* **2017**, *121* (33), 7924-7933.
181. Hu, H.; Larson, R. G., Analysis of the Effects of Marangoni Stresses on the Microflow in an Evaporating Sessile Droplet. *Langmuir* **2005**, *21* (9), 3972-3980.
182. Efstratiou, M.; Christy, J.; Sefiane, K., Crystallization-Driven Flows within Evaporating Aqueous Saline Droplets. *Langmuir* **2020**, *36* (18), 4995-5002.
183. Hatte, S.; Pandey, K.; Pandey, K.; Chakraborty, S.; Basu, S., Universal evaporation dynamics of ordered arrays of sessile droplets. *J. Fluid Mech.* **2019**, *866*, 61-81.
184. Yu, Y.-S.; Yang, Z.; Zhao, Y.-P., Role of Vertical Component of Surface Tension of the Droplet on the Elastic Deformation of PDMS Membrane. *J. Adhes. Sci. Technol.* **2008**, *22* (7), 687-698.
185. Nguyen, T. A. H.; Nguyen, A. V.; Hampton, M. A.; Xu, Z. P.; Huang, L.; Rudolph, V., Theoretical and experimental analysis of droplet evaporation on solid surfaces. *Chem. Eng. Sci.* **2012**, *69*, 522.
186. Carrier, O.; Shahidzadeh-Bonn, N.; Zargar, R.; Aytouna, M.; Habibi, M.; Eggers, J.; Bonn, D., Evaporation of water: evaporation rate and collective effects. *J. Fluid Mech.* **2016**, *798*, 774-786.
187. Laghezza, G.; Dietrich, E.; Yeomans, J. M.; Ledesma-Aguilar, R.; Kooij, E. S.; Zandvliet, H. J. W.; Lohse, D., Collective and convective effects compete in patterns of dissolving surface droplets. *Soft Matter* **2016**, *12* (26), 5787-5796.
188. Don, W. G.; Robert, H. P., *Perry's Chemical Engineers' Handbook, Eighth Edition*. 8th ed. / ed.; McGraw-Hill Education: New York, 2008.
189. An, D. T.; Teng, T. T.; Sangster, J. M., Vapour pressures of CaCl<sub>2</sub>-NaCl-H<sub>2</sub>O and MgCl<sub>2</sub>-NaCl-H<sub>2</sub>O at 25 °C. Prediction of the water activity of supersaturated NaCl solutions. *Can. J. Chem.* **1978**, *56* (14), 1853-1855.
190. Hilder, M. H.; van den Tempe, M., Diffusivity of water in groundnut oil and paraffin oil. *Journal of Applied Chemistry and Biotechnology* **1971**, *21* (6), 176-178.
191. Benavides, A. L.; Aragonés, J. L.; Vega, C., Consensus on the solubility of NaCl in water from computer simulations using the chemical potential route. *The Journal of Chemical Physics* **2016**, *144* (12), 124504.



192. Vitagliano, V.; Lyons, P. A., Diffusion Coefficients for Aqueous Solutions of Sodium Chloride and Barium Chloride. *JACS* **1956**, *78* (8), 1549-1552.
193. Bhamidi, V.; Kenis, P. J. A.; Zukoski, C. F., Probability of Nucleation in a Metastable Zone: Induction Supersaturation and Implications. *Cryst. Growth Des.* **2017**, *17*, 1132.
194. Bhamidi, V.; Varanasi, S.; Schall, C. A., Measurement and Modelling of Protein Crystal Nucleation Kinetics. *Cryst. Growth Des.* **2002**, *2*, 395.
195. Gao, Y.; Yu, L. E.; Chen, S. B., Efflorescence Relative Humidity of Mixed Sodium Chloride and Sodium Sulfate Particles. *The Journal of Physical Chemistry A* **2007**, *111* (42), 10660-10666.
196. Nakamuro, T.; Sakakibara, M.; Nada, H.; Harano, K.; Nakamura, E., Capturing the Moment of Emergence of Crystal Nucleus from Disorder. *JACS* **2021**, *143* (4), 1763-1767.
197. Jiang, H.; Haji-Akbari, A.; Debenedetti, P. G.; Panagiotopoulos, A. Z., Forward flux sampling calculation of homogeneous nucleation rates from aqueous NaCl solutions. *The Journal of Chemical Physics* **2018**, *148* (4), 044505.